

Acta Universitatis  
Lappeenrantaensis  
826



Raimo Juntunen

## LCL FILTER DESIGNS FOR PARALLEL-CONNECTED GRID INVERTERS

---



Raimo Juntunen

## **LCL FILTER DESIGNS FOR PARALLEL-CONNECTED GRID INVERTERS**

Thesis for the degree of Doctor of Science (Technology) to be presented with  
due permission for public examination and criticism in the lecture hall 2303  
at Lappeenranta University of Technology, Lappeenranta, Finland on the 4<sup>th</sup> of  
December 2018, at noon.

Acta Universitatis  
Lappeenrantaensis 826

Supervisors	Professor Pertti Silventoinen LUT School of Energy Systems Lappeenranta University of Technology Finland
	Professor Olli Pyrhönen LUT School of Energy Systems Lappeenranta University of Technology Finland
	Professor Juha Pyrhönen LUT School of Energy Systems Lappeenranta University of Technology Finland
Reviewers	Senior principal scientist, Adjunct professor Lennart Harnefors ABB Department of Electric Power and Energy Systems KTH Royal Institute of Technology Sweden
	Associate professor Tamás Kerekes Department of Energy Technology Aalborg University Denmark
Opponent	Senior principal scientist, Adjunct professor Lennart Harnefors ABB Department of Electric Power and Energy Systems KTH Royal Institute of Technology Sweden

ISBN 978-952-335-298-8  
ISBN 978-952-335-299-5 (PDF)  
ISSN-L 1456-4491  
ISSN 1456-4491

Lappeenrannan teknillinen yliopisto  
LUT Yliopistopaino 2018

# Abstract

Raimo Juntunen

**LCL Filter Designs for Parallel-Connected Grid Inverters**

Lappeenranta 2018

256 pages

Acta Universitatis Lappeenrantaensis 826

Dissertation Lappeenranta University of Technology

ISBN 978-952-335-298-8, ISBN 978-952-335-299-5 (PDF), ISSN-L 1456-4491, ISSN 1456-4491

Power generation has become more dispersed as a result of the increasing popularity of the renewable energy sources, which interface with the utility grid with power electronic converters. Higher power levels can be achieved by using parallel-connected inverters, which require at least individual inductors.

This doctoral dissertation studies *LCL* filter designs in parallel-connected grid inverters at a system level. The component optimization is not covered in the study. However, some implications of the component design are discussed. It is investigated how the filter design differs from the single inverter case, and the analysed filter topologies are compared to find differences between them.

Different filter configurations were modelled and a theoretical study of the filter designs was made to compare the resonance frequencies, the effects of parallel connection of the filters, and the energies stored in the filter components. Simulations were made to verify the calculations and to test the effect of component value tolerances.

In general, the filter design is in many ways similar for both the single inverter and the parallel-connected inverters. However, parallel-connected inverters have differences that either lead to special design constraints or increased degrees of freedom in the design. With parallel-connected inverters, the resonance interaction between the inverters has to be addressed in the design process. Some of the filter components can be common for all inverters, which reduces the redundancy but increases the modularity of the configuration. Furthermore, the parallel connection also provides a topology-related means to reduce the sizes of the filter components.

The *LCL* filter designs present different levels of modularity in the design, which gives more freedom for the designer to choose the most suitable filter design for the system.

Keywords: Grid inverter, *LCL* filter, resonance frequency, component energy



## Acknowledgements

As I was close to graduating as a M.Sc. (Tech) in summer 2011, I felt that I did not know enough. It was clear to me that I want to know more about power electronic converters and their applications. The first couple of years of my doctoral studies consisted of working in projects that focused on the design and manufacture of robust power electronics. Although I learned a lot, these projects did not really push my research forward. In 2014 I stumbled on grid filter designs and parallel-connected inverters and realized that it was an interesting topic that could also benefit from my contribution. The work of this dissertation was carried out between 2014 and 2018. From February 2016 onwards, the project was more of a hobby as I moved to work in the industry; nevertheless, I wanted to finish what I started.

I want to thank my supervisors, especially professor Pertti Silventoinen, who has been very encouraging and has given me great support in the course of this long work/ hobby. His belief in me helped also me to believe that I will complete this work. In addition, I could not have done this work without the guidance of Dr. Juhamatti Korhonen, with whom I started working on this research topic and who has been providing help and guidance throughout the whole project—Thank you.

I wish to thank my colleagues and friends from the time at LUT. Especially, Dr. Arto Sankala and Dr. Janne Hannonen gave me good comments that helped me to improve my dissertation. My thanks go to Dr. Mikko Qvintus (né Purhonen); our prototype setup allowed me to perform experiments for my dissertation also. I also thank by boss Mr. Mikko Valtee and my colleagues for their support during this project.

I would like to thank the Walter Ahlström Foundation, the Ulla Tuominen Foundation, and the Research Foundation of Lappeenranta University of Technology for the grants that allowed me for instance to travel to conferences to present my research and to learn what others had done.

I want to thank my parents for their support during this endeavour.

Finally, first and foremost, I would like to express my gratitude to my wife Viivi and daughter Aliisa. They both carried me through the toughest part of the work; my wife was adamant that I must finish this, and my daughter did not like it when I was not always able to play with her. I did not like it either. I know, this took too much time and I thank you from the bottom of my heart for your patience. I love you both.

Raimo Juntunen  
31st October 2018  
Ylöjärvi, Finland



*Oves luki vedä, mä työnsin sen auki.*

*- Elastinen*



# Contents

## Abstract

## Acknowledgements

## Contents

<b>Nomenclature</b>	<b>13</b>
<b>1 Introduction</b>	<b>19</b>
1.1 Motivation of the work .....	22
1.2 Objective of the work .....	22
1.3 Research methods.....	23
1.4 Scientific contribution .....	23
1.5 Scientific publications .....	23
<b>2 Filtering and control of grid-connected inverters</b>	<b>25</b>
2.1 Harmonics of inverter output voltage.....	25
2.2 Space vectors and transformations .....	29
2.3 Grid filters .....	32
2.3.1 Simple line inductance .....	32
2.3.2 High-order filters.....	33
2.4 Common-mode filtering .....	38
2.5 General grid filter design constraints .....	40
2.5.1 Limits for harmonic current emissions .....	41
2.5.2 General <i>LCL</i> filter design guidelines .....	43
2.6 Design of grid inverter control .....	47
2.6.1 Synchronous reference frame PI control.....	47
<b>3 LCL filter configurations for paralleled inverters</b>	<b>57</b>
3.1 Assumptions and framework for the comparative analysis.....	58
3.2 Modelling of parallel-connected inverters .....	59
3.2.1 <i>N</i> parallel-connected identical inverters with <i>LCL</i> filters .....	60
3.2.2 <i>LC</i> and <i>LLCL</i> filters .....	64
3.2.3 Individual <i>L</i> -filters and common <i>C</i> and <i>L</i> .....	65
3.2.4 Open-end grid inverter with the <i>LCL</i> filter .....	67
3.3 Component dimensioning and resonance frequencies .....	68
3.3.1 Resonance frequencies .....	69
3.3.2 Resonance shift resulting from parallel connection .....	70
3.3.3 Resonance interaction between the inverters .....	76
3.4 Comparison of the physical sizes of filter components.....	81
3.4.1 Changing the capacitor and grid-side inductor value.....	90
3.4.2 Average filter designs .....	101

3.5	Open-end v. two paralleled inverters .....	104
3.5.1	Attenuation and components.....	107
3.5.2	Practical limitations of the open-end system .....	112
3.6	Distinct filter components .....	113
3.6.1	Circulating current .....	115
3.6.2	Resonances.....	117
3.7	Modularity.....	130
3.8	Discussion and Conclusion – Chapter 3 .....	134
3.8.1	Components and modularity .....	135
3.8.2	Resonances.....	135
3.8.3	Energy .....	137
3.8.4	Open-end inverter .....	138
3.8.5	Conclusion .....	139
<b>4</b>	<b>Simulations and experimental tests</b>	<b>141</b>
4.1	Closed-loop system stability .....	141
4.1.1	Parallel-connected inverters .....	141
4.1.2	Open-end inverter .....	147
4.2	Simulations.....	148
4.2.1	Control system .....	150
4.2.2	Identical filters .....	151
4.2.3	Distinct filter values .....	166
4.2.4	Open-end inverter .....	186
4.3	Experimental tests .....	203
4.3.1	Measurement of parallel-connected inverters .....	205
4.3.2	Open-end grid inverter .....	207
4.4	Discussion and Conclusion – Chapter 4 .....	210
4.4.1	Identical filter parameters .....	211
4.4.2	Distinct filters .....	213
4.4.3	Open-end inverter .....	215
<b>5</b>	<b>Discussion and Conclusion</b>	<b>219</b>
<b>References</b>		<b>223</b>
<b>Appendix A: Model derivations for a single inverter</b>		<b>236</b>
<b>Appendix B: Model derivation for paralleled inverters</b>		<b>239</b>
<b>Appendix C: Per-unit values</b>		<b>245</b>
<b>Appendix D: Nominal resonance frequencies</b>		<b>246</b>
<b>Appendix E: Derivation of phasor equations</b>		<b>247</b>
<b>Appendix F: Filter fundamental energies</b>		<b>250</b>

<b>Appendix G: Randomized tolerances</b>	<b>251</b>
<b>Appendix H: Basic simulation models</b>	<b>252</b>



## Nomenclature

### Latin alphabet

<i>A</i>	Area, cross-sectional area	$\text{m}^2$
<i>a</i>	Lower limit for random number calculation	—
<i>B</i>	Magnetic flux density	$\text{Vs}/\text{m}^2$
<i>b</i>	Upper limit for random number calculation	—
<i>C</i>	Capacitance	$\text{F}$
<i>C</i>	Control flag	—
<i>E</i>	Energy	$\text{J}$
<i>e</i>	Grid voltage matrix	$\text{V}$
<i>f</i>	Frequency	$\text{Hz}$
<i>G</i>	Transfer function	—
<b>G</b>	Complex transfer function matrix	—
<i>h</i>	Integer harmonic of fundamental frequency	—
<i>H</i>	Maximum harmonic number	—
<i>i</i>	Current	$\text{A}$
<b>i</b>	Complex current vector	$\text{A}$
<i>j</i>	Complex variable	—
<i>k</i>	Gain, index number	—
<i>L</i>	Inductance	$\text{H}$
<b>L</b>	Loop transfer function matrix	—
<i>M</i>	Measurement flag	—
<i>m</i>	Modulation index	—
<i>n</i>	Number of parallel-connected inverters, integer multiple	—
<i>N</i>	Number of winding turns	—
<i>P</i>	Active power	$\text{W}$
<i>P</i>	Pole transfer function	—
pu	per-unit	—
<b>Q</b>	Reactive power	$\text{VAr}$
<i>r</i>	Random number	—
<b>S</b>	Apparent power	$\text{VA}$
<i>t</i>	Time	$\text{s}$
<b>T</b>	Closed-loop transfer function matrix	—
<i>u</i>	Voltage	$\text{V}$
<b>u</b>	Complex-valued voltage vector	$\text{V}$
<b>v</b>	Voltage vector	$\text{V}$
<b>W</b>	Cross-coupling matrix	$\Omega$
<i>x</i>	Phase variable of a three-phase system	—
<i>x</i>	Time variance of the carrier wave	$\text{rad}$
<i>x</i>	Design factor	—
<i>Y</i>	Admittance	$\text{S}$
<i>y</i>	Time variance of the fundamental	$\text{rad}$

<b>Y</b>	Complex-valued admittance function matrix	—
<b>Z</b>	Impedance	$\Omega$
<b>Z</b>	Complex-valued impedance vector, impedance function matrix	$\Omega$

**Greek alphabet**

$\gamma$	Design factor	—
$\Delta$	Change in variable, tolerance matrix	—
$\delta$	Change in variable	—
$\eta$	Efficiency	—
$\theta$	Phase angle, displacement angle	rad
$\zeta$	Damping factor	—
$\varphi$	Phase shift angle	rad
$\omega$	Electric angular frequency	rad/s

**Superscripts**

*	Reference	—
dq	Synchronous reference frame, direct-quadrature axis	—
s	Stationary reference frame	—

**Subscripts**

1	Inverter-side, index number 1, fundamental harmonic
2	Grid-side, index number 2
2Par	Two paralleled
3	Index number 3
4	Index number 4
5	Index number 5
6	Index number 6
0	No load (losses), zero-sequence
10%	10 % current ripple
15%	15 % current ripple
25%	25 % current ripple
+	Positive node
-	Negative node
$\alpha$	Real component of a complex-valued variable
$\beta$	Imaginary component of a complex-valued variable
A	Phase A
a	Non-invertible all-pass
ad	Active damping
B	Bandwidth, phase B
b	Base
C	Capacitor, phase C, capacitor branch
c	Carrier, cross coupling, control

cc	Current controller
Cu	Copper (losses)
CM	Common-mode
cap	Capacitive
core	Inductor core
cross	Cross coupling
d	Direct-axis component in synchronous reference frame, diagonal, decoupled
d	Damping, delay
DC	DC link, DC
DM	Differential-mode
diff	Difference
est	Estimated
ext	External
g	Grid
f	Filter
flag	Trigger flag
h	Harmonic index number
i	Integral (gain), Integration (time)
ident	Identical
identical	Identical
in	Internal, input
ind	Inductive
j	Index for source
k	Index for target, short-circuit voltage
L	Inductor, inductance, $L$ -filter configuration
LC	$LC$ filter configuration, capacitor branch inductor
LCL	$LCL$ filter configuration
LLCL	$LLCL$ filter configuration
L-L	Line-to-line
L1	Inverter-side inductor
L2	Grid-side inductor
Lg	Grid inductance
lp	Low-pass
Lump	Lumped
m	Index number variable
m	Minimum-phase, magnetizing
max	Maximum
min	Minimum
n	Index number variable, nominal value
nom	Nominal
OE	Open-end
oe	Open-end
on	On-time (conduction) value
out	Output

---

p	Proportional (gain), pole
parN	Paralleled with $N-1$ units
parN2	Paralleled with $N-2$ units
peak	Peak value
ph	Phase quantity
ph-ph	Phase-to-phase quantity
pll	Phase-locked loop
pri	Primary
PWM	Pulse-width modulation
q	Quadrature-axis component in synchronous reference frame
r	Resonance
rc	Resonance, cross coupling
ref	Reference
rms	Root mean square
s	Sample (time), snubber
sc	Short circuit
sw	Switching
sec	Secondary
single	Single inverter
Th	Thevenin's equivalent
tol	Tolerance
tolerance	Tolerance
tot	Total
update	Updating trigger signal
x	Phase variable of a three-phase system
y	Phase to neutral

**Abbreviations**

2L	Two-level
2Par	Two inverters in parallel
3L	Three-level
5L	Five-level
AC	Alternating current
BTB	Back-to-back
CM	Common-mode
DC	Direct current
DFIG	Doubly-fed induction generator
DM	Differential-mode
DSP	Digital signal processor
FC	Fuel cell
FPGA	Field-programmable gate array
GI	Grid inverter
HV	High-voltage

IEC	International Electrotechnical Commission
IEEE	Institute of Electrical and Electronics Engineers
IGBT	Insulated gate bipolar transistor
IMC	Internal model control
<i>LC</i>	Inductance ( <i>L</i> ) - capacitance ( <i>C</i> ) circuit
<i>LCL</i>	Inductance ( <i>L</i> ) – capacitance ( <i>C</i> ) – inductance ( <i>L</i> ) circuit
<i>LLCL</i>	Inductance ( <i>L</i> ) – inductance ( <i>L</i> ) and capacitance ( <i>C</i> ) – inductance ( <i>L</i> ) circuit
LHP	Left-half-plane
LV	Low-voltage
MV	Medium-voltage
MIMO	Multiple input multiple output
NP	Neutral point
PEC	Power electronic converter
PI	Proportional-integral
PR	Proportional-resonant
PLL	Phase-locked loop
PWM	Pulse-width modulation
PV	Photovoltaic
RB	Rectifier bridge
RHP	Right-half-plane
rms	Root mean square
VSC	Voltage source converter
VSI	Voltage source inverter
SCR	Short-circuit ratio
SG	Synchronous generator
SP	Solar power
SRF	Synchronous reference frame
SRF-PLL	Synchronous reference frame phase-locked loop
SPWM	Sinusoidal pulse width modulation
SVM	Space vector modulation
SVPWM	Space vector pulse width modulation
TDD	Total demand distortion
THD	Total harmonic distortion
WP	Wind power
ZCM	Zero common-mode
ZVS	Zero zero-sequence voltage



## 1 Introduction

The energy generation is undergoing a transformation from conventional centralized production towards more distributed production systems, in which an increasing proportion of the energy is produced in smaller, dispersed units (Figure 1.1). In Europe, the main driving force in the increase in the penetration of distributed generation (DG) has been the European Union's (EU) 20-20-20 policy, which obliges the member countries to increase renewable energy generation, cut emissions, and enhance energy efficiency by 20 % by the year 2020. In the road map for 2050, the aims are being set even higher (the Ministry of Employment and the Economy, Finland, 2013). In addition, the Fukushima nuclear accident in 2011 caused Germany to shut down its nuclear power generation on a large scale. Major contributors in this transformation are micro-turbines and renewable energy sources, such as wind power (WP), solar power (SP), and fuel cell technology (FC). National subsidy policies and global awareness of the climate change have contributed to the increase in the renewable energy generation. As the cost of solar panels and power electronics has decreased, small-scale solar power production has become an attractive choice for house owners and small businesses.

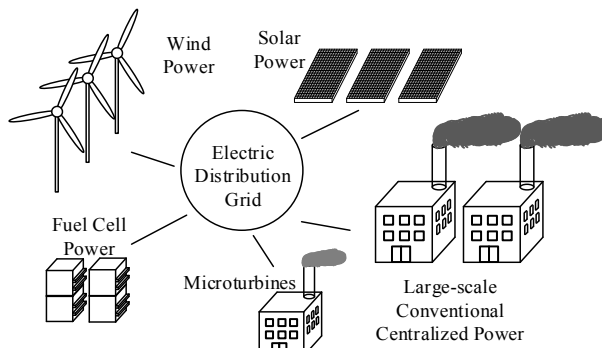


Figure 1.1. Power generation system with conventional large-scale production units and multiple distributed generation units.

A common property of the renewable sources is that they typically interface the grid with power electronic converters (PEC) instead of conventional synchronous generators (SG) as in micro-turbines (Teodorescu et al., 2011) (Kirubakaran et al., 2011). Full back-to-back (BTB) converters are used in wind power to control both the generator and the grid-injected current (Figure 1.2), whereas solar power and fuel cells can operate with a grid inverter bridge. However, both solar power and fuel cells may need power electronic converters to boost the DC link voltage to adequate levels. The full-scale power converter in Figure 1.2 consists of a rectifier bridge (RB), a common DC link, and a grid inverter (GI). In addition, some wind generators such as doubly-fed induction generators (DFIG) require power converters, which commonly have to be dimensioned to meet only 30 % of the generator power (Zhi and Xu, 2007).

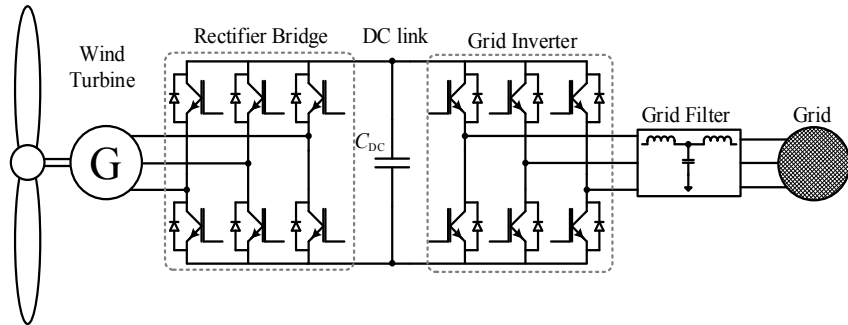


Figure 1.2. Wind turbine connected to the utility grid with a full-scale power electronic converter and a grid filter. The power converter is a conventional two-level (2L) converter.

With the increasing demand for energy, also the unit size of the distributed generation increases (Borrega et al., 2013) (Isidori et al., 2014). With the low-voltage (LV) semiconductor technology, the currents with high power become large, which results in larger components and cables. Medium-voltage (MV) and high-voltage (HV) semiconductor technologies have emerged in high-power applications, but their disadvantage is their fairly low switching frequency (Abu-Rub et al., 2010). As a solution to this problem, multilevel (MV) inverter technology has gained attention (Franquelo et al., 2008). Capable of operating at low switching frequencies for single switching devices, the multilevel inverters also produce less harmonics, which allows the use of smaller filters (Holmes and Lipo, 2003). With a higher number of levels, the inverter voltage is a more accurate approximation of the sinusoidal reference (Figure 1.3)

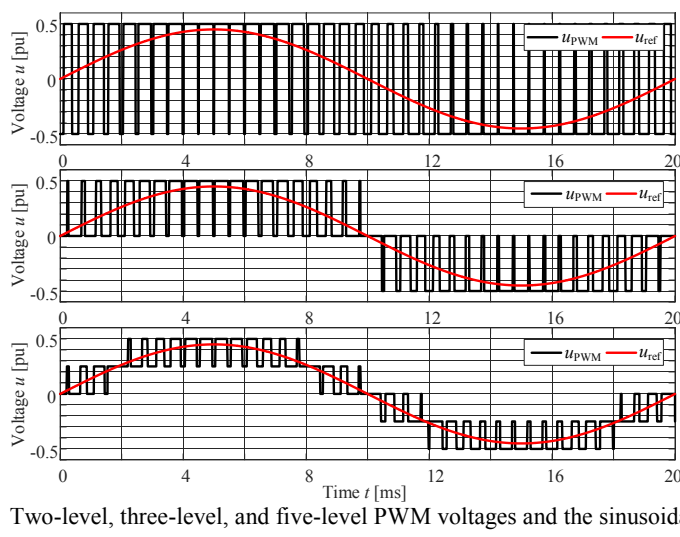


Figure 1.3. Two-level, three-level, and five-level PWM voltages and the sinusoidal references.

In addition to the multilevel technology, the parallel connection of inverters can be used to increase the power level of the application with lower current ratings of the power electronics. Parallel connection can also enhance the availability of the power generation (Yu and Khambadkone, 2012). If one inverter fails, the other inverters in the system are still available for operation with a partial power proportional to the nominal power even during the maintenance. This power is limited by the power ratings of the functioning inverters. Usually, the parallel-connected inverters share a common transformer but have individual filters. The reasons for this are the high costs of grid frequency transformers and practical issues such as the distance between the inverters. Figure 1.4 illustrates the three most common grid filter topologies.

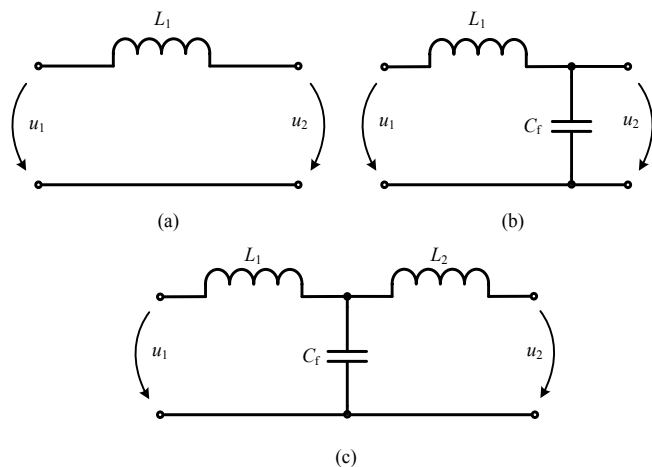


Figure 1.4. Single-phase circuits of the most common filters used at the grid interface: an  $L$ -filter (a), an  $LC$  filter (b), and an  $LCL$  filter (c).  $L_1$  denotes the inverter-side inductor,  $L_2$  the grid-side inductor, and  $C_f$  the filter capacitor. The voltages  $u_1$  and  $u_2$  are the inverter- and grid-side voltages, respectively.

The grid filter has two main functions. It has to attenuate the harmonic voltages and currents produced by the inverter, and it also has to be inductive enough to allow the inverter to be connected safely to a voltage-source-like system such as the utility grid (Teodorescu et al., 2011). The harmonic limits are set by national and international standards, such as IEC 61000-3-2 and IEEE 519-1992/2014. A simple line inductor, or an  $L$ -filter, is adequate for high-switching-frequency applications. However, in high-power applications usually operating with a low switching frequency, the  $L$ -filter results in large and bulky components, which cause an excessive voltage drop in the filter. For this reason, high-order  $LC$  and  $LCL$  filters have become popular as grid filters. Assuming constant component values at all frequencies, the single-order  $L$ -filter provides 20 dB/dec, the second-order  $LC$  filter 40 dB/dec, and the third-order  $LCL$  filter 60 dB/dec attenuation for switching-frequency harmonics. The drawback of high-order filters is their resonance frequencies, which can cause either unwanted gain for harmonics or a control system unbalance.

### **1.1 Motivation of the work**

The increasing energy demand and tighter grid requirements lay emphasis on the efficiency of power generation. In addition, with the high penetration of distributed generation, the reliability and availability of power generation rise in importance. As the demand for power increases, it becomes attractive to use parallel-connected inverters to decrease the required current rating of the power electronics and improve the supply reliability.

Standards such as the IEEE 519-1992/2014 and the IEC EN 61000-3-2 determine limits for the harmonics injected into the grid. In addition, the maximum total harmonic distortion limits are set. Parallel connection of inverters with individual filters provides a variety of opportunities to implement the grid filter, which produces the required attenuation for current harmonics. Filter configurations have distinct qualities, and the feasibility of a certain design in a particular application calls for more research. In addition, the effect of parallel connection on the electrical dimensioning and physical sizes of the filter components has not been studied in detail so far. For instance, parallel connection provides interesting opportunities for topology choices, which affect the filter design requirements.

For practical reasons, a single power electronic converter interfacing the grid is usually designed based on specific assumptions of grid conditions and the operating point. In addition, the design constraints and optimization of a single grid filter are well covered in the literature. However, the effects of the parallel connection on the filter design have not been exhaustively studied. One unit affects the other, which leads to a situation where the operating point differs considerably from the design point. Yet, it remains unclear what kind of an effect this change has on the filter components and the control effectiveness of the grid-connected inverters.

### **1.2 Objective of the work**

The main objective of this doctoral dissertation is to perform a thorough analysis of grid filter designs in parallel-connected inverters. The filter design constraints and the effect of parallel connection on them are analysed. Further, the operating performance is studied by simulations.

The main research questions are:

- Q1: Which are the constraints and design guidelines for the filter design in parallel-connected inverters and how do they differ from conventional constraints?
- Q2: What are the differences of the filter configurations suitable for paralleled grid-connected inverters and how they impact the control design and stability?

### 1.3 Research methods

Analytical calculations are used in the derivation and analysis of the parallel-connected inverter models. Numerical simulations such as Bode plots are used in the analysis of the models. The verification of the models is performed with simulations in a circuit simulator. In addition, simulations are used in the control design and verification. Parallel-connected inverters are simulated and the currents and voltages of the filter components are analysed. This analysis is compared with the analytical results.

### 1.4 Scientific contribution

The scientific contributions of this doctoral dissertation are:

- 1) Analysis of filter design constraints for parallel-connected grid inverters.
- 2) Comparative analysis of different *LCL* filter configurations for parallel-connected grid inverters.
- 3) Analysis of the effect of parallel connection on filter components and their dimensioning.

### 1.5 Scientific publications

This doctoral dissertation contains material from the following papers. The rights have been granted by the publishers to include the material in the dissertation.

- I. Juntunen, R., Korhonen, J., Musikka, T., Smirnova, L., Pyrhönen, O., and Silventoinen, P. (2015), "Identification of resonances in parallel connected grid inverters with LC-and LCL-filters," in *Proceedings of the IEEE 2015 Applied Power Electronics Conference and Exposition (APEC)*, Charlotte NC, pp. 2122–2127.
- II. Juntunen, R., Korhonen, J., Musikka, T., Smirnova, L., Pyrhönen, O., and Silventoinen, P. (2015), "Comparative analysis of LCL-filter designs for paralleled inverters," in *Proceedings of the IEEE 2015 Energy Conversion Congress and Exposition (ECCE)*, Montreal QC, pp. 2664–2672.



## 2 Filtering and control of grid-connected inverters

In this chapter, the filtering in grid-connected inverters is presented in general. The origin of harmonics in the output of pulse-width-modulated inverters as well as basic filter circuits are addressed. In addition, the space vector theory and the basic control system design for a grid-connected inverter is presented for further use in this doctoral dissertation.

### 2.1 Harmonics of inverter output voltage

A voltage-source inverter (VSI) produces the desired output voltage from a suitable combination of voltage pulses. Typically, the PWM method is based on a simple comparison of the reference wave and the carrier wave, which is usually a triangle or sawtooth wave having a much higher frequency than the reference. The result of the comparison is the duty cycle of the inverter switching components. In practice, the  $u_{\text{PWM}}$  in Figure 2.1 is a close approximation of the area above or below 0 of  $u_{\text{ref}}$  for positive and negative half-cycle, respectively. The accuracy of the approximation depends on the switching frequency and the modulation method applied. Multilevel modulation methods use a higher number of voltage levels, included with zero, to produce a closer approximation of the sinusoidal reference signal resulting in inherently better voltage quality than two-level inverters (Holmes and Lipo, 2003).

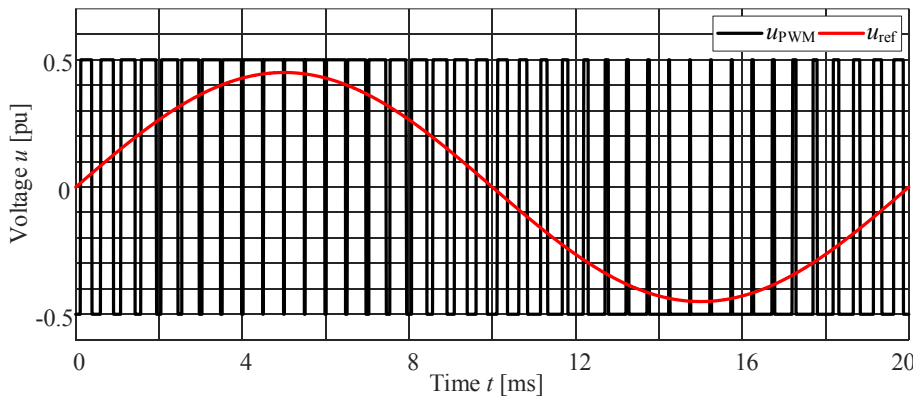


Figure 2.1. Sinusoidal pulse-width-modulated (SPWM) waveform (black) with a sinusoidal reference (red)

The broad-spectrum harmonic content of a PWM-modulated waveform is due to the fast rising edges of the pulses. To illustrate the origin of the harmonics in  $u_{\text{PWM}}$ , an ideal square wave (Figure 2.2), which contains an infinite number of harmonic frequencies, is taken as an example. The square-wave function in Figure 2.2 is a periodic function with a period  $T = 2\pi$ . The function is odd, for which it holds that  $f(-t) = -f(t)$ .

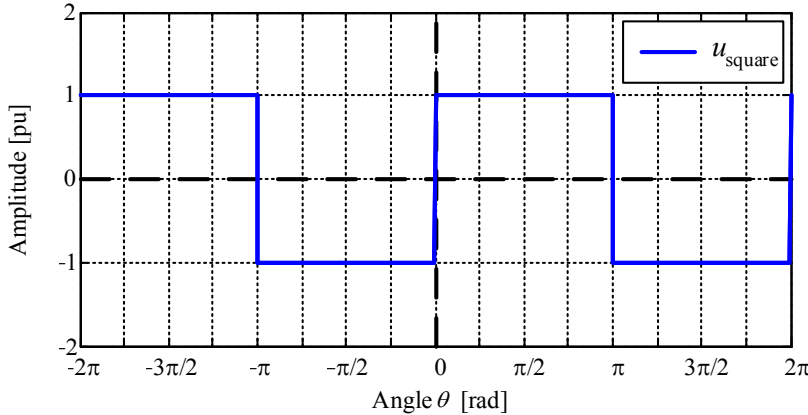


Figure 2.2. Odd square-wave function with an amplitude of 1 and a period of  $2\pi$ .

The Fourier series of periodic functions

$$f(t) = \frac{a_0}{2} + \sum_{n=1}^{\infty} (a_n \cos(n\omega t) + b_n \sin(n\omega t)), \quad (2.3)$$

where  $\omega = 2\pi/T$ , can be used to calculate the amplitudes for each harmonic that exists in the signal. The coefficients  $a_n$  and  $b_n$  of (2.3) can be calculated by

$$a_n = \frac{2}{T} \int_0^T f(t) \cos\left(n \frac{2\pi}{T} t\right) dt \quad (2.4a)$$

$$b_n = \frac{2}{T} \int_0^T f(t) \sin\left(n \frac{2\pi}{T} t\right) dt. \quad (2.4b)$$

Depending on whether  $f(t)$  is even or odd, (2.4a) and (2.4b) can be determined as

$$a_n = \frac{4}{T} \int_0^{T/2} f(t) \cos\left(n \frac{2\pi}{T} t\right) dt \quad (2.5a)$$

$$b_n = 0 \quad (2.5b)$$

for even  $f(t)$  and

$$a_n = 0 \quad (2.6a)$$

$$b_n = \frac{4}{T} \int_0^{T/2} f(t) \sin\left(n \frac{2\pi}{T} t\right) dt \quad (2.6b)$$

for odd  $f(t)$ .

For an odd function, only (2.6b) has to be used for the amplitude calculation of the Fourier series terms. After computing (2.6b) and some manipulation, the coefficient  $b_n$  becomes

$$b_n = \frac{2}{n\pi} (1 - (-1)^n). \quad (2.7)$$

With the substitution of (2.6a) and (2.7) into (2.3), the harmonic content of an odd square-wave function can be calculated by

$$f(t) = \sum_{n=1}^{\infty} \left( \frac{2}{n\pi} (1 - (-1)^n) \sin(n \frac{2\pi}{T} t) \right), \quad (2.8)$$

where  $n = 1, 3, \dots, \infty$ .

Figure 2.3 presents the fundamental component, the sum of the first three odd harmonics, the sum of the first 15 odd harmonics, and the sum of the first 25 odd harmonics, respectively. It can be seen that with the increased number of harmonics summed together, the waveform starts to resemble the square wave in Figure 2.2.

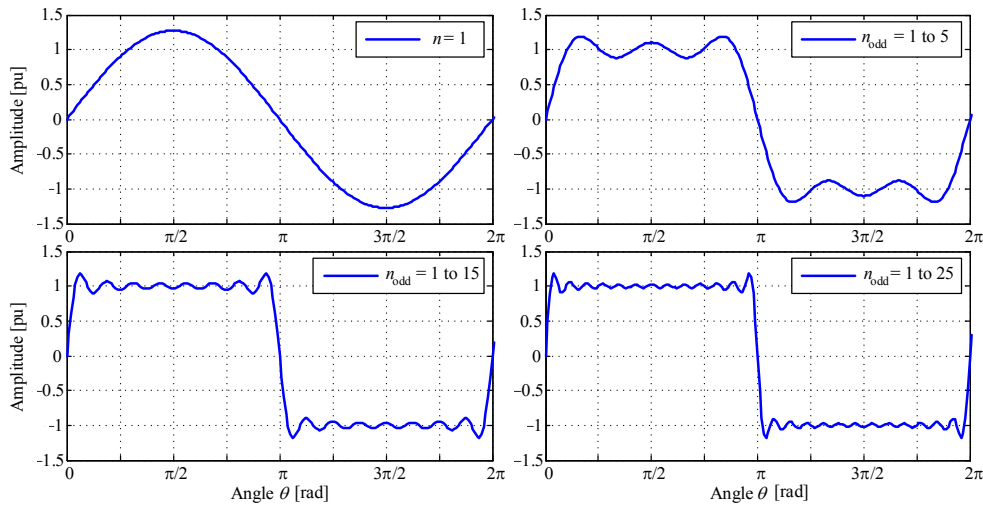


Figure 2.3. Top left figure presents the fundamental with the rms value of 1 pu. The top right and both bottom figures depict the increased number of odd harmonics summed to the fundamental thereby transforming the fundamental sinusoid closer to a square-wave signal.

In practice, the PWM pulses show finite rise times as depicted in Figure 2.4(a). For instance, the rise times for insulated gate bipolar transistors (IGBT) are typically on the scale of 50 ns to 400 ns, depending on the voltage and current ratings of the device (Saunders et al., 1996). The Fourier coefficients of a trapezoid wave decrease with a rate of 20 dB/dec until reaching the bandwidth determined as

$$f_B = \frac{1}{\pi t_r}, \quad (2.9)$$

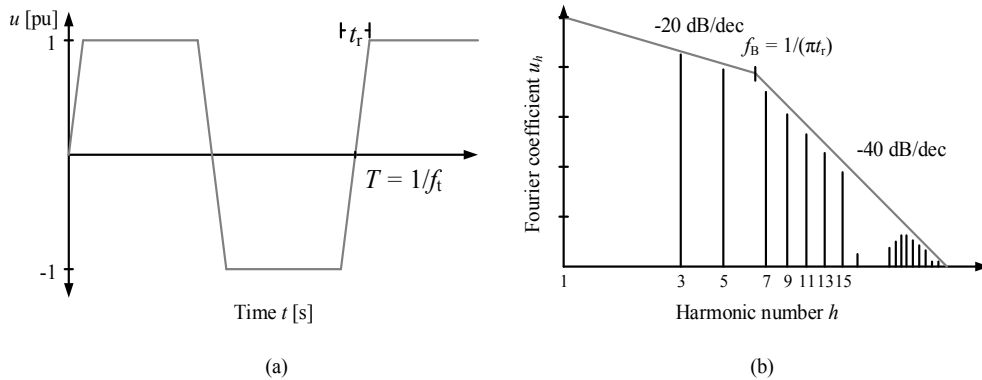


Figure 2.4. (a) Trapezoid wave with a finite rise time  $t_r$  and a frequency  $f_r$ . (b) Envelope of the Fourier coefficients calculated for the trapezoid wave. The amplitudes of the Fourier coefficients decrease by 20 dB/dec until  $f_B$ , after which the amplitudes decrease at a rate of -40 dB/dec (Ott, 1988).

where  $t_r$  is the rise time from the negative peak value to the positive peak value as depicted in Figure 2.4(a). As indicated by (2.9), the faster is the rise time of the pulse, the broader is the harmonic spectrum and the more energy is transferred at higher frequencies (Ott, 1988).

Because of the finite rise times of voltage pulses, the calculation of the Fourier series for an actual PWM waveform becomes a more challenging task. An approach for the PWM waveform harmonic analysis was developed in (Bowes and Bird, 1975). The approach was based on the work of (Bennet, 1933) and (Black, 1953) in communication systems, and it was further analysed in (Holmes and Lipo, 2003). The PWM waveform is a function of two time variables representing the time variation of the carrier and the reference signal. The development for the equations of the following double Fourier series can be found from (Holmes and Lipo, 2003).

The double Fourier series for a general case considering a signal with a period of  $T = 2\pi$  is determined as

$$\begin{aligned} f(x,y) = & \frac{a_{00}}{2} + \sum_{n=1}^{\infty} [a_{0n} \cos(ny) + b_{0n} \sin(ny)] \\ & + \sum_{m=1}^{\infty} [a_{m0} \cos(mx) + b_{m0} \sin(mx)] \\ & + \sum_{m=1}^{\infty} \sum_{n=-\infty}^{\infty} \sum_{(n \neq 0)} [a_{mn} \cos(mx+ny) + b_{mn} \sin(mx+ny)], \end{aligned} \quad (2.10)$$

where  $x = \omega_c t + \theta_c$ , and  $y = \omega_1 t + \theta_1$  describing the time variance of the carrier and the fundamental reference, respectively. The coefficients of the double Fourier series can be calculated from

$$a_{mn} = \frac{1}{2\pi^2} \int_{-\pi}^{\pi} \int_{-\pi}^{\pi} f(x,y) \cos(mx + ny) dx dy \quad (2.11a)$$

$$b_{mn} = \frac{1}{2\pi^2} \int_{-\pi}^{\pi} \int_{-\pi}^{\pi} f(x,y) \sin(mx + ny) dx dy, \quad (2.11b)$$

which in a complex form can be written as

$$a_{mn} + jb_{mn} = c_{mn} = \frac{1}{2\pi^2} \int_{-\pi}^{\pi} \int_{-\pi}^{\pi} f(x,y) e^{j(mx + ny)} dx dy. \quad (2.12)$$

Because modern computers provide substantial computational power, a conventional, heuristic method to analyse the frequency spectrum is the Fast Fourier Transform (FFT) performed for simulated or measured data.

## 2.2 Space vectors and transformations

A three-phase system can be expressed with a complex vector and a real zero sequence component. This vector is commonly known as a space vector. The theory of space vectors was first introduced by Park (1929) and applied to describe the transient behaviour of synchronous machines. In (Stanley, 1938), Park's theory was applied to induction machines and in (Kovács and Rácz, 1959), the mathematical and physical descriptions were presented. Although the space vector theory was intended for electric machines, it can be used to analyse also other systems.

The phase voltages of a three-phase system are

$$u_a(t) = \hat{u}_a \cos(\omega_1 t + \varphi_a) \quad (2.13a)$$

$$u_b(t) = \hat{u}_b \cos(\omega_1 t + \varphi_b) \quad (2.13b)$$

$$u_c(t) = \hat{u}_c \cos(\omega_1 t + \varphi_c), \quad (2.13c)$$

where  $\omega_1$  is the system angular frequency,  $\hat{u}_{a,b,c}$  the peak values of the voltages,  $\varphi_{a,b,c}$  the initial phases of the voltages, and  $\mathbf{u}_{a,b,c}$  are the corresponding phase voltage vectors. The three-phase voltages in (2.13a), (2.13b), and (2.13c) can be expressed as a single complex vector and a real zero sequence component as

$$\mathbf{u}^s = \frac{2}{3} K [u_a(t)e^0 + u_b(t)e^{j2\pi/3} + u_c(t)e^{j4\pi/3}] \quad (2.14a)$$

$$u_0 = \frac{1}{3} K_0 [u_a(t) + u_b(t) + u_c(t)], \quad (2.14b)$$

where the superscript s denotes the stationary reference frame and K and  $K_0$  are scaling factors, which can be determined as

$$\text{peak value scaling} \quad K = K_0 = 1 \quad (2.15a)$$

rms value scaling                     $K = K_0 = \frac{1}{\sqrt{2}}$                     (2.15b)

power invariant scaling             $K = \sqrt{3/2} ; K_0 = \sqrt{3}$ .                    (2.15c)

Figure 2.5 presents the construction of a voltage space vector. The instant values of phase voltage vectors on the axes  $u_a$ ,  $u_b$ , and  $u_c$  can be calculated by (2.13a), (2.13b), and (2.13c), respectively, with the magnitude  $\hat{u}_a = \hat{u}_b = \hat{u}_c = 1$ . The phase angles  $\varphi_a$ ,  $\varphi_b$ , and  $\varphi_c$  are 0,  $-2\pi/3$  and  $-4\pi/3$ , respectively. In Figure 2.5, the space vector angle  $\theta = \omega t = \pi/3$  and the direction of  $u_a$  is chosen to be the direction of the  $\alpha$ -axis component. The scaling factor  $K = 1$  for the peak value scaling. As the instant values of the phase voltages are substituted into (2.14a), the space vector becomes

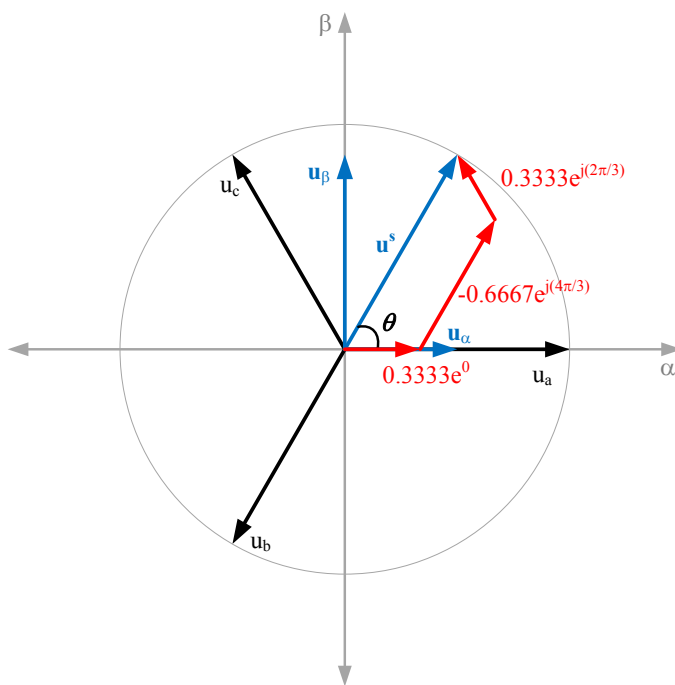


Figure 2.5. Construction of a voltage space vector for a positive-sequence three-phase system. The stationary reference frame is conventionally known as the  $\alpha\beta$  frame. The red vectors represent the components of  $\mathbf{u}^s$  (2.1), which is shown as a blue vector along its real and imaginary components  $\mathbf{u}_\alpha$  and  $\mathbf{u}_\beta$ . The space vector  $\mathbf{u}_s$  real component is aligned with the axis of the phase a.

$$\mathbf{u}^s = \underbrace{\frac{1}{\sqrt{3}} e^0}_{u_a} + \underbrace{\frac{1}{\sqrt{3}} e^{j2\pi/3}}_{u_b} + \underbrace{\left(-\frac{2}{\sqrt{3}}\right) e^{j4\pi/3}}_{u_c} = \frac{1}{\sqrt{3}} + j \frac{\sqrt{3}}{\sqrt{3}}. \quad (2.16)$$

As indicated in Figure 2.5 and (2.1), the space vector  $\mathbf{u}^s$  is a complex-valued vector with two components  $u_\alpha$  and  $u_\beta$  as real and imaginary components, respectively.

### Transformation to a stationary reference frame

The transformation from a three-phase to a two-phase equivalent system was developed in (Clarke, 1943). Commonly, the transformation is known as the Clarke transformation, the equations of which can be computed from (2.14a) by expressing the exponential phase shift operators in a component form. The transformation, including the zero sequence, presented in a matrix form is

$$\begin{bmatrix} u_\alpha \\ u_\beta \\ u_0 \end{bmatrix} = \frac{2}{3} K \underbrace{\begin{bmatrix} 1 & -1/2 & -1/2 \\ 0 & \sqrt{3}/2 & -\sqrt{3}/2 \\ 1/2 & 1/2 & 1/2 \end{bmatrix}}_{T_{\alpha\beta 0}} \begin{bmatrix} u_a \\ u_b \\ u_c \end{bmatrix}. \quad (2.17)$$

The inverse transformation into a three-phase system can be computed by

$$\begin{bmatrix} u_a \\ u_b \\ u_c \end{bmatrix} = \frac{3}{2K} \underbrace{\begin{bmatrix} 2/3 & 0 & 2/3 \\ -1/3 & \sqrt{3}/3 & 2/3 \\ -1/3 & -\sqrt{3}/3 & 2/3 \end{bmatrix}}_{T_{\alpha\beta 0}^{-1}} \begin{bmatrix} u_\alpha \\ u_\beta \\ u_0 \end{bmatrix}. \quad (2.18)$$

If  $u_a + u_b + u_c = 0$ , that is, the system is symmetrical, and there are no current paths for the zero sequence, the bottom row of the transformation matrix  $T_{\alpha\beta 0}$  in (2.1) and the last column of the inverse transformation matrix  $T_{\alpha\beta 0}^{-1}$  in (2.1) can be neglected. Although in real systems there are always some minute differences between the phases, those systems can typically be considered symmetrical with adequate accuracy.

### Transformation into a synchronous reference frame

The Park transformation (Park, 1929) can be used to remove the rotation of the vector by transforming it into a synchronous reference frame, which itself rotates. The synchronous reference frame has a direct axis and a quadrature axis, for which the frame is commonly known as the dq frame. The advantage of this transformation is that it yields constant steady-state DC quantities, for which the controller design is simpler than for AC quantities. The synchronous reference rotates with the angular frequency of  $\mathbf{u}^s$ , which for grid-connected inverters is the fundamental angular frequency of the grid. The Park transformation and the inverse Park transformation can be computed by

$$\begin{bmatrix} u_d \\ u_q \\ u_0 \end{bmatrix} = \underbrace{\begin{bmatrix} \cos(\theta) & \sin(\theta) & 0 \\ -\sin(\theta) & \cos(\theta) & 0 \\ 0 & 0 & 1 \end{bmatrix}}_{T_{dq0}} \begin{bmatrix} u_\alpha \\ u_\beta \\ u_0 \end{bmatrix}. \quad (2.19)$$

and

$$\begin{bmatrix} u_\alpha \\ u_\beta \\ u_0 \end{bmatrix} = \underbrace{\begin{bmatrix} \cos(\theta) & -\sin(\theta) & 0 \\ \sin(\theta) & \cos(\theta) & 0 \\ 0 & 0 & 1 \end{bmatrix}}_{T_{dq0}^1} \begin{bmatrix} u_d \\ u_q \\ u_0 \end{bmatrix}, \quad (2.20)$$

where  $\theta$  is the angle of the space vector calculated by

$$\theta = \int_0^t \omega_1 dt + \theta_0, \quad (2.21)$$

where  $\theta_0$  is the starting angle.

## 2.3 Grid filters

In this chapter, the basic filter topologies are presented and discussed. The idea is to present general, basic information of grid filters so that the analysis made later in this doctoral dissertation can be carried out in a straightforward manner. The pu values are scaled according to the low-power values found in Appendix C.

### 2.3.1 Simple line inductance

The simplest filter is a line inductance, which is most often called an *L*-filter (Figure 2.6). Ideally, the impedance of the inductor increases when the frequency rises, thus raising the attenuation for high-frequency signals. The transfer function matrix of an *L*-filter in the Laplace domain is simply written as

$$\mathbf{Y}_L^s = \begin{bmatrix} \frac{1}{sL_f + R_L} & 0 \\ 0 & \frac{1}{sL_f + R_L} \end{bmatrix}, \quad (2.22)$$

where  $L_f$  is the inductance and  $R_L$  the resistance of the filter component.

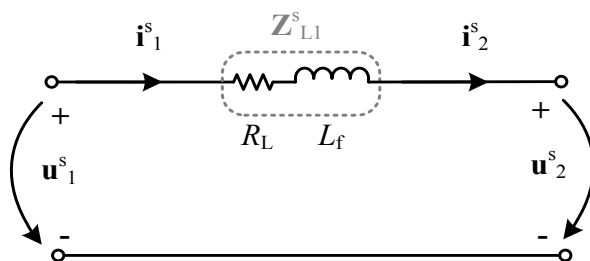


Figure 2.6. Simplified schematic of an *L*-filter. For the sake of consistency, the grid-injected current is represented by the subscript 2 even though the current is the same on both sides of the inductor.

Since the system (2.2) is symmetrical, Figure 2.7 presents the Bode plot of an  $L$ -filter, for only one axis of (2.22). It can be seen that the  $L$ -filter is most suitable for applications with high switching frequencies. In order to get adequate attenuation at low switching frequencies, the inductance of the filter must be significantly increased, which easily leads to impractically large and bulky filter inductors. The attenuation increases with the rate of 20 dB/dec. Naturally, this rate assumes that the inductance is constant over the whole frequency band under study.

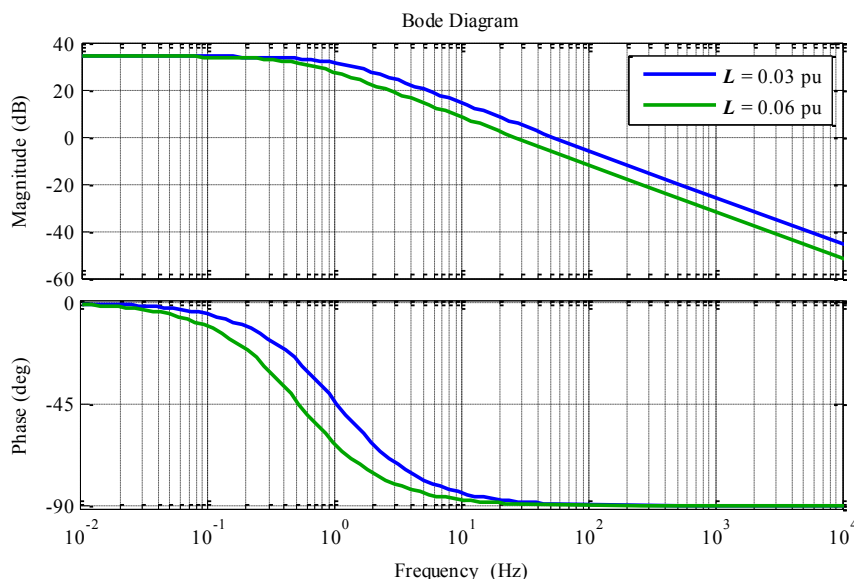


Figure 2.7. Bode plot of an  $L$ -filter with two different values for  $L$ . The blue colour represents an inductance of 0.03 pu and green twice as large an inductance, 0.06 pu. The base values used in this (low-power) case can be found in Appendix C.

### 2.3.2 High-order filters

Figure 2.8 presents equivalent circuits in a stationary reference frame for series and parallel  $LC$  filters. A series connection of inductance and capacitance results in a resonance circuit, which has ideally a zero impedance at the resonance frequency. These series  $LC$  circuits, which are called traps, can be tuned to a specific frequency such as a multiple of the fundamental frequency or the inverter switching frequency. In addition to the series circuits in parallel, the traps can be implemented with parallel  $LC$  circuits in series. The impedance of a parallel resonance circuit at the resonance frequency is ideally infinite, thus blocking all current at the determined frequency. If many frequencies have to be removed, the complexity of the filter arrangement will increase considerably. In addition, the tuning of the traps becomes more challenging, because all the components interact with each other. Since the traps are for a single frequency, they are usually used

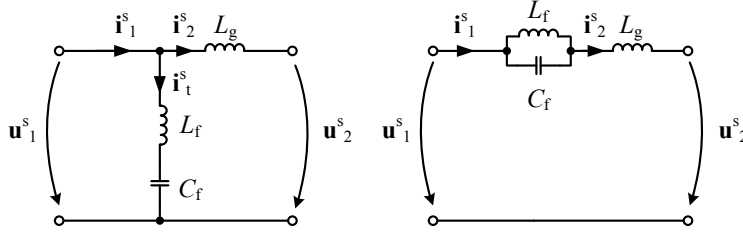


Figure 2.8. Tuned trap filter equivalent circuits. On the left, the series  $LC$  circuit to exclude particular undesired harmonic frequencies from the current  $i_s^s_2$ . On the right, the parallel  $LC$  circuit used to block the frequency corresponding to the resonance frequency of the trap. Both the inductors and capacitors include the component resistances found in the equations.

as additional filters. Commonly, traps are used to remove one or more of the 5<sup>th</sup>, 7<sup>th</sup>, 11<sup>th</sup>, and 13<sup>th</sup> harmonic frequencies before they reach the point of common coupling (PCC). The transfer function matrices for the trap filters connected to an inductive load are

$$\mathbf{Y}_{I,\text{ser}}^s = \begin{bmatrix} \frac{s^2 C_f (L_f + L_g) + s C_f (R_L + R_C + R_g) + 1}{s^3 A + s^2 B + s D + R_g} & 0 \\ 0 & \frac{s^2 C_f (L_f + L_g) + s C_f (R_L + R_C + R_g) + 1}{s^3 A + s^2 B + s D + R_g} \end{bmatrix}, \quad (2.23)$$

where

$$A = C_f L_f L_g \quad (2.24a)$$

$$B = C_f (L_f R_g + L_g (R_L + R_C)) \quad (2.24b)$$

$$D = L_g + C_f R_g (R_L + R_C). \quad (2.24c)$$

$$\mathbf{Y}_{I,\text{par}}^s = \begin{bmatrix} \frac{s^2 C_f L_f + s C_f (R_L + R_C) + 1}{s^3 A + s^2 B + s D + R_L + R_g} & 0 \\ 0 & \frac{s^2 C_f L_f + s C_f (R_L + R_C) + 1}{s^3 A + s^2 B + s D + R_L + R_g} \end{bmatrix}, \quad (2.25)$$

where

$$A = C_f L_1 L_2 \quad (2.26a)$$

$$B = C_f (L_g (R_L + R_C) + L_f (R_C + R_g)) \quad (2.26b)$$

$$D = (C_f (R_g (R_L + R_C) + R_L R_C) + L_f + L_g). \quad (2.26c)$$

Figure 2.9 presents the forward self-admittance functions of both a single series and a single parallel trap. Both of the traps are tuned to remove the 13<sup>th</sup> harmonic of the

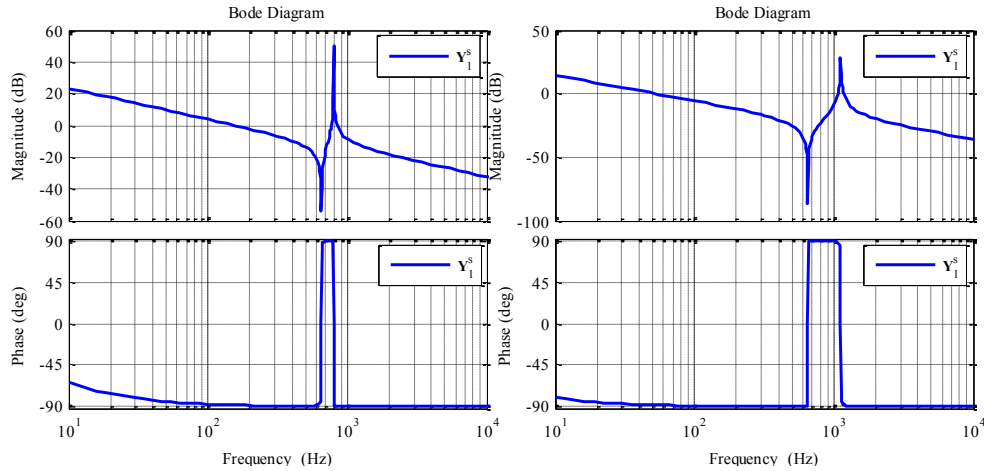


Figure 2.9. Bode plots for  $\mathbf{Y}^s_1$  for the parallel-connected series trap (left) and the series-connected parallel trap (right). The traps are tuned to remove the 13<sup>th</sup> harmonic from the grid-injected current. The fundamental frequency is 50 Hz. The series trap  $C_f = 0.1996$  pu and  $L_f = 0.0196$  pu. For the parallel trap,  $C_f = 0.3012$  pu and  $L_f = 0.0196$  pu.  $L_g = 0.01$  pu for both.

fundamental 50 Hz. Because the traps are connected to an inductive branch ( $L_g$ ), the forward self-transmittance function for both presents a resonance peak, which is caused by the series resonance circuit consisting of the trap and the load branch. Before and after the resonances, the attenuation increases by 20 dB/dec. This is due to the  $L_g$  inductance in the load branch. A much simpler choice for a grid filter is a proper low-pass filter, which provides filter action over the whole frequency range.

Figure 2.10 presents equivalent circuits for  $LC$ ,  $LCL$ , and  $LLCL$  filters, which provide substantial attenuation with fairly small components. Because of the cabling and transformer inductance, the  $LC$  filter and the  $LCL$  filter yield the same attenuation with the distinction that the  $LCL$  filter includes a second inductor. This additional component results in a larger filter arrangement, which in many cases is a drawback of the  $LCL$  filter. However, the grid-side inductor is usually much larger in inductance than the cable and transformer inductances combined. A large enough grid-side inductor provides an opportunity to use a smaller filter capacitor. A trade-off between the grid-side inductor and capacitor dimensioning can have a significant effect on the physical dimensions of the filter components (Rockhill et al., 2011).

The transfer function matrix for an  $LCL$  filter is

$$\mathbf{Y}_{2,LCL}^s = \begin{bmatrix} \frac{sC_fR_C + 1}{s^3A + s^2B + sD + R_1 + R_2} & 0 \\ 0 & \frac{sC_fR_C + 1}{s^3A + s^2B + sD + R_1 + R_2} \end{bmatrix}, \quad (2.27)$$

where

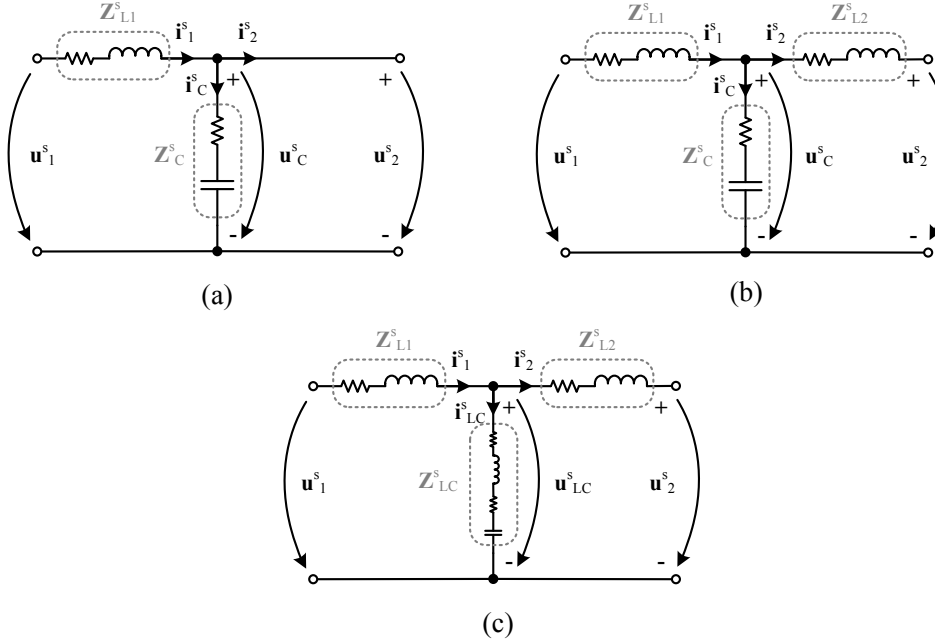


Figure 2.10. High-order filter circuits: an  $LC$  filter (a), an  $LCL$  filter (b), and an  $LLCL$  filter (c). Most popular of these are the  $LC$  and  $LCL$  filter.

$$A = C_f L_1 L_2 \quad (2.28a)$$

$$B = C_f (L_1(R_2 + R_C) + L_2(R_1 + R_C)) \quad (2.28b)$$

$$D = (C_f(R_1(R_2 + R_C) + R_2R_C) + L_1 + L_2). \quad (2.28c)$$

The transfer function matrix for an  $LLCL$  filter is

$$\mathbf{Y}_{2,LLCL}^s = \begin{bmatrix} \frac{sC_f L_C + s(C_f R_C + C_f R_{LC}) + 1}{s^3 A + s^2 B + sD + R_1 + R_2} & 0 \\ 0 & \frac{sC_f L_C + s(C_f R_C + C_f R_{LC}) + 1}{s^3 A + s^2 B + sD + R_1 + R_2} \end{bmatrix}, \quad (2.29)$$

where

$$A = C_f(L_1 L_2 + L_C(L_1 + L_2)) \quad (2.30a)$$

$$B = C_f(L_1(R_2 + R_C + R_{LC}) + L_2(R_1 + R_C + R_{LC}) + L_C(R_1 + R_2)) \quad (2.30b)$$

$$D = (C_f(R_1(R_2 + R_C + R_{LC}) + R_2(R_C + R_{LC})) + L_1 + L_2) \quad (2.30c)$$

In the *LLCL* filter, the capacitor branch includes a series inductance, which increases the order of the filter. All three filters present 60 dB/dec attenuation for the switching frequency and sideband harmonics after the resonance peak. However, for the *LLCL* filter, the series resonance circuit in the capacitor branch causes a resonance sag, which has, ideally, an infinite attenuation. After this second resonance, the attenuation rate of change is 20 dB/dec. The resonance frequency of the  $L_C - C_f$  branch should be set at the switching frequency of the grid inverter to give maximum attenuation for switching frequency harmonics (Wu et al., 2012) (Liu et al., 2012). By doing this, the size of the additional inductance  $L_C$  remains much smaller than the *LCL* filter inductances  $L_1$  and  $L_2$ . In addition, with a low  $L_C$ , the *LLCL* filter resembles the *LCL* filter at low frequencies. The lower  $L_C$  is, the closer to an *LCL* filter the *LLCL* filter is. Figure 2.11 presents the Bode plots of  $\mathbf{Y}^s_2$  for the *LCL* filter and the *LLCL* filter. The filter inductances  $L_1$  and  $L_2$  are kept constant while the  $L_C$  value is presented as a percentage of the summed filter inductance  $L_{\text{tot}} = L_1 + L_2$  to point out the division of the inductance in the filter arrangement.

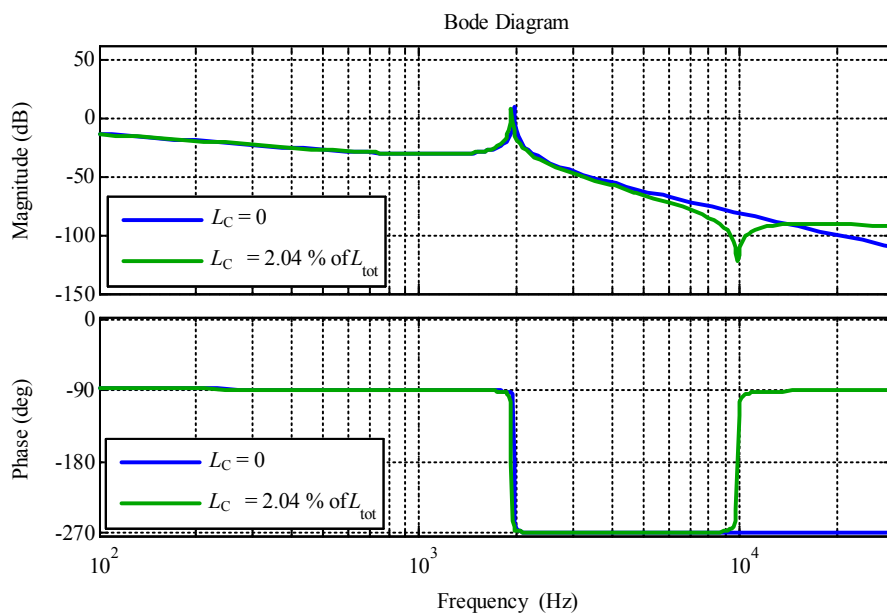


Figure 2.11. Bode plots of  $\mathbf{Y}^s_2$  for *LC/LCL* filters (blue) and an *LLCL* filter (green). The *LLCL* filter provides greater attenuation after the resonance peak. However, it has another resonance frequency, which causes the attenuation to decrease at a lower rate of 40 dB/dec.

The designer can use  $L_C$  to decrease the total series inductance and the capacitance required for adequate filtering (Wu et al., 2012), (Huan et al., 2015). Figure 2.12 presents Bode plots for two cases. On the left, a very small amount of series inductance is added to the *LCL* filter capacitor branch providing an *LLCL* filter with very similar characteristics as the *LCL* filter. In this case, the  $L_C$  only contributes to the increase in the

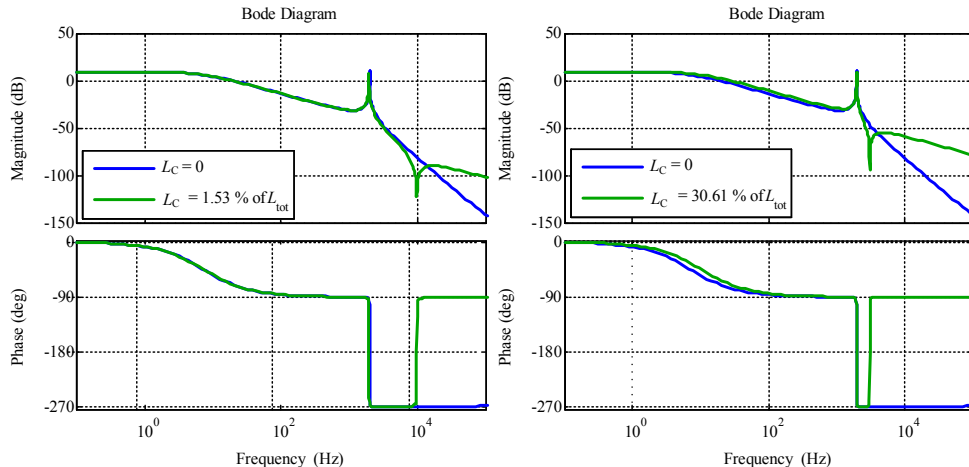


Figure 2.12. Bode plots of  $\mathbf{Y}^s_2$  for an *LCL* filter (blue) and an *LLCL* filter (green) with two different  $L_C$  values. In both cases, the *LLCL* filter is dimensioned to match the *LCL* filter but with the distinction that on the right-hand side Bode plot, the inductors  $L_1$  and  $L_2$  are reduced by 50 %.

total filter inductance. On the right, the *LCL* filter inductances  $L_1$  and  $L_2$  are decreased to half of the *LCL* filter values while  $L_C$  is increased to match the resonance peaks. In this example, the total series inductance of the filter decreases to 50 % of the previous value if a large  $L_C$  is used to match the designs. When  $L_C$  is taken into account, the total inductance of the filter decreases to 64.32 %. As it can be seen from Figure 2.12, the low-frequency characteristics remain quite similar, which means that the use of an *LLCL* filter would not result in increased control difficulties. Naturally, the trade-off that can be achieved between the total series inductance and the size of  $L_C$  is highly dependent on the application. However, in applications with a high power, viz. a high current, the option of using smaller inductances remains a very attractive choice.

## 2.4 Common-mode filtering

Common-mode (CM) voltage, which drives common-mode current, is defined as the average phase voltage as in

$$u_{\text{CM}} = \frac{u_a + u_b + u_c}{3}, \quad (2.31)$$

where  $u_a$ ,  $u_b$ , and  $u_c$  are the phase voltages of a three-phase inverter. The fundamental frequency of the CM voltage is the same as the switching frequency. The CM voltage changes in steps of  $U_{\text{DC}}/3$  for 2L inverters. Figure 2.13 presents a typical  $u_{\text{CM}}$  of a three-phase PWM inverter, which employs SVM for duty cycle calculation. The maximum value for  $u_{\text{CM}}$  is  $U_{\text{DC}}/2$ , which means that the amplitude can be several hundreds of volts in three-phase inverters, and it can cause degradation of the output current quality. Common-mode voltage is a known problem from AC drives, where it causes bearing currents and shaft voltage (Erdman et al., 1996), (Chen et al., 1996), and (Skibinski et al.,

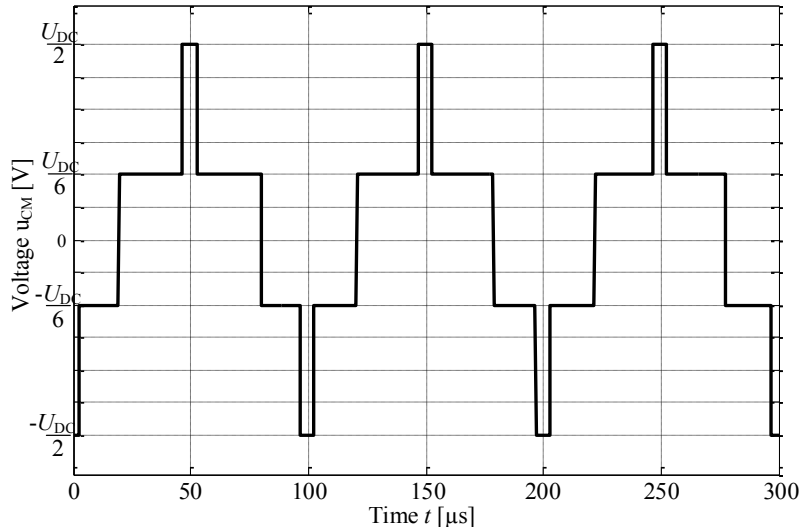


Figure 2.13. Three periods of two-level SVM common-mode voltage. Switching frequency  $f_{sw} = 10$  kHz.

1999). It couples through parasitic capacitances from the stator windings to the rotor and returns through the motor bearings to the stator enclosure, which is grounded. For grid solutions, common-mode voltage can be a problem in large photovoltaic (PV) plants, where the ground capacitance of the solar panel array forms a closed loop between paralleled inverters when the inverters are connected to a common transformer (Purhononen, 2014).

Because the differential-mode (DM) inductance provides poor attenuation of CM current, CM filters should be used. These filters can be separate CM chokes in the output of the inverter (Lai et al., 2010), (Muetze and Sullivan, 2011), and (Heldwein et al., 2011), or they can be implemented with filter capacitors or additional capacitors added to the filter (Heldwein et al., 2010), (Hedayati et al., 2013). Zhu et al. (2012) have used both an integrated CM inductor and a capacitor-based common-mode filter.

A CM choke consists of a shared magnetic core, which the common-mode current magnetizes in the same direction. This leads to a high inductance resisting the common-mode current flow. The same inductor does not resist differential-mode current as much, because the magnetic fluxes cancel each other (Figure 2.14). Although Figure 2.14 presents a two-phase system, a three-phase common-mode choke can be built in the same manner. For an application with high currents such as MW grade inverters, the construction of a CM choke becomes a challenging task because of the high currents, which can cause a very high magnetic flux in a small core leading to impractically large core sizes. Common-mode chokes have been exhaustively studied and reported in the literature (Hemphill and Wallertz, 1995), (Baiju et al., 2004), (Heldwein et al., 2010), (Muetze and Sullivan, 2011), (Lope et al., 2013), and their detailed presentation is out of the scope of this doctoral dissertation.

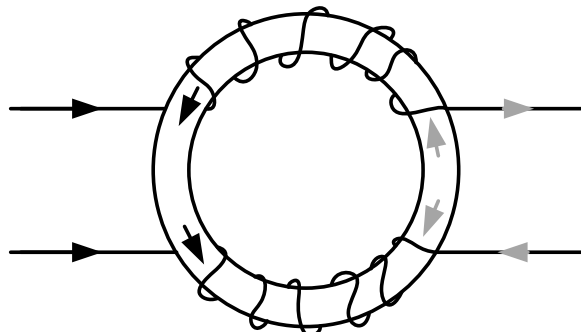


Figure 2.14 Simplified presentation of the common-mode choke. Common-mode current (black) magnetizes the core in the same direction, while differential-mode current (grey) produces opposing magnetization, ideally cancelling each other.

Another method for common-mode filtering in grid inverters can be implemented with capacitors. The path for common-mode current can be achieved by connecting the star point of the filter capacitor to the DC link neutral point or to the DC link minus bus bar (Figure 2.15). For floating star point or delta-connected capacitors, a specific  $C_{CM}$  can be used to common-mode filtering. The objective of this CM filter is to provide a low-impedance current path for the CM current preventing it to be fed to the mains. Heldwein et al. (2010) and Hedayati et al. (2013) present CM filter designs where they have applied this capacitor-based method.

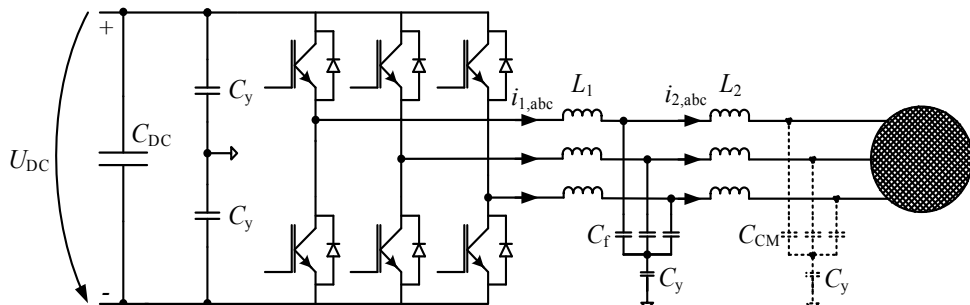


Figure 2.15. Example of common-mode filtering. The filter capacitor  $C_f$  star point is connected through  $C_y$  to the neutral point of the DC link. If the filter capacitor is delta connected or the star-point is left floating, a specific  $C_{CM}$  after the grid filter can be used to produce the path for the common-mode current. This additional filter component is indicated by dashed lines.

## 2.5 General grid filter design constraints

The filter design and analysis comprises the terms ‘total harmonic distortion’ (THD), ‘total demand distortion’ (TDD), and ‘short-circuit ratio’ (SCR), which are determined as follows.

*THD* is the ratio of the root sum square of the harmonic content expressed as a percentage of the fundamental. The *THD* can be calculated by

$$THD = \sqrt{\sum_{h=2}^H \left(\frac{i_h}{i_1}\right)^2}, \quad (2.32)$$

where  $H$  is the maximum number of integer harmonics considered. In Europe  $H = 40$  and in North America  $H = 50$  (IEC, 2009), (IEEE, 2014).

Sometimes, it is advantageous to use weighted *THD* (*WTHD*), which can be calculated as

$$WTHD = \sqrt{\sum_{h=2}^H \left(\frac{i_h/h}{i_1}\right)^2}. \quad (2.33)$$

Similarly to *THD*, *TDD* is the ratio of the harmonic content root sum square expressed as a percentage of the maximum demand current, determined as

$$TDD = \sqrt{\sum_{h=2}^H \left(\frac{i_h}{i_L}\right)^2}. \quad (2.34)$$

The *TDD* is calculated of the 10–30 minute averaged value of load current, which is generally the fundamental component (IEEE, 2014).

*SCR* describes the ratio of the grid-supplied short-circuit current to the rated current of the application, and it is determined as

$$SCR = \frac{i_{sc}}{i_{nom}}, \quad (2.35)$$

where  $i_{sc}$  is the grid short-circuit current and  $i_{nom}$  is the nominal rated current (fundamental frequency component) of the application. In per-unit systems, the *SCR* translates directly into per-unit inductance for grid modelling purposes.

### 2.5.1 Limits for harmonic current emissions

There are a few standards that cover the interconnection of distributed generation to the power grid. In addition to these, the standards concerning the current harmonic limits for equipment can be used to determine the limits guiding the filter designs. The international standard IEC 61000-3-2 determines the harmonic current emissions limits for equipment with the input current  $\leq 16$  A per phase. The harmonic limits for Class A equipment are shown in Table 2.1. According to the standard, grid-connected small-power three-phase grid inverters belong to Class A. The harmonic limits in this standard are given in amperes instead of percentage of the fundamental, which is used in other standards. The IEC 61000-3-2 standard does not define a specific limit for the current *THD*. However, the practice is that the *THD* is less than 8 %, which is the *THD* if only the odd harmonics of

Table 2.1 are used in the calculation. The standards IEC 61000-3-4 and 61000-3-5 define the current harmonic limits for equipment with a current greater than 16 A and 75 A, respectively.

Table 2.1. Limits for Class A Equipment (IEC, 2009)

Harmonic order $h$	$I_{h,\max}$ [A]
odd harmonics	
3	2.30
5	1.14
7	0.77
9	0.40
11	0.33
13	0.21
$15 \leq h \leq 39$	$2.25/n$
even harmonics	
2	1.08
4	0.43
6	0.30
$8 \leq h \leq 40$	$1.84/n$

The standard IEEE 1547-2003 describes the harmonic current limits for distributed generation units and the standard IEEE 519-1992 (the latest update 2014), for any system connected to the grid. Table 2.2 presents the limits in IEEE 519-1992, which is commonly applied as the general standard, mainly because it accurately defines the limits for *TDD*, which is directly used as the *THD* limits. The reason for this fusion of limits is obvious: *TDD* is calculated as a relation of the current harmonics to the 10–30 minute average value of the load current fundamental component. In practice, *TDD* can be taken for an average *THD* over some specific time period. The IEEE 1547-2003 standard defines the same harmonic current limits for the distributed generation as the 519-1992 shown in Table 2.2. Although Table 2.2 presents only the harmonic current limits for cases with  $SCR < 20$ , the standard itself determines that all equipment must fall within these limits, even though the standard presents limits for different *SCR* values.

In this doctoral dissertation, the filtering is analysed with the IEEE 519-1992 limits, and adequate filtering must achieve a *THD* of 5 % as instructed in Table 2.2.

Table 2.2. Current distortion limits for systems rated 120 V through 69 kV (IEEE, 2014)

Maximum harmonic current distortion in per cent of the maximum demand current						
	odd harmonics					
SCR	$3 \leq h < 11$	$11 \leq h < 17$	$17 \leq h < 23$	$23 \leq h < 35$	$35 \leq h \leq 50$	TDD
< 20	4.0	2.0	1.5	0.6	0.3	5.0
even harmonics limited to 25 % of the odd limits above						

### 2.5.2 General *LCL* filter design guidelines

The *LCL* filter design procedure can be divided into two main parts: first, the inverter-side inductor  $L_1$  is dimensioned to limit the inverter-side current ripple  $\Delta i_1$ , and second, the capacitor  $C_f$  and the grid-side inductor  $L_2$  are dimensioned to provide adequate attenuation for the grid-side current. In addition, the trade-off between  $C_f$  and  $L_2$ , (later referred to as the *CL* trade-off) affects the placement of the resonance peak, which is essential when considering the design and stability of a control system. The capacitance value should be limited to 5–10 % of the rated power of the inverter and the inductive voltage drop over the series inductance to less than 10 % (Liserre et al., 2005), (Channegowda and John, 2010), (Rockhill et al., 2011), and (Meyer and Mertens, 2012).

The inverter-side current ripple depends on the topology and, in some cases, on the modulation method. In this doctoral dissertation, space vector modulation (SVM) is applied. In the SVM, the output voltage is generated as a combination of the voltage vectors that the inverter bridge can generate. Figure 2.16(a) presents the vector diagram for the 2L SVM, which shows the possible voltage vectors  $\mathbf{v}_{0-6}$  and the reference vector  $\mathbf{v}_{\text{ref}}$ . Here, seven-sequence switching is applied to create a symmetrical switching pattern over the switching time period. The average volt-seconds applied to the inductor can be written as

$$T_{\text{sw}} \mathbf{v}_{\text{ref}} = T_2 \mathbf{v}_2 + T_3 \mathbf{v}_3 + T_0 \mathbf{v}_0, \quad (2.36)$$

where  $T_{\text{sw}}$  is the switching period, and  $T_2$ ,  $T_3$ , and  $T_0$  are the dwell times of the vectors  $\mathbf{v}_2$ ,  $\mathbf{v}_3$ , and  $\mathbf{v}_0$ , respectively. The maximum current ripple, which is determined as the maximum deviation of the average value within one switching cycle, occurs when the dwell time of the zero vector is zero. This takes place when the length of the reference vector  $\mathbf{v}_{\text{ref}}$  is the maximum linear length, and it lies in the middle of a sector. Figure 2.16(b) presents the switching sequence over one switching cycle, in which the dwell time of  $\mathbf{v}_0$  equals 0. Observing Figure 2.16(b), it can be determined that the volt-seconds over the inductor contributing to the maximum  $\Delta i_1$  are

$$u_L \Delta t = \frac{U_{\text{DC}}}{3} \frac{T_{\text{sw}}}{4}, \quad (2.37)$$

which with the substitution of the inductor voltage become

$$L_1 \frac{\Delta i_1}{\Delta t} \Delta t = \frac{U_{DC}}{3} \frac{T_{sw}}{4}. \quad (2.38)$$

The required inductance to limit the current ripple to the desired value can now be written as

$$L_1 = \frac{U_{DC}}{3} \frac{T_{sw}}{4} \frac{1}{\Delta i_1} = \frac{U_{DC}}{12 \Delta i_1 f_{sw}}, \quad (2.39)$$

where  $U_{DC}$  is the total DC link voltage and  $f_{sw}$  the switching frequency. Rockhill et al. (2011) present the same derivation for a three-phase three-level space-vector-modulated inverter, for which the required inductance is

$$L_1 = \frac{U_{DC}}{24 \Delta i_1 f_{sw}}, \quad (2.40)$$

which is due to the inherently better voltage quality of the 3L inverter compared with the 2L inverter. In the 3L inverter, the difference between the average and peak volt-seconds over the inductor is  $U_{DC}/6$  instead of  $U_{DC}/3$  in the 2L inverter (Figure 2.16(b)). For instance, for the 5L inverter this volt-second difference decreases to  $U_{DC}/12$  resulting in an even smaller inductor.

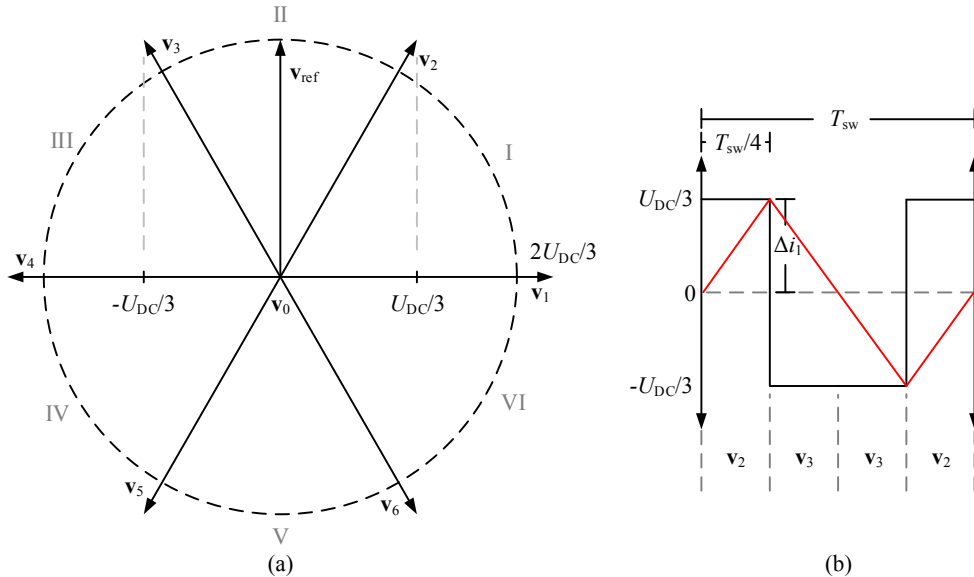


Figure 2.16. (a) Vector diagram for two-level space vector modulation (SVM).  
(b) Maximum inverter-side current  $i_1$  ripple over one switching cycle.

### Capacitor dimensioning

Commonly, the filter capacitor is dimensioned according to the rated power of the inverter system as

$$C_f = \frac{\gamma P_n}{\omega_1 u_n^2}, \quad (2.41)$$

where  $\gamma$  is the desired percentage of the nominal power  $P_n$ ,  $\omega_1$  is the grid angular frequency, and  $u_n$  is the nominal voltage. With appropriate base value determination, (2.41) can be presented in a simpler form as

$$C_f = \gamma C_b, \quad (2.42)$$

where  $C_b$  is the base capacitance.

In several publications, such as (Liserre et al., 2005), (Liu et al., 2012), (Reznik et al., 2014), and (Jiao and Lee, 2015), the maximum value is suggested to be limited to 5 % of the nominal power/base capacitance at most in order to avoid serious over-dimensioning of the inverter when the objective is to provide a unity power factor at the grid interface. Usually, the inverter-side current is controlled. This leads to a need to supply reactive current to the capacitor to compensate for the phase shift of the capacitor. In addition, for some applications, especially in wind power, the grid codes often require full power operation at least within the range of 0.9<sub>ind</sub>–0.9<sub>cap</sub> (Tsili and Papathanassiou, 2009), (Rockhill et al., 2011).

### Grid-side inductor dimensioning

The grid-side inductor  $L_2$  is commonly dimensioned along with  $C_f$  in order to place the resonance frequency of the filter. The  $LCL$  filter has two resonance frequencies, which can be calculated as

$$f_{r1} = \frac{1}{2\pi\sqrt{(L_2 + L_g)C_f}} \quad (2.43)$$

$$f_{r2} = \frac{1}{2\pi\sqrt{\frac{L_1 + L_2 + L_g}{L_1(L_2 + L_g)C_f}}} \quad (2.44)$$

A common guideline for the resonance frequency placement is

$$10f_1 \leq f_{r2} \leq \frac{f_{sw}}{2}, \quad (2.45)$$

where  $f_1$  is the grid frequency and  $f_{sw}$  the switching frequency.

In addition to the resonance frequency placement, the switching frequency attenuation can be used in the  $L_2$  dimensioning. In (Liserre et al., 2005),  $L_2$  was chosen as a percentage

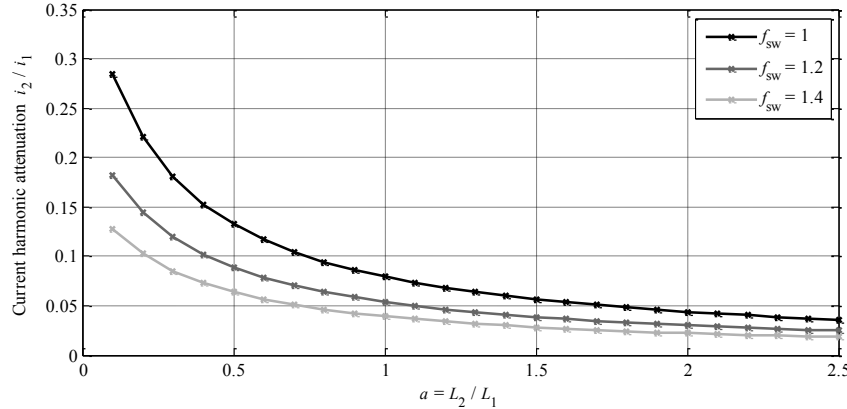


Figure 2.17. Effect of  $L_2$  on switching frequency attenuation when  $C_f$  is kept constant. The switching frequency  $f_{sw}$  is normalized to 5 kHz.

of  $L_1$  with respect to the switching frequency attenuation. The value for  $L_2$  is determined as

$$L_2 = aL_1, \quad (2.46)$$

where  $a$  is the ratio between  $L_1$  and  $L_2$ . Figure 2.17 presents the effect of  $L_2/L_1$  on current harmonic attenuation at the switching frequency with three different switching frequencies. The aim of the figure is to illustrate that the higher the switching frequency is, the less an increase in  $L_2$  affects the attenuation. For this reason, the dimensioning of  $L_2$  should be combined with the capacitor dimensioning.  $L_2$  contributes to the size of the filter, which suggests that the  $L_2$  should be kept as small as possible. Together with the dimensioning of  $C_f$ , the filter size can be optimized while keeping the resonance frequency at the desired value. In addition, a general guideline for the  $L_2$  dimensioning is to keep the voltage over the inductances of the filter less than 10 % in order not to increase the required inverter voltage and thereby the inverter DC link voltage (Liserre et al., 2005).

Furthermore, in high-power grid-connected inverters, limitation of the inductance saturation harmonic propagation for instance within a wind power plant is among the most critical issues. These aims dictate that the capacitance generally is small in pu values while the filter is designed with higher inductance pu values compared with the low-power inverter, where cost and size matter more (Teodorescu et al., 2011). These issues have a significant effect on the resonance placement trade-off between  $C_f$  and  $L_2$ .

### Weak or stiff grid?

To begin with, the terms ‘stiff’ and ‘weak grid’ have to be determined. Naturally, there is no specific and tight border between these two types of grid. Instead, the grid turns gradually from a stiff grid to a weak grid when  $L_g$  is increased. Table 2.2 shows that the lowest limits for harmonics are for  $SCR$  less than or equal to 20. This upper border

translates into 0.05 pu grid inductance, which can be considered a stiff grid. However, the limits set on this region are the tightest, and thus, they have to apply to weak grids also. In (Teodorescu et al., 2011), the limit set for a stiff grid is 0.01 pu impedance and 0.10 pu for a weak grid.

For conservative values, the stiff grid is determined to have an inductance of 0.03 pu or less, and a weak grid 0.10 pu or more. By doing this, grid inductances are taken further away from the grey area, which lies in the middle of these two values. In addition, it should be kept in mind that the larger the power (i.e. current) of the application is, the less impedance is needed to cause a significant voltage loss. The grids in this study are mainly considered inductive, based on the nature of power networks.

## 2.6 Design of grid inverter control

In this section, the basic design principles for the synchronous reference frame vector control are presented. The control system used in the simulations and experiments later in this work are based on this section.

### 2.6.1 Synchronous reference frame PI control

Figure 2.18 presents the synchronous reference frame, which is synchronized with the grid voltage space vector  $\mathbf{u}_g^s$  rotating at an angular frequency  $\omega_g$ . When  $\omega_g$  is known, the angle  $\theta$  can be obtained simply by computing an integral of the angular frequency as in (2.2). As the components of the space vector stationary reference frame are known, the transformation into a synchronous coordinate system is achieved by Park's transformation (2.1). This requires a method for detecting the grid frequency.

There are several methods for grid synchronization. Blaabjerg et al. (2006) present an overview of grid synchronization for distributed generation, and Teodorescu et al. (2011) provide a review and detailed analysis of grid synchronization in single-phase and three-phase power converters. In (Luna et al., 2015), grid synchronization methods for distributed generation under distorted grid conditions are presented and analysed.

A phase-locked loop (PLL) is probably the most common method to implement grid synchronization. A simple PLL under distorted utility conditions is studied in (Kaura and Blasko, 1997). Lee et al. (2013) study grid synchronization PLL, which is based on an adaptive low-pass notch filter, and McGrath et al. (2005) present power converter line synchronization based on a discrete Fourier transform (DFT).

Despite the fact that the grid synchronization affects the control system performance, especially in a distorted or unbalanced grid, its detailed study is out of the scope of this doctoral dissertation. Therefore, only the basic idea and tuning of the synchronous reference frame PLL (SRF-PLL) are discussed here.

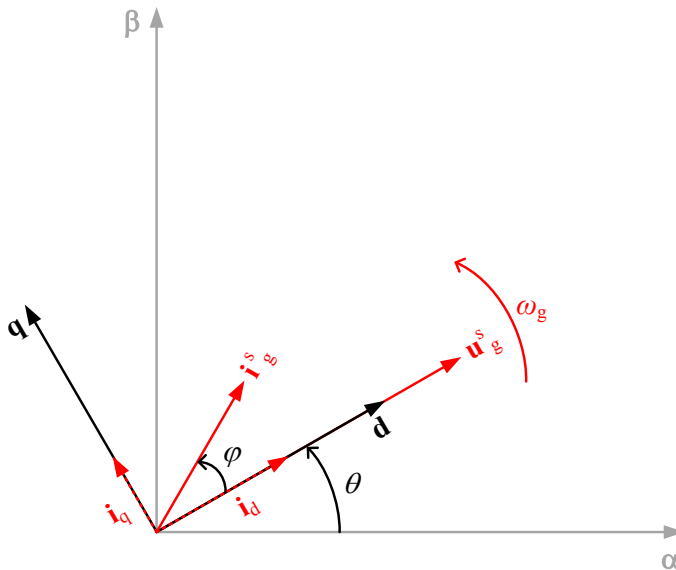


Figure 2.18. Synchronous reference frame, also known as the dq frame, synchronized with the grid voltage space vector rotating clockwise at the angular frequency  $\omega_g$ . The angle of the vector  $\mathbf{u}_g^s$  is  $\theta$ . The current vector  $\mathbf{i}_g^s$  is ahead of the voltage vector by the angle of  $\varphi$ , and its direct- and quadrature-axis components are displayed as dashed red vectors. In addition, the stationary reference frame is shown in grey.

### Basic SRF-PLL structure and operation

The SRF-PLL (Figure 2.19) is a PI controller, the output of which, after integration, is fed back to Park's transformation closing the loop. With perfect synchronization, the SRF-PLL controls the q-axis component  $u_q$  to zero, which means that the dq axis is aligned with the grid voltage vector.

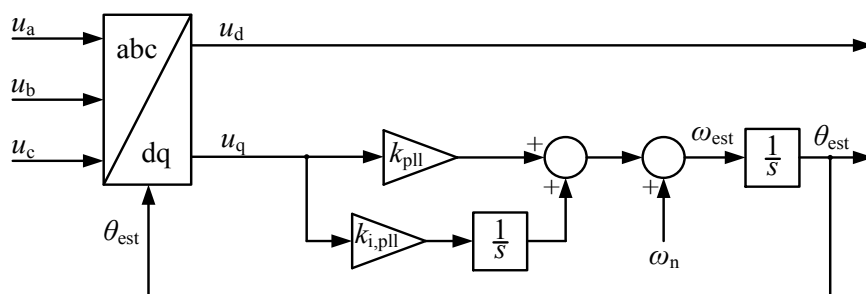


Figure 2.19. Schematic of the synchronous reference frame PLL. The q-axis voltage  $u_q$  is taken into the PI controller, the output of which is added with the nominal grid angular frequency  $\omega_n$  to produce  $\omega_{\text{est}}$ . The estimated angle is then fed back to Park's transformation.

Kaura and Blasko (1997) analyse the tuning of the SRF-PLL. The plant can be considered

$$G_{\text{pll}}(s) = \frac{1}{1+sT_s} \frac{U}{s}, \quad (2.47)$$

where the gain  $U$  is the grid voltage and  $T_s$  is the sampling time. The system consists of a first-order lag circuit and an integrator. The open-loop transfer function with the PI controller is now

$$G_{\text{ol}}(s) = \left( k_{\text{p,pll}} + \frac{k_{\text{i,pll}}}{s} \right) \frac{1}{1+sT_s} \frac{U}{s}, \quad (2.48)$$

where  $k_{\text{p,pll}}$  is the proportional gain and  $k_{\text{i,pll}}$  is the integral gain. Kaura and Blasko have used a symmetrical optimum method (Leonhardt, 2001) by which the PI controller gains become

$$k_{\text{p,pll}} = \frac{1}{\alpha} \frac{1}{UT_s} \quad (2.49)$$

$$k_{\text{i,pll}} = \frac{1}{\alpha^3} \frac{1}{UT_s^2}, \quad (2.50)$$

where the  $\alpha$  is a normalizing factor, which is related to the damping factor  $\zeta$  as

$$\zeta = \frac{\alpha - 1}{2}. \quad (2.51)$$

According to (2.51),  $\alpha = 2.42$  results in a damping factor  $\zeta = 0.707$ , which corresponds to a critically damped system. By varying  $\alpha$ , the damping and system bandwidth can also be varied.

### Internal model control

The current controllers are tuned with the principle of internal model control (IMC), introduced in (Garcia and Morari, 1985). Originally, it was used in the control of chemical processes such as distillation (Murad et al., 1996). Since then, the IMC has gained popularity in electric machine control (Lee et al., 1995), (Harnefors and Nee, 1995), and (Harnefors and Nee, 1998). Park et al. (2001) used the IMC in active power filter control. Figure 2.20 presents the IMC structure as a conventional feedback control system structure. The following presentation of the IMC is mainly based on the presentation given in (Pöllänen, 2003).

The inner loop in Figure 2.20 is the series controller, which can be written as

$$\mathbf{F}_c(s) = [\mathbf{I} - \mathbf{K}(s)\widehat{\mathbf{G}}(s)]^{-1} \mathbf{K}(s), \quad (2.52)$$

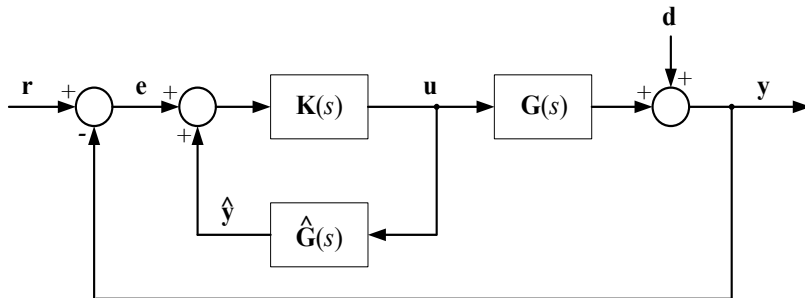


Figure 2.20. Internal model control block diagram represented in the conventional feedback form. The variables are vectors or matrices (Pöllänen, 2003).

where  $\mathbf{I}$  is the identity matrix,  $\mathbf{K}(s)$  is the controller transfer function matrix, and  $\hat{\mathbf{G}}(s)$  is the internal model of the plant  $\mathbf{G}(s)$ . Integral action in a steady state is achieved if the steady-state gain of (2.51) is infinite, which is achieved if the steady-state gain is

$$\mathbf{K}(0)\hat{\mathbf{G}}(0) = \mathbf{I}. \quad (2.53)$$

With no disturbance  $\mathbf{d}$ , the feedback error  $\mathbf{e}$  is zero when the internal model matches with the plant model. Then, the loop function is

$$\mathbf{L}(s) = \mathbf{K}(s)\mathbf{G}(s), \quad (2.54)$$

the stability of which is determined by the stability of both  $\mathbf{K}(s)$  and  $\mathbf{G}(s)$ . Setting

$$\mathbf{K}(s) = \mathbf{G}^{-1}(s), \quad (2.55)$$

the closed-loop gain would be

$$\mathbf{L}(s) = \mathbf{I}. \quad (2.56)$$

Ideally, the use of inverse dynamics in the control would result in a system which produces an output  $\mathbf{y}$  that follows the reference  $\mathbf{r}$  instantly and accurately. In practice,  $\mathbf{G}(s)$  may have right-half-plane (RHP) zeros, which would be unstable poles of  $\mathbf{G}^{-1}(s)$ . Further, time delays in  $\mathbf{G}(s)$  result in a non-invertible system. In addition,  $\mathbf{G}^{-1}(s)$  may have a higher-degree numerator polynomial than the denominator polynomial so that its implementation is not possible. Cancellation of process dynamics may result in control signals of very large magnitudes, and the method itself suffers greatly from model errors (Skogestad and Postlethwaite, 2005).

As a solution to aforementioned problems, the plant model should be factorized into invertible minimum-phase and non-invertible all-pass parts

$$\mathbf{G}(s) = \mathbf{G}_m(s)\mathbf{G}_a(s), \quad (2.57)$$

where  $\mathbf{G}_m(s)$  is the minimum-phase part and  $\mathbf{G}_a(s)$  is the all-pass part, which includes all RHP zeros and time delays of  $\mathbf{G}(s)$ .

A stable controller can now be obtained by setting

$$\mathbf{K}(s) = \mathbf{G}_m^{-1}(s). \quad (2.58)$$

The system sensitivity to model errors can be improved by detuning the system with a low-pass filter  $\mathbf{G}_{lp}(s)$

$$\mathbf{G}_{lp}(s) = \begin{bmatrix} \frac{\alpha_1^n}{(s + \alpha_1)^n} & \dots & 0 \\ \vdots & \ddots & \vdots \\ 0 & \dots & \frac{\alpha_m^n}{(s + \alpha_m)^n} \end{bmatrix}, \quad (2.59)$$

where  $\alpha_n$  is a design parameter,  $m$  is the number of plant outputs, and  $n$  is a positive integer which, when chosen large enough, makes  $\mathbf{K}(s)$  proper. The value of  $\alpha_n$  affects both the closed-loop performance and robustness of the control, and therefore, the selection of its value is a trade-off between these two.

Direct synthesis (Seborg et al., 1989) is a special case of the IMC, in which the current controller is designed using  $\mathbf{G}^{-1}(s)$ , the inverse of  $\mathbf{G}(s)$ . This is known from motor control, where the motor parameters are usually known (Harnefors and Nee, 1995), (Harnefors and Nee, 1998). When the plant has no RHP zeros or time delays and  $\mathbf{K}(s)$  is made proper with  $n = 1$ , the controller becomes

$$\mathbf{K}(s) = \frac{\alpha}{s + \alpha} \mathbf{G}^{-1}(s), \quad (2.60)$$

Using (2.52) and (2.60), we get

$$\mathbf{F}_c(s) = \left(1 - \frac{\alpha}{s + \alpha}\right)^{-1} \frac{\alpha}{s + \alpha} \mathbf{G}^{-1}(s) = \frac{\alpha}{s} \mathbf{G}^{-1}(s), \quad (2.61)$$

which gives the closed-loop dynamics of

$$\mathbf{G}_{cl}(s) = \frac{\alpha}{s + \alpha} \mathbf{I}, \quad (2.62)$$

which, in fact, is a first-order system with a bandwidth of  $\alpha$ . The closed-loop bandwidth  $\omega_B$  is the frequency at which the  $|\mathbf{G}_{cl}(s)| = 1/\sqrt{2}$  from above (Skogestad and Postlethwaite, 2005).

### Current controller tuning of the grid inverter with the IMC

Figure 2.21 presents the magnitude of the Bode plot of the transfer functions describing an *LCL* filter and an *L*-filter approximation, which is implemented with the total series

inductance of the filter included with the grid inductance. As it can be seen, the *LCL* filter behaves like an *L*-filter at low frequencies where the control is performed. For this reason, the control design for an *LCL* filter can be carried out with the *L*-filter approximation.

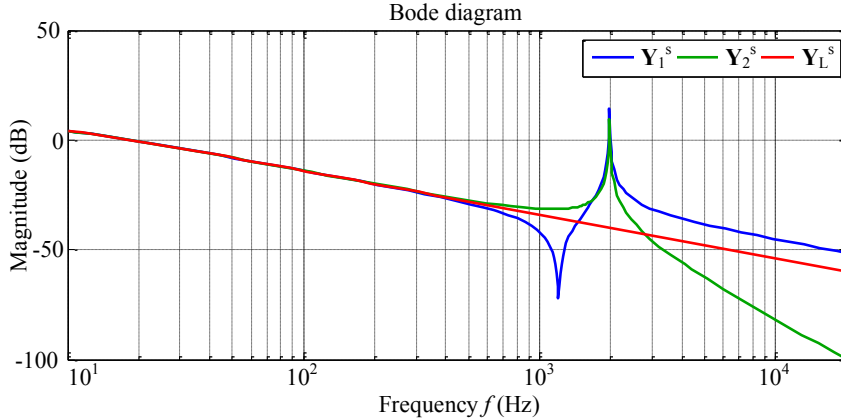


Figure 2.21. Magnitude plot of the Bode diagram for an *LCL* filter.  $\mathbf{Y}_1^s$  is the forward self-admittance function (inverter-side current),  $\mathbf{Y}_2^s$  is the forward trans-admittance function (grid-side current), and  $\mathbf{Y}_L^s$  is the *L*-filter approximation of the *LCL*.

An *L*-filter model (Figure 2.6) transformed into synchronous coordinates is written as

$$\frac{d}{dt} \begin{bmatrix} i_d \\ i_q \end{bmatrix} = \underbrace{\begin{bmatrix} -R_L/L_f & \omega \\ -\omega & -R_L/L_f \end{bmatrix}}_A \begin{bmatrix} i_d \\ i_q \end{bmatrix} + \underbrace{\begin{bmatrix} -1/L_f & 0 \\ 0 & -1/L_f \end{bmatrix}}_B \begin{bmatrix} u_{1d} - u_{2d} \\ u_{1q} - u_{2q} \end{bmatrix}, \quad (2.63)$$

where  $i_d$  and  $i_q$  are the current components,  $u_{1d}$  and  $u_{1q}$  are the inverter voltages,  $u_{2d}$  and  $u_{2q}$  are the grid voltages,  $R_L$  is the resistance of the filter, and  $L_f$  is the filter inductance. Now, the transfer function matrix can be calculated by

$$\mathbf{G}(s) = \mathbf{C}[\mathbf{sI} - \mathbf{A}]^{-1}\mathbf{B} = \frac{1}{(sL_f + R_L)^2 + \omega^2 L_f^2} \begin{bmatrix} sL_f + R_L & \omega L_f \\ -\omega L_f & sL_f + R_L \end{bmatrix}, \quad (2.64)$$

where  $\mathbf{C} = \mathbf{I}$ , because both currents are measured.

The inversed transfer function matrix is

$$\mathbf{G}^{-1}(s) = \begin{bmatrix} sL_f + R_L & -\omega L_f \\ \omega L_f & sL_f + R_L \end{bmatrix}, \quad (2.65)$$

which can be divided into two diagonal matrices separating the cross coupling of the dq frame as

$$\mathbf{G}^{-1}(s) = \mathbf{G}_d(s) - \mathbf{W} = \begin{bmatrix} sL_f + R_L & 0 \\ 0 & sL_f + R_L \end{bmatrix} - \begin{bmatrix} 0 & \omega L_f \\ -\omega L_f & 0 \end{bmatrix}. \quad (2.66)$$

With the decoupling scheme (Figure 2.22), the controlled plant becomes

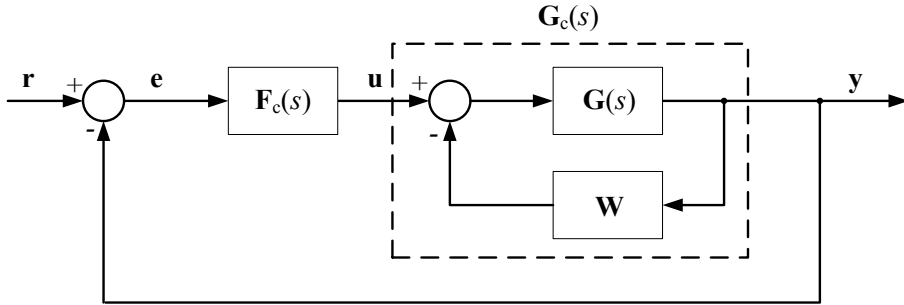


Figure 2.22. Decoupling represented as a feedback loop constituting the controlled plant  $\mathbf{G}_c(s)$  (Pöllänen, 2003).

$$\begin{aligned} \mathbf{G}_c(s) &= [\mathbf{I} - \mathbf{G}(s)\mathbf{W}]^{-1}\mathbf{G}(s) = [\mathbf{G}(s)(\mathbf{G}^{-1}(s) + \mathbf{W})]^{-1}\mathbf{G}(s) \\ &= [(\mathbf{G}^{-1}(s) + \mathbf{W})]^{-1} = \mathbf{G}_d^{-1}(s) \end{aligned} \quad (2.67)$$

Substituting (2.67) into (2.61) as  $\mathbf{G}(s)$ , we get a controller

$$\mathbf{F}_c(s) = \frac{\alpha}{s} [\mathbf{G}_d^{-1}(s)]^{-1} = \frac{\alpha}{s} \begin{bmatrix} sL_f + R_L & 0 \\ 0 & sL_f + R_L \end{bmatrix}. \quad (2.68)$$

Comparing (2.62) with

$$\mathbf{G}_{PI}(s) = \begin{bmatrix} k_p + \frac{k_i}{s} & 0 \\ 0 & k_p + \frac{k_i}{s} \end{bmatrix}, \quad (2.69)$$

the PI controller gains can be determined as

$$k_p = \alpha \hat{L}_f \quad (2.70)$$

$$k_i = \alpha \hat{R}_L. \quad (2.71)$$

Since the control is designed with an inverse plant model, the pole of the plant is cancelled, at least ideally, when the model parameters match the actual plant parameters ( $\hat{L}_f = L_f$  and  $\hat{R}_L = R_L$ ).

This controller tuning is a special case of direct synthesis. Because of pole cancellation used in the method, the characteristics of the IMC method in this case is poor rejection of load disturbances. Modifying the integral gain can be used to increase the performance but with the risk of increasing overshoots with changed references. In fact, another solution would be to increase the resistance, but this increases the losses of the system. In (del Blanco et al., 1999) a method of inner feedback loop was proposed. Resistance is added virtually, which costs nothing in terms of losses but still yields the same effect. This kind of a controller is called the two-degrees-of-freedom controller. Figure 2.23 presents the internal feedback loop, which together with the decoupled plant transfer function matrix  $\mathbf{G}_c$  constitutes a transfer function

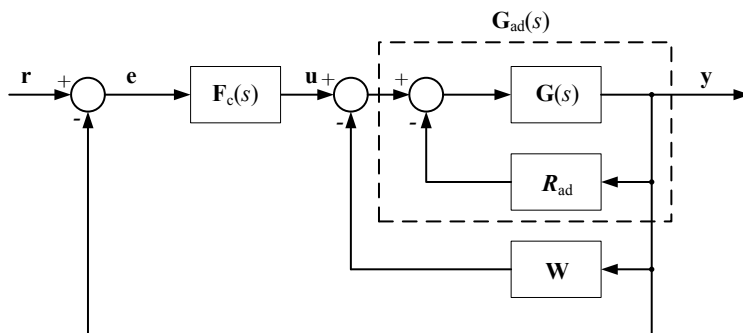


Figure 2.23. Additional virtual resistor as an inner feedback loop to increase the resistance of the controlled plant.

$$\mathbf{G}_{ad}(s) = \mathbf{G}_c(s)[\mathbf{I} + \mathbf{R}_{ad}\mathbf{G}_c(s)]^{-1} = \begin{bmatrix} \frac{sL_f + R_L}{1 + R_{ad}(sL_f + R_L)} & 0 \\ 0 & \frac{sL_f + R_L}{1 + R_{ad}(sL_f + R_L)} \end{bmatrix}, \quad (2.72)$$

where  $R_{ad}$  is the virtual active damping resistor. With the help of (2.67), (2.72) leads into control tuning of

$$\mathbf{F}_c(s) = \frac{\alpha}{s} [\mathbf{G}_{ad}^{-1}(s)]^{-1} = \frac{\alpha}{s} \begin{bmatrix} sL_f + R_L + R_{ad} & 0 \\ 0 & sL_f + R_L + R_{ad} \end{bmatrix}, \quad (2.73)$$

where the controller gains can be derived as

$$k_p = \alpha \hat{L}_f \quad (2.74)$$

$$k_i = \alpha (\hat{R}_L + R_{ad}). \quad (2.75)$$

A good value of  $R_{ad}$  can be found by

$$R_{ad} = \alpha \hat{L}_f - \hat{R}_L \quad (2.76)$$

making the inner loop of the virtual resistor as fast as the total closed-loop system. Substituting (2.76) into (2.75) yields integral gain of

$$k_i = \alpha^2 \hat{L}_f. \quad (2.77)$$

### DC link voltage controller

The DC link voltage is controlled through the input-output power balance. Figure 2.24 presents a simple schematic of the power balance. The basis of the controller design is that the power taken out of the DC link ( $P_{\text{out}}$ ) equals the power fed into the DC link ( $P_{\text{in}}$ ). Assuming a lossless system, the grid-injected power is equal to  $P_{\text{out}}$ .

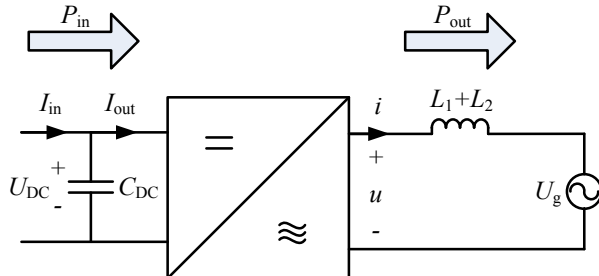


Figure 2.24. Grid-connected inverter, where the power flows are depicted.  $P_{\text{in}}$  is the power flowing to the DC link;  $P_{\text{out}}$  flows out of the DC link and is injected into the grid. The inverter output current is  $i$  and the inverter output voltage  $u$ .

Assuming a perfect grid synchronization, the DC link power equation in the dq frame can be written as

$$\frac{3}{2}(u_d i_d + u_q i_q) = -U_{\text{DC}} C_{\text{DC}} \frac{dU_{\text{DC}}}{dt} + U_{\text{DC}} I_{\text{in}}. \quad (2.78)$$

Small-signal linearization is made by perturbing (2.72), which yields

$$\begin{aligned} \frac{3}{2}((u_d + \tilde{u}_d)(i_d + \tilde{i}_d) + (u_q + \tilde{u}_q)(i_q + \tilde{i}_q)) &= -(U_{\text{DC}} + \tilde{U}_{\text{DC}}) C_{\text{DC}} \frac{d(U_{\text{DC}} + \tilde{U}_{\text{DC}})}{dt} \\ &+ (U_{\text{DC}} + \tilde{U}_{\text{DC}})(I_{\text{in}} + \tilde{I}_{\text{in}}), \end{aligned} \quad (2.79)$$

where  $\tilde{u}_d$ ,  $\tilde{i}_d$ ,  $\tilde{u}_q$ ,  $\tilde{i}_q$ ,  $\tilde{U}_{\text{DC}}$ , and  $\tilde{I}_{\text{in}}$  are the perturbations in the inverter output voltage and current dq components, DC link voltage, and input current, respectively. Assuming the other perturbations and the second-order perturbations zero and taking into account that the derivative of a steady-state value equals zero, (2.78) can be written as

$$\frac{3}{2}(u_d i_d + u_q i_q) + \frac{3}{2}(u_d \tilde{i}_d) = -U_{\text{DC}} C_{\text{DC}} \frac{d\tilde{U}_{\text{DC}}}{dt} + \tilde{U}_{\text{DC}} I_{\text{in}} + U_{\text{DC}} I_{\text{in}}. \quad (2.80)$$

Assuming

$$\frac{3}{2}(u_d i_d + u_q i_q) = U_{DC} I_{in} \quad (2.81)$$

and

$$R_{DC} = \frac{U_{DC}}{I_{in}}, \quad (2.82)$$

for the equivalent DC link resistance, while setting  $U_{DC} = \sqrt{3}u_d$ , the transfer function  $\tilde{U}_{DC}/\tilde{i}_d$  can be solved from (2.79) as

$$G_{DC}(s) = \frac{\tilde{U}_{DC}}{\tilde{i}_d} = \frac{\sqrt{3}}{2} \frac{R_{DC}}{1 - sC_{DC}R_{DC}}. \quad (2.83)$$

Figure 2.25 presents the DC link voltage control loop, where  $K(s)$  is the controller, and  $G_{cc}(s)$  represents the current control loop, the time constant of which is determined by the current controller bandwidth  $\alpha$ . It can be seen that the loop function includes a double integrator, which implies that the suitable controller tuning method would be a symmetrical optimum method; see for instance Pöllänen (2003) and Teodorescu et al. (2011).

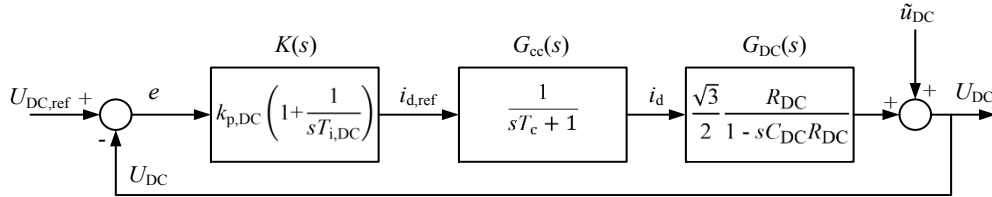


Figure 2.25. DC link voltage control loop representing the PI controller, the first-order transfer function as a current control loop with a time constant of  $T_c$ , and the DC link transfer function (2.74). The output of the DC link voltage is added with the disturbance voltage  $\tilde{u}_{DC}$ , which includes both the generator and grid disturbances.

For a symmetrical optimum, the PI controller gain and integration time can be determined as

$$K = \frac{C_{DC}}{2\sqrt{3}\alpha T_s} \quad (2.84)$$

$$T_i = \alpha^2 T_s, \quad (2.85)$$

where  $\alpha$  is a design parameter determined by the phase margin  $\varphi$  as

$$\alpha = \frac{1 + \sin \varphi}{\cos \varphi}, \quad (2.86)$$

where  $\varphi$  is the phase margin. To ensure stability  $T_i > T_s$ .

### 3 LCL filter configurations for paralleled inverters

This chapter presents and analyses five different LCL filter configurations for paralleled grid-connected inverters. A single output inductor or an L-filter is excluded because it is quite rarely used alone in high-power inverters. The configurations analysed in this dissertation are the most commonly known high-order filters, LCL and LC, and their variations. A newer topology of an LLCL filter is also included in the analysis. The models of the configurations are presented for each configuration. A comparative analysis is made between the filter configurations by studying the resonance frequencies, filter component dimensioning, and energies stored in them. The inverters are considered to have identical parameters. However, distinct components and their effect on the inverter performance and the filter components are studied. Further, the effect of tolerances in component values is studied.

The aim of this chapter is to give an insight into how different components and changing their electrical dimensioning affects the filter and its performance. It is investigated whether the filter should be designed for each configuration separately (i.e. according to the number of paralleled inverters) or whether general filter design could work over the whole range of paralleled inverters. Efficiency and resistive losses in the filters are not considered in this comparative study.

The LCL configuration consists of individual LCL filters with  $6n$  inductors and  $3n$  capacitors, where  $n$  is the number of paralleled units. The LLCL configuration, again, has  $n$  inductors more when compared with the LCL configuration while the other components are the same. In LC configurations, the inverters have individual LC filters and a common grid-side inductor, if needed, resulting in an LC+L configuration. This common inductor increases the number of inductors to  $3n + 3$ , whereas the number of capacitors remains at  $3n$  for each three-phase filter in the configuration. The L-configuration includes the least number of filter components. Each inverter has an individual inverter-side inductor while the filter capacitor and the grid-side inductor are common. This yields a configuration with  $3n + 3$  inductors and three capacitors. Table 3.1 presents the number of components for each configuration and Figure 3.1 depicts the filter configurations.

Table 3.1. Number of components per each three-phase filter configuration

Component	LCL	LLCL	LC+L	LC	L
$L_1$	$3n$	$3n$	$3n$	$3n$	$3n$
$L_2$	$3n$	$3n$	$3^*$	—	$3^*$
$C_f$	$3n$	$3n$	$3n$	$3n$	3
$L_C$	—	$3n$	—	—	—

\*Common grid-side inductor can be neglected if necessary

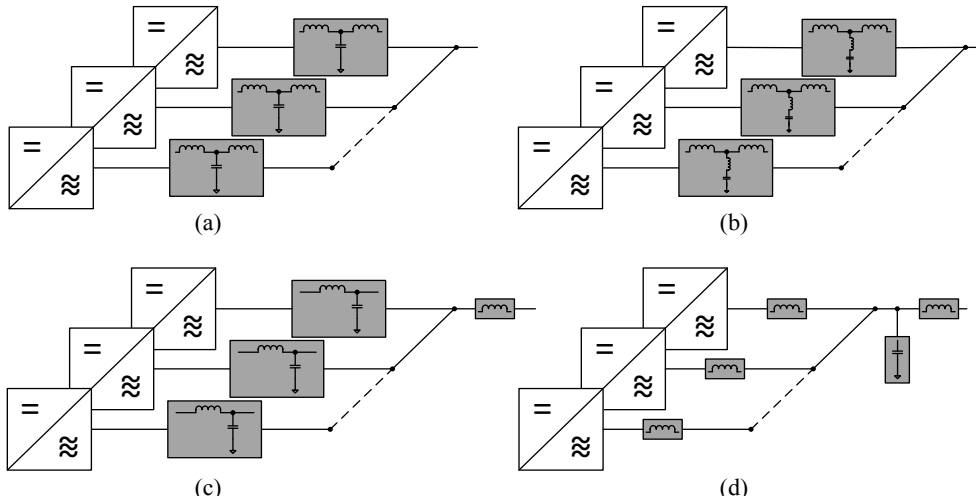


Figure 3.1. Three different filter configurations for parallel-connected inverters, which all produce an *LCL*-filter-like attenuation and an *LLCL* filter configuration. The inverters can have individual *LCL* filters (a), individual *LLCL* filters (b), individual *LC* filters, and a common grid-side inductor (c), and individual *L*-filters with a common capacitor and grid-side inductor. Naturally, the common  $L_2$  from the grid branch in both the *LC+L* and *L*-configuration can be excluded.

### 3.1 Assumptions and framework for the comparative analysis

The analysis in the chapter is based on the assumption that the filter components are identical. This assumption simplifies the models and allows a specific design point for the analysis. Obviously, filter components have some tolerances, depending on the manufacturing process, materials, and even the component design. This variation is later discussed in sections considering component tolerances. Further, the number of parallel-connected inverters in this study is limited to  $n = 6$  because the largest number of paralleled inverters in industrial applications is typically around this value.

It would be an impossibly large task to perform an analysis for a wide array of filter component values. In addition, a common approach is to assume that the filter components remain constant over the relevant frequency range. However, it is important to analyse the effect of tolerances and differences in the filter components. This is done in section 3.6. Moreover, the filter configurations and their designs are analysed by assuming that there is no circulating current between the inverters. The circulating current causes extra losses and can compromise the system stability as will be discussed in the following sections. In practice, the circulating current cannot be removed totally, but there are two approaches to minimize it; independent controls of the parallel-connected inverters or a centralized control with synchronized carriers for each inverter. The circulating current issue is discussed further in section 3.6.1.

Table 3.2 presents the nominal values of a single inverter unit. The nominal power is 1000 kVA, and it is assumed that the grid line-to-line voltage is 690 V<sub>rms</sub>. For a high-power inverter, the switching frequencies are commonly less than 5 kHz in order to limit the switching losses. The switching frequency is chosen to be 3 kHz, which is fairly high, but still, does not complicate the basic filter design too much. In other words, 3 kHz leaves room for the resonance placement.

Table 3.2. High-power inverter unit values for filter design and analysis

Symbol	Quantity	Value
$S_n$	Nominal power	1000 kVA
$u_n$	Nominal voltage	690 V <sub>L-L,rms</sub>
$i_n$	Nominal current	836.74 A <sub>rms</sub>
$f_{sw}$	Switching frequency	3 kHz
$U_{DC}$	DC Link voltage	1100 V

## 3.2 Modelling of parallel-connected inverters

Paralleled inverters and their modelling have been extensively studied in the literature, especially over the recent years. Itkonen (2010) has studied modelling, control, and mitigation of circulating current in parallel-connected inverters with  $L$ -filters. In his work, a general state-space model was derived. Moreover, Zhang et al. (2010) have investigated paralleled inverters with  $L$ -filters, with a special emphasis on how modulator carriers affect AC passive components, that is, the filter inductors. Chen et al. (2010) and He et al. (2012) and (2013) have examined paralleled inverters with  $LCL$  filters in PV applications and microgrids. Agorreta et al. (2011) and Borrega et al. (2013) have worked on modelling and control of  $N$  paralleled inverters for photovoltaic applications. In (Lu et al., 2015) and (Lu et al., 2017), resonance interaction and stability issues in parallel-connected inverters have been studied.

The model derivations for a single inverter and two paralleled inverters are presented in detail in Appendices A and B, respectively. Parallel-connected inverters can be analysed by connecting single inverter models in parallel to provide a model of the complete system. The admittance function matrices presented and discussed in this chapter comply with the nomenclature as follows.

In  $\mathbf{Y}^s_{ik,n}$ , the subscript  $i = 1$  for the forward self-admittance function matrix (inverter-side current) and  $i = 2$  for the forward trans-admittance function matrix (grid-side current). The subscript  $k$  denotes the particular inverter whose current is studied, and  $n$  denotes the inverter whose voltage causes the current. The superscript  $s$  stands for a stationary reference frame. For instance,  $\mathbf{Y}^s_{21,1}$  is the forward trans-admittance function matrix from the inverter 1 voltage to the grid-side current of the inverter 1 output filter. The function  $\mathbf{Y}^s_{22,1}$  would be the forward trans-admittance function from the inverter 1 voltage to the inverter 2 grid-side current of the inverter 2 output filter.

Similarly, the notations for voltages and currents are given as follows.  $\mathbf{u}^s_{1n}$  represents a particular inverter voltage;  $n = 1$  corresponds to inverter 1,  $n = 2$  to inverter 2, and so forth.  $\mathbf{u}^s_2$  is used as the PCC voltage. For currents, the notations become more complex but follow a fairly simple logic. The summed output currents of each inverter will be written as  $\mathbf{i}_{xn}$ , where  $x$  denotes inverter-side 1 or grid-side 2 in the same manner as for the admittance functions described above, and  $n$  denotes the inverter whose current is considered. When the current components are considered, the first part of the subscript remains the same, but one more index, separated with a comma, is introduced. In  $\mathbf{i}_{xn,m}$ , the index  $m$  denotes the inverter that causes the current. For instance,  $\mathbf{i}^s_{21}$  is the grid-side current of inverter 1, and  $\mathbf{i}^s_{21,1}$  is the component of  $\mathbf{i}^s_{21}$  caused by the inverter 1 voltage. Similarly,  $\mathbf{i}^s_{21,2}$  is the component of  $\mathbf{i}^s_{21}$  caused by the inverter 2 voltage. The same current components for the inverter-side currents would be  $\mathbf{i}^s_{11,1}$  and  $\mathbf{i}^s_{11,2}$ .

Juntunen et al. (2015) presents the modelling of *LCL*, *LC*, and *LC+L* configurations.

### 3.2.1 *N* parallel-connected identical inverters with *LCL* filters

To start with, let us consider the two-inverter system described in Appendix B. If the inverters and filters are identical, the systems in (B.14) and (B.21) are essentially simplified. Both the diagonal and off-diagonal elements are identical to each other, giving

$$\begin{bmatrix} \mathbf{i}_{11}^s \\ \mathbf{i}_{12}^s \\ \mathbf{i}_g^s \end{bmatrix} = \begin{bmatrix} \mathbf{Y}_{11,1}^s & -\mathbf{Y}_{12,1}^s & -\mathbf{Y}_{11,g}^s \\ -\mathbf{Y}_{12,1}^s & \mathbf{Y}_{11,1}^s & -\mathbf{Y}_{11,g}^s \\ -\mathbf{Y}_{g,1}^s & -\mathbf{Y}_{g,1}^s & \mathbf{Y}_{g,g}^s \end{bmatrix} \begin{bmatrix} \mathbf{u}_{11}^s \\ \mathbf{u}_{12}^s \\ \mathbf{e}_g^s \end{bmatrix} \quad (3.1)$$

for the forward self-admittance function matrix and

$$\begin{bmatrix} \mathbf{i}_{21}^s \\ \mathbf{i}_{22}^s \\ \mathbf{i}_g^s \end{bmatrix} = \begin{bmatrix} \mathbf{Y}_{21,1}^s & -\mathbf{Y}_{22,1}^s & -\mathbf{Y}_{21,g}^s \\ -\mathbf{Y}_{22,1}^s & \mathbf{Y}_{21,1}^s & -\mathbf{Y}_{21,g}^s \\ -\mathbf{Y}_{g,1}^s & -\mathbf{Y}_{g,1}^s & \mathbf{Y}_{g,g}^s \end{bmatrix} \begin{bmatrix} \mathbf{u}_{11}^s \\ \mathbf{u}_{12}^s \\ \mathbf{e}_g^s \end{bmatrix} \quad (3.2)$$

for the forward trans-admittance function matrix.

If current control reference tracking is under investigation, the grid voltage can be considered a disturbance and removed from (3.1) and (3.2). This excludes the last row and column from both equations. For the control design of a grid inverter, this is quite a common way to proceed, because the grid voltage is either only a disturbance, or it is taken into account by the feedforward term in the control. The better the reference tracking is, the less sensitive the control system is to output disturbances (Skogestad and Postlethwaite, 2005).

Now, the transfer function matrices for one inverter in a parallel-inverter system can be written as follows.

Let the inverter 1 currents  $i_{11}^s$  and  $i_{21}^s$  be the ones that are under interest. Both currents can be written as

$$i_{11}^s = \mathbf{Y}_{11,1}^s \mathbf{u}_{11}^s - \mathbf{Y}_{12,1}^s \mathbf{u}_{12}^s \quad (3.3)$$

and

$$i_{21}^s = \mathbf{Y}_{21,1}^s \mathbf{u}_{11}^s - \mathbf{Y}_{22,1}^s \mathbf{u}_{12}^s. \quad (3.4)$$

Now, when the inverters are identical, (3.3) and (3.4) can be written as

$$i_{11}^s = (\mathbf{Y}_{11,1}^s - \mathbf{Y}_{12,1}^s) \mathbf{u}_{11}^s \quad (3.5)$$

and

$$i_{21}^s = (\mathbf{Y}_{21,1}^s - \mathbf{Y}_{22,1}^s) \mathbf{u}_{11}^s. \quad (3.6)$$

From (3.5) and (3.6) we get the transfer function matrices  $\mathbf{Y}_{11}^s$  and  $\mathbf{Y}_{21}^s$ .

$$i_{11}^s [\mathbf{u}_{11}^s]^{-1} = \mathbf{Y}_{11}^s = \mathbf{Y}_{11,1}^s - \mathbf{Y}_{12,1}^s \quad (3.7)$$

and

$$i_{21}^s [\mathbf{u}_{11}^s]^{-1} = \mathbf{Y}_{21}^s = \mathbf{Y}_{21,1}^s - \mathbf{Y}_{22,1}^s. \quad (3.8)$$

When (3.7) and (3.8) are computed, the transfer function matrices for one inverter in a two parallel-inverter system with individual *LCL* filters becomes

$$\mathbf{Y}_{11}^s = \begin{bmatrix} \frac{Z_{L2}^s + Z_C^s + 2Z_{Lg}^s}{Z_{L1}^s(Z_{L2}^s + Z_C^s + 2Z_{Lg}^s) + Z_C^s(Z_{L2}^s + 2Z_{Lg}^s)} & 0 \\ 0 & \frac{Z_{L2}^s + Z_C^s + 2Z_{Lg}^s}{Z_{L1}^s(Z_{L2}^s + Z_C^s + 2Z_{Lg}^s) + Z_C^s(Z_{L2}^s + 2Z_{Lg}^s)} \end{bmatrix} \quad (3.9)$$

$$\mathbf{Y}_{21}^s = \begin{bmatrix} \frac{Z_C^s}{Z_{L1}^s(Z_{L2}^s + Z_C^s + 2Z_{Lg}^s) + Z_C^s(Z_{L2}^s + 2Z_{Lg}^s)} & 0 \\ 0 & \frac{Z_C^s}{Z_{L1}^s(Z_{L2}^s + Z_C^s + 2Z_{Lg}^s) + Z_C^s(Z_{L2}^s + 2Z_{Lg}^s)} \end{bmatrix} \quad (3.10)$$

It should be noted that in (3.7)–(3.10) the subscripts lack the last index, thus pointing out that we are dealing with models applicable to both of the inverters in the system.

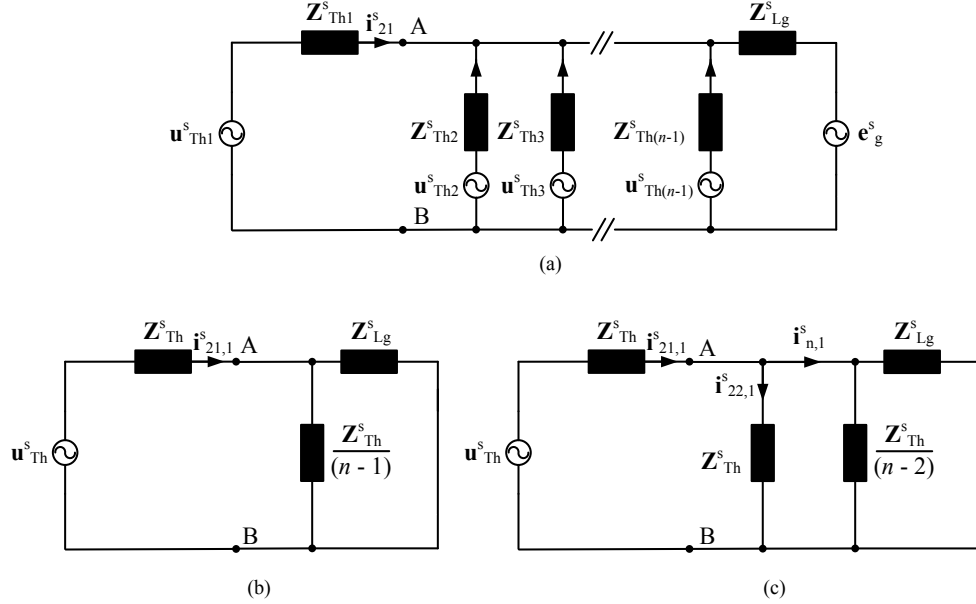


Figure 3.2. (a)  $N$  inverters in parallel presented with equivalent models.  
(b) Equivalent circuit for determining the transfer function matrix for a single inverter in the system.  
(c) Equivalent circuit for determining the transfer function matrix for the cross-coupling effects between the paralleled inverters.

### $N$ parallel-connected inverters

For  $N$  paralleled inverters, the model derivation follows a similar process as above. Figure 3.2 presents an equivalent circuit for  $N$  parallel-connected inverters (a) and the equivalent circuits for deriving the self-transfer function (b) and the cross-coupling transfer function matrices (c). The self-transfer function matrices are the diagonal components of the full system matrix, and the cross-coupling matrices are the off-diagonal matrices (e.g. in (3.1)).

Because the inverters are considered identical, the rest of the parallel-connected inverters can be lumped together as presented in Figure 3.2. The diagonal elements of the system model can be determined as

$$\mathbf{Y}_{21,1}^s = \frac{Z_C^s}{Z_{L1}^s + Z_C^s} \begin{bmatrix} \frac{Z_{Lg}^s(n-1) + Z_{Th}^s}{Z_{Th}^s(Z_{Lg}^s(n-1) + Z_{Th}^s) + Z_{Th}^s Z_{Lg}^s} & 0 \\ 0 & \frac{Z_{Lg}^s(n-1) + Z_{Th}^s}{Z_{Th}^s(Z_{Lg}^s(n-1) + Z_{Th}^s) + Z_{Th}^s Z_{Lg}^s} \end{bmatrix}. \quad (3.11)$$

The off-diagonal elements require a separation for one inverter as indicated in Figure 3.2(c). Current division between another equivalent inverter model and the rest of the inverter added with the grid yields a transfer function matrix

$$\mathbf{Y}_{22,1}^s = \frac{Z_{Th}^s Z_{Lg}^s}{Z_{Th}^s Z_{Lg}^s + Z_{Th}^s (Z_{Lg}^s (n - 2) + Z_{Th}^s)} \mathbf{Y}_{21,1}^s. \quad (3.12)$$

The system model, neglecting the grid voltage for simplicity, becomes now

$$\begin{bmatrix} \mathbf{i}_{21}^s \\ \mathbf{i}_{22}^s \\ \mathbf{i}_{23}^s \\ \vdots \\ \mathbf{i}_{2n}^s \end{bmatrix} = \begin{bmatrix} \mathbf{Y}_{21,1}^s & -\mathbf{Y}_{22,1}^s & -\mathbf{Y}_{22,1}^s & -\mathbf{Y}_{22,1}^s & -\mathbf{Y}_{22,1}^s \\ -\mathbf{Y}_{22,1}^s & \mathbf{Y}_{21,1}^s & -\mathbf{Y}_{22,1}^s & -\mathbf{Y}_{22,1}^s & -\mathbf{Y}_{22,1}^s \\ -\mathbf{Y}_{22,1}^s & -\mathbf{Y}_{22,1}^s & \mathbf{Y}_{21,1}^s & -\mathbf{Y}_{22,1}^s & -\mathbf{Y}_{22,1}^s \\ \vdots & \vdots & \vdots & \vdots & \vdots \\ -\mathbf{Y}_{22,1}^s & -\mathbf{Y}_{22,1}^s & -\mathbf{Y}_{22,1}^s & -\mathbf{Y}_{22,1}^s & \mathbf{Y}_{21,1}^s \end{bmatrix} \begin{bmatrix} \mathbf{u}_{11}^s \\ \mathbf{u}_{12}^s \\ \mathbf{u}_{13}^s \\ \vdots \\ \mathbf{u}_{1n}^s \end{bmatrix}, \quad (3.13)$$

where the diagonal and off-diagonal elements are the same, and presented here with the notation for inverter 1. Because there are  $N$  inverters in parallel, there are always  $n - 1$  inverters that affect the one under study. The other  $n - 1$  inverters supply current to the studied inverter, which has to be taken into account. Similarly as in (3.15)–(3.18), the transfer function matrix for one inverter can be derived as

$$\mathbf{i}_{21}^s [\mathbf{u}_{11}^s]^{-1} = \mathbf{Y}_{21}^s = \mathbf{Y}_{21,1}^s - (n - 1) \mathbf{Y}_{22,1}^s. \quad (3.14)$$

For the inverter-side current, the transfer function matrix can be developed similarly as described above and in section 3.1. The result is similar as in (3.11)

$$\mathbf{i}_{11}^s [\mathbf{u}_{11}^s]^{-1} = \mathbf{Y}_{11}^s = \mathbf{Y}_{11,1}^s - (n - 1) \mathbf{Y}_{12,1}^s. \quad (3.15)$$

One can see that (3.14)–(3.15) are similar to (3.7)–(3.8) but with the multiplication term of  $(n - 1)$ . If  $n = 2$  is substituted into the (3.14) and (3.15), the actual transfer function matrices will reduce back to (3.1) and (3.2).

When (3.14) and (3.15) are computed, the final transfer function matrices describing one inverter in a parallel-inverter system become

$$\mathbf{Y}_{11,LCL}^s = \begin{bmatrix} \frac{Z_{L2}^s + Z_C^s + nZ_{Lg}^s}{Z_{L1}^s (Z_{L2}^s + Z_C^s + nZ_{Lg}^s) + Z_C^s (Z_{L2}^s + nZ_{Lg}^s)} & 0 \\ 0 & \frac{Z_{L2}^s + Z_C^s + nZ_{Lg}^s}{Z_{L1}^s (Z_{L2}^s + Z_C^s + nZ_{Lg}^s) + Z_C^s (Z_{L2}^s + nZ_{Lg}^s)} \end{bmatrix} \quad (3.16)$$

$$\mathbf{Y}_{21,LCL}^s = \begin{bmatrix} \frac{Z_C^s}{Z_{L1}^s (Z_{L2}^s + Z_C^s + nZ_{Lg}^s) + Z_C^s (Z_{L2}^s + nZ_{Lg}^s)} & 0 \\ 0 & \frac{Z_C^s}{Z_{L1}^s (Z_{L2}^s + Z_C^s + nZ_{Lg}^s) + Z_C^s (Z_{L2}^s + nZ_{Lg}^s)} \end{bmatrix} \quad (3.17)$$

$$\mathbf{G}_{\text{LCL}}^s = \mathbf{Y}_{21,\text{LCL}}^s [\mathbf{Y}_{11,\text{LCL}}^s]^{-1} = \begin{bmatrix} \frac{Z_C^s}{Z_{L2}^s + Z_C^s + nZ_{Lg}^s} & 0 \\ 0 & \frac{Z_C^s}{Z_{L2}^s + Z_C^s + nZ_{Lg}^s} \end{bmatrix}. \quad (3.18)$$

The transfer function matrix  $\mathbf{G}_{\text{LCL}}^s$  describes the attenuation from the inverter-side current to the grid-side current.

### 3.2.2 LC and LLCL filters

In the case of *LC* and *LLCL* filters, the model derivation is a similar process as shown in the previous section. For the *LC* filter case, if the filter has a common grid-side inductor, one can either include it in  $Z_{Lg}^s$  or have it as a discrete component in the equivalent circuit as in Figure 3.3(a). If there is no  $L_2$  in the filter arrangement, one can set  $Z_{L2}^s = 0$ . For both cases, the *LCL* filter equations apply. Similarly, for the *LLCL* filter, one can take advantage of the *LCL* filter models and simply set  $Z_C^s = Z_{LC}^s + Z_C^s$  as in Figure 3.3(b).

$$\mathbf{Y}_{11,\text{LC}}^s = \begin{bmatrix} \frac{Z_C^s + n(Z_{L2}^s + Z_{Lg}^s)}{Z_{L1}^s(Z_C^s + n(Z_{L2}^s + Z_{Lg}^s)) + Z_C^s n(Z_{L2}^s + Z_{Lg}^s)} & 0 \\ 0 & \frac{Z_C^s + n(Z_{L2}^s + Z_{Lg}^s)}{Z_{L1}^s(Z_C^s + n(Z_{L2}^s + Z_{Lg}^s)) + Z_C^s n(Z_{L2}^s + Z_{Lg}^s)} \end{bmatrix} \quad (3.19)$$

$$\mathbf{Y}_{21,\text{LC}}^s = \begin{bmatrix} \frac{Z_C^s}{Z_{L1}^s(Z_C^s + n(Z_{L2}^s + Z_{Lg}^s)) + Z_C^s n(Z_{L2}^s + Z_{Lg}^s)} & 0 \\ 0 & \frac{Z_C^s}{Z_{L1}^s(Z_C^s + n(Z_{L2}^s + Z_{Lg}^s)) + Z_C^s n(Z_{L2}^s + Z_{Lg}^s)} \end{bmatrix} \quad (3.20)$$

$$\mathbf{G}_{\text{LC}}^s = \mathbf{Y}_{21,\text{LC}}^s [\mathbf{Y}_{11,\text{LC}}^s]^{-1} = \begin{bmatrix} \frac{Z_C^s}{Z_C^s + n(Z_{L2}^s + Z_{Lg}^s)} & 0 \\ 0 & \frac{Z_C^s}{Z_C^s + n(Z_{L2}^s + Z_{Lg}^s)} \end{bmatrix}. \quad (3.21)$$

$$\mathbf{Y}_{11,\text{LLCL}}^s = \begin{bmatrix} \frac{Z_{L2}^s + Z_C^s + Z_{LC}^s + nZ_{Lg}^s}{Z_{L1}^s(Z_{L2}^s + Z_C^s + Z_{LC}^s + nZ_{Lg}^s) + (Z_C^s + Z_{LC}^s)(Z_{L2}^s + nZ_{Lg}^s)} & 0 \\ 0 & \frac{Z_{L2}^s + Z_C^s + Z_{LC}^s + nZ_{Lg}^s}{Z_{L1}^s(Z_{L2}^s + Z_C^s + Z_{LC}^s + nZ_{Lg}^s) + (Z_C^s + Z_{LC}^s)(Z_{L2}^s + nZ_{Lg}^s)} \end{bmatrix} \quad (3.22)$$

$$\mathbf{Y}_{21,\text{LLCL}}^s = \begin{bmatrix} \frac{Z_C^s + Z_{LC}^s}{Z_{L1}^s(Z_{L2}^s + Z_C^s + Z_{LC}^s + nZ_{Lg}^s) + (Z_C^s + Z_{LC}^s)(Z_{L2}^s + nZ_{Lg}^s)} & 0 \\ 0 & \frac{Z_C^s + Z_{LC}^s}{Z_{L1}^s(Z_{L2}^s + Z_C^s + Z_{LC}^s + nZ_{Lg}^s) + (Z_C^s + Z_{LC}^s)(Z_{L2}^s + nZ_{Lg}^s)} \end{bmatrix} \quad (3.23)$$

$$\mathbf{G}_{\text{LLCL}}^s = \mathbf{Y}_{21,\text{LLCL}}^s [\mathbf{Y}_{11,\text{LLCL}}^s]^{-1} = \begin{bmatrix} \frac{Z_C^s + Z_{LC}^s}{Z_{L2}^s + Z_C^s + Z_{LC}^s + nZ_{Lg}^s} & 0 \\ 0 & \frac{Z_C^s + Z_{LC}^s}{Z_{L2}^s + Z_C^s + Z_{LC}^s + nZ_{Lg}^s} \end{bmatrix}. \quad (3.24)$$

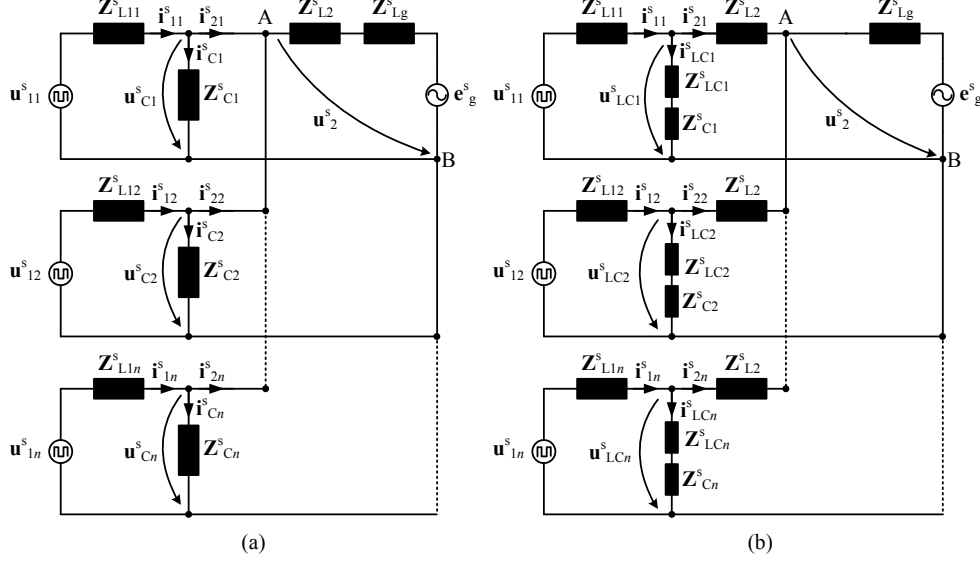


Figure 3.3. (a)  $N$  inverters with individual  $LC$  filters and a common  $L_2$  in parallel.  
(b)  $N$  inverters with individual  $LLCL$  filters in parallel.

### 3.2.3 Individual $L$ -filters and common $C$ and $L$

Figure 3.4(a) presents the filter configuration with individual inverter-side inductors and common  $C$  and  $L_2$ . The model derivation requires some calculations compared with the  $LC$  and  $LLCL$  configurations, which are inherently  $LCL$  filters. However, the model development follows the same process as for the  $LCL$  filter case. The forward self-admittance matrix  $\mathbf{Y}_{11,1}^s$  can be determined as

$$\mathbf{Y}_{11,1L}^s = \begin{bmatrix} \frac{Z_{L1}^s + (n-1)Z_{\text{par}N}^s}{Z_{L1}^s(Z_{L1}^s + nZ_{\text{par}N}^s)} & 0 \\ 0 & \frac{Z_{L1}^s + (n-1)Z_{\text{par}N}^s}{Z_{L1}^s(Z_{L1}^s + nZ_{\text{par}N}^s)} \end{bmatrix}, \quad (3.25)$$

where  $Z_{\text{par}N}^s$  is the parallel connection of the rest  $n - 1$  inverter-side inductors of other inverters and the capacitor and the grid branch determined as

$$Z_{\text{par}N}^s = \frac{Z_{L1}^s}{n-1} \parallel (Z_C^s \parallel (Z_{L2}^s + Z_{Lg}^s)). \quad (3.26)$$

Now, the coupling term can be determined as

$$\begin{aligned} \mathbf{Y}_{12,1L}^s &= \mathbf{Z}_{\text{par}N2}^s [Z_{L1}^s + \mathbf{Z}_{\text{par}N2}^s]^{-1} \mathbf{Y}_{11,1L}^s \\ &= \begin{bmatrix} \frac{Z_C^s(Z_{L2}^s + Z_{Lg}^s)}{Z_{L1}^s(Z_{L1}^s(Z_C^s + Z_{L2}^s + Z_{Lg}^s) + Z_C^s Z_{L1}^s n(Z_{L2}^s + Z_{Lg}^s))} & 0 \\ 0 & \frac{Z_C^s(Z_{L2}^s + Z_{Lg}^s)}{Z_{L1}^s(Z_{L1}^s(Z_C^s + Z_{L2}^s + Z_{Lg}^s) + Z_C^s Z_{L1}^s n(Z_{L2}^s + Z_{Lg}^s))} \end{bmatrix}, \end{aligned} \quad (3.27)$$

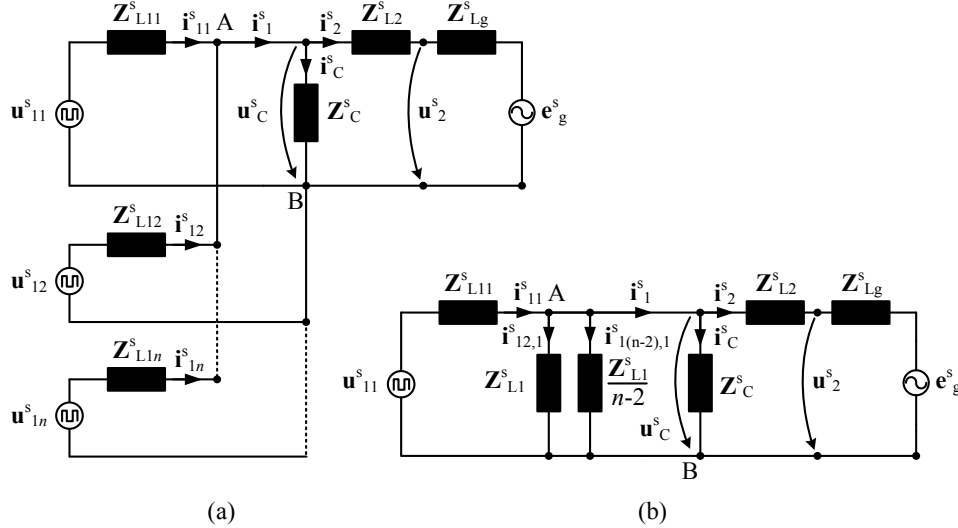


Figure 3.4. (a) \$N\$ inverters with individual \$L\$-filters and common \$L\_2\$ and \$C\$ in parallel.  
(b) Equivalent circuit for calculating the coupling terms of the models.

where the impedance matrix  $\mathbf{Z}_{\text{parN2}}^s$  is a diagonal matrix having elements of

$$\mathbf{Z}_{\text{parN2}}^s = \frac{Z_{L1}^s}{n-2} \parallel \left( Z_C^s \parallel (Z_{L2}^s + Z_{Lg}^s) \right). \quad (3.28)$$

Now, the forward self-admittance matrix function for each inverter in the \$N\$ inverter system can be computed

$$\mathbf{Y}_{11L}^s = \mathbf{Y}_{11,1L}^s - (n-1)\mathbf{Y}_{12,1L}^s, \quad (3.29)$$

which after some manipulation becomes

$$\mathbf{Y}_{11L}^s = \begin{bmatrix} \frac{Z_C^s + Z_{L2}^s + Z_{Lg}^s}{Z_{L1}^s(Z_C^s + Z_{L2}^s + Z_{Lg}^s) + Z_C^s n (Z_{L2}^s + Z_{Lg}^s)} & 0 \\ 0 & \frac{Z_C^s + Z_{L2}^s + Z_{Lg}^s}{Z_{L1}^s(Z_C^s + Z_{L2}^s + Z_{Lg}^s) + Z_C^s n (Z_{L2}^s + Z_{Lg}^s)} \end{bmatrix}. \quad (3.30)$$

This equation (3.30) is very similar to  $\mathbf{Y}_{11LC}^s$  with the difference that \$n\$ does not exist in the numerator of the diagonal terms.

It is evident from Figure 3.4(b) that it is not possible to determine a forward trans-admittance function for one inverter with this filter configuration. However, there are two approaches to analyse the current harmonic attenuation over the filter arrangement. First, one can determine the forward self- and trans-admittance functions for an equivalent inverter, which has  $\mathbf{Z}_{L1}^s/n$  for the inverter-side impedance. From this transfer function, the transfer function from the equivalent inverter voltage to the grid-injected current can

be determined by simple current division. The second option is to perform the same calculation with (3.30) and then determine the current harmonic attenuation. For both options, the result is the same, which can be seen in Figure 3.4(b); the attenuation only depends on the capacitor branch and the grid branch impedances  $\mathbf{Z}^s_C$ ,  $\mathbf{Z}^s_{L2}$ , and  $\mathbf{Z}^s_{Lg}$ , as it is with a single  $LC$  filter.

### 3.2.4 Open-end grid inverter with the $LCL$ filter

Considering the aspects of topology, a parallel connection provides certain opportunities, which affect the filter design. A special case of two paralleled inverters is an open-end inverter topology (Somasekhar et al., 2001) presented in Figure 3.5. In the grid use, the open-end inverters are known from the STATCOM (Surendra Babu and Fernandes, 2014), (Ponnaluri et al., 2004), and Static Var Compensator (SVC) (Kawabata et al., 2004) use. Grandi et al. (2007) have studied the use of an open-end inverter in a PV application.

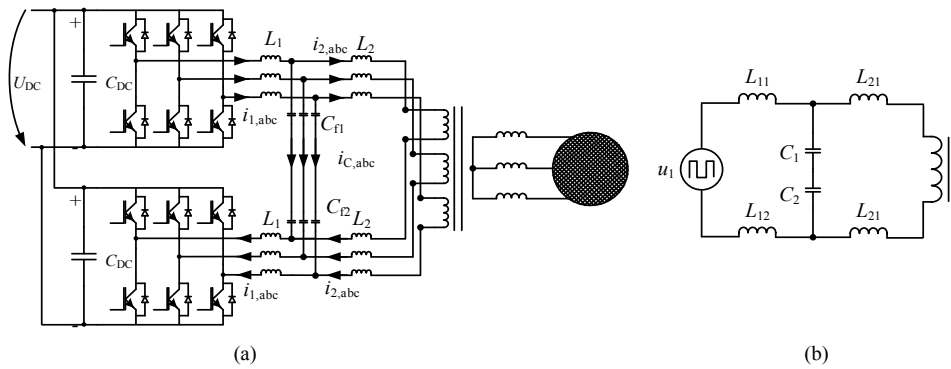


Figure 3.5. (a) Open-end transformer driven with two stacked inverters. This topology is called an open-ended inverter.  
 (b) Single phase equivalent circuit for the filter design of the open-ended inverter.

An open-end inverter consists of two inverters connected in parallel to the same DC link while driving the inductor coils from both ends. The inverter 1 phase A half-bridge is connected to the transformer phase A positive end while the inverter 2 phase A half-bridge is connected to the negative end. In other words, each of the phases is driven by a full-bridge inverter, which can produce three-level voltage when inverters 1 and 2 are both two-level inverters. The open-ended topology makes it possible to decrease the number and sizes of filter components, which is analysed further in the following sections.

The transfer functions for an open-ended inverter are

$$Y_{1,oe} = \frac{2Z_2 + Z_C + Z_g}{(2Z_2Z_C + Z_CZ_g + 2Z_1(2Z_2 + Z_C + Z_g))} \quad (3.31)$$

$$Y_{2,\text{oe}} = \frac{Z_c}{(2Z_2Z_C + Z_CZ_g + 2Z_1(2Z_2 + Z_C + Z_g))} \quad (3.32)$$

$$G_{\text{oe}} = \frac{Z_C}{2Z_2 + Z_C + Z_g} \quad (3.33)$$

One can see that in this case the capacitor is represented and modelled with two discrete capacitors. However, if only one filter capacitor per phase is used, this halves the number of capacitors required when compared with conventional paralleled inverters with *LCL* filters.

### 3.3 Component dimensioning and resonance frequencies

To analyse the resonance frequencies in parallel-inverter systems, filter parameters dimensioned according to the general filter design guidelines from section 2.5 and values of Table 3.2 in section 3.1 are needed.

The inverter-side inductor is dimensioned nominally to limit the inverter-side current ripple to less than 15 % of the nominal peak value. Commonly, the maximum allowed current ripple is around 20–25 % in order to limit the inverter power stage losses (Liserre et al., 2005) and (Rockhill et al., 2011). In addition,  $L_1$  is also dimensioned according to 10 % and 25 % for analysis purposes. Incidentally, these two other ripple limits correspond to 2 kHz and 5 kHz switching frequencies with a 15 % ripple limit for both cases. For the nominal values presented in Table 3.2 in section 3.1, the inverter-side inductor values for current ripples of 10 %, 15 %, and 25 % become 0.1709 pu (259  $\mu$ H), 0.1142 pu (173  $\mu$ H), and 0.0686 pu (104  $\mu$ H), respectively. These values can later be referred with  $L_{1,(10\%)}$ ,  $L_{1,(15\%)}$ , and  $L_{1,(25\%)}$ .

The nominal capacitor value is 3 % of the base capacitance (Appendix C), which translates into  $C_f = 200.57 \mu\text{F}$ . Assuming a stiff grid ( $L_g \leq 0.03L_b$ ) and setting the grid-side inductor to  $L_2 = 0.033 \mu\text{H}$  (50  $\mu\text{H}$ ), the nominal resonance frequencies become  $f_{r1,\text{LCL,nom}} = 23.004 \mu\text{Hz}$  (1150.2 Hz) and  $f_{r2,\text{LCL,nom}} = 28.656 \mu\text{Hz}$  (1432.8 Hz) for a resonance sag and a peak, respectively. In a weak grid ( $L_g \geq 0.10L_b$ ), to have the resonance frequencies close to the stiff grid case, the capacitors are changed to  $C_f = 0.015C_b$  (100.29  $\mu\text{F}$ ) and the grid-side inductor  $L_2$  to  $L_2 = 0.0132 \mu\text{H}$  (20  $\mu\text{H}$ ). To serve the reader, the nominal resonance frequencies and the respective configuration are compiled into Table D.1 and Table D.2 for a stiff and a weak grid, respectively (Appendix D). The *LC* and *LLCL* configurations are related to their nominal designs, and the *LCL*, *LC+L*, and *L*-configurations to the nominal *LCL* filter design.

The results of these normalized frequencies are then compared. In this study, the *LCL*, *LC+L*, and *L*-filters are not completely matched to produce the same harmonic attenuation. However, this was done in (Juntunen et al., 2015). Instead, the designs are made according to the same design criteria. This comparison provides knowledge about the robustness of each design for grid branch multiplication and grid impedance variation

in parallel designs. In addition, as it was shown in section 2.3.2, the *LCL* filter and the *LLCL* filter resonances and current harmonic attenuation are close to each other, which makes it interesting to compare these two configurations against each other.

### 3.3.1 Resonance frequencies

Resonance frequencies for each filter configuration can be solved from the elements of the transfer function matrices  $\mathbf{Y}^s_{11}$  and  $\mathbf{Y}^s_{21}$ , respectively.

$$f_{r1,LCL} = \frac{1}{2\pi} \frac{1}{\sqrt{C_f(L_2 + nL_g)}} \quad (3.34)$$

$$f_{r1,LLCL} = \frac{1}{2\pi} \frac{1}{\sqrt{C_f(L_2 + L_C + nL_g)}} \quad (3.35)$$

$$f_{r1,LC+L} = \frac{1}{2\pi} \frac{1}{\sqrt{C_f n(L_2 + L_g)}} \quad (3.36)$$

$$f_{r1,L} = \frac{1}{2\pi} \frac{1}{\sqrt{C_f(L_2 + L_g)}} \quad (3.37)$$

And the resonance peaks

$$f_{r2,LCL} = \frac{1}{2\pi} \sqrt{\frac{L_1 + L_2 + nL_g}{C_f L_1 (L_2 + nL_g)}} \quad (3.38)$$

$$f_{r2,LLCL} = \frac{1}{2\pi} \sqrt{\frac{L_1 + L_2 + nL_g}{C_f ((L_1 + L_C)(L_2 + nL_g) + L_1 L_C)}} \quad (3.39)$$

$$f_{r2,LC+L} = \frac{1}{2\pi} \sqrt{\frac{L_1 + n(L_2 + L_g)}{C_f L_1 n(L_2 + L_g)}} \quad (3.40)$$

$$f_{r2,L} = \frac{1}{2\pi} \sqrt{\frac{L_1 + n(L_2 + L_g)}{C_f L_1 (L_2 + L_g)}}. \quad (3.41)$$

Because of the additional inductor in the capacitor branch, the *LLCL* configuration presents a third resonance frequency at

$$f_{r3,LLCL} = \frac{1}{2\pi} \frac{1}{\sqrt{C_f L_C}}. \quad (3.42)$$

The additional inductance  $L_C$  of the *LLCL* filter can be solved from (3.42), which for the 3 kHz (60 pu) switching frequency is  $L_C = 0.0093$  pu (14.07  $\mu$ H) in the stiff grid case. The higher the switching frequency is, the smaller inductance is needed for a particular

capacitance. Similarly, the lower the switching frequency is, the larger  $L_C$  becomes when the capacitance is left unchanged.

### 3.3.2 Resonance shift resulting from parallel connection

Figure 3.6 presents the Bode plot for the current harmonic attenuation function of a single, two, three, and four parallel-connected inverters with  $LCL$  filters. As the number of paralleled inverters increases, the resonance frequency  $f_{r1}$  tends to lower frequencies as it can be seen from (3.34)–(3.37). Similarly, the higher resonance frequency  $f_{r2}$  moves lower as  $n$  is increased. However, since  $f_{r2}$  is also dependent on  $L_1$ , the shift towards lower frequencies is smaller compared with the shift of  $f_{r1}$ . This means that the  $L_1$  dimensioning is more important with respect to the resonance placement in paralleled inverters than it is with one inverter, where it is mainly designed to limit the ripple current. The designer should consider the dimensioning of  $L_1$  both from the inverter-side current ripple point of view and consider  $L_1$  as a balancing factor in cases of, possibly highly, variable grid inductance. Of course, the current ripple and  $L_1$  inductor losses are in direct relation to the inverter bridge losses. The smaller the ripple current is made, the more losses are generated in the inductor and less in the inverter bridge. Allowing a larger current ripple leads to greater losses in the inverter bridge while the inductor losses are smaller.

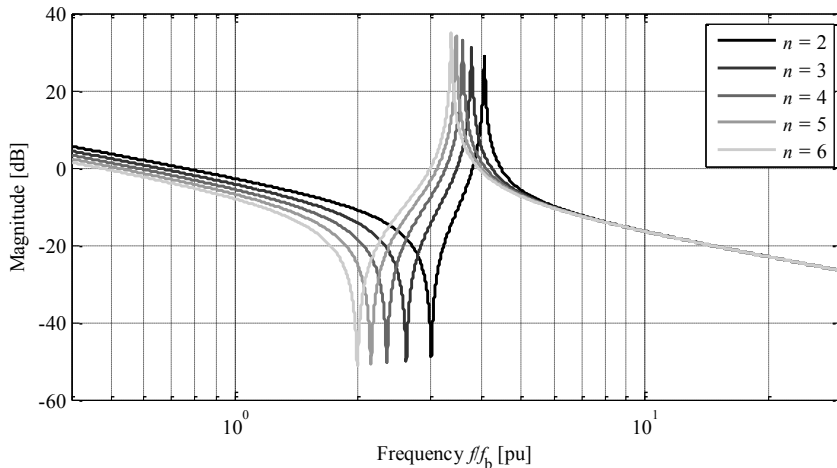


Figure 3.6. Bode plot of the forward self-admittance  $\mathbf{Y}_{11,LCL}^s$  for a single and two, three, and four parallel-connected inverters with the same filter design as for the single one.

The other filter configurations experience a similar effect except for the  $L$ -configuration. The resonance peak of  $\mathbf{Y}_{21,L}^s$  increases as  $n$  increases as can be seen from (3.41). This action is quite evident when paralleled inverters are modelled as one equivalent inverter, as it was discussed in 3.2.3.  $\mathbf{Z}_{L1}^s$  of the equivalent inverter is divided by  $n$ , as  $n$  inverter-side inductors are connected in parallel. This leads to a situation where the resonance peak tends to higher frequencies as  $n$  increases. The lower resonance, however, is not affected by parallel connection, since the common components determine the resonance peak of the current harmonic attenuation function  $\mathbf{G}^s$ .

Figure 3.8 presents a bar diagram of the normalized resonance frequencies for the  $LC$ ,  $LCL$ ,  $LLCL$ , and  $LC+L$  configurations for the nominal filter design. Dimensioning the inverter-side inductor  $L_1$  has an impact on the higher resonance frequency. The larger  $L_1$  is in value, the lower the frequency is originally. However, a smaller  $L_1$  increases the impact of parallel connection by increasing the resonance shift as  $n$  is increased. Both Figure 3.6 and Figure 3.7 show that the resonance shift decreases as there are more inverters in parallel. From (3.34)–(3.37) we can see that the lower resonance frequency tends to 0 as  $n$  increases. The higher frequency, however, has a saturation value, which for the  $LCL$  configuration can be determined as

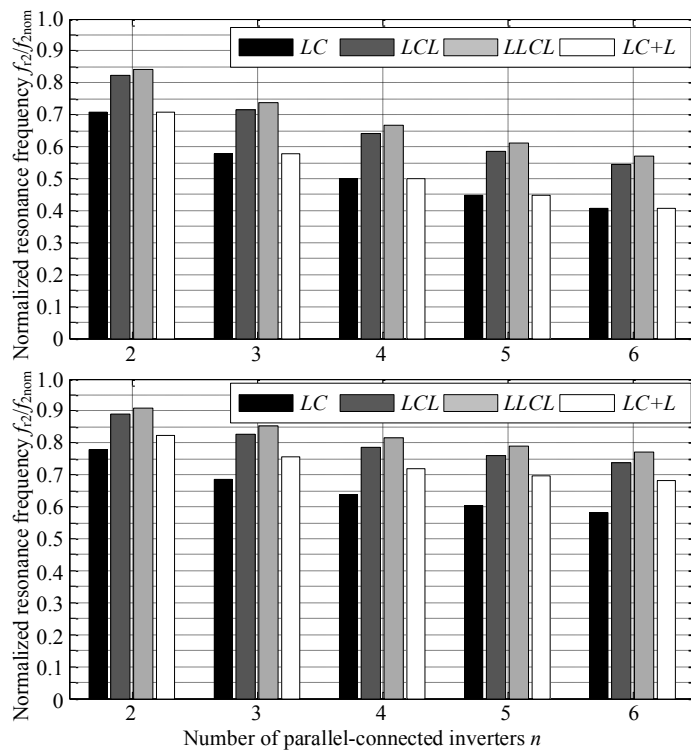


Figure 3.7.

Resonance frequencies  $f_{r1}$  and  $f_{r2}$  normalized to the nominal frequencies with five different values of  $n = 2\text{--}6$  in the case of a stiff grid and a nominal filter design with the inverter-side current ripple of  $\Delta i_1 = 15\%$ .

$$\lim_{n \rightarrow \infty} f_{r2,LCL} = \frac{1}{2\pi} \sqrt{\frac{\frac{L_1}{n} + \frac{L_2}{n} + L_g}{\frac{C_f L_1 L_2}{n} + C_f L_1 L_g}} = \frac{1}{2\pi} \sqrt{\frac{1}{C_f L_1}}. \quad (3.43)$$

The limits for the  $LC$  and  $LC+L$  configurations are the same as (3.43). For the  $LLCL$  configuration, the limit is removed with  $L_1$  and becomes  $1/2\pi\sqrt{1/C_f(L_1 + L_C)}$ . For the  $L$ -configuration, there is no upper limit for the resonance frequency.

Dimensioning the inverter-side inductor  $L_1$  for a different ripple current has an impact on the resonance shift. The larger  $L_1$  is, the more significant the resonance shift becomes at the higher resonance frequency. With a small  $L_1$ , the resonances remain higher for a greater number of  $n$ , which allows more flexibility into the filter configuration design. Figure 3.8 presents the normalized higher resonance frequencies for the  $LC$ ,  $LCL$ ,  $LLCL$ , and  $LC+L$  configurations with the inverter-side inductors  $L_{1,(10\%)}$  (top figure) and  $L_{1,(25\%)}$  (bottom figure). For all of the four configurations, the resonance shift is less with  $L_{1,(25\%)}$  than with  $L_{1,(10\%)}$ . The difference between the  $LC$  and  $LC+L$  configurations is the common grid-branch inductor of the  $LC+L$  configuration. Making the inverter-side inductor smaller emphasizes the effect of common grid-branch inductor by reducing the severity of the resonance shift. For the  $LCL$  and  $LLCL$  configurations, the difference between the configurations remains virtually the same.

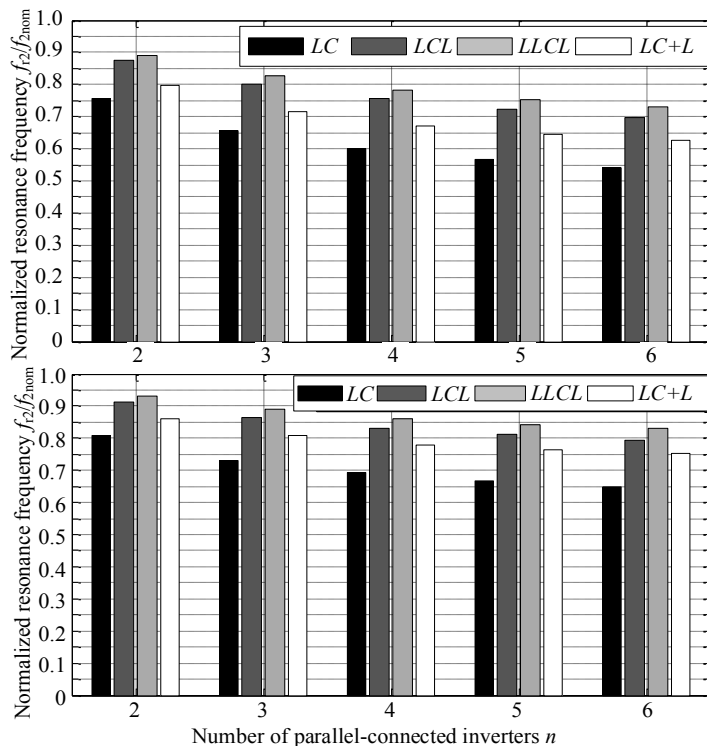


Figure 3.8. Resonance frequency  $f_{r2}$  normalized to the nominal frequencies with five different values of  $n = 2\text{--}6$  in the case of a stiff grid and a filter design with inverter-side inductors of  $L_{1,(10\%)}$  (top) and  $L_{1,(25\%)}$  (bottom).

Comparing Figure 3.7 and Figure 3.8, we can see that for the  $LLCL$  configuration, the resonance shift remains below 20 % for even  $n = 6$ . For the  $LCL$  configuration, the resonance shifts slightly below 80 % at  $n = 6$  showing that adjusting the  $L_1$  value can help to dimension the filter over a certain range of a number of paralleled inverters.

Changing the capacitor from the nominal has no impact on the resonance shift. Naturally, the capacitor affects the resonance frequencies, but the resonance shift is an outcome of a comparison between a single inverter resonance frequency (filter nominal frequency) and the parallel-connected inverter resonance frequency. The capacitances in the denominator (3.34)–(3.41) and in the nominal frequencies cancel each other out, rendering the capacitor ineffective against the resonance shift. The grid-side inductor, however, has an impact on the resonance shift. The larger the inductance is, the less the resonances shift, which demonstrates the difference between the *LC* and *LC+L* configurations.

For the *LC* and *LC+L* configurations, the shift follows  $1/\sqrt{n}$ . The higher resonance frequency follows

$$\frac{f_{r2LC+L}}{f_{r2nom}} = \sqrt{1 - \frac{L_1(n-1)}{n(L_1 + L_2 + L_g)}} \quad (3.44)$$

for both configurations with the exception that for the *LC* configuration  $L_2 = 0$ .

Because in the case of the *LCL* and *LLCL* configurations the grid-branch multiplication affects only the grid inductance, the relation is somewhat different. For the *LCL* configuration the relation follows

$$\frac{f_{r1LCL}}{f_{1nom}} = \sqrt{\frac{L_2 + L_g}{L_2 + nL_g}} \quad (3.45)$$

and for the *LLCL* configuration the relation follows

$$\frac{f_{r1LLCL}}{f_{1nom}} = \sqrt{\frac{L_2 + L_C + L_g}{L_2 + L_C + nL_g}}. \quad (3.46)$$

Similarly, the relations for higher resonance frequencies are

$$\frac{f_{r2LCL}}{f_{2nom}} = \sqrt{1 - \frac{L_1L_g(n-1)}{(L_2 + nL_g)(L_1 + L_2 + L_g)}} \quad (3.47)$$

for the *LCL* configuration and

$$\frac{f_{r2LLCL}}{f_{2nom}} = \sqrt{1 - \frac{L_1^2L_g(n-1)}{((L_2 + nL_g)(L_1 + L_C) + L_1L_C)(L_1 + L_2 + L_g)}}. \quad (3.48)$$

for the *LLCL* configuration.

The capacitor branch inductor  $L_C$  limits the shift of the resonance frequency. The larger  $L_C$  is in value, the less  $f_{r1LLCL}$  shifts to a lower frequency. This additional component

causes the small difference between the *LCL* and *LLCL* configurations regarding the resonance shift.

The lower resonance frequency  $f_{r1,L}$  of the *L*-configuration is not affected by the parallel connection, and  $f_{r2,L}$  behaves inversely compared with the other configurations. The resonance shift for  $f_{r2,nom}$  of the *L*-configuration increases in the relation of

$$\frac{f_{r2L}}{f_{r2,LCL,nom}} = \sqrt{\frac{n(L_2 + L_g) + L_1}{(L_1 + L_2 + L_g)}}. \quad (3.49)$$

It can be seen from (3.49) that the increase in  $f_{r2,L}$  depends on  $n(L_2 + L_g)$ . The initial assumption was that the parallel connection of  $L_1$  leading to  $L_1/n$  is causing the increase. However, as there is no  $n$  in the denominator of (3.49), the value of  $L_1$  has a significant effect on the rate at which (3.49) increases. Figure 3.9 presents the normalized higher resonance frequency  $f_{r2L}$  for the *L*-configuration with three different  $\Delta i_{1max}$  requirements, in other words, three different values of  $L_1$ . It can be seen that with a larger  $L_1$  the increase in (3.49) is slower when compared with smaller values of  $L_1$ .

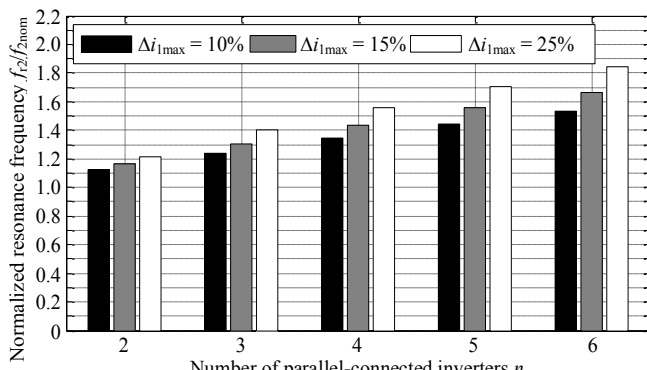


Figure 3.9. Higher resonance frequency  $f_{r2,L}$  of the *L*-configuration normalized to the nominal frequency  $f_{r2,LCL,nom}$  with five different values of  $n$  for three different  $\Delta i_{1max}$  requirements.

In weak grids, the resonance shift is generally greater compared with the stiff grid case because both the grid inductance is larger, and commonly, the grid-side filter inductance is small or omitted. As it was mentioned above, decreasing the  $L_2$  inductor value results in a greater resonance shift especially for the lower resonance frequency, which is only dependent on the filter capacitor and grid-side inductor values along with the grid inductance.

For a large grid inductance, the capacitor does not have to be dimensioned large to lower the resonance frequency, because the resonance is low already. Again, the smaller the capacitance is, the higher the limit frequency for the higher resonance frequency becomes as can be seen from (3.43), which, from the viewpoint of control system design, may be advantageous in terms of damping issues. Of course, the capacitor dimensioning has to

take into account the application power and not to over-dimension the capacitor, which increases the need for reactive current from the inverter.

Figure 3.10 presents the resonance shifts for the *LC*, *LCL*, *LLCL*, and *LC+L* configurations in a weak grid with the nominal inverter-side inductor  $L_{1,(15\%)}$ . Because of the small  $L_2$ , the impact on the lower resonance frequency is greater in the weak grid than in the stiff grid for the *LCL* and *LLCL* configurations. The *LC* and *LC+L* configurations experience the same resonance shift in the stiff and weak grids when considering the lower resonance frequency. In the weak grid, changing the inverter-side inductor value has a greater impact on the resonance shift compared with the stiff grid case, thereby making the inductor a more critical component in terms of resonance placement. Varying the value of the grid-side inductor has a smaller impact in the weak grid because the inductor is already small. Comparing the *LC* and *LC+L* configurations, the necessity of the common grid-side inductor of the *LC+L* configuration can be questioned.

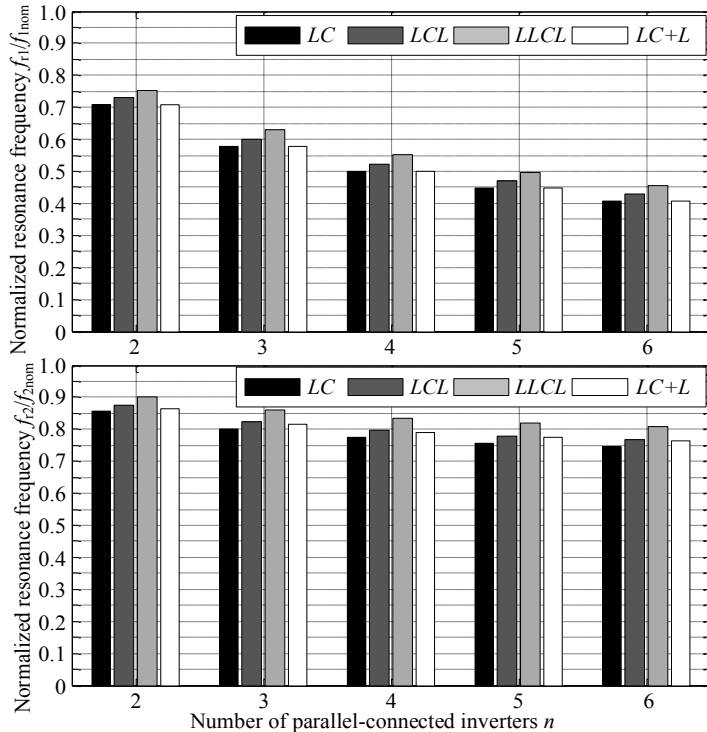


Figure 3.10. Resonance frequencies  $f_{r1}$  and  $f_{r2}$  normalized to the nominal frequencies with five different values of  $n$  in the case of a weak grid with  $L_1$  designed according to the nominal current ripple  $\Delta i_{1,\max} = 15\%$ .

Figure 3.11 presents the normalized  $f_{r2}$  for the *L*-configuration, which, compared with the stiff grid case, increases faster because of  $L_{g,weak} > (L_{2,stiff} + L_{g,stiff})$ . This relation suggests that the common grid-side inductor of the *L*-configuration can be neglected from the filter

design, resonance frequency, and resonance shift viewpoints, because it does not have a significant impact on the resonance shift.

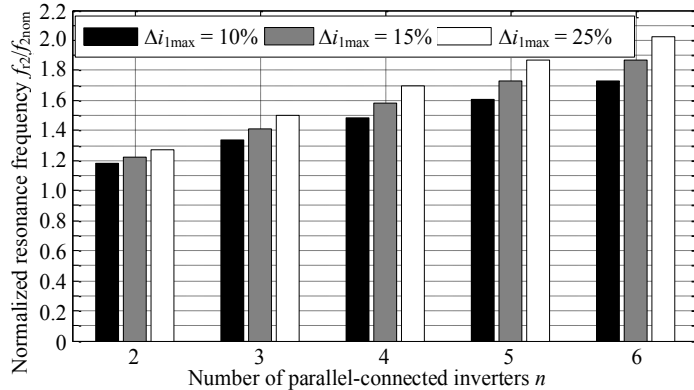


Figure 3.11. Higher resonance frequency  $f_{r2,L}$  of the  $L$ -configuration normalized to the nominal frequency  $f_{2,LCL,nom}$  with  $n = 2\text{--}6$  for three different  $\Delta i_{1max}$  requirements in a weak grid.

### Key findings considering the resonance shift

- The larger  $L_1$  is, the larger the resonance shift becomes.
- The smaller  $C_f$  is, the lower the limit frequency of  $f_{r2}$  becomes.
- Especially in a weak grid, the common  $L_2$  of the  $LC+L$  and  $L$ -configurations has an insignificant impact on the larger frequency shift.
- The  $LLCL$  configuration and the  $LCL$  configuration show the highest robustness against the resonance shift.
- The  $L$ -configuration shows an inverse resonance shift in  $f_{r2}$  compared with the other configurations.

### 3.3.3 Resonance interaction between the inverters

With paralleled inverters, there is resonance interaction between the paralleled inverters as a result of the coupling through the grid impedance. There is a third harmonic frequency that only depends on the plant parameters and not on the grid, and it has to be considered in the filter design. This interaction and resonance damping in paralleled PV inverters is studied in (He et al., 2012) and in parallel-inverter-based microgrids in (He et al., 2013). Lu et al. (2015) and (2017) have studied resonance interaction with a paralleled inverter with  $LCL$  filters.

This cross-coupling resonance frequency  $f_{rc}$  is present both in the diagonal and off-diagonal terms in the transfer function matrix as in (3.13). For the  $LCL$  configuration, the equation for  $f_{rc}$  is

$$f_{rc,LCL} = \frac{1}{2\pi} \sqrt{\frac{L_1+L_2}{C_f L_1 L_2}}, \quad (3.50)$$

which confirms that the frequency does not depend on the grid inductances like the two other frequencies. Similarly, the cross-coupling frequency for the *LLCL* configuration is determined as

$$f_{rc,LLCL} = \frac{1}{2\pi} \sqrt{\frac{L_1+L_2}{C_f(L_C(L_1 + L_2) + L_1 L_2)}}, \quad (3.51)$$

where the capacitor branch inductor  $L_C$  can be found from the denominator.

Figure 3.12 presents the Bode magnitude plot for the  $Y_{21,1}$  transfer function of the *LCL* configuration. This transfer function describes the relation of the inverter 1 grid-side inductor current to the inverter's own voltage, while the other voltages of the system are short circuited. As in the previous section, the higher *LCL* filter resonance frequency tends to lower frequencies as  $n$  increases. However, the cross-coupling frequency remains the same as stated above.

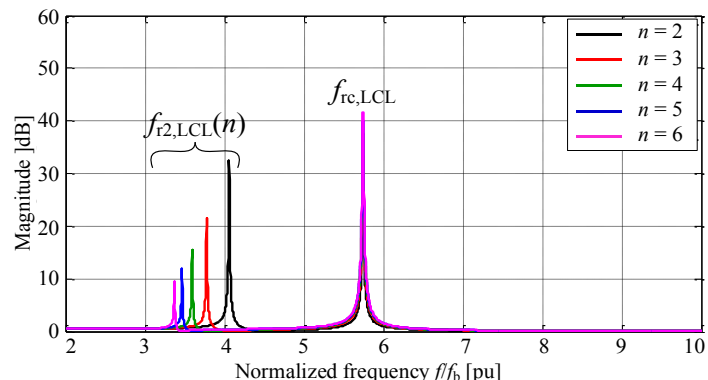


Figure 3.12. Bode magnitude plot for  $Y_{21,1}$  of the *LCL* configuration with the number of paralleled inverters going from  $n = 2$ –6. The values used in this figure are the nominal filter values for the *LCL* configuration with a 0.0021 pu (1 mΩ) resistance in the inductors and capacitors.

With the nominal filter values,  $f_{rc} = 36.08$  pu (1804 Hz), which is fairly low considering the switching frequency of  $f_{sw} = 60$  pu (3 kHz). In this case, the cross-coupling frequency is not likely to cause problems as it is quite far from the switching frequency and close to the area where the resonance peaks would normally be planned. In normal operation, the inverters would not see this frequency. However, with the existence of circulating current, this frequency can cause severe problems and degradation of filter performance.

Ideally, the *LC* and *LC+L* configurations do not present this extra resonance because of the lack of a coupling inductance between the inverters. However, the cables or busbars connecting the inverters in parallel always have some inductance and resistance, which

serve as the coupling inductance in this case.  $L_2$ , which sets the cross-coupling resonance frequency, can be solved from (3.50) as

$$L_2 = \frac{L_1}{4\pi^2 f_{rc}^2 C_f L_1 - 1}. \quad (3.52)$$

Similarly for the *LLCL* filter,  $L_2$  can be determined with

$$L_2 = \frac{L_1 \cdot 4\pi^2 f_{rc}^2 C_f L_1 L_C}{4\pi^2 f_{rc}^2 C_f (L_C + L_1) - 1}, \quad (3.53)$$

the outcome of which is virtually zero at the switching frequency. Removing  $L_{2,LLCL}$  would result in  $f_{rc,LLCL}$  being over the switching frequency while the capacitor branch inductor is designed to place the resonance sag over the same frequency. This results in no cross-coupling resonance peak. However, taking the conductors into consideration, there is a resonance peak present, and it is shifted below the resonance frequency, which could cause unwanted amplification of switching frequency side-band harmonics.

The lower limit for the grid-side inductors of the *LCL* filters and the *LLCL* filters can now be determined from (3.52) and (3.53). Further, the critical cable inductances for the *LC* filters can be studied with (3.52). The smaller the grid-side inductor is, the higher the cross-coupling resonance peak is located. The resonance should be set around the same frequency range as the original resonance peak  $f_{r2}$ , which is conventionally set below  $f_{sw}/2$ . Figure 3.13 presents the required  $L_2$  to set  $f_{rc}$  to the half of the switching frequency for the *LCL* and *LLCL* filters. For the *LC* filters, the frequency is set to  $f_{sw}$ , and the bars in the figure show how small an inductance suffices to push the resonance over the switching frequency. It can be seen that the smaller the inverter-side inductor is, the more inductance on the grid side is needed to keep the cross-coupling resonance around the targeted  $f_{sw}/2$ . For the *LCL* filters, the inductance is quite close to the nominal value of  $L_{2,n} = 0.033$  pu (50  $\mu$ H) but as  $L_1$  decreases, the required  $L_2$  increases to over two times the nominal value. For the *LLCL* filter, the  $L_2$  value is practically the nominal with  $L_{1,(10\%)}$ , and with the smaller  $L_1$ , the  $L_2$  increases only up to around 0.0462 pu (70  $\mu$ H), which is slightly less than the smallest value with the *LCL* filter. A clear benefit of the *LLCL* filter topology over the *LCL* one is the ability to have the cross-coupling resonance around the designed frequency with smaller grid-side inductors than the *LCL* filter.

Considering the *LC* filters, where there are no grid-side inductors, not much inductance is needed to place the cross-coupling resonance over the switching frequency. The *LC* filter resonance frequency is commonly determined by the capacitor dimensioning while the inverter-side inductor limits the current ripple. The larger the capacitor is, the less inductance is required as Figure 3.13 shows. However, as the value of the inductor also affects the resonances, this should be kept in mind in this context.

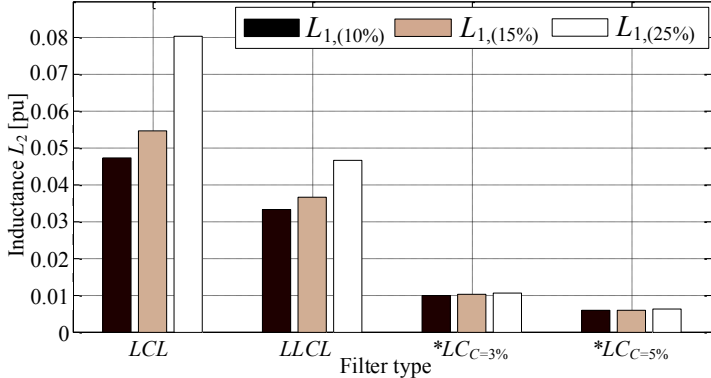


Figure 3.13. Minimum grid-side inductor value to set the cross-coupling resonance to  $f_{sw}/2$  with the stiff grid case and three different values for  $L_1$ . For the  $LC$  filters, the inductance is also calculated with the 5% capacitor.

\*For the  $LC$  filters, the cross-coupling resonance is set to  $f_{sw}$ .

Here, the switching frequency is considered to be 60 pu (3 kHz). Applications with higher switching frequencies are more vulnerable to this cross-coupling resonance as less inductance is needed. For instance, for the 100 pu (5 kHz) switching frequency, the inverter-side inductors would have to be 0.0686 pu (104  $\mu$ H) to limit the current ripple to 15 %. With this value for  $L_1$  and the 5 % capacitor, the cable inductance to make  $f_{rc} = 100$  pu (5 kHz) would be 0.0021 pu (3.12  $\mu$ H).

By designing the higher resonance frequency of the  $LCL$  and  $LLCL$  filters to  $f_{r2} \leq f_{sw}/2$ , the cross-coupling resonance is also present close to this limit frequency. However, the margin between  $f_{r2}$  and  $f_{rc}$  depends on the grid inductance. The higher the grid inductance is, the smaller filter components are required, which results in a high cross-coupling frequency, meaning that with a high-inductance grid connection, the paralleled inverters may require quite a significant amount of inductance on the grid side to keep  $f_{rc}$  low enough.

The difference between the higher resonance peak and the cross-coupling resonance depends on the grid inductance. The smaller the grid inductance is, the closer to each other the two frequencies are. From (3.38)–(3.39) with  $n = 1$  and (3.50)–(3.51), the relation between the two frequencies can be solved as

$$\frac{f_{rc,LCL}}{f_{r2,LCL}} = \sqrt{\frac{(L_1 + L_2)(L_2 + L_g)}{L_2(L_1 + L_2 + L_g)}}, \quad (3.54)$$

for the  $LCL$  filter and

$$\frac{f_{rc,LLCL}}{f_{r2,LLCL}} = \sqrt{\frac{((L_1 + L_C)(L_2 + L_g) + L_1 L_C)(L_1 + L_2)}{(L_1 + L_2 + L_g)(L_C(L_1 + L_2) + L_1 L_2)}}, \quad (3.55)$$

for the *LLCL* filter. Now, if  $L_g$  is increased, (3.54) and (3.55) will converge into

$$\lim_{L_g \rightarrow \infty} \frac{f_{rc,LCL}}{f_{r2,LCL}} = \sqrt{\frac{L_1 + L_2}{L_2}} \quad (3.56)$$

and

$$\lim_{L_g \rightarrow \infty} \frac{f_{rc,LLCL}}{f_{r2,LLCL}} = \sqrt{\frac{(L_1 + L_2)(L_1 + L_C)}{L_1 L_2 + L_C(L_1 + L_2)}}, \quad (3.57)$$

for the *LCL* and *LLCL* filters, respectively.

By substituting (2.45) into (3.56) and (3.57), we get simpler forms of

$$\lim_{L_g \rightarrow \infty} \frac{f_{rc,LCL}}{f_{r2,LCL}} = \sqrt{\frac{a+1}{a}} \quad (3.58)$$

and

$$\lim_{L_g \rightarrow \infty} \frac{f_{rc,LLCL}}{f_{r2,LLCL}} = \sqrt{\frac{(L_1 + L_C)a + L_1 + L_C}{(L_1 + L_C)a + L_C}}, \quad (3.59)$$

The form in (3.58) for the *LCL* filter is perhaps more useful because it directly tells the designer how far higher the cross-coupling resonance can rise for a specific  $L_2/L_1$  ratio. In the *LLCL* filter case, the capacitor branch inductor adds some complexity. The higher the switching frequency is, the smaller  $L_C$  is for a given  $C_f$ , and as a result, the smaller the result of (3.59) is.

Figure 3.14 presents the relations (3.54) and (3.55) with a varying grid-connection *SCR*. It can be seen that with the same component values for  $L_1$ ,  $L_2$ , and  $C_f$ , the *LLCL* filters present a cross-coupling frequency that is closer to the resonance peak of the filter. This confirms that with the *LLCL* filter, the cross-coupling resonance can be pushed closer to the safe area of  $f_{sw}/2$  with smaller grid-side inductors than with the *LCL* filter. This difference is also emphasized with a lower *SCR*, that is, a weaker grid.

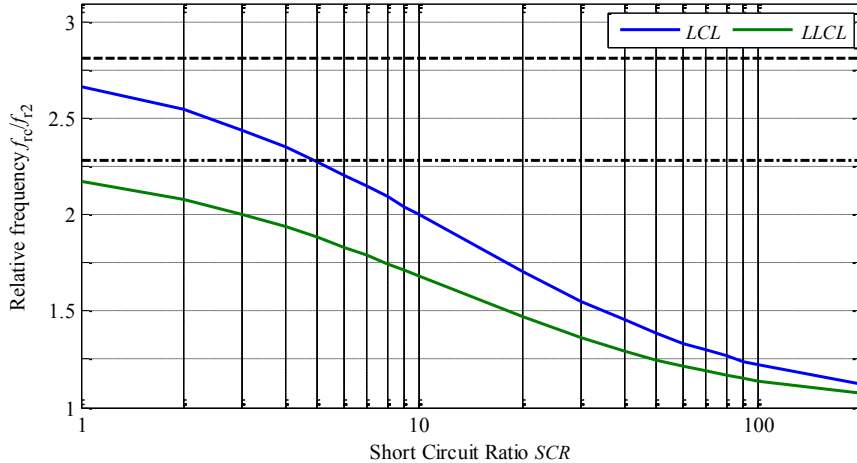


Figure 3.14. Relation of the cross-coupling resonance frequency to the higher resonance frequency  $LCL$  (blue) and  $LLCL$  (green) filters with respect to the grid connection short-circuit ratio. The dashed and dashed-dotted lines are the limits for the cross-coupling frequencies of the  $LCL$  and  $LLCL$  configurations, respectively.

### 3.4 Comparison of the physical sizes of filter components

The energy stored in inductors and capacitors can be used to assess the physical sizes of the components. The more energy is stored in the component, the larger the components must be to handle the energy. The peak energies of inductors and capacitors can be calculated by

$$\hat{E}_L = \frac{1}{2} L \hat{i}^2 \quad (3.60)$$

and

$$\hat{E}_C = \frac{1}{2} C \hat{u}^2, \quad (3.61)$$

where  $\hat{i}$  and  $\hat{u}$  are the peak values of currents and voltages.

To compute the total energies by (3.60) and (3.61), all harmonics have to be considered. However, the most significant component transferring energy, in other words, deciding the size of the component, is the fundamental frequency, which can be used to compare the sizes of the filter components. Assuming that the switching frequency ripple current is at its maximum value, for instance  $0.15I_{\max}$ , the energy of the ripple frequency component would be 2.25 % of the fundamental frequency energy with the nominal filter parameters. As it was shown in section 2.5.2, the maximum ripple occurs only when the dwell time of a zero vector equals zero. Otherwise, the ripple current is lower resulting in a lower ripple energy. If the ripple current is allowed to be 25 % of the nominal current,

its energy is raised to 6.25 % of the fundamental component energy, and the 10 % ripple current results in 1 % energy at the switching frequency. Furthermore, for the *LLCL* filter, the  $L_C C_f$  series connection in the capacitor branch is designed to have its resonance, and thus, the minimum impedance at the switching frequency. The worst-case effect of  $L_C$  can be assessed with the maximum current ripple. For the 60 pu (3 kHz) switching frequency,  $L_C = 0.0093$  pu (14.03  $\mu$ H). With the ripple current of 15 %, the high-frequency energy would be  $E_{Lc} = 1.04 \times 10^{-4}$  pu. Even with the 25 % current ripple, the energy would be only in the range of  $E_{Lc} = 2.89 \times 10^{-4}$  pu.

Figure 3.15 depicts the notation used in the energy calculations. It is assumed that the sensed grid voltage  $u_2$  does not change significantly, and all the paralleled inverters are controlled in phase to inject the same current to the grid.

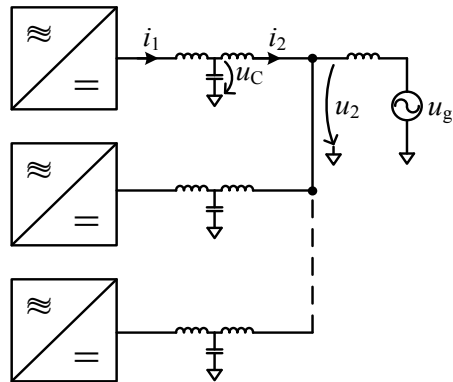


Figure 3.15. Parallel-connected inverters to depict the notation for the currents and voltages used in the calculation of component energies.

Phasor equations for the inverter-side current  $i_1$  and the capacitor voltage  $u_C$  of an *LCL* filter can easily be derived from the differential equations describing the system

$$\underline{i}_{1,LCL} = j\omega_1 C \underline{u}_2 + (1 - C(L_2 + L_g)\omega_1^2) \underline{i}_2, \quad (3.62)$$

$$\underline{u}_{C,LCL} = \frac{1}{1 - C(L_2 + L_g)\omega_1^2} (\underline{u}_2 + j\omega_1 (L_2 + L_g) \underline{i}_{1,LCL}), \quad (3.63)$$

where  $\underline{i}_2$  is the grid-side current phasor,  $\underline{u}_2$  is the grid voltage,  $L_g$  is the grid inductance, and  $\omega_1$  is the grid angular frequency (fundamental). With constant power at the grid interface,  $i_2$  being kept constant and  $u_2$  not varying considerably, the required inverter-side current and the capacitor voltage can be calculated and the effect of the *CL* trade-off analysed. Because the inverters and their filters are assumed identical, only one inverter and its filter has to be calculated. The effect of parallel connection is taken into account when the grid inductance  $L_g$  is multiplied by the number of paralleled inverters  $n$ . The *LC*, *LC+L*, and *L*-configurations can be analysed by (3.62) and (3.63) with the distinction that the *LC* configuration only has  $L_g$  in the grid branch,  $L_2$  is also multiplied by  $n$  for the

$LC+L$  case, and the  $L$ -configuration is modelled as a single equivalent full-power inverter with  $L_1$  divided by  $n$ . For the  $LC$  configuration,  $L_2$  is omitted from (3.62) and (3.63).

The phasor equations for the  $LLCL$  filter are very similar to (3.62) and (3.63) as can be seen from

$$\underline{i}_{1,LLCL} = \frac{1}{1 - CL_C\omega_1^2} \left( j\omega_1 C \underline{u}_2 + (1 - C(L_2 + L_g + L_C)\omega_1^2) \underline{i}_2 \right) \quad (3.64)$$

and

$$\underline{u}_{C,LLCL} = \frac{1}{1 - C(L_2 + L_g + L_C)\omega_1^2} \left( \underline{u}_2 + j\omega_1 (L_2 + L_g) \underline{i}_{1,LLCL} \right). \quad (3.65)$$

The derivation of (3.62)–(3.65) is presented in more detail in Appendix E.

In many cases, the grid-connected inverters are required to satisfy a particular power over a determined power factor range. For instance, the Finnish high-voltage transmission system operator Fingrid requires power-generating facilities with the active power rating of  $10 \text{ MW} \leq P_{\max} < 25 \text{ MW}$  to operate on full power within the range of  $0.995_{\text{ind}} \leq PF \leq 0.995_{\text{cap}}$ . For power generation facilities with  $25 \text{ MW} \leq P_{\max} < 100 \text{ MW}$ , the power factor limits are  $0.95_{\text{ind}} \leq PF \leq 0.95_{\text{cap}}$  (entso-e, 2013), (Fingrid, 2013).

For lower power levels there are no reactive power generation guidelines available. In this study, the total power of the paralleled inverters is generally less than 10 MW. However, as the distributed generation increases, it would be advisable to take account of the possibility that reactive power would be required from smaller than 10 MW facilities also. It is assumed that the grid-connected inverter system is expected to operate at the nominal power  $S_n = 1000 \text{ kVA}$  within the power factor range of  $0.9_{\text{ind}} \leq PF \leq 0.9_{\text{cap}}$  for each paralleled inverter. The power factor range was deliberately chosen to be wide to give a better insight into the effect of different operating points on the component energies. A single inverter is under study, and the relative sizes of the total filter arrangement are assessed by multiplying the energies by  $n$ .

Figure 3.16 presents the energies of the components of a single filter in a parallel-inverter system for stiff (a) and weak grid (b) cases for the  $LCL$ ,  $LLCL$ ,  $LC$ , and  $LC+L$  configurations. While a single inverter sees the grid branch multiplied by  $n$ , the total energy varies. The result is similar to the case of varying the grid-side inductor for a single inverter. The  $LC$  configuration presents the lowest energy in Figure 3.16, and the similar results for the  $LC+L$  configuration come from omitting the common  $L_2$  from the figure. This is done to compare the  $LC$  parts of the  $LC$  and  $LC+L$  configurations. However, the energy of the common  $L_2$  naturally grows by the factor  $n^2$ , leading to the largest energy already from  $n = 2$ .

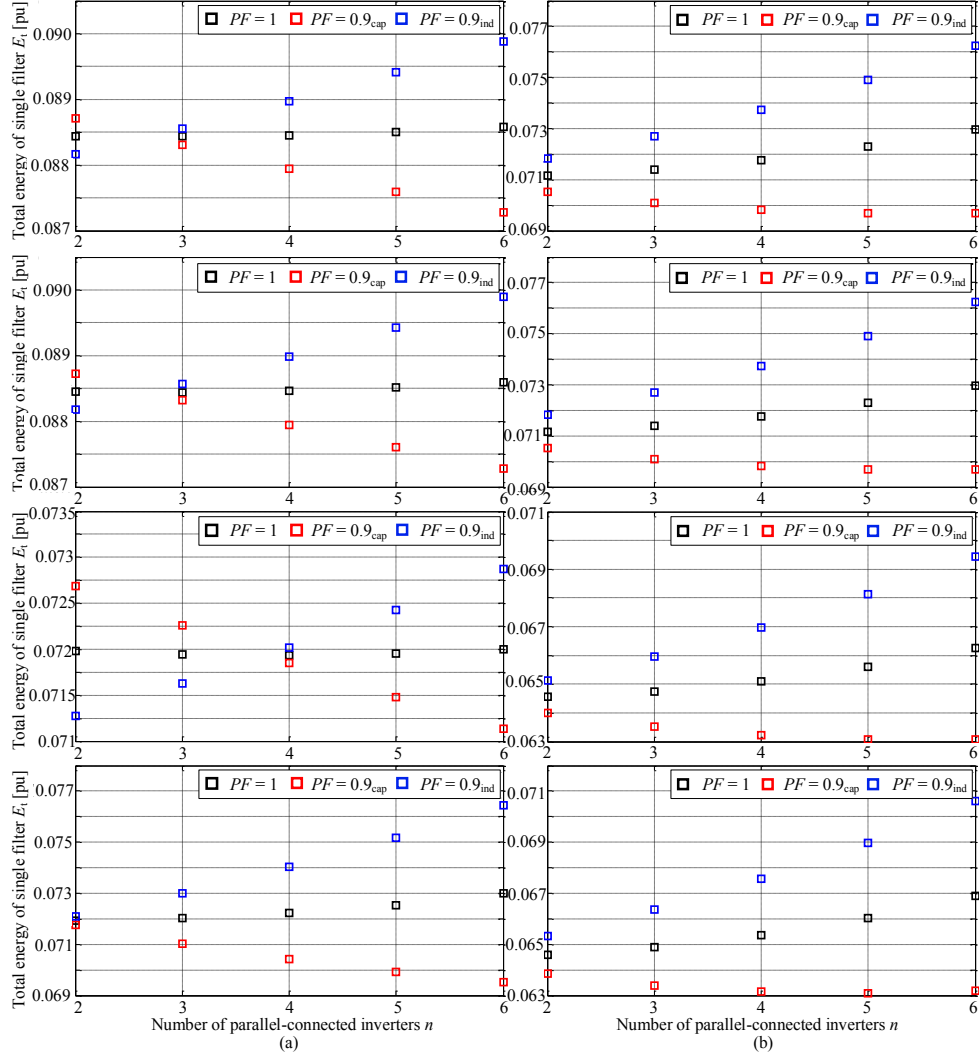


Figure 3.16 From top to bottom, single filter sum energy of the *LCL*, *LLCL*, *LC*, and *LC+L* configurations in a stiff grid (a) and a weak grid (b). The filter components are the nominal values and  $L_1$  according to 15 % maximum inverter-side current ripple. For the *LC+L* configuration, the common grid-side inductor  $L_2$  is neglected.

Figure 3.16 shows that by parallel-connecting several inverters, the point of minimum energy stored in a single filter changes. The minimum energy point is defined as the point where the energies for all three power factors are closest to each other, resulting in the smallest maximum energy for any  $PF$ . For instance, the stiff grid case of the *LCL* filter results in the minimum energy point to be with  $n = 3$ . With an inductive power factor, the energy of a single filter tends to increase, whereas with a capacitive power factor, the energies decrease as  $n$  increases. For  $PF = 1$ , the sum energy decreases until  $n = 3$  and

then starts to increase. However, the change is minimal compared with cases with  $PF = 0.9_{\text{cap}}$  or  $0.9_{\text{ind}}$ , and with the scale of the figure, it is difficult to notice. It is noteworthy that below the minimum energy point, the maximum energy is obtained with a capacitive power factor, and above the point, the inductive power factor results in the maximum energy.

Increasing the  $L_1$  value to make the ripple current smaller shifts the minimum energy point towards higher values of  $n$  for the stiff grid case. For the weak grid case, the point is not moved from  $n = 2$  but the values for different power factors are pushed closer to each other. The total energy per one filter in the configuration is increased by the increase of  $L_1$  because the fundamental experiences more inductance. This applies to both the stiff and weak grid cases. Decreasing  $L_1$  results in an opposite outcome for the stiff grid case. The minimum energy point is shifted towards a lower number of paralleled inverters, while the total energy of one filter in the configuration is decreased by less inductance facing the fundamental current. For the weak grid case, the minimum energy point remains at  $n = 2$ , but the difference between the different power factors is increased.

Figure 3.16 shows that with parallel-connected inverters, there is a risk that the filter components are designed to handle too small energy if the analysis is not properly done over the whole targeted range of  $n$ . Furthermore, it is possible that the filter is designed based on a wrong power factor. For instance for the *LCL* configuration, with  $n = 2$ , the capacitive power factor case is the case for dimensioning the arrangement, but with  $n \geq 3$ , the inductive power factor produces the highest energy.

As  $n$  is increased, the increase in the energy is mainly due to the capacitor energy. With an inductive power factor, the capacitor voltage is increased thereby increasing the energy of the component, whereas a capacitive power factor decreases the capacitor voltage as  $n$  increases for the *LCL*, *LLCL*, *LC*, and *LC+L* configurations. It is also noteworthy that the energies of the *LC* parts of the *LC* and *LC+L* configurations differ from each other. The minimum energy point is shifted down for the *LC+L* configuration by the effect of the common grid-side inductor. If the filter arrangement is designed as an *LC* configuration, adding a common grid-side inductor can cause too large an energy to be stored in the inverter-side inductor and the capacitor. Thinking of modularity, which is further assessed in section 3.7, designing the filter arrangement as *LC+L* and then removing the common grid-side inductor can increase the modularity of the filter configuration.

Table 3.4 and Table 3.3 present the smallest and largest maximum energies of a single filter for the stiff and weak grid cases. The smallest maximum energy occurs when energies for all three power factors are closest to each other. In the tables, this energy is referred to as  $E_{\min}$  while the largest maximum energy is referred to simply as  $E_{\max}$ . From the filter component design perspective, this  $E_{\max}$  affects most the dimensioning of the filter components. On the other hand, to minimize the physical dimensions of the filter components, the design should be made in such a way that  $E_{\min}$  occurs.

Table 3.3. Single filter sum energies with the max. and min. difference in a weak grid with nominal values.

Configuration	$E_{\min}$	$n$	$E_{\max}$	$n$	$E_{\max}/E_{\min} [\%]$
$LCL$	0.07182	2	0.07623	6	106.2
$LLCL$	0.07182	2	0.07624	6	106.5
$LC$	0.06511	2	0.06945	6	106.7
$LC+L$	0.06532	2	0.07060	6	108.1

Table 3.4. Single filter sum energies with the max. and min. difference in a stiff grid with nominal values.

Configuration	$E_{\min}$	$n$	$E_{\max}$	$n$	$E_{\max}/E_{\min} [\%]$
$LCL$	0.08855	3	0.08988	6	101.5
$LLCL$	0.08856	3	0.08989	6	101.5
$LC$	0.07202	4	0.07287	6	101.2
$LC+L$	0.07210	2	0.07645	6	106.0

In the stiff grid case, the grid-side inductance is larger, which results in a larger energy stored in the inductance compared with the weak grid case. Furthermore, a larger grid-side inductance makes especially the  $LCL$  and  $LLCL$  configurations less susceptible to the grid branch multiplication. The difference between the minimum energy point and the maximum energy is only 1.5 % for the  $LCL$  and  $LLCL$  configurations and 1.2 % for the  $LC$  configuration. It is quite clear that  $L_C$  in the capacitor branch of the  $LLCL$  configuration has no real effect on the maximum energy of the filter. However, for the  $LC+L$  configuration, the difference is 6 % even in the stiff grid. This is due to the common  $L_2$  in the grid branch, which is also multiplied by  $n$ . This can lead to a situation in which the  $LC$  circuit of the  $LC+L$  configuration stores more energy than with the  $LC$  configuration, even though the values are the same for both configurations.

With the weak grid case, the  $LC+L$  configuration does not deviate essentially from the stiff grid, although its difference between the minimum and maximum is increased and it is at largest with the value of 8.1 %. The  $LCL$ ,  $LLCL$ , and  $LC$  configurations present 6.2 %, 6.5 %, and 6.7 % differences between the minimum and maximum values, respectively. This difference is smaller than for the stiff grid because in the weak grid case the common  $L_2$  is designed to be of smaller inductance.

Increasing the  $L_1$  value to limit the inverter-side current ripple results in a smaller difference between  $E_{\min}$  and  $E_{\max}$ , while decreasing the  $L_1$  value results in a wider gap between the two energies. This suggests that if the aim is to design the filters for a particular range of  $n$ ,  $L_1$  should be designed large so that with a small  $n$  the filter components would not be excessively over-dimensioned.

The  $L$ -configuration energies cannot be directly compared with the other configurations, because the configuration only has one three-phase capacitor and one three-phase grid-side inductor. However, the inverter-side inductors and the total energies of the filter

arrangement can be compared. Unlike the other four configurations, the *L*-configuration inverter-side inductor energies seem to differ somewhat from the other configurations. Figure 3.17 and Figure 3.18 present the inverter-side inductor energies for one inverter in a parallel-inverter system for the *L*-configuration and the *LCL* configuration, respectively. It can be seen that in both the stiff and weak grid, the *L*-configuration  $L_1$  energies in all power factors tend to each other, while in the *LCL* configuration the  $L_1$  energies of a single inverter decrease approximately at the same rate regardless of the power factor. The *LLCL*, *LC*, and *LC+L* configurations behave like the *LCL* one. For all of the configurations, the capacitive power factor case presents the largest energy. The *LCL*, *LLCL*, *LC*, and *LC+L* configurations have 1.4 %, 1.4 %, 1.6 %, and 0.8 % more energy stored in  $L_1$  for all current ripple cases. With the weak grid case, there is no difference between the configurations in terms of the  $L_1$  energies.

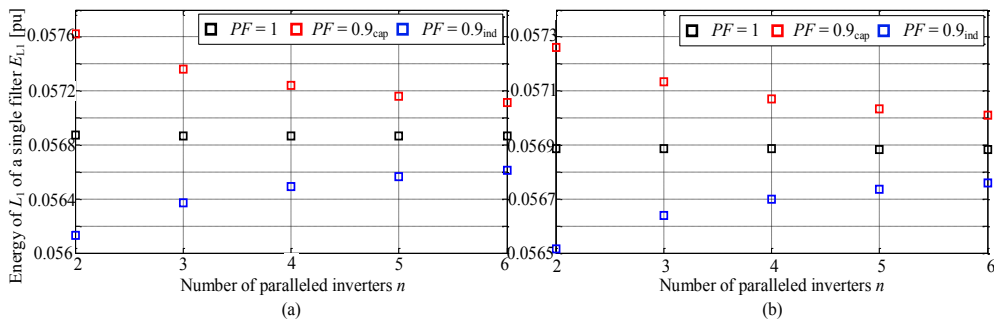


Figure 3.17 Inverter-side inductor  $L_1$  energies of a single *L* filter in an *L*-configuration in a stiff grid (a) and a weak grid (b).

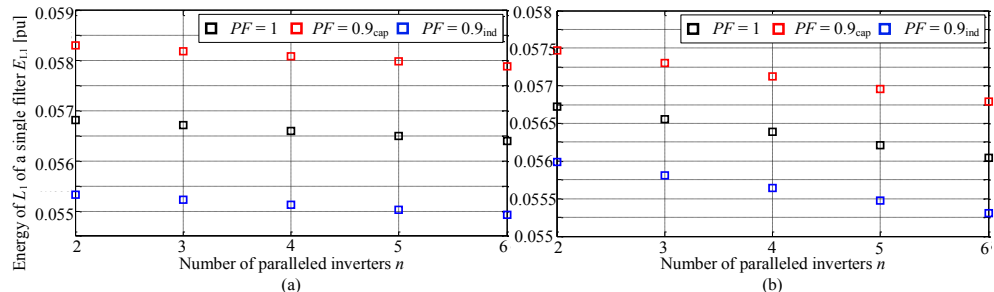


Figure 3.18 Inverter-side inductor  $L_1$  energies of a single *LCL* filter in an *LCL* configuration in a stiff grid (a) and a weak grid (b).

Figure 3.19 presents the total energies of the filter arrangements for each configuration in the stiff grid (a) and the weak grid (b). The values are calculated with the nominal filter values. It can be seen that with only a few inverters in parallel, there is no significant difference between the different cases of power factors. With a higher number of inverters paralleled, there appears to be some difference, especially in the weak grid case. The least energy is stored in the *LC* configuration and the most in the *LC+L* configuration. The difference mainly comes from the vast energy stored in the common  $L_2$  of *LC+L* configuration. Similarly, the common  $L_2$  of the *L*-configuration causes the total energy

increase much faster compared with the *LCL*, *LLCL*, and *LC* configurations. The extra inductors of the *LLCL* configuration virtually have no impact at all on the total energy of the filter arrangement.

For low-voltage designs, such as the ones studied in this dissertation, the common grid-side inductor becomes impractically large and bulky after only a few inverters are connected in parallel because of the multiplied current flowing through it. In the inductor design, it is known that the maximum inductance that can be obtained with a particular core can be calculated by

$$L_{\max} = \frac{NA_{\text{core}}\widehat{B}_{\text{core}}}{I}, \quad (3.66)$$

where  $N$  is the number of winding turns,  $A_{\text{core}}$  is the core cross-section,  $\widehat{B}_{\text{core}}$  is the peak magnetic flux density, and  $I$  is the peak current.

Now, it is assumed that  $L$  is fixed. The peak magnetic flux density  $\widehat{B}_{\text{core}}$  is limited to the saturation flux density of the particular core material. For laminated cores (iron), which are used in high-power inductors at the grid frequency, the saturation occurs around a maximum of 2.0 T (Erickson, 1999). In order to limit  $\widehat{B}_{\text{core}}$  below the saturation limit and to a desired value, the only parameters that can be used are  $A_{\text{core}}$  and  $N$ . By increasing one or both of these parameters,  $\widehat{B}_{\text{core}}$  can be kept at a suitable level. This can be seen directly when  $\widehat{B}_{\text{core}}$  is solved from (3.66). In addition, the larger the current is, the larger the conductors are, and the larger a core is needed.

This problem can be overcome by decreasing the common grid-side inductor by the factor of  $1/n$ , which was done in (Juntunen et al., 2015). Ideally, the outcome would be that the *LC+L* common grid-side inductor would then match the individual grid-side inductors of *LCL*. Furthermore, the resonance frequencies would be the same with this kind of a design. Similarly for the *L*-configuration, the common grid-side inductor should be decreased to avoid huge energies in the inductor. If the capacitor were increased by the factor  $n$ , the design would match again the *LCL* filter, but the energies would differ because of different capacitor voltages in the designs. This would lead to a situation where the *L*-configuration would store significantly more energy compared with the other configurations, even though it has the least components.

Table F.1 and Table F.2 in Appendix F present the maximum total energies of the filter arrangements for each configuration in the stiff and grid. Table F.3 and Table F.4 in Appendix F present the maximum total energies of the filter arrangements for each configuration in the weak grid.

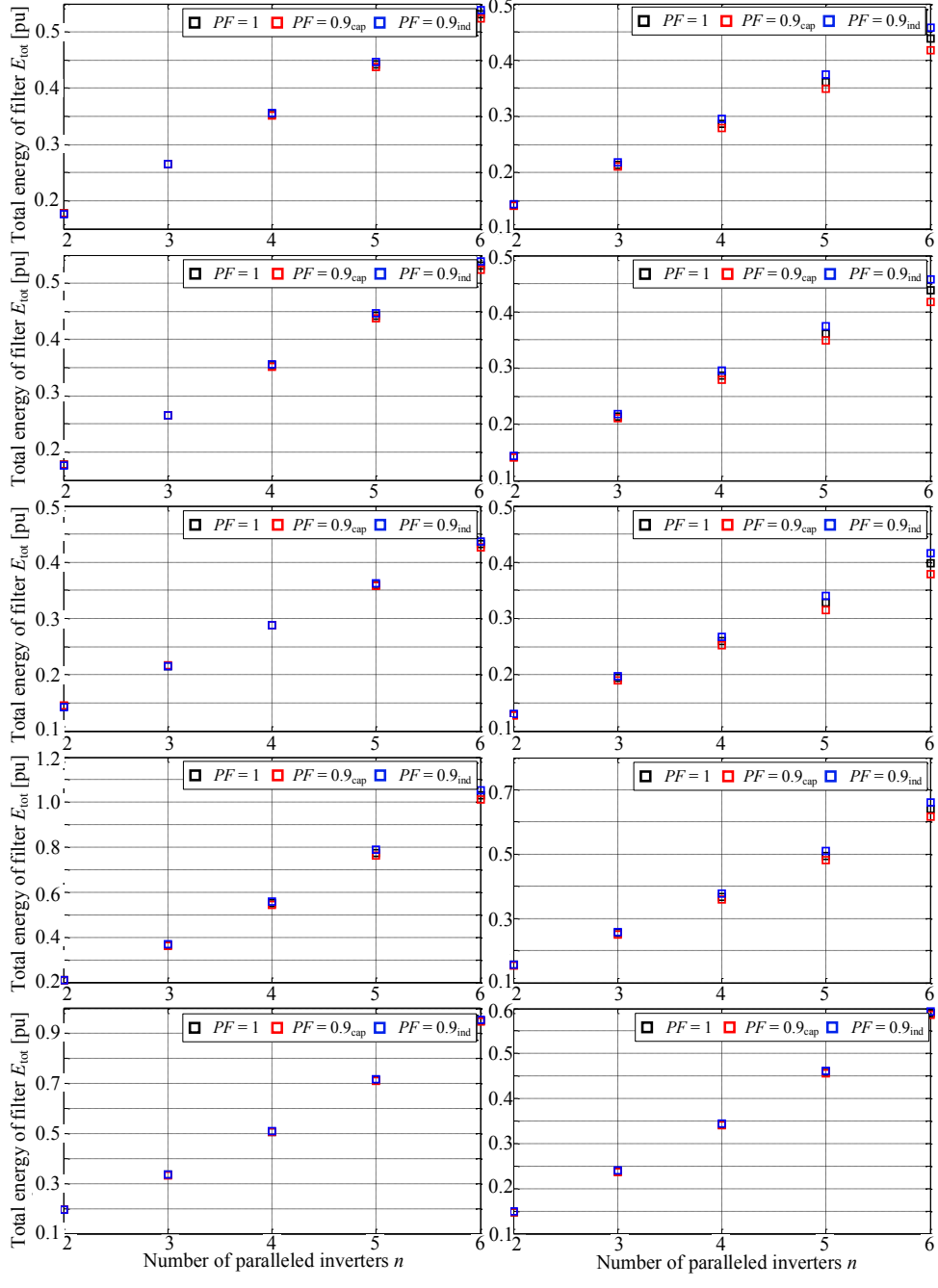


Figure 3.19 Total energy of the filter arrangement from top to bottom for the  $LCL$ ,  $LLCL$ ,  $LC$ ,  $LC+L$ , and  $L$ -configurations in a stiff (a) and a weak (b) grid. The filters are with nominal design values with  $L_1 = L_{1,(15\%)}$  for each configuration.

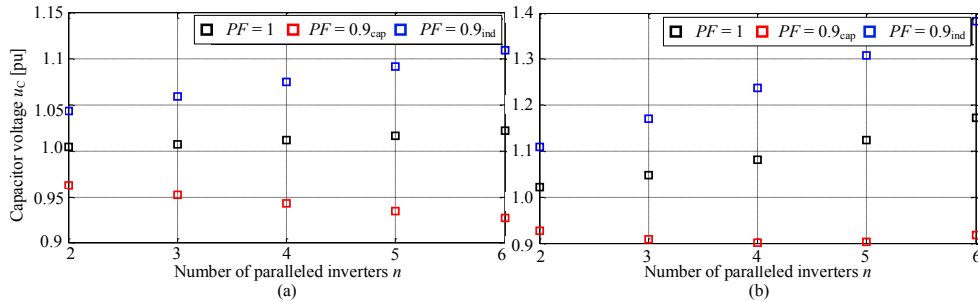


Figure 3.20 Capacitor voltage  $u_C$  of a single *LCL* filter in the stiff grid (a) and the weak grid (b) for the number of paralleled inverters being from two to six.

### 3.4.1 Changing the capacitor and grid-side inductor value

Nominally, the capacitor voltage  $u_C$  can be assumed to match the measured grid voltage  $u_2$ , but owing to the varying operation conditions and power factors,  $u_C$  can differ from  $u_2$ . The capacitor voltage is also affected by the inductance between the capacitor and the grid connection point and the current flowing through it. Nevertheless, this suggests that the electrical dimensioning of the capacitor has a significant impact on the energy stored in the component and the whole filter. Figure 3.20 presents the capacitor voltage of a single *LCL* filter with two to six inverters connected in parallel. There is a significant difference between the stiff grid case (a) and the weak grid case (b). In the weak grid case,  $u_C$  starts from higher values and the rise in the capacitor voltage with  $PF = 0.9_{\text{ind}}$  is much greater. Even though the capacitor is dimensioned as half of the stiff grid case, the energy stored in the capacitor is 56.4 % and 77.3 % of the capacitor energy of the stiff grid case with  $n = 2$  and  $n = 6$ , respectively.

When only the capacitor is changed for both the stiff and weak grid cases, it is revealed that the capacitor voltage in each power factor case does not change any configuration. The effect of capacitor value on the capacitor voltage was studied by computing the voltages for nominal, halved, and doubled capacitor values for all designs. The results did not change with different  $L_1$  values either. Because the capacitor itself does not affect its voltage, the capacitance plays a key role in determining the capacitor energy, that is, the size.

The grid-side inductor value has a great impact on the total energy of a single filter. When the current through the inductor is kept constant, decreasing or increasing the inductance has a directly proportional effect on the component energy. Figure 3.21 presents the total energies of the filter components in a single *LCL* filter in a parallel-inverter system with three different values for  $L_2$ . When  $L_2$  is 50 % larger than the nominal value, the energy is the largest for all  $PF$  in the figure. Similarly, when  $L_2$  is only 50 % of the nominal value, the energy is less than in the nominal case (middle). It can be seen that the larger the grid-side inductor is, the more energy is stored in the component, and the more the

total energy of the filter is. The inductor value has virtually no effect on the capacitor voltage and energy, especially when considering the *LCL* and *LLCL* configurations.

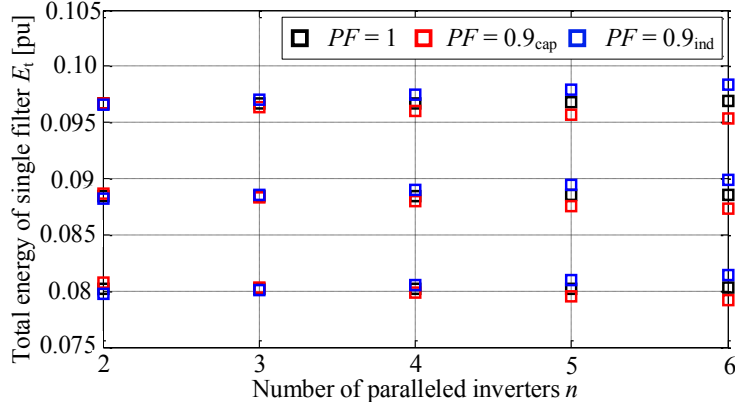


Figure 3.21 Single *LCL* filter energies with three different values for  $L_2$ ;  $L_2 = 1.5L_{2,\text{nom}}$  (top),  $L_2 = L_{2,\text{nom}}$  (middle), and  $L_2 = 0.5L_{2,\text{nom}}$  (bottom).

For the *LC+L* and *L*-configurations, which have a common  $L_2$  and even larger current flowing through it, the value of the grid-side inductor has a minimal effect on the capacitor voltage. However, the larger  $L_2$  is, the larger its voltage drop will be, which requires an increased capacitor voltage to drive the power to the grid. This causes the capacitor energy to increase. The point of minimum energy is located at a smaller number of  $n$  when  $L_2$  is increased. However, because of the drawback that the total energy is increased, the value of  $L_2$  alone should not be used to place the minimum energy at a small value of  $n$ .

From the perspective of filter design, especially regarding the resonance frequencies and their importance in the control system design, it would be advantageous to adjust the capacitor and grid-side inductor both to limit the energy and keep the resonance frequencies unchanged or within a specified range from the original value.

If the target is to keep the resonance frequencies constant over the whole range of  $n$  while the grid-side inductor is not changed, the relations presented in section 3.3.2 should be used. It should be noted that because the capacitor is already inside the square root in the resonance frequency equations, the relations have to be applied squared to get rid of their roots. For the *LC* and *LC+L* configurations, the capacitor should be multiplied by  $1/n$  in order for the lower frequency to be kept at  $f_{r1,\text{nom}}$ . Using (3.44) for the higher resonance of both configurations, the frequency is kept at nominal but for the *LC* configuration it must be  $L_2 = 0$ .

For the *LCL* and *LLCL* configurations, the relations for  $f_{r1}$  and  $f_{r2}$  are (3.45) and (3.47) for *LCL*, and (3.46) and (3.48) for *LLCL*, respectively. The *L*-configuration does not suffer from the resonance shift in  $f_{r1}$ , but for  $f_{r2}$  (3.49) should be used. It should be noted that with the *LLCL* configuration, the relations (3.46) and (3.48) include  $L_C$ , the value of which

depends on  $C_f$  and  $f_{sw}$ . If  $f_{sw}$  is not allowed to change, it is impossible to keep  $f_{r1}$ ,  $f_{r2}$ , and  $f_{r3}$  constant with (3.46) and (3.48). However, one simple solution would be to first change the  $C_f$  value and then compute a new  $L_C$  value to keep  $f_{r3}$  at  $f_{sw}$ . This leads to fairly good results with the two other resonance frequencies, especially with  $f_{r2}$ .

With the above-mentioned conditions and based on keeping the resonances constant, an exhaustive computational study was performed. The energies were computed for each configuration with three different values for  $L_1$  limiting the inverter-side current ripple to 10 %, 15 % (nominal), and 25 % for both the stiff grid and weak grid cases. The calculations were performed by keeping first  $f_{r1}$  and then  $f_{r2}$  constant. For the *LLCL* configuration,  $L_C$  has to be changed if  $C_f$  is changed in order to keep the third resonance frequency at the switching frequency. The value of  $L_C$  has an effect on both  $f_{r1}$  and  $f_{r2}$ , which means that keeping  $f_{r3}$  constant, neither of the lower frequencies remains constant. However, the calculations indicate that this is an advantageous quality for the *LLCL* configuration rather than a disadvantage. The effect of  $L_2$  was tested by performing the calculations with three different values for the grid-side inductor;  $L_2 = 0.5L_{2,nom}$ ,  $L_2 = L_{2,nom}$ , and  $L_2 = 1.5L_{2,nom}$ . Together with the nominal value calculations, the study includes over 300 sets of calculations, which give an insight into how changing the capacitor and grid-side inductor values affect the filter energies and resonances.

Generally, it can be stated that regardless of the configuration or whether the case is a stiff or a weak grid, the larger the inverter-side inductor  $L_1$  is, the less the total energy stored in the filter components rises with an increasing  $n$ . In addition, increasing the grid-side inductor has a small effect on this rise of energy when also the capacitor is changed. The larger  $L_2$  is, the more the energy increases, but for instance the difference remains under 1 % with the  $L_2$  values tested. It should be noted that in this analysis the maximum energy of all three *PF* cases is considered. Between the different *PF* cases, the results can vary in such a way that the energy rises more with a decreased value of  $L_2$  instead of an increased value.

Figure 3.22 presents the capacitor values for each configuration when  $f_{r1}$  is kept constant (a) and when  $f_{r2}$  is kept constant (b) with nominal inverter-side and grid-side inductor values. As it is already evident by looking at (3.43) and (3.47)–(3.50), both resonance frequencies cannot be kept constant with the same capacitor values when  $n$  is increased. Common for the *LCL*, *LLCL*, *LC*, and *LC+L* configurations is that  $f_{r2}$  requires a larger capacitance to be kept steady, and for both  $f_{r1}$  and  $f_{r2}$  the capacitor must be decreased. However, the *L*-configuration differs from the rest as its capacitor has to be increased in order to keep  $f_{r2}$  constant. The lower resonance frequency is constant anyway, so this can be considered an advantage for the configuration. Moreover, this is very much in line with the general *LCL* filter design guidelines, especially with (2.40), which states that the capacitor should be designed according to a particular percentage of the active power. Because the capacitor is common in the *L*-configuration, increasing the number of paralleled inverters also increases the required power rating of the common capacitor.

The effect of  $L_1$  is to limit the rate of change required in the capacitor. The smaller the value of  $L_1$  is, the less the capacitor has to be changed. This action is common for all configurations. The effect of  $L_2$  is similar; the larger  $L_2$  is, the less capacitor has to be decreased or increased depending on the configuration. Of course, if  $L_2$  is changed, the capacitor has to be changed to keep  $f_{r1}$  at the nominal design value for the  $L$ -configuration.

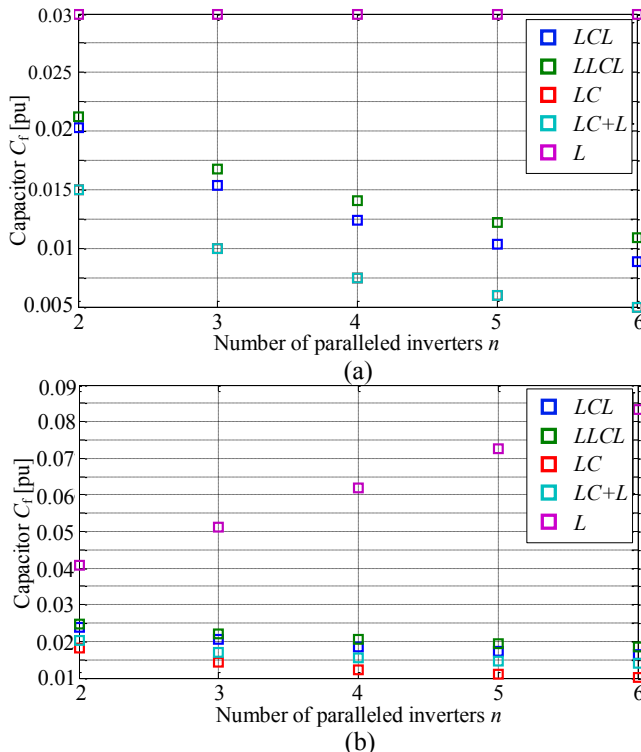


Figure 3.22 Filter capacitor valued required to keep  $f_{r1}$  constant (a) and  $f_{r2}$  constant (b).

### ***LCL* and *LLCL* configurations**

Figure 3.23 presents the total energy and resonance frequencies for the *LCL* configuration with adjusted  $C$  and  $L_2$  related to the nominal case with the number of inverters in parallel varying from two to six. The blue colour indicates the case when  $L_2$  is not changed and the capacitor is changed by (3.45) and (3.47) for  $f_{r1}$  and  $f_{r2}$  made constant, respectively. The red colour indicates the case when the inductor is half of the nominal value, magenta indicates a 50 % higher inductor value, and green a case where the inductor is at the nominal value. For red, green, and magenta, the capacitor value was computed directly from the resonance frequency equations. It can be seen that the green and blue cases are equal. Figure 3.23(b) presents the frequencies in such a way that for instance for  $f_{r1}, f_{r2}$  is constant but not plotted in the figure. The square symbols in both parts of Figure 3.23 are related to the same case. For instance, by looking at the top figures, the square symbol in Figure 3.23(a) indicates the *LCL* configuration energy in the stiff grid in the case when

$f_{r1}$  is kept constant. The square symbol in Figure 3.23(b) in the top figure denotes  $f_{r2}$  when  $f_{r1}$  is kept constant. The same rule applies also to the diamond symbols.

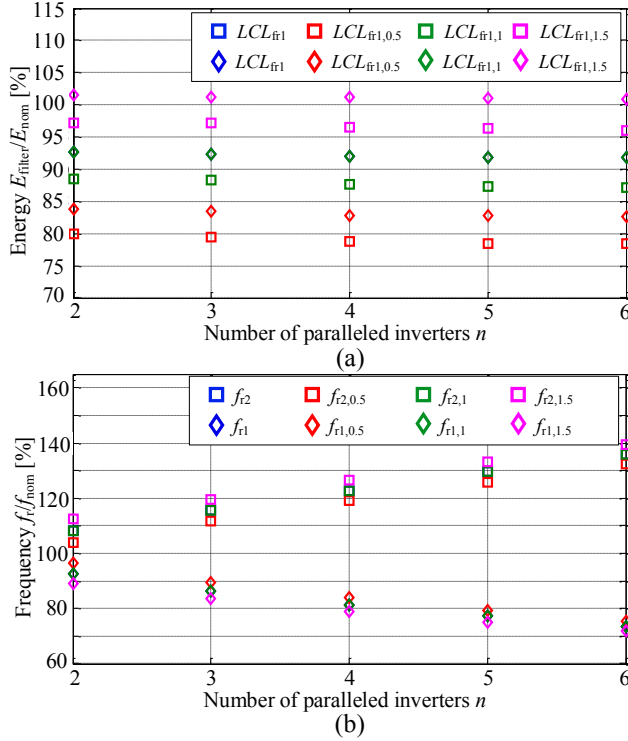


Figure 3.23 (a)  $LCL$  configuration filter energies with changed  $C_f$  and  $L_2$  values related to the nominal design energies in the stiff grid. (b) Respective resonance frequencies as a percentage of the nominal resonance frequency. The inverter-side inductor is at its nominal value of  $L_{1,(15\%)}$ . It should be noted that in (b), the frequency that is kept constant is not plotted. For instance,  $f_{r2}$  increases (squares) and  $f_{r1}$  stays at 100 %, but is not plotted for the sake of readability.

When  $f_{r1}$  is kept constant, the energy in the filter components of the  $LCL$  configuration remains lower compared with the situation of  $f_{r2}$  being kept constant. When  $f_{r1}$  is kept constant,  $f_{r2}$  tends to increase, which can be an advantageous design quality considering the filter and control system design, which are practically the same. Parker et al. (2014), Tang et al. (2015), and Lu et al. (2016) have studied the active damping with  $LCL$ -filter-based grid inverters. When  $f_{r2}$  is above the critical frequency  $f_s/6$ , no damping is required, whereas if  $f_{r2}$  is below this limit, damping is required. Parker et al. (2014) also conclude that if the resonance frequency is at the limit, capacitor current feedback-based active damping that they use does not work. In addition, the higher  $f_{r2}$  is placed, the weaker the attenuation of the switching frequency harmonics becomes. The general guideline upper limit is  $f_{r2} \leq f_{\text{sw}}/2$ , which should be kept in mind with paralleled inverters also.

The smaller the  $L_1$  is, the larger is the difference between these two cases. This is due to the fact that with a large  $L_1$  the capacitor has to be decreased less to keep either of the frequencies constant. The same effect also holds for the resonance frequencies. Further, a large  $L_1$  decreases the rate of change for the resonances for both scenarios.

Because the current flowing through the grid-side inductor is not affected by the number of paralleled inverters, the energy stored in the filter components is directly proportional to the  $L_2$  value. The value of  $L_2$  has a minor effect on the differences between the two cases, but this is mainly seen in the resonance frequencies as an offset as can be seen from Figure 3.23(b).

The energies of the *LLCL* configuration are very similar to the *LCL* configuration. The only difference is due to the additional capacitor branch inductor  $L_C$ , which contributes to the increased energy. However, the difference is generally less than 1 %. Although  $L_C$  does not significantly contribute to the energy, it has a greater effect on the resonance frequencies.

Figure 3.24 presents the resonance frequencies  $f_{r1}$  and  $f_{r2}$  of the *LLCL* configuration in the stiff grid when the capacitor and the grid-side inductor are changed. Here, the blue and green cases do not match completely. This is due to the additional inductor, which is an additional degree of freedom in setting the highest resonance frequency  $f_{r3}$ . The capacitor for each case is calculated by (3.48) and (3.50) (blue) or directly from the resonance frequencies (red, green, and magenta) and then, a new value of  $L_C$  is calculated to keep  $f_{r3}$  constant. In the blue case,  $L_C$  is not increased as much as in the green case to give an insight into how a larger  $L_C$  affects the system.

The dimensioning of  $L_C$  naturally has an effect also on the two lower frequencies, which means that instead of keeping  $f_{r1}$  or  $f_{r2}$  constant, they are kept close to constant. For the remainder,  $f_{r3}$  is the frequency that should be dimensioned to be equal with  $f_{sw}$ . It should also be noted that in Figure 3.24, both the frequencies are always from the same case unlike in the *LCL* configuration in Figure 3.23, where the constant frequency is not plotted.

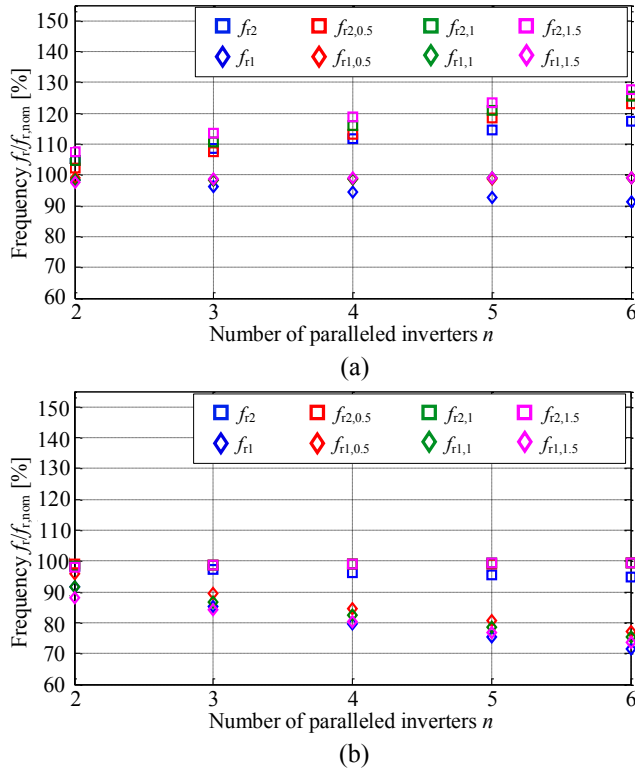


Figure 3.24 (a)  $LLCL$  configuration resonance frequencies as a percentage of the nominal frequencies in the stiff grid when  $f_{r1}$  is kept close to constant and (b) when  $f_{r2}$  is kept close to constant. The inverter-side inductor is at its nominal value of  $L_{1,(15\%)}$ .

Because  $f_{r3}$  is a constant frequency, the resonance frequencies  $f_{r1}$  and  $f_{r2}$  of the  $LLCL$  configuration do not divert into different directions as much as they do for the  $LCL$  configuration. For instance, if the aim is to keep  $f_{r1}$  close to constant, the redimensioned  $L_C$  causes  $f_{r1}$  gradually to decrease, while  $f_2$  is increased. The larger the grid-side inductor is, the less  $f_{r1}$  is decreased at the expense of more increased  $f_{r2}$ . However, the effect of  $L_2$  can mainly be seen in  $f_{r2}$  and not in  $f_{r1}$ . Considering  $f_{r1}$ , the red, green, and magenta are so close to each other that they are on top of each other. Similarly, when  $f_{r2}$  is kept close to constant, red, green, and magenta overlap each other. The smaller  $L_2$  is, the less the frequency differs from the nominal value. This suggests that for  $LLCL$  filters in paralleled configurations, the grid-side inductors should be as small as possible if the resonance frequency placement is critical. Comparing the green and blue from Figure 3.24(a), it can be seen that the more the capacitance is decreased, resulting in an increased  $L_C$ , the closer to the nominal  $f_{r1}$  stays whereas  $f_{r2}$  increases more (green). In the blue case, capacitance is decreased less leading to  $L_C$  which is increasing less and the resulting  $f_{r1}$  decreases more compared with the green case. At the same time,  $f_{r2}$  increases less. In Figure 3.24(b), the effect is somewhat different. Both frequencies for the blue case always decrease more

than for the green case. Similarly to the *LCL* configuration, a large inverter-side inductor decreases the change in the frequencies whereas a small inductor increases it.

The main differences between the stiff and weak grid cases are that in the weak grid the energies remain closer to each other with the addition that the energy is decreased slightly more in the weak grid case. However, the drawback is that both the resonance frequencies shift more in the weak grid case. This is due to the small grid-side inductor for both configurations, which requires larger changes in capacitance.

### **LC and LC+L configurations**

The *LC* configuration does not have a grid-side inductor, and thus, only a capacitor can be used to adjust the frequencies. Figure 3.25 presents the energies of the *LC* and *LC+L* configurations and Figure 3.26 depicts the respective resonance frequencies in the stiff grid. The achieved smaller energies are a result of allowing a large change in the resonance frequencies by allowing a small capacitor value. For both cases, the change in the resonance frequency that is not made constant is virtually the same but in the opposite direction.

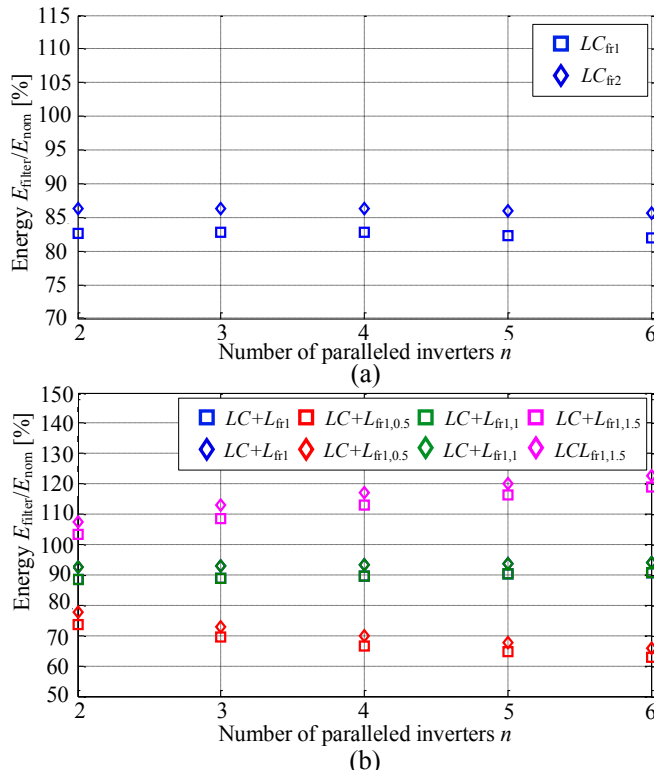


Figure 3.25 (a) *LC* configuration and (b) *LC+L* configuration filter energies in the stiff grid with changed  $C$  and  $L_2$  values related to the nominal design energies. The inverter-side inductor is at its nominal value of  $L_{1,(15\%)}$ .

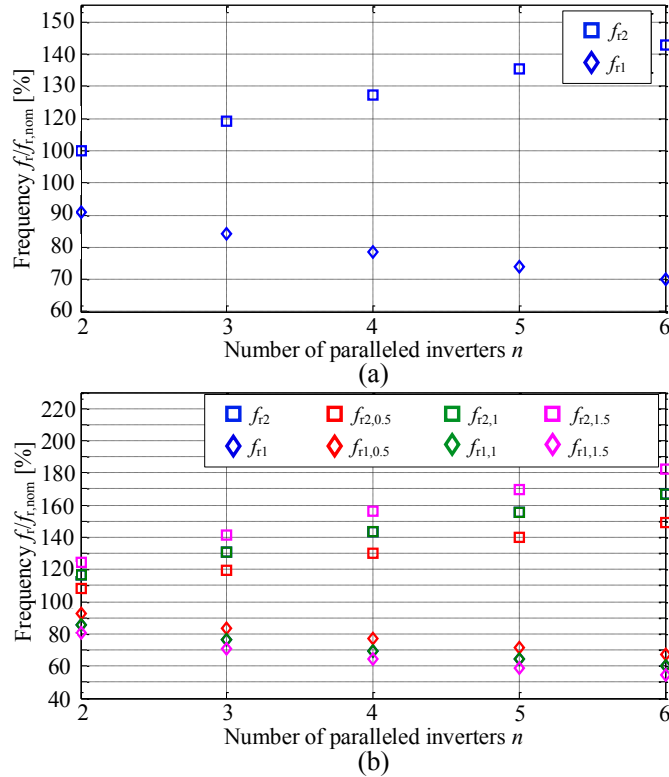


Figure 3.26 (a) *LC* configuration and (b) *LC+L* configuration filter resonance frequencies as a percentage of the nominal resonance frequency in the stiff grid with changed  $C$  and  $L_2$  values related to the nominal design energies. The inverter-side inductor is at its nominal value of  $L_{1,(15\%)}$ .

With  $f_{r1}$  kept constant (squares), the energies for the *LC* filters decrease more with larger  $L_2$  values, which counters the increase in the energy of  $L_2$ . With a larger  $L_2$  than nominal, the total energy of the filter configuration increases above the nominal design. The squares and diamonds in Figure 3.25Figure 3.26 approach each other with a larger  $n$ . This is due to the fact that  $C_f$  is decreased to keep the frequencies constant, and with a small  $C_f$  it is mainly the inductors that set the filter configuration energy. The larger  $L_1$  is, the more there is difference between the two cases and the more the resonance frequencies change. When compared with the *LCL* configuration, the *LC+L* configuration seems to experience a larger increase in the filter component energy. For instance, in the *LCL* configuration the maximum energy remains under 105 % of the nominal case energy even with the largest  $L_2$  value. For the *LC+L* configuration, the energy is already at this value with  $n = 2$  and increases towards 120 % when  $n$  increases to six. This is due to the common  $L_2$ .

Similarly to the *LCL* and *LLCL* configurations, in the weak grid case the energy of the *LC+L* configuration decreases slightly more compared with the stiff grid case. However, this does not hold for the *LC* configuration because it has no grid-side inductor. The

capacitor is the component that can be used to adjust the resonance frequencies. In the weak grid case, the capacitor is already small in value, and the change required to keep the frequencies constant is small compared with the original capacitor value. Compared with the stiff grid case, both configurations experience larger shifts in the frequency that is not made constant.

### L-configuration

The *L*-configuration presents a similar outcome as the *LC+L* configuration. Normally,  $f_{rl}$  remains constant for this configuration, which means that the only component that contributes to the change in energy is the common grid-side inductor. By looking at the top figure of Figure 3.27(a), we can see that the case when  $f_{r2}$  is kept constant starts with a larger increase in energy than the  $f_{rl}$  case. This is because the capacitor is increased to keep  $f_{r2}$  constant. With an increased current through the common  $L_2$ , the effect of the capacitors decreases in relation to the inductive energy. For this reason, the two cases approach each other as the number of paralleled inverters increase.

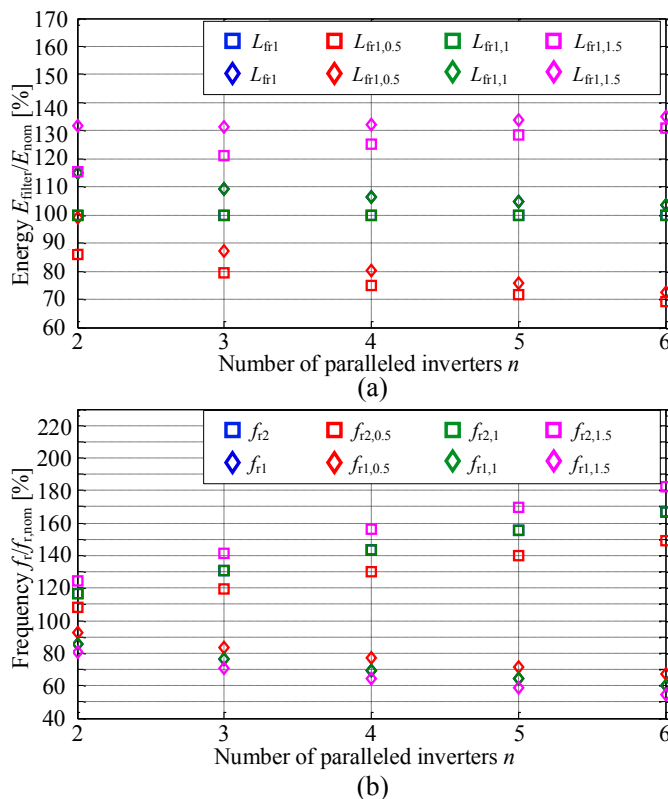


Figure 3.27 (a) *L*-configuration filter energies in the stiff grid with changed  $C$  and  $L_2$  values related to the nominal design energies. (b) Respective resonance frequencies as a percentage of the nominal resonance frequency. The inverter-side inductor is at its nominal value of  $L_{1,(15\%)}$

Changing the value of the inverter-side inductor has a great impact on the energies of the *L*-configuration. In the case of a large  $L_1$ , the difference between the energies of the two cases of frequencies kept constant is smaller than with a small  $L_1$ . However, this holds for the smaller number of paralleled inverters. When  $n$  is increased, the difference between the two frequency cases with larger  $n$  values is larger with a small  $L_1$  rather than a large  $L_1$ .

In a weak grid, the energy is decreased more than in the stiff grid case but at the expense of a larger change in the frequency that is not made constant.

### **Key findings summarized**

- By making  $L_2 < L_{2,\text{nom}}$ , the energy is decreased below the nominal case.
- Making  $L_2 > L_{2,\text{nom}}$ , the energy is increased above the nominal case.
- The smaller  $L_2$  is, the more the capacitor has to be changed, which leads to a smaller energy.
- The energies of the *LCL* and *LLCL* configurations are very similar when  $C$  is adjusted. Increasing or decreasing  $L_1$  and  $L_2$  has no significant effect on the difference.
- Since the *LC* configuration has no  $L_2$ , changing the capacitor has the greatest impact on the filter energy.
- The larger  $L_2$  is, the more  $f_{r1}$  shifts when  $f_{r2}$  is kept constant or close to constant (*LLCL*).
- The larger  $L_2$  is, the more  $f_{r2}$  shifts while  $f_{r1}$  is kept constant or close to constant (*LLCL*).
- When  $f_{r2}$  is kept constant or close to constant (*LLCL*),  $f_{r1}$  changes less than  $f_{r2}$  changes when  $f_{r1}$  is made constant with changing the capacitance.
- Because of  $f_{r3}$  of the *LLCL* filter, this configuration experiences the least changes in resonances.
- The *L*-configuration requires an increased value for the capacitor to keep  $f_{r2}$  constant while the other configurations result in decreasing values for the capacitor. This has a direct impact on the *L*-configuration energy.

### 3.4.2 Average filter designs

In the previous section, changes in the filter energies based on changing the capacitor and grid-side inductor value were presented. It is quite clear that when increasing the grid-side inductor, the energy is also increased. Moreover, even the nominal inductance can be difficult or even impossible to design for high currents in the configurations that have a common grid-side inductor. As the grid branch inductance is effectively multiplied by the number of paralleled inverters, the attenuation becomes better without the expense of increased energy. This action suggests that the grid-side inductor should be decreased to keep the attenuation at the design value. If not, the attenuation is increased, which can be considered an advantage.

Based on the observations from the study in the previous section, it may be advantageous for some configurations to design the filter capacitor as an average value over a range of  $n$  over which the designer wants the same filter design to work. It is quite clear that the filter performance can be suboptimized over a specific range within certain limits for attenuation and resonance frequencies. This kind of a filter design serves the case where the system is designed as a modular one and the power is increased only by connecting more units in parallel.

With the averaged capacitor, the designer must accept some decrease in the attenuation for switching frequency harmonics. However, this does not hold for all of the configurations. As the *LLCL* configuration maintained the resonance frequencies closer to each other or the desired frequency compared with the other configurations because of the  $f_{r3}$  frequency, this third resonance is advantageous also in retaining the attenuation at the switching frequency when the capacitor is decreased. The third frequency is designed at the switching frequency. Ideally, it yields infinite attenuation, but in real systems the resistances cut the resonance sag to some degree.

Table 3.5 presents the difference in the switching frequency attenuation and the nominal case energy related to the average capacitor case energy for each configuration. The average capacitor was computed from the values for keeping  $f_{r2}$  constant. This was done, because the values for  $f_{r1}$  being kept constant would result in a small capacitor and high resonance frequencies for the design, which again would be destructive when considering the attenuation. The inverter-side inductor is the value for 15 % ripple and the grid-side inductor is the nominal. The difference in attenuation was calculated by subtracting the average case value from the nominal case value. Some resistances were also added to the filter equations to obtain results closer to reality; 0.0021 pu (1 mΩ) were included in the inductors  $L_1$  and  $L_2$  and 0.0048 pu (2.3 mΩ) in the capacitor. The additional capacitor branch inductor of *LLCL* configuration was assumed also to have 0.0021 pu (1 mΩ) resistance as well as the grid branch.

Table 3.5. Difference between the nominal capacitor design and the average capacitor design in the stiff grid.

	LCL		LLCL		LC		LC+L		L	
<i>n</i>	A <sub>diff</sub> [dB]	E <sub>diff</sub>								
2	-6.26	0.94	-1.70	0.94	-12.56	0.88	-8.52	0.93	6.30	1.08
3	-5.48	0.94	-1.25	0.94	-11.19	0.88	-8.12	0.94	7.02	1.05
4	-5.05	0.94	-0.99	0.94	-10.48	0.88	-7.94	0.94	7.87	1.04
5	-4.79	0.94	-0.82	0.94	-10.05	0.88	-7.83	0.95	8.91	1.03
6	-4.60	0.94	-0.70	0.94	-9.76	0.88	-7.76	0.95	10.22	1.02

It can be seen that for the *LCL* and *LC+L* configurations, the attenuation is up to 6.26 dB less for *LCL* and 8.52 dB less for *LC+L* while the energy is at least 94 % of the nominal value case for *LCL* and 88 % for the *LC+L* configuration. The energy relation for the *LLCL* configuration is at a similar level to the *LCL* configuration but the attenuation is virtually not affected because of the resonance sag placed on top of the switching frequency. Although the 1.7 dB difference on the absolute scale is approx. a 18 % difference, it should be kept in mind that in the resonance sag attenuation is ideally infinite and at least 60 dB.

For the *LC* configuration, the average capacitor design may be very disadvantageous if the resonance frequency is already high because the attenuation decreases very much in this case. However, at the same time, the smaller capacitor results in a much smaller energy than the nominal design. The *L*-configuration suffers most from the averaging when considering the energy stored in the filter components. This is because the capacitor has to be increased in order to keep the frequencies constant. However, as the capacitor is increased, the attenuation also increases. With a fairly low increase in the filter component energy (i.e. sizes), the attenuation is accomplished much better. Given that there is only one capacitor, the energy of which is increased, this option seems quite a reasonable bargain to achieve proper attenuation and fairly small components.

Figure 3.28 presents the filter resonance frequencies of average cases for a single inverter in the *LCL* configuration as a percentage of the original nominal design frequencies. It can be seen that the each of the three cases of the average designs experience less shift in resonances compared with the nominal cases. Each of the resonance frequencies is normalized to the original nominal resonance frequency. It can be seen that for instance in the case where the designer allows resonance frequencies at  $\pm 20\%$  of the nominal resonance frequencies,  $L_2 = 0.5L_{2,\text{nom}}$  and  $L_2 = L_{2,\text{nom}}$  are valid with  $n = 2-4$ . For the  $0.5L_{2,\text{nom}}$  case, the lower resonance frequency starts at 109.5 % with  $n = 2$  and decreases to 81.9 % when  $n = 4$ . Similarly, the higher resonance frequency starts at 113.6 % and decreases only to 97.5 %.

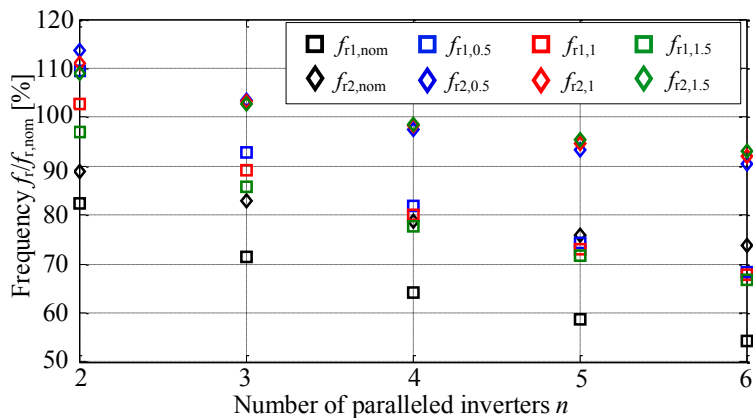


Figure 3.28 *LCL* configuration resonance frequencies change over  $n = 2\text{--}6$  with average capacitor and nominal  $L_{1,(15\%)}$  in the stiff grid.

If the average capacitor is designed to keep  $f_{r1}$  constant, the inverter-side inductor value has no effect on the capacitance with any of the configurations. However, increasing the grid-side inductor leads to a smaller capacitance required to keep  $f_{r1}$  at the design value. With  $f_{r2}$ , the inverter-side inductor has an effect on the capacitance. The larger  $L_1$  is, the smaller capacitance is needed. Increasing the  $L_2$  value leads also to a decreased capacitance required to keep  $f_{r2}$  at the design value.

Considering the differences between the configurations, the *LC* and *LC+L* configurations require the smallest capacitances while the *L*-configuration requires the largest, being the only one that requires a larger capacitance than the nominal value.

With the weak grid case, where the capacitor already is fairly small, the attenuation and filter component energy decreases less compared with the stiff grid case. For the *L*-configuration, the attenuation increases more, but as  $n$  is increased, the higher resonance frequency is increased to the switching frequency and above causing potential problems in the control system design, and in the worst case, destructive gain for the switching frequency harmonics. Further, the energy of the *L*-configuration increases slightly more as  $n$  increases compared with the stiff grid case.

### Key findings summarized

- It seems feasible to design the filter to work over a particular range of numbers of paralleled inverters, and the *LLCL* configuration is most suitable for this kind of a design.
- The *LLCL* configuration suffers least from the decreased attenuation at the switching frequency, excluding the *L*-configuration.
- The *LC* configuration suffers most of the decreased attenuation while the *LC+L* configuration benefits from the common grid-side inductor in this respect.
- The *LC* configuration energy decreases most with the average capacitor design.

- The *L*-configuration attenuation increases with the average capacitor design, but this results in an increased energy compared with the nominal design.

The average designs are commented in Chapter 4 to give more insight into how much the decreased attenuation actually affects the filter performance. When the attenuation of the switching frequency harmonics decreases, the switching frequency disturbances from other inverters and the grid voltage harmonics can cause degradation of the control performance and power quality.

### 3.5 Open-end v. two paralleled inverters

As two paralleled inverters is perhaps the most common case of parallel connection used in the industry, it is interesting to compare it with the open-end system. Of course, it should be kept in mind that although the open-end system can be implemented with inverters identical to the common two parallel-inverter system, the load and its dimensioning differ between topologies; the power would be equal but the current and voltage not. As it was presented in Figure 3.5 in section 3.2.4, the open-end inverter is able to produce three-level voltage, which has an inherently better harmonic content compared with two-level voltage. This allows smaller inverter-side inductors. However, it should be remembered that this applies only to certain applications. For instance, in motor applications, no low-pass filter is commonly used. While the motor inductances are small, the zero-sequence minimizing modulation method (Korhonen et al., 2017) must be used to avoid destructive conditions.

Figure 3.29 presents a single-phase schematic for an open-end inverter system with an *LCL* filter. Both of the  $L_1$  inductors have to be dimensioned to limit the ripple as a conventional two-level inverter case according to

$$L_{1,\text{OE}} = \frac{U_{\text{DC}}}{12\Delta i_1 f_{\text{sw}}}, \quad (3.67)$$

which comes from the fact that both ends are driven by half-bridge inverters. As a whole, they constitute an H-bridge inverter. An H-bridge can be operated as a voltage doubler. Instead of producing a bipolar PWM waveform, the H-bridge can produce a unipolar waveform, whose pulses take values between  $[0, U_{\text{DC}}]$ , and  $[0, -U_{\text{DC}}]$ , where  $U_{\text{DC}}$  is the total DC link voltage (Wu, 2006). This allows the open-end system to operate, ideally, with half of the DC link voltage of the conventional parallel-connected two-level system, leading to

$$L_{1,\text{OE}} = \frac{U_{\text{DC,OE}}}{12\Delta i_1 f_{\text{sw}}} = \frac{\frac{U_{\text{DC}}}{2}}{12\Delta i_1 f_{\text{sw}}} = \frac{U_{\text{DC}}}{24\Delta i_1 f_{\text{sw}}}, \quad (3.68)$$

which is the three-level equation (2.39). If three-level modulation is used for the open-end inverter, a circulating current of a higher frequency driven by the common-mode voltage, often called as zero-sequence voltage, of the inverter is introduced to the system.

When this circulating common-mode current is added to (3.68), the inductor must be dimensioned larger than (3.68) advices. Sometimes, this common-mode current and voltage are referred to as zero-sequence current and voltage.

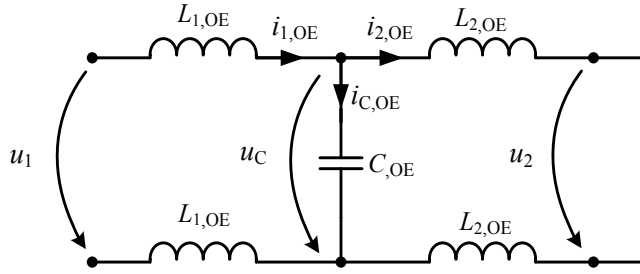


Figure 3.29 Single-phase equivalent circuit for an open-end system with an *LCL* filter.

The common-mode voltage of the open-end inverter is determined as

$$U_{CM,OE} = \frac{1}{6}(U_{A+} + U_{B+} + U_{C+} + U_{A-} + U_{B-} + U_{C-}), \quad (3.69)$$

where the  $U_{A,B,C+}$  are the voltages of the positive node of each phase and  $U_{A,B,C-}$  are the voltages of the negative nodes of each phase (Srinivasan et al., 2010). If no common-mode elimination modulation is used, the current circulating in the open-end system has to be assessed by

$$I_{circ} = \frac{U_{CM,OE}}{Z_{CM,OE}}, \quad (3.70)$$

where  $Z_{CM,OE}$  is the impedance on the path of the circulating current. Practically, the impedance can be assumed to be  $Z_{CM,OE} = Z_{L1} + Z_{Cf} + Z_{L1}$  because the impedance of the grid-side inductors and the transformer is  $Z_{L2+Lg} \gg Z_{Cf}$ , meaning that the grid branch can be neglected in the calculation. The current has to be assessed in the design process to decide whether  $L_1$  has to be overdimensioned to limit this current as well as to take into account the maximum current in the inductor design.

As mentioned above, the relation of the inductors of the both systems is highly dependent on the application, which is analysed next with the following assumptions:

- Both the open-end (OE) inverter and two-paralleled inverters (2Par) supply equal power to the same grid.
  - The open-end system has half the DC link voltage of the 2Par system.
- Both the OE and 2Par supply the same power to grids with different voltages, for instance through dedicated transformers and voltages.

- The open-end has the same DC link voltage as the 2Par system.

In Case 1, both systems are connected to the same grid. Let the DC link voltage of the 2Par system be  $U_{DC,2Par} = U_{DC}$  and the open-end system  $U_{DC,OE} = U_{DC}/2$ . Both the systems also supply the same power to the grid. For the 2Par system, the current per inverter is  $i_{1,2Par} = i_1$ , which on the other side of the filter makes a total of  $i_{g,2Par} = (i_{21,2Par} + i_{22,2Par})$ , where  $i_{21,2Par}$  and  $i_{22,2Par}$  are the grid-side inductor currents for the 2Par system inverters. Because the open-end system comprises only one drive, it must supply the current of  $i_{1,OE} = 2i_{1,2Par} = 2i_1$  to be at the same power level as 2Par. The switching frequency for both systems is considered to be  $f_{sw}$ . Now, the required minimum values for the inverter-side inductors can be calculated as

$$L_{1,2Par} = \frac{U_{DC}}{12\Delta i_1 f_{sw}} \quad (3.71)$$

for the 2Par system and

$$L_{1,OE} = \frac{U_{DC,OE}}{12\Delta i_1 f_{sw}} = \frac{\frac{U_{DC}}{2}}{12(2\Delta i_1) f_{sw}} = \frac{U_{DC}}{48\Delta i_1 f_{sw}} \quad (3.72)$$

for the open-end system.

Now, the relation  $L_{1,2Par}/L_{1,OE}$  is

$$\frac{L_{1,2Par}}{L_{1,OE}} = \frac{\frac{U_{DC}}{12\Delta i_1 f_{sw}}}{\frac{U_{DC}}{48\Delta i_1 f_{sw}}} = 4. \quad (3.73)$$

The result of (3.73) means that the open-end system inverter-side inductors can, in the best case, be dimensioned as one-fourth of the size of the conventional 2Par system inductances. However, this applies only when the DC links are isolated, and now circulating current flows through the inductors. The total inductance in the inverter-side circuit, however, is half of the 2Par system because the inverters drive the phase from both ends (Figure 3.29). This halved inductance corresponds directly to a three-level voltage inductance.

In Case 2, the output voltage of the system is larger than that of the 2Par system realized for instance by a dedicated transformer for case 2 open-end. Now, the DC link voltage of the OE is the same as for the 2Par system, making  $U_{DC,OE} = U_{DC,2Par} = U_{DC}$ . This allows the open-end system to have an output phase-to-phase voltage of  $u_{1,OE} = 2U_{DC}/\sqrt{2} = \sqrt{2}U_{DC} = 2u_{1,2Par}$ . Because the open-end inverter is a one-inverter system, to drive the equal power to the grid, the open-end system still has to supply the same current as the 2Par system, that is,  $i_{1,OE} = i_{1,2Par} = i_1$ . Now, the inductance for the open-end system is

$$L_{1,OE} = \frac{U_{DC}}{12(\Delta i_1) f_{sw}}, \quad (3.74)$$

which is the same as the 2Par system inverter-side inductance. If the open-end system was compared with one inverter with the same power, the increased voltage would lead to smaller current and thus, a smaller inverter-side inductor value of

$$\frac{L_1}{L_{1,\text{OE}}} = \frac{\frac{U_{\text{DC}}}{12\Delta i_1 f_{\text{sw}}}}{\frac{U_{\text{DC}}}{12(\Delta i_1/2) f_{\text{sw}}}} = \frac{1}{2}. \quad (3.75)$$

The circulating common-mode current in the Case 2 system can easily be larger than in the Case 1 system because of the larger common-mode voltage, even though the inductors of the Case 2 system are larger.

### 3.5.1 Attenuation and components

Figure 3.30 presents the forward self- and trans-admittance function Bode magnitude plots for both the open-end and 2Par systems (a) and (b), respectively. The plots are made using the same component values for both systems. Because the open-end system has two inverter-side inductors and two grid-side inductors, the attenuation with the same capacitor value is greater than with the 2Par system. However, this is dependent on the grid (transformer inductance), which for the 2Par system is multiplied by 2. If  $(L_1 + L_2) < L_g$ , the attenuation for the 2Par system is greater with the same components. However, if the grid inductance is larger than the filter inductances, namely the inverter-side inductance, low-order harmonics can be introduced to the output and stability issues may occur (Sun, 2011).

The lower resonance frequency

$$f_{r1,\text{OE}} = \frac{1}{2\pi} \frac{1}{\sqrt{C_f(2L_2 + L_g)}} \quad (3.76)$$

is approximately the same for both systems in Figure 3.30(a). This is due to the fact that with these values, the grid-side and grid inductances are close to each other.

For the open-end system,  $L_2$  is doubled in (3.76), while for the 2Par system  $L_g$  is doubled. Similarly for the higher resonance frequency

$$f_{r2,\text{OE}} = \frac{1}{2\pi} \sqrt{\frac{2L_1 + 2L_2 + L_g}{2C_f L_1 (2L_2 + L_g)}}, \quad (3.77)$$

$L_1$  is also doubled along with  $L_2$  in (3.77). Because of the double number of inductive components,  $f_{r2,\text{OE}} < f_{r2,\text{2Par}}$  with the same component values.

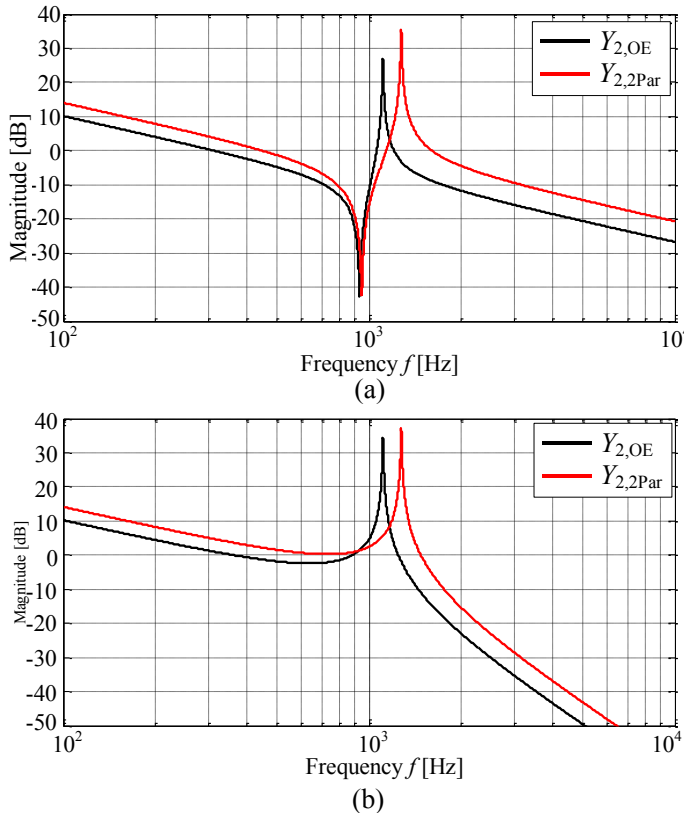


Figure 3.30 (a) Forward self-admittance function Bode plots for both systems and (b) forward trans-admittance function Bode plots when  $L_1 = L_{1,(15\%)}$  and the component values are the same for both systems.

With  $L_{1,OE}$  dimensioned as one-fourth of  $L_{1,2Par}$  as in Case 1 above, the situation turns around. This, together with the fact that to make the grid-side inductance match between the designs, it is required that  $L_{2,OE} = 0.5L_{2,2Par}$ , which also decreases the attenuation and shifts the resonances higher as can be seen from Figure 3.31(a) and Figure 3.31(b).

To compensate for this shift towards higher frequencies, the capacitor must be increased. The required capacitor increase is simple to compute from the resonance frequencies of both systems. To make  $f_{r1}$  equal, is required that

$$x_1 = \frac{L_{2,2Par} + 2L_g}{2L_{2,OE} + L_g} \quad (3.78)$$

and to make  $f_{r2}$  equal, the open-end system capacitor has to be set as

$$x_2 = \frac{2L_{1,2\text{Par}}(L_{2,2\text{Par}} + 2L_g)(2L_{1,\text{OE}} + 2L_{2,\text{OE}} + L_g)}{2L_{1,\text{OE}}(2L_{2,\text{OE}} + L_g)(L_{1,2\text{Par}} + L_{2,2\text{Par}} + 2L_g)}. \quad (3.79)$$

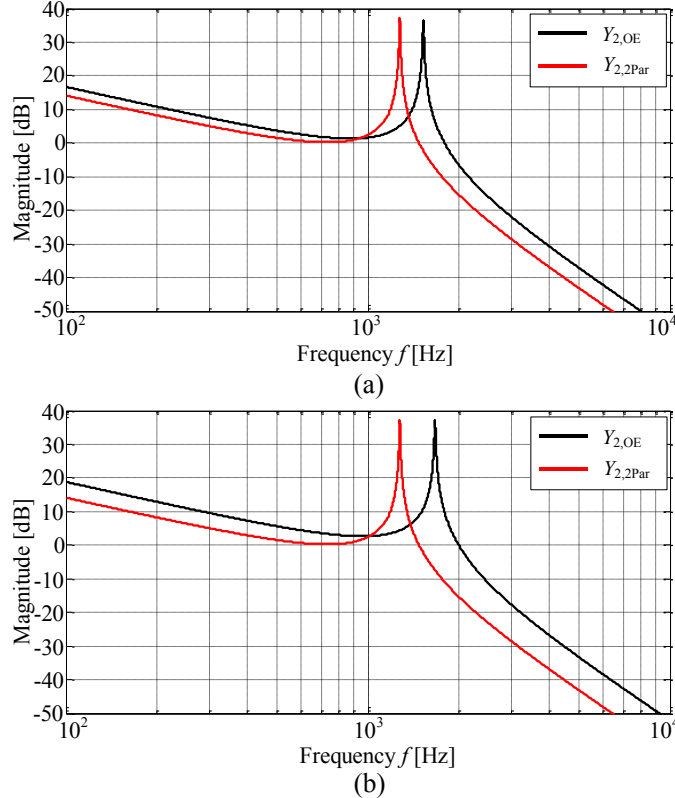


Figure 3.31 (a) Forward trans-admittance function Bode plots with  $L_{1,\text{OE}} = L_{1,2\text{Par}} / 4$  and (b) with  $L_{1,\text{OE}} = L_{1,2\text{Par}} / 4$  and  $L_{2,\text{OE}} = L_{2,2\text{Par}} / 2$ .

For the same inductances in both systems, the open-end system capacitor has to be  $C_{\text{OE}} = 0.9688C_{2\text{Par}}$  for  $f_{r1}$  to be equal and  $C_{\text{OE}} = 0.7584C_{2\text{Par}}$  for  $f_{r2}$ . When  $L_{1,\text{OE}} = L_{1,2\text{Par}}/4$  and  $L_{2,\text{OE}} = L_{2,2\text{Par}}/2$ , the capacitors are  $C_{\text{OE}} = 1.4762C_{2\text{Par}}$  and  $C_{\text{OE}} = 1.7114C_{2\text{Par}}$  for equal  $f_{r1}$  and  $f_{r2}$  cases, respectively. With  $L_{1,\text{OE}} = L_{1,2\text{Par}}$  and  $L_{2,\text{OE}} = L_{2,2\text{Par}}/2$ , as in Case 2,  $C_{\text{OE}} = 1.4762C_{2\text{Par}}$  and  $C_{\text{OE}} = 1.038C_{2\text{Par}}$  are required to make  $f_{r1}$  and  $f_{r2}$  match between the systems, respectively. If  $L_{2,\text{OE}}$  were removed from the circuit to make the  $LC$  filter for the open-end system, the capacitors would have to be  $C_{\text{OE}} = 3.0998C_{2\text{Par}}$  and  $C_{\text{OE}} = 1.9327C_{2\text{Par}}$  when  $L_1$  in both designs is equal. With  $L_{1,\text{OE}} = L_{1,2\text{Par}}/4$ , the  $f_{r1}$  equalizing capacitance remains the same, but  $f_{r2}$  requires a somewhat larger capacitance  $C_{\text{OE}} = 2.6061C_{2\text{Par}}$ . Removing the grid-side inductors from the  $LCL$  filters results in a situation where both resonance frequencies become the same with  $C_{\text{OE}} = 2C_{2\text{Par}}$ .

Figure 3.32 presents the open-end and 2Par system Bode plots for forward self-admittance functions (a) and forward trans-admittance functions (b) when the inverter-side inductors of the open-end system are designed according to Case 2. The higher

resonance frequency is almost the same, and the lower and higher resonance frequencies are closer to each other in the open-end system. For both transfer functions, the attenuation is better for the open-end system with these values.

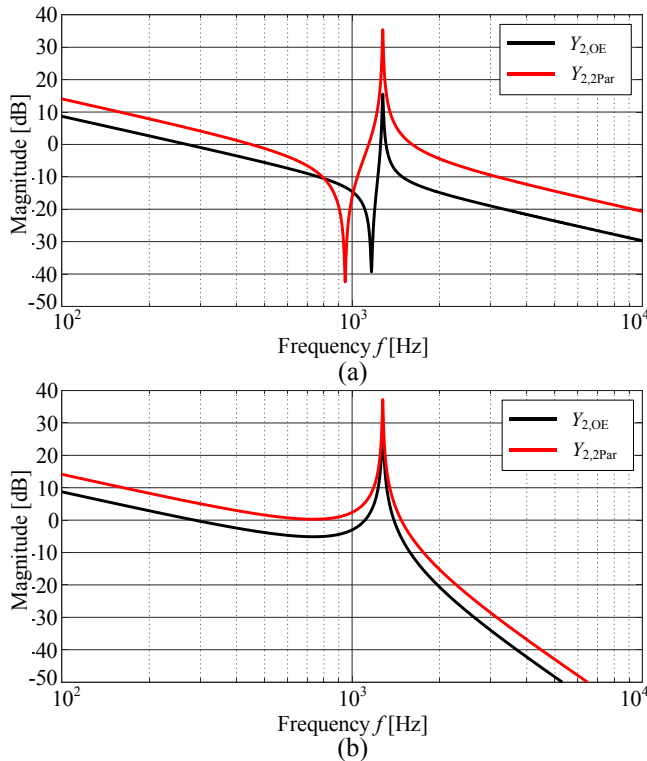


Figure 3.32 (a) Forward self-admittance functions and (b) forward trans-admittance for both systems with  $L_{1,OE} = L_{1,2Par}$ ,  $L_{2,OE} = L_{2,2Par}/2$ , and  $C_{f,OE} = C_{f,2Par}$

### Component energies Case 1

The open-end inverter schematics can be presented as an equivalent inverter, which has twofold  $L_1$  and  $L_2$  and the filter capacitor of the open-end system. The component energies of the equivalent inverter model can be analysed by the same equations as the normal *LCL* filter inverter. The inverter voltage  $u_1$  is three-level voltage in this open-end system. However, the fundamental is ideally the same regardless of whether the voltage is two- or three-level.

With equal component values for both the open-end and 2Par system and both systems driving the same power to the grid, the total grid-side inductor energy of the open-end system, related to the same component of the 2Par system is

$$\frac{E_{L2,OE}}{E_{L2,2Par}} = 4, \quad (3.80)$$

which holds for all three power factors;  $PF = 1$ ,  $PF = 0.9_{\text{cap}}$ , and  $PF = 0.9_{\text{ind}}$ .

Because the inverter-side current is not equal to the grid-side current in neither of the systems, the relation of the inverter-side inductors is not the same as in (3.80). Instead, it varies around the same value as follows:

$$\left. \frac{E_{L1,\text{OE}}}{E_{L1,2\text{Par}}} \right|_{PF=1} = 3.9966, \quad (3.81)$$

$$\left. \frac{E_{L1,\text{OE}}}{E_{L1,2\text{Par}}} \right|_{PF=0.9\text{cap}} = 3.9456, \quad (3.82)$$

and

$$\left. \frac{E_{L1,\text{OE}}}{E_{L1,2\text{Par}}} \right|_{PF=0.9\text{ind}} = 4.0503. \quad (3.83)$$

The results of (3.81)–(3.83) differ from the value 4 by less than 1.5 %. Considering the capacitors, the relations are 1.0280, 0.9374, and 1.1051 for  $PF = 1$ ,  $PF = 0.9_{\text{cap}}$ , and  $PF = 0.9_{\text{ind}}$ , respectively. It can be seen that the variation in the capacitor energy is greater than with the inverter-side inductor.

When the inductors are designed as  $L_{1,\text{OE}} = L_{1,2\text{Par}}/4$  and  $L_{2,\text{OE}} = L_{2,2\text{Par}}/2$ , the relation of the energy stored in the inverter-side inductors becomes 1.0011, 0.9883, and 1.0146 for  $PF = 1$ ,  $PF = 0.9_{\text{cap}}$ , and  $PF = 0.9_{\text{ind}}$ . The capacitor energies of the open-end topology are also reduced. The relations for the capacitors are now 1.0072, 0.9768, and 1.0330. In this case, the capacitor energy in the open-end system differs from the 2Par system by only 3.3 %. It should be noted that this applies to one capacitor. The 2Par system has two filter capacitors, and thus,  $E_{C,\text{OE}}/E_{C,2\text{Par}} < 2$  indicates that the open-end system stores less energy in the filter capacitors in total. For the capacitive power factor, the total energy stored in the filter components is smaller for the open-end system. However, from the filter design perspective, the design should be made considering the maximum energy, which is larger for the open-end system.

When the capacitors are adjusted according to (3.80)–(3.81) to match the resonances, the relation of  $L_1$  energies remains around 1 with less than 0.5 % deviation. The capacitor energies are changed as a result of the changed capacitor values. When individual component energies are compared, the open-end system capacitor energies are increased in the same relation that the capacitor is increased. However, when  $E_{C,\text{OE}}$  is related to the energy of both the 2Par system capacitors, the results are again in favour of the open-end system considering the total energy stored in the capacitive components.

### Component energies Case 2

In this scenario, the grid voltage of the open-end system is two times as large as for the 2Par system. For equal power, the current of the open-end system is the same as that of

the 2Par system. Because the current remains the same the grid-side inductors of the open-end system store the same energy compared with the grid-side inductors of the 2Par system when the inductors are of the same inductance. The same applies for the inverter-side inductors as well; the same values with the same current lead to the same energy. However, with the capacitor, the two times higher voltage leads to four times the energy causing that  $E_{C,OE} \approx 4E_{C,2Par}$ .

As the inverter-side inductors have to be designed as  $L_{1,OE} = L_{1,2Par}$  and there are two of them, the energy of the inverter-side inductors of the open-end system is that of the inverter-side inductors of the 2Par system. However, since the filter circuits are not completely identical, some very small deviation can be expected in the relation of the energies. The capacitor value adjusted according to (3.78)–(3.79) has virtually no effect on the inverter-side inductor energies in the open-end system. Making  $f_{r1}$  equal causes a slightly larger deviation in the energies of different power factors. Considering the capacitor energy relation, making equal  $f_{r1}$  increases the relation to around 5.9 while equalizing  $f_{r2}$  has only marginal effect.

### 3.5.2 Practical limitations of the open-end system

Although in an ideal case the open-end system can operate with the same DC link voltage as the 2Par system, there can be limitations in practice. The emphasis is on the word *can* as it has not been proven that overcoming these limitations is impossible. Nevertheless, the question of how the limitations presented in this section are solved is out of the scope of this dissertation, yet they should be acknowledged here.

Figure 3.33 depicts the open-end system schematic for a single phase. Because the phases of the open-end system are not connected in a star or delta at the transformer, there is no cancellation of the zero-sequence or common-mode component that is induced to the output voltage of the inverter. To achieve doubled apparent switching frequency, the open-end inverter has to be modulated with carriers that are in the opposite phase. This phase shift leads to high-frequency circulating current driven by the common-mode voltage. To mitigate this current and the extra losses caused by it, common-mode filters may have to be used. However, there are still two filter inductors on the path of this current, which attenuate the current. If the modulation method is adjusted by synchronizing the carriers, this common-mode current component is minimized, but at the same time, the doubled apparent switching frequency is lost. A lower switching frequency leads to larger inductances, which practically ruins the point of this three-level voltage inverter. Thus, the only advantage that the grid-connected open-end inverters still have is the ability to produce double voltage.

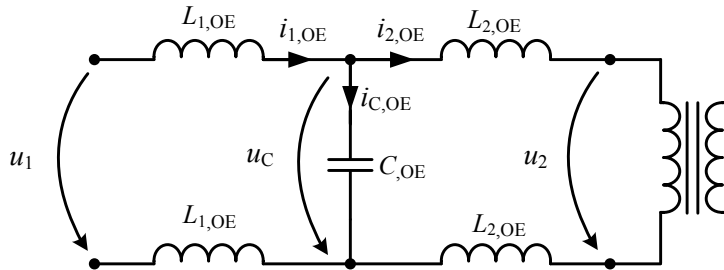


Figure 3.33 Single-phase circuit for an open-end inverter system.

Although the capacitor provides a low-impedance current path for high-frequency components, the low-frequency common-mode components can flow through the transformer. For modulation schemes that employ a low-frequency zero-sequence component such as third-harmonic injection or space-vector modulation, there is no cancellation of this added zero-sequence component at the transformer, which can lead to severe distortion of the output current. This problem is encountered also in motor drives, where modulation methods are adapted to decrease the zero-sequence component by clamping modulation (Kiadehi et al., 2016) or by adding a closed-loop controller to control the zero-sequence to zero (An et al., 2016).

For both a motor and a grid transformer, the third harmonic as a zero-sequence component can cause saturation and severe distortion of the current while producing excess stress on the transformer or motor insulation. In addition, extra frequencies result in increased losses. Saturation in transformers cause a drop in the magnetizing inductance, which then allows large currents. A known property of transformer saturation is that an odd number harmonics emerge into the current, especially third harmonic (Aura, 1986), which cause distortion in the current. If a three-phase transformer is used to produce an open-end transformer, the minor asymmetries in the windings can cause overvoltages in some windings. This then easily saturates the transformer leading to increased harmonics, especially the 3<sup>rd</sup> and 5<sup>th</sup> ones, in the current (Liu and Zhenyan, 1998), (Daut et al., 2010). Further, cross coupling through leakage flux results in a decreased magnetizing inductance known from transformer design (Dick and Watson, 1981).

A special transformer design in which the zero-sequence component could be trapped into a tertiary winding would be beneficial to tackle this problem. The use of single-phase transformers per phase could also decrease the magnetic coupling between the phases and help in maintaining the magnetizing impedances per each phase. This single-phase transformer issue and the saturation problem are further addressed in the next chapter with simulations.

### 3.6 Distinct filter components

In this dissertation, the filter designs are studied mainly with identical components for filters of paralleled inverters. Although a thorough analysis with different components is

not provided in this dissertation, the problems caused by different components are presented here.

First, the potential effects of the mismatch of components should be assessed. Figure 3.34 presents a simplified schematic for two paralleled inverters and the respective phasor diagrams. The inverters are represented as voltage sources  $u_{11}$  and  $u_{12}$ , their filters as impedances  $Z_1$  and  $Z_2$ , and the grid connection point voltage as  $u_2$

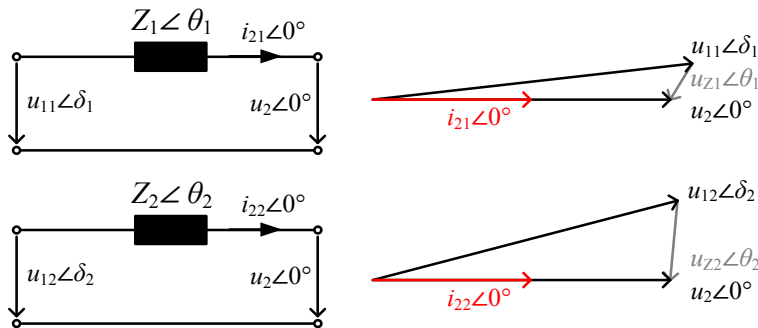


Figure 3.34 Simplified presentation of two parallel-connected inverters both connected to the same point having voltage  $u_2 \angle 0^\circ$  and their respective phasor diagrams.

Let us assume that the inverters drive the same current to the grid. When the impedances are equal, both inverters have to produce the same voltage  $u_1$  to drive the current  $i_2$  in the same phase to the grid. At the power frequency, for instance 50 Hz, the impedance of the filter capacitor is very large, meaning that no significant current flows through it and the capacitor tolerances have virtually no effect on the inverter voltage when the capacitor is designed according to the basic guidelines. Furthermore, the larger the inductances are in relation to the capacitor, the less effect the capacitor tolerances present. The capacitor, however, has a direct impact on the resonance frequencies because it is located in each resonance circuit.

The inductors, however, have a much larger impact on the voltages. Figure 3.35 presents the voltage phasors for the grid-side voltage  $u_2$  and the inverter-side voltages for two inverters  $u_{11}$  and  $u_{12}$  when inverter 2 has inverter-side inductances of 80 % of the inverter 1 value in Figure 3.35(a) and 120 % in Figure 3.35(b). It can be seen that the inverter having a larger inductance produces voltage that is leading the other. Naturally, this holds also for a greater number of paralleled inverters than two.

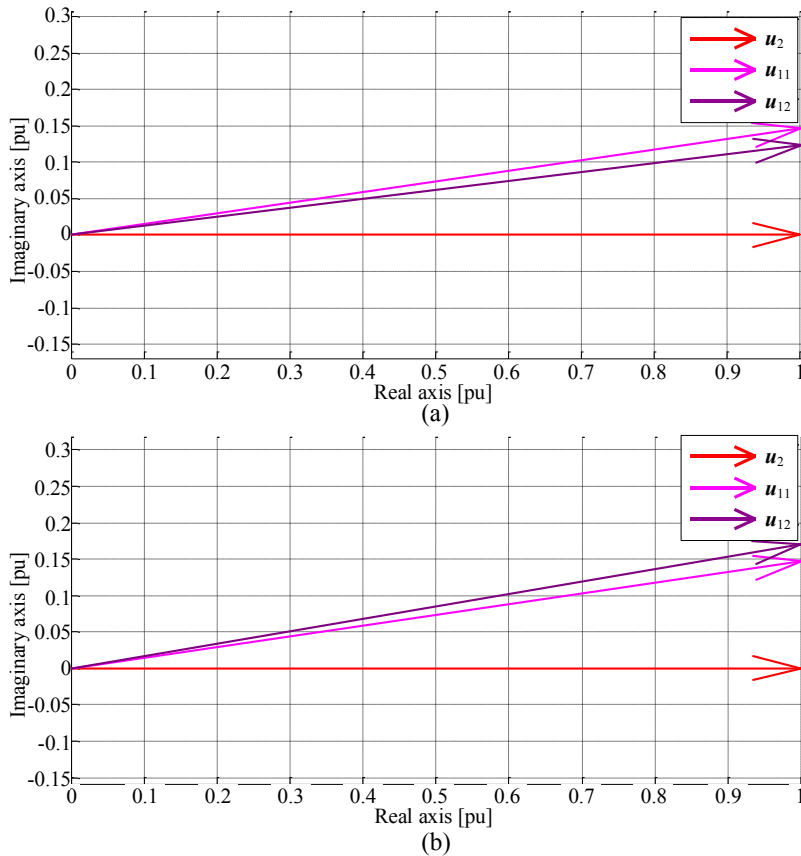


Figure 3.35 Phasors for the inverter-side voltages  $u_{11}$  and  $u_{12}$  and the grid voltage  $u_2$  with  $L_{12} = 0.8L_{11}$  (a) and  $L_{12} = 1.2L_{11}$  (b).

### 3.6.1 Circulating current

Considering a situation that the grid-side current is controlled to the same value while there is a significant difference in the filter components, mainly inductances, the outcome is that the inverters produce a different voltage but no real problems occur. In case the inverters drive a different power to the grid, a circulating current will occur, because the voltage at the inverter terminals is now different. This is seldom the design point for the filters nor is it welcomed because of the additional losses in the power stage. The differential circulating current at the fundamental frequency is controlled to zero while all paralleled inverters drive the same power to the grid. However, there is still a zero-sequence circulating current at the switching frequency.

For instance, zero-sequence circulating currents can occur unwantedly while there is a route for them between individual inverters that are connected to the same transformer. In motor drives, usually directly paralleled inverters are used to increase the power rating

of the drive while the ground capacitances of the PV arrays close the loop for the circulating current (Itkonen, 2010) and (Purhonen, 2014). Figure 3.36 presents the circulating current paths for two directly paralleled inverters. The current flows through the DC link capacitors when the upper and lower switches of the same phase in the opposite inverter are switched on at the same time. The current direction depends on which inverter has the upper switch conducting and which the lower one. Similarly, the zero-sequence current circulates in the open-end system, in which it has to be taken into account especially when dimensioning the inverter-side inductors. The route for the zero-sequence current in the open-end system is mainly through the inverter-side inductors and the filter capacitor while the circulating current is of high frequency for sinusoidal PWM and may contain lower harmonics, 150Hz and its multiples, with space vector modulation. The transformer and the possible  $L_2$  inductor combined impedance  $Z_{L2+Lg} \gg Z_{Cf}$ .

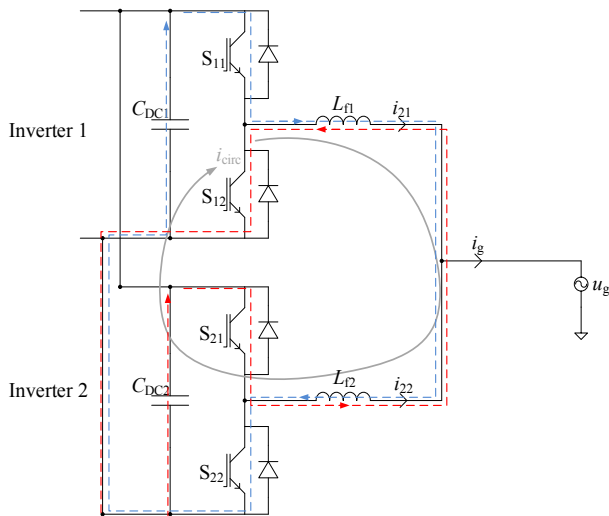


Figure 3.36 Single-phase circuits representing two paralleled inverters connected to the grid through the line filters  $L_{f1}$  and  $L_{f2}$ . The circulating current  $i_{circ}$  route is closed by the common DC link connections and the individual DC capacitors. The blue dashed line indicates the current flowing through  $C_{DC1}$  when  $S_{11}$  and  $S_{22}$  conduct at the same time. The red dashed line represents the opposite current flowing through  $C_{DC2}$  when  $S_{21}$  and  $S_{12}$  conduct at the same time.

The PWM-modulated two-level inverters always produce common-mode voltage, which drives this high-frequency circulating current. On the AC side, the common-mode voltage of two paralleled inverters can be approximated as the arithmetic mean of the generated common-mode voltages. The presentation for the common-mode voltage of  $n$  paralleled identical inverters and further studies of circulating current in paralleled PV inverters can be found in (Purhonen, 2014).

In some cases, allowing circulating current can lead to an opportunity to decrease the sizes of the passive filter components. Asiminoaei et al. (2006) present an interleaved active power filter with reduced-size components. Zhang et al. (2010) have studied

interleaved carriers in paralleled inverters. By interleaving, the switching frequency ripple in the inverter-side current is decreased when *L*-filters are used. However, interleaving creates circulating current between the inverters. The minimization of grid current distortion by carrier interleaving was studied in (Siva Prasad and Narayanan, 2013).

Interleaving would work for the *L*-configuration, but for the other filters the filter capacitors would remove the benefit. However, as the power is high, the resulting circulating current reduces the efficiency of the system as more conductive and switching losses in the inverters are introduced. For this reason, it may not be very advantageous for high-power devices. Normally, of course, the circulating current is controlled to zero because it is not an advantage. The control and reduction of circulating currents in parallel inverters is studied for instance in (Cacciato et al., 1999), (Purhonen, 2014), (Zhang et al., 2017).

### 3.6.2 Resonances

A complete study of the effects of the tolerances would be a huge task, and would probably be a topic worth a dissertation of its own. The purpose of the study in this section is to assess the effect of tolerances and to give an insight into what kind of an effect they exert on the resonances, and tolerances should be assessed as a design criterion of the filters. The resonances of the filter configurations of this dissertation are studied by performing a sensitivity analysis with partial derivatives. For simplicity, it is assumed that the individual components are identical as it is done in filter design. Filters with non-identical components are also studied in brief. The tolerances of individual components are considered as  $\pm 20\%$  of the expected value, which is quite a common approach in the component tolerance analysis. An extensive study of the tolerances is not included in this dissertation.

Figure 3.37 presents the partial derivatives computed for the resonance frequencies  $f_{r1}$  and  $f_{r2}$  for the *LCL*, *LLCL*, *LC*, *LC+L*, and *L*-configurations with the nominal filter design in a stiff grid, and Figure 3.38 in the weak grid. The figures show that all configurations experience a negative change in resonances when the filter components increase. Also all configurations except for the *L*-configuration suffer similar transition when  $n$  is increased while  $f_{r2}$  of the *L*-configuration faces inversed transition, as shown already in section 3.3.1. From the figures, the following observations can be made.

Filter capacitor generally is the most sensitive component for both the resonance frequencies  $f_{r1}$  and  $f_{r2}$ . In the weak grid case, this sensitivity is further increased, which is mainly due to the decreasing of the capacitor. A similar increase in sensitivity for the stiff grid case can be seen by halving the capacitance to match the capacitor of the weak grid case. The sensitivity to the grid inductance variations can be as large as for the capacitor, when the grid-side inductor is small enough. This can be seen by comparing the top and middle graphs of Figure 3.37. In fact, computing the derivatives with decreasing any of the filter parameters, the sensitivity of the resonances to the other parameters increases.

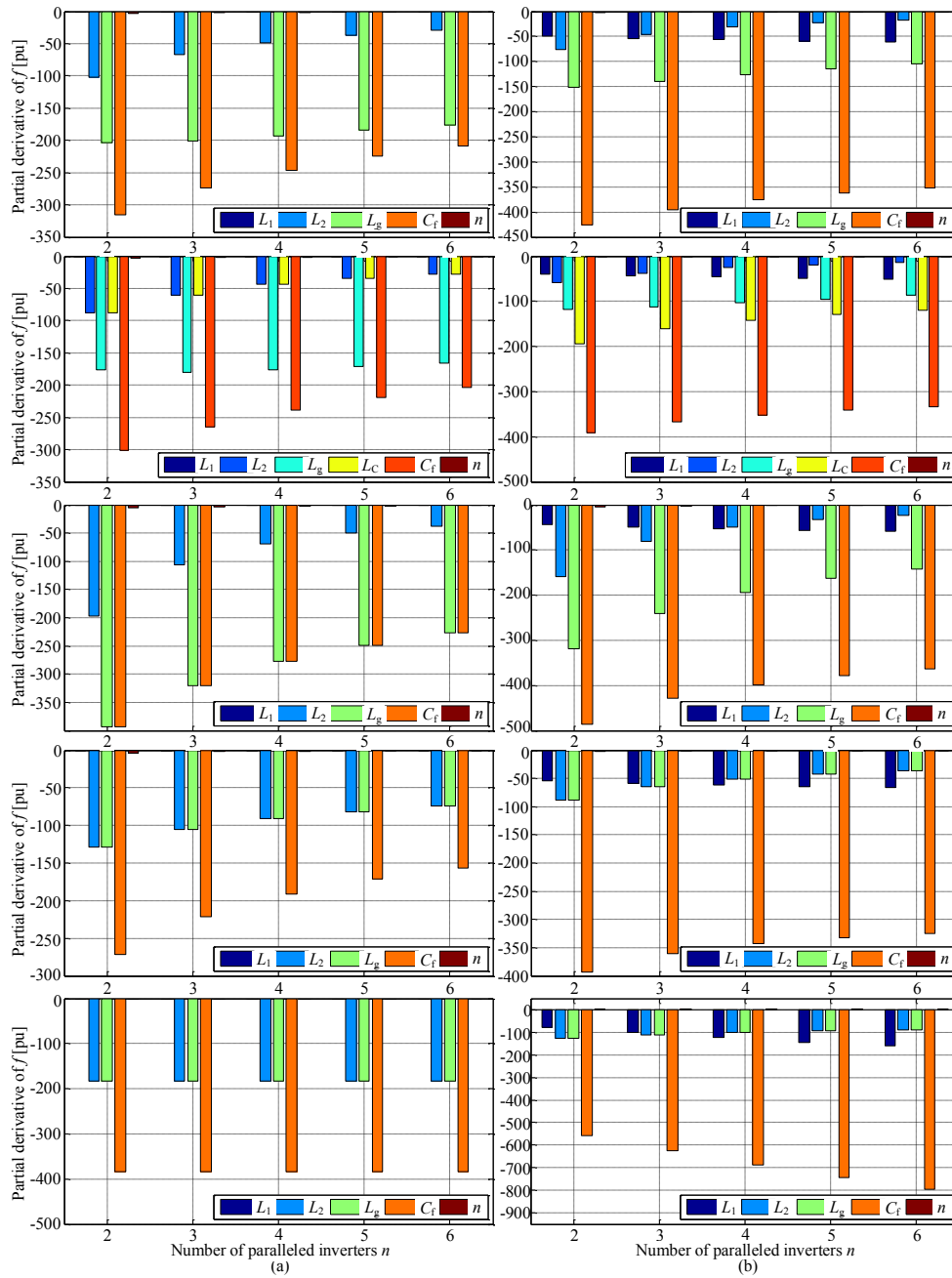


Figure 3.37 Partial derivatives of the filter resonance frequencies  $f_{r1}$  (a) and  $f_{r2}$  (b) for the  $LCL$ ,  $LLCL$ ,  $LC$ ,  $LC+L$ , and  $L$ -configurations, respectively, from top to bottom. The legend in each bar graph depicts which variable partial derivative is computed. The values used in the calculations are the nominal stiff grid values with  $L_1 = 0.1142$  pu,  $L_2 = 0.033$  pu,  $C_f = 0.03$  pu,  $L_g = 0.03$  pu,  $L_C = 0.093$  pu, and  $n = 2-6$ . For the  $LC$  configuration, a cable inductance of  $L_2 = 6.5986 \times 10^{-4}$  pu is assumed after the capacitor.

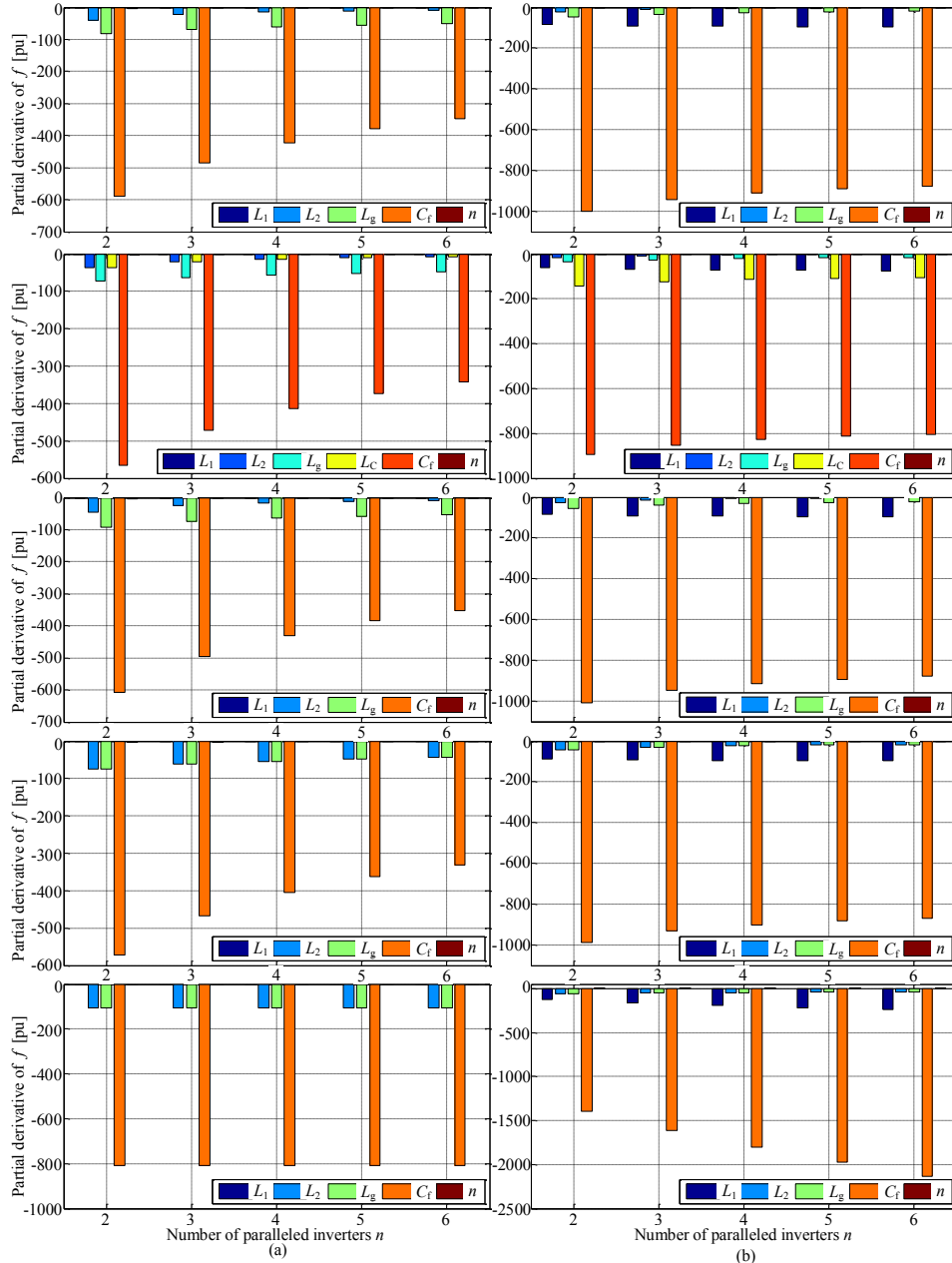


Figure 3.38 Partial derivatives of the filter resonance frequencies  $f_{r1}$  (a) and  $f_{r2}$  (b) for the  $LCL$ ,  $LLCL$ ,  $LC$ ,  $LC+L$ , and  $L$ -configurations, respectively, from top to bottom. The legend in each bar graph depicts which variable partial derivative is computed. The values used in the calculations are the nominal weak grid values with  $L_1 = 0.1142$  pu,  $L_2 = 0.0132$  pu,  $C_f = 0.015$  pu,  $L_g = 0.1$  pu,  $L_c = 0.0185$  pu, and  $n = 2-6$ . For the  $LC$  configuration, a cable inductance of  $L_2 = 6.5986 \times 10^{-4}$  pu is assumed to exist after the capacitor.

While the grid-side inductor in the stiff grid case is of similar-sized inductance as the grid in this case, the sensitivity to the grid-side inductor is smaller than for the grid inductance. This holds for the *LCL* and *LLCL* configurations, which have individual grid-side inductors. Furthermore, the *LC* configuration with the cable inductance presents a similar relation between the sensitivities to the grid-side inductor and the grid inductance. For the *LC+L* and *L*-configurations, the equality of the inductances is also seen in the sensitivities. In the weak grid, the results for the grid-side inductor are similar. However, as the grid inductance is already much larger than the grid-side inductor inductance, the sensitivity to both is decreased.

The inverter-side inductor has no effect on  $f_{r1}$ , but considering  $f_{r2}$ , the more inverters are connected in parallel, the larger the sensitivity against the inverter-side inductor becomes. For other variables, the sensitivities decrease as  $n$  increases except for the *L*-configuration and the sensitivity to the grid inductance in  $f_{r1}$  for the *LLCL* configuration. The sensitivity to the inverter-side inductor variations and for the capacitor variations increases for the *L*-configuration when  $n$  increases. However, the sensitivities to the other variables remain unchanged with respect to  $n$ .

To compare the sensitivities of the configurations, Figure 3.39 presents the  $f_{r1}$  sensitivities in the stiff grid case (a) and the weak grid case (b) normalized to the *LCL* configuration. Generally, the differences between each configuration are larger with the stiff grid case, where the capacitor and the grid-side inductor both are larger than in the weak grid case.

In both the stiff and weak grid cases, the *LLCL* configuration presents smaller sensitivities to each of the component that affects the lower resonance frequency  $f_{r1}$ . Of course, this comparison does not include the extra capacitor branch inductor as it is only present in the *LLCL* configuration.

The *LC* configuration presents a larger sensitivity than the *LCL* configuration to all of the components in both the stiff and weak grid cases. However, in the weak grid, the difference between the two configurations is decreased to less than 10 % at the largest for any of the variables.

The *LC+L* configuration presents a smaller sensitivity to the grid-side inductor and the capacitor values than the *LCL* configuration. In addition, the sensitivity to the number of paralleled inverters decreases fast below the *LCL* configuration value as  $n$  increases. The sensitivity to the grid inductance for the *LC+L* configuration is larger compared with the *LCL* configuration and increases with  $n$ . These observations can be made also for the weak grid cases, but the difference between the configurations is reduced again.

In the stiff grid, the *LC* configuration also presents the highest sensitivity to the capacitor and  $n$ . For  $n = 2$ , the *LC* configuration presents the highest sensitivity to the grid-side inductor but starting from  $n = 3$ , the *L*-configuration overtakes the *LC* configuration. Considering the parameter  $n$ , the *L*-configuration remains insensitive. However, the sensitivities to other parameters seem to increase the larger  $n$  gets, which means that it is

incorrect to state that the  $L$ -configuration  $f_{rl}$  would be insensitive to  $n$ . The  $L$ -configuration sensitivities compared with the  $LCL$  configuration quickly increase above all the other configurations except for the stiff grid case, and sensitivity to the capacitor, to which the  $LC$  configuration remains the most sensitive. However, as it can be seen, the  $L$ -configuration would surpass  $LC$  configuration soon after  $n$  increases above  $n = 6$ .

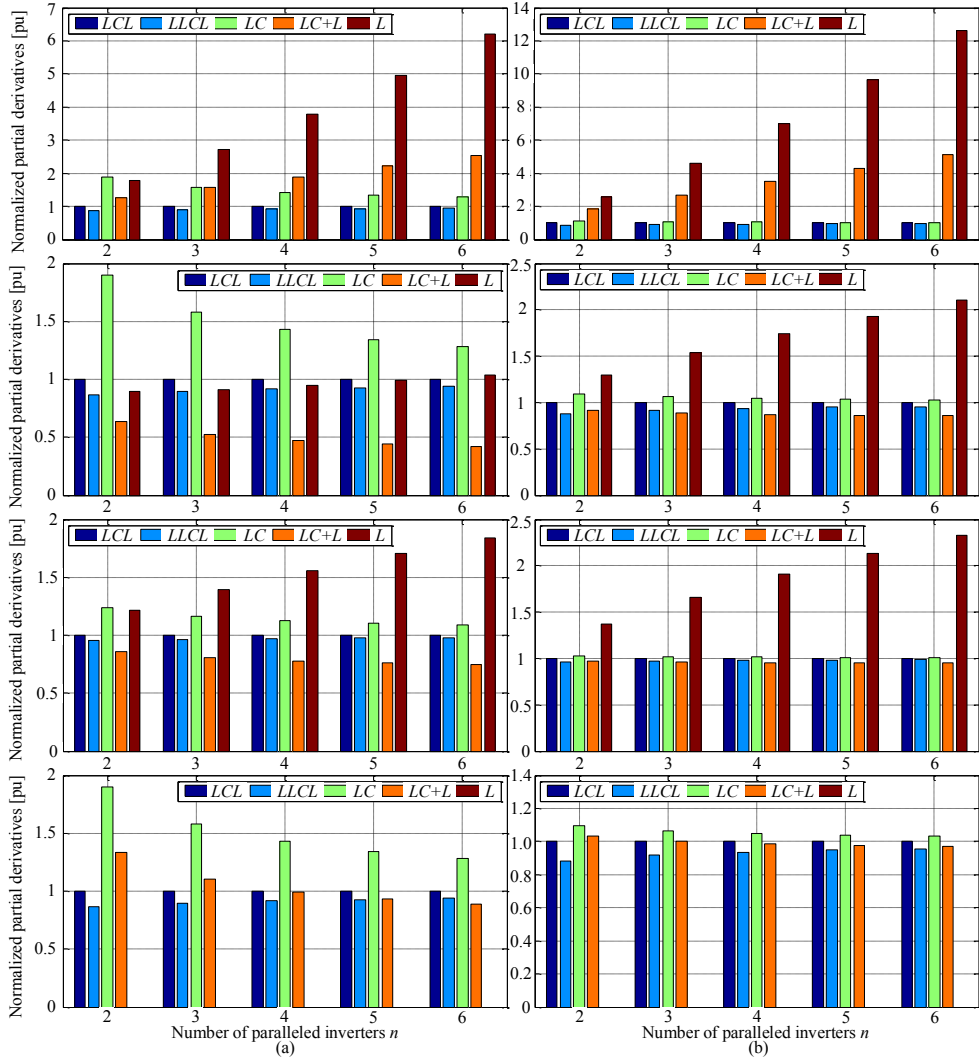


Figure 3.39 Partial derivatives of the lower resonance frequency  $f_{rl}$  in the stiff grid case (a) and the weak grid case (b) for the  $LCL$ ,  $LLCL$ ,  $LC$ ,  $LC+L$ , and  $L$ -configurations normalized to  $LCL$  configuration. From top to bottom, the variables under consideration are  $L_2$ ,  $L_g$ ,  $C_g$ , and  $n$ . The values used in the calculations are the nominal stiff and weak grid values. The  $LC$  configuration was added with a cable inductance as  $L_2 = 6.5986 \times 10^{-4}$  pu.

Figure 3.40 presents the sensitivities of  $f_{r2}$  for all configurations normalized to the  $LCL$  configuration. All configurations except the  $L$ -configuration show quite the same sensitivity to inverter-side inductor variation in both the stiff and weak grid cases. The least sensitive one is the  $LLCL$  configuration while the  $LC$  is very close to it. Both the  $LLCL$  configuration sensitivity and the  $LC$  configuration sensitivity increase towards the  $LCL$  configuration sensitivity as  $n$  increases. The  $LC+L$  configuration presents a slightly larger sensitivity to  $L_1$  than the  $LCL$  configuration, and it is independent of  $n$ . In the weak grid case the difference is already very small with  $n = 2$ . In the weak grid case, the relations remain virtually the same except for the  $LC+L$  and  $L$ -configurations, for which the difference from the  $LCL$  configuration is decreased.

The sensitivities to the grid-side inductor variation are more dispersed compared with the inverter-side inductor sensitivity. The  $LLCL$  configuration sensitivity is again around 80 % of the  $LCL$  configuration sensitivity. The  $LC$  configuration starts with the highest sensitivity, but at  $n = 3$  the  $L$ -configuration surpasses the  $LC$  because the  $L$ -configuration sensitivity increases with  $n$  whereas the  $LC$  configuration sensitivity decreases. Furthermore, the  $LC+L$  configuration experiences an increasing sensitivity to the grid-side inductance as the number of parallel inverters increases. At  $n = 4$ , the  $LC$  and  $LC+L$  configurations are very close to each other. The same holds for weak grid cases with the difference that the  $L$ -configuration is the largest already at  $n = 2$  and also the  $LC+L$  one is above  $LC$  at this point.

The sensitivity to the grid inductance is very similar to the grid-side inductor for the  $LC$  configuration, which suffers from the largest sensitivity to the grid inductance variation because of the lack of grid-side inductors. For the stiff grid case, the sensitivity of the  $L$ -configuration to the grid inductance changes at a similar rate as the  $LCL$  filter, while for the weak grid case, the  $L$ -configuration clearly has the largest sensitivity to the grid inductance variation. The  $LC+L$  configuration has the lowest sensitivity to the grid inductance variation because of the common grid-branch inductor of the configuration. This same inductor effect can also be seen in the  $L$ -configuration. As the grid-side inductor is smaller in the weak grid case, the sensitivity to the grid inductance is increased.

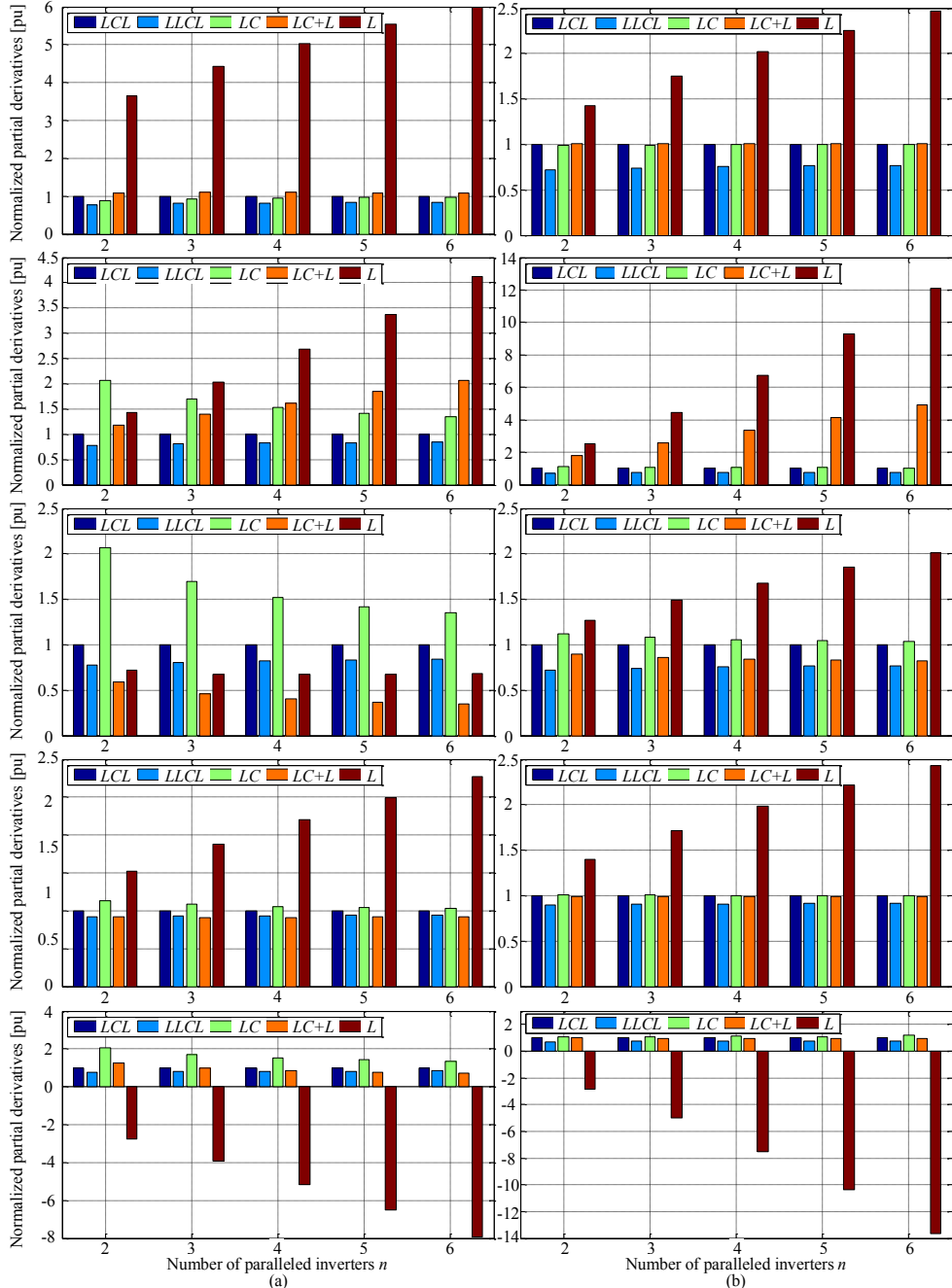


Figure 3.40 Partial derivatives of the higher resonance frequency  $f_{r2}$  in the stiff grid case (a) and the weak grid case (b) for the LCL, LLCL, LC, LC+L, and L-configurations normalized to LCL configuration. From top to bottom, the variables under consideration are  $L_1$ ,  $L_2$ ,  $L_g$ ,  $C_f$ , and  $n$ . The values used in the calculations are the nominal stiff and weak grid values. LC configuration was added with a cable inductance as  $L_2 = 6.5986 \times 10^{-4}$  pu.

The sensitivities to the capacitor variations for the *LCL*, *LLCL*, *LC*, and *LC+L* configurations are very close to each other. Both the *LLCL* and *LC+L* configurations present a smaller sensitivity to the capacitor as the *LCL* configuration while the *LC* configuration is more sensitive in both the stiff and weak grid. The *L*-configuration is the most sensitive configuration to the capacitor variation with an increasing effect as the  $n$  increases. The *LC* and *LC+L* configurations have a larger sensitivity to  $n$  as the *LCL* or *LLCL* filter. The sensitivity to  $n$  for both configurations in relation to the *LCL* configuration decreases as  $n$  increases. For the *LC* configuration after  $n = 3$ , the sensitivity to a larger number of parallel-connected inverters is smaller than the *LCL* configuration sensitivity. The same holds for both the stiff and weak grid cases. The *L*-configuration, again, is the most sensitive component to the  $n$  variation. The sign of the sensitivity to  $n$  is also different from the others. As for the other configurations, increasing  $n$  leads to a negative sensitivity, (decreased frequency), whereas the *L*-configuration experiences a positive sensitivity (increased frequency) with respect to an increased  $n$ .

Figure 3.41 presents the sensitivity of the cross-coupling resonance  $f_{rc}$  for the stiff grid case (a) and the weak grid case (b) for the *LCL*, *LLCL*, and *LC* configurations with two different cable inductances. The *LC+L* configuration experiences the same  $f_{rc}$  as the *LC* in the case where it is assumed that there is some cable inductance after the capacitor. For this reason it is not included here.

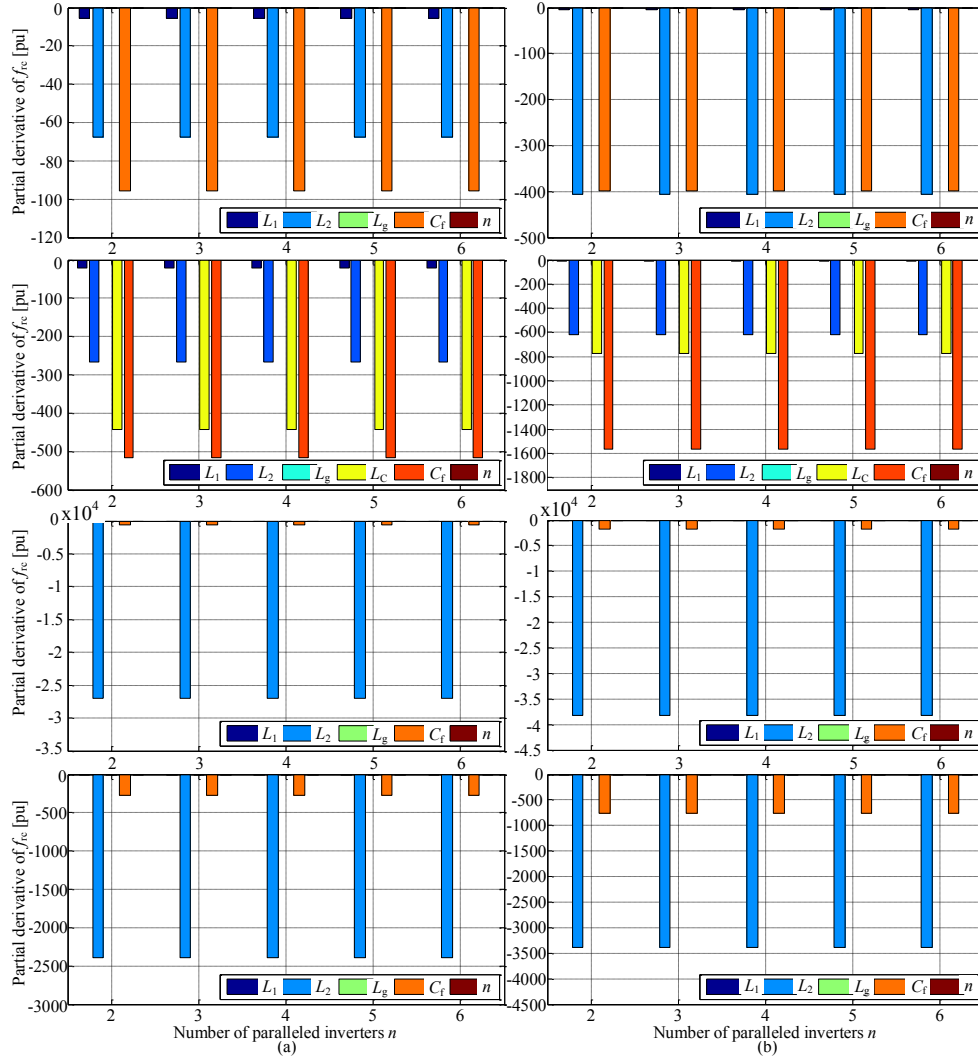


Figure 3.41 Partial derivatives of the cross-coupling resonance frequencies  $f_{rc}$  in the stiff grid design (a) and the weak grid case (b) for  $LCL$ ,  $LLCL$ , and  $LC$  with a cable inductance of  $L_2 = 6.5986 \times 10^{-4}$  pu, and an  $LC$  cable inductance of  $L_2 = 0.0033$  pu, respectively, from top to bottom. The legend in each bar graph depicts which variable partial derivative is computed. The values used in the calculations are the nominal stiff and weak grid values.

The cross-coupling resonance is not sensitive at all to the grid inductor and the number of paralleled inverters. For the  $LCL$  configuration, the capacitor is clearly the most sensitive component in the stiff grid case, whereas in the weak grid case the decreased values of the grid-side inductor and the capacitor result in quite even sensitivities to these two components. For the  $LLCL$  configuration, the capacitor and the additional inductor in the capacitor branch are the two most sensitive components in the stiff grid case. For the weak grid case, the capacitor sensitivity is increased similarly to the grid-side inductor

sensitivity while the sensitivity to the capacitor branch inductor is decreased with respect to the capacitor sensitivity. The *LC* configuration experiences the largest sensitivity to the grid-side inductance, which in this case is the cable inductance. The smaller the cable inductance is, the larger the sensitivity to this variable is.

The notable difference between the *LCL* and *LLCL* configurations is that  $f_{rc}$  of the *LLCL* configuration presents a much larger sensitivity to both the grid-side inductor and the capacitor. The only difference between the configurations is that the *LLCL* configuration has an extra inductor in series with the capacitor. It is fairly safe to locate the source of this difference in the extra capacitor branch inductance.

### Single component tolerance

As the parallel-connected inverters can be analysed with the superposition method, the effect of component tolerances can also be studied in a similar manner. Each component tolerance affects in a certain manner, and the end result is the sum of their individual effects. Here, only the resonance peaks are considered, because they are more vital for the filter and control system design. It is assumed that the filter inductors and capacitors contain a small 1 mΩ resistance each.

Let us consider two, three, and four paralleled inverters with individual *LCL* filters and the transfer function  $Y_{21,1}$  from the inverter 1 grid-side current to its own voltage. The inverter sees its own filter tolerances in a similar manner as a single inverter would see. Of course, the effect on the resonances is smaller because in a parallel-inverter system, the other inverters take part in the resonance circuits. If the components are larger than expected, the resonances are at lower frequencies than expected and vice versa for components that are smaller than nominal.

Figure 3.42 and Figure 3.43 present the resonance peaks of  $Y_{21,1}$  with variation in the inverter 1 filter components one at a time. The capacitor is the most critical component because it takes part in all resonances. The inverter-side inductor also presents a larger effect on both  $f_{r2}$  and  $f_{rc}$  than the grid-side inductor. This is due to the fact that with the values used,  $L_1 > 3L_2$ . If  $L_2$  were larger in size and closer to  $L_1$ , the quite natural outcome would be an increased effect of  $L_2$  variance and a decreased effect of  $L_1$  variance. The capacitor is located in the denominator of the resonance frequencies, which means that larger capacitors lead to smaller changes caused by inductor variance.

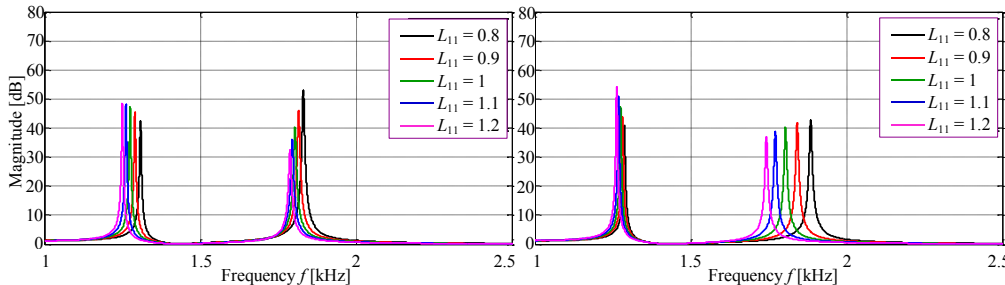


Figure 3.42 Bode magnitude plots of  $Y_{21,1}$  with two paralleled inverters when the inverter 1 filter inductors  $L_{11}$  and  $L_{21}$  are varied one at a time from 80 % to 120 % of nominal with 10 % steps.

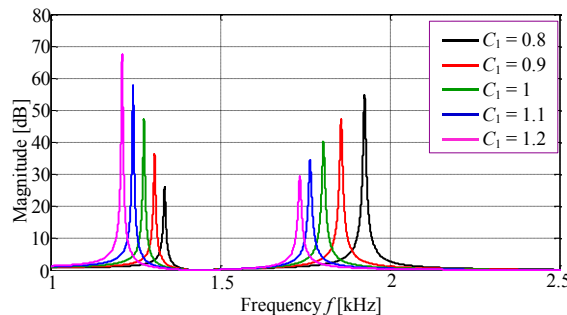


Figure 3.43 Bode magnitude plot of  $Y_{21,1}$  with two paralleled inverters when the inverter 1 filter capacitor  $C_1$  is varied from 80 % to 120 % of nominal with 10 % steps.

If the inverter 1 filter components are exact, the variance in the inverter 2 components produce the same outcome. A component tolerance of the same direction amplifies the effect of tolerance while the tolerance of a different direction counters the effect of another as seen from Figure 3.44. In the case of mutually amplifying tolerances, the resonance frequencies can very well be misplaced by a few hundred hertz as on the right side of Figure 3.44. The red peaks are located at 1275 Hz and 1804 Hz while the black and green peaks are at 1246 Hz and 2017 Hz and 1164 Hz and 1647 Hz for  $f_{r2}$  and  $f_{rc}$ , respectively. The most severe case would be that all of the filter components had the same tolerance leading to a wider band where the resonance frequency can be located. The black peaks would be at 1532 Hz and 2255 Hz and the green peaks at 1097 Hz and 1504 Hz. The increase in  $f_{rc}$  would be more than tripled in this case.

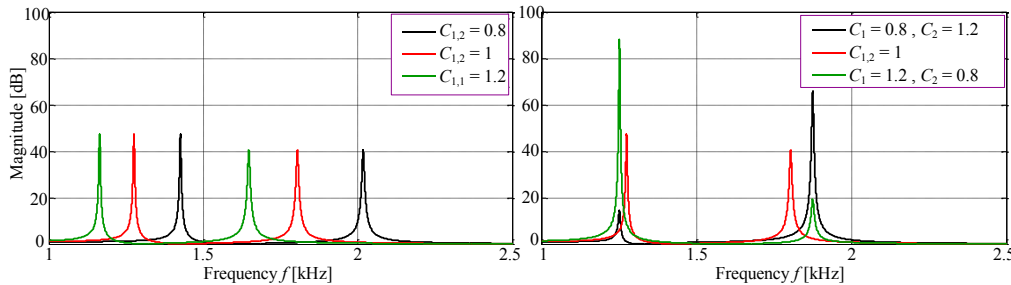


Figure 3.44 Bode magnitude plot of  $Y_{21,1}$  with two paralleled inverters while both the filter capacitors  $C_1$  and  $C_2$  have the same tolerances (left figure) and opposite tolerances (right figure) of -20 %, zero tolerance, and +20 %.

When the number of paralleled inverters is increased, the filter resonance is naturally lowered. In the case of the same tolerance in the same component of each filter, the cross-coupling resonance  $f_{rc}$  remains the same as shown in Figure 3.45, while  $f_{r2}$  is pushed toward lower frequencies. It can be seen from Figure 3.45 that with a larger number of paralleled inverters, the deviation caused by tolerance in always the same component decreases. Considering different tolerances in the same component, the tolerances even each other out again. Figure 3.46 shows that when one capacitor, in this case  $C_2$ , has a tolerance of -20 %, adding 20 % to the third capacitor, the resonances shift towards lower frequencies.

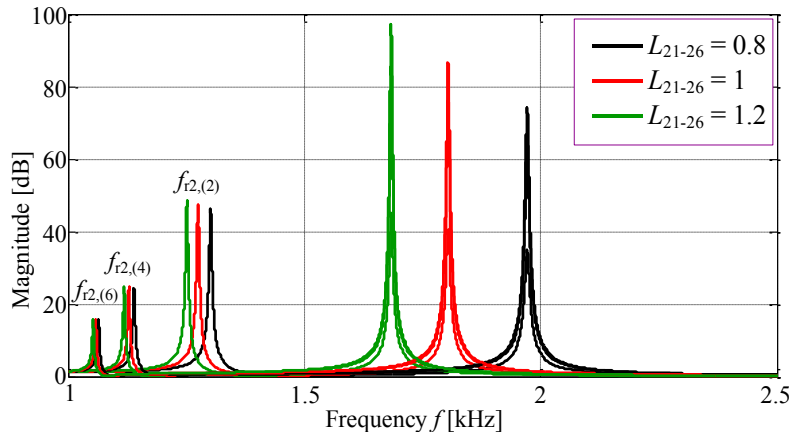


Figure 3.45 Bode magnitude plot of  $Y_{21,1}$  with two, four, and six paralleled inverters while all the grid-side inductors have the same tolerances of -20 %, zero tolerance, and +20 %.

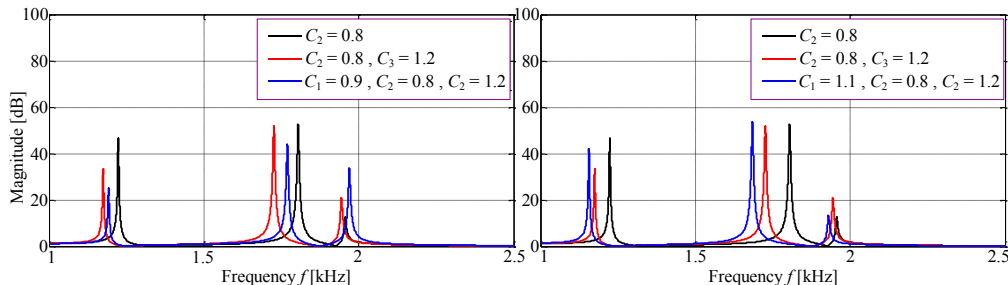


Figure 3.46 Bode magnitude plot of  $Y_{21,1}$  with three paralleled inverters while the filter capacitors have different amounts of tolerance.

Component variations of different proportions can cause more resonances around the cross-coupling resonance. This is of course a direct result of different series resonances caused by different component values. Figure 3.47 presents the transfer function  $Y_{21,1}$  Bode plots for  $n = 2\text{--}6$  with component tolerances generated randomly within the range of  $\pm 20\%$  of the nominal value. Tolerances are applied to all filter inductors and capacitors while the resistances are assumed to be  $1\text{ m}\Omega$  for each component. The tolerances for the figure can be found from Appendix F.

Figure 3.47 shows that even with different components the filter resonance peak is only shifted lower or higher depending on the tolerances and how they sum together. The filter resonance peak that the inverter sees is dominated mainly by the inverter's own filter. Around the cross-coupling resonance, however, there can be extra resonances caused by the interaction of the different resonance circuits. For instance, on the left side of the top graphs, the lowest peak of the three resonances over 1500 Hz is not seen in the Bode plots with two, three, and four inverters in parallel. Instead, the lowest peak here is now caused by the interaction of the fifth and sixth inverter in the system. Similar resonances can be seen on the other two rows. For instance, the Bode plot with two paralleled inverters presents a stiff resonance between 1500 Hz and 2000 Hz, which is not seen when other inverters are connected in parallel. The cross-coupling resonance with these extra resonances caused by the tolerances can lead to potentially destructive conditions if not damped properly.

As all of the tolerances together produce a total effect, the boundaries for the highest and lowest of these resonances can be assumed to be present in a situation where all the filters have the same tolerances of  $-20\%$  and  $+20\%$ . By computing (3.50) and (3.51) with tolerances and then relating them to the nominal value results, the cross-coupling resonance can be located within an interval of

$$\frac{1}{\delta_{\min}}f_{rc,n} \leq f_{rc} \leq \frac{1}{\delta_{\max}}f_{rc,n}, \quad (3.84)$$

where  $\delta_{\min}$  and  $\delta_{\max}$  are the minimum and maximum tolerances and  $f_{rc,n}$  is the cross-coupling frequency with nominal values. Substituting  $\delta_{\min} = 0.8$  and  $\delta_{\max} = 1.2$  into (3.84),

the range of the maximum deviation for  $f_{rc}$  can be determined as [0.8337,1.2500]. This range holds also for other configurations.

The  $LLCL$ ,  $LC$ ,  $LC+L$ , and  $L$ -configurations experience the tolerances in a similar manner as the  $LCL$  configuration considered above. If the component values are increased, the resonances are pushed below, and vice versa. The extra capacitor inductor of the  $LLCL$  configuration mitigate the effect of other components as could be seen from the partial derivatives studied before this section. For the  $L$ -configuration, there is no cross-coupling resonance, and a further clear benefit of having a single capacitor is that there are no other capacitors, which would make it different from the other configurations.

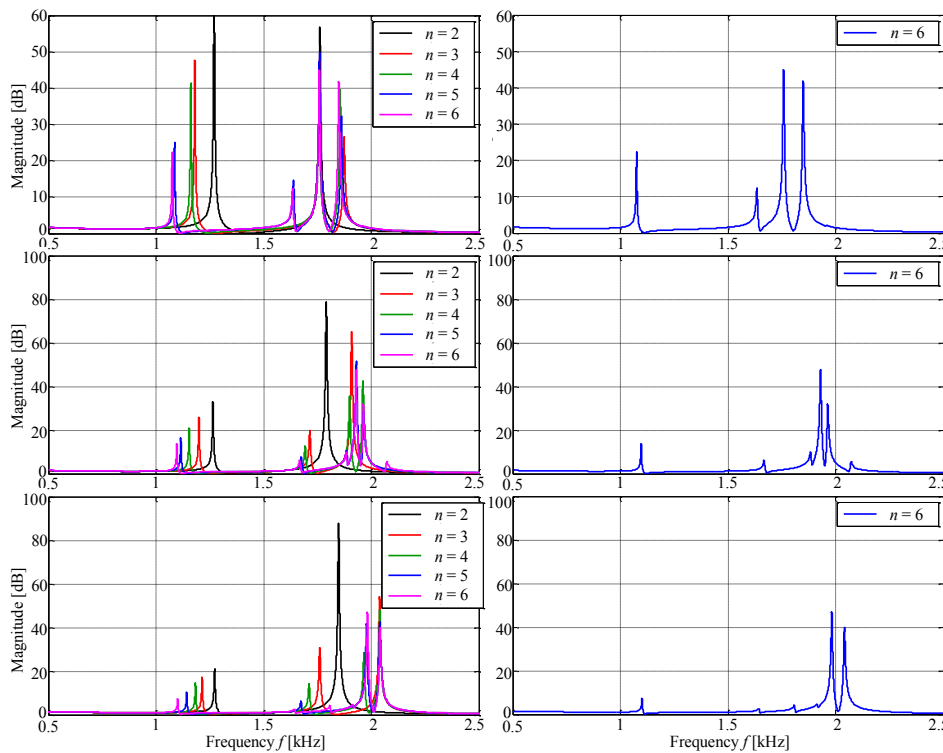


Figure 3.47 Bode magnitude plot of  $Y_{21,1}$  with  $n = 2\text{--}6$  (left) and  $n = 6$  (right) for three different sets of random tolerances from a range of  $\pm 20\%$ .

### 3.7 Modularity

The filter configurations differ at the level of modularity. Modularity can be studied from a number of perspectives, which are for instance *changes in attenuation, resonances, and energy* and further, the *maintenance* perspective.

The first perspective consists of two subviews; *modularity by design* and *modularity by retrofit*. The first one relates to a situation where the filtering is optimized in the design

phase for a particular range of paralleled inverters, whereas the second view relates to a situation where the filters are not designed according to the modular design criteria but for instance the application power is increased by adding more inverters in parallel.

From the perspective of maintenance, the modularity of each design is analysed based on how much components have to be changed in the case of faulty components, excessive tolerances in component values, or redesign changes in the filter configuration. In the modular design, the maintenance modularity is at highest when the least number of components have to be replaced. A good analogy would be that a passenger car is modular from the maintenance point of view whereas a television is not. When a car breaks, parts are replaced in order to make the car run again, but when a television breaks, normally the whole TV set is replaced.

The configuration that experiences the least resonance shift can be considered the most modular one from the viewpoint of resonance shift. A similar principle applies also to the other properties. The configuration that can be maintained by changing the least components is the most modular one from the viewpoint of maintenance. Further, the attenuation is closely connected to the location of the resonance peak  $f_{r2}$ . The lower the frequency is, the better the attenuation at high frequencies is.

Considering the resonance shift for each configuration, there are some clear differences between the configurations. In the *L*-configuration, there is no resonance shift in the lower resonance frequency. However, the higher resonance shifts towards higher frequencies, which may become a problem if the frequency is already close to the upper limit of  $f_2 \leq f_{sw}/2$ .

In other configurations, both frequencies shift towards lower frequencies as the number of paralleled inverters increases. The *LLCL* configuration experiences the least resonance shift in both resonance frequencies amongst the *LCL*, *LC*, and *LC+L* configurations. The *LLCL* configuration clearly benefits from the additional resonance frequency produced by the third inductor in series with the capacitor. As the number of paralleled inverters is increased, it can be seen that the difference between the *LLCL* and *LCL* configurations remains approximately the same for lower resonances, but for higher resonances the difference increases as  $n$  increases.

The *LC* and *LC+L* configurations have the same resonance shift in the lower resonance frequency but the *LC+L* configuration shows less shift in the higher resonance because of the common grid-branch inductor in the configuration. However, this benefit is diminished by the very large energy stored in the component rendering the configuration impractical.

The *L*-configuration does not present an interactive cross-coupling resonance, which generally can be taken as an advantage in control design. From the other configurations, *LLCL* and *LCL* benefit from their grid-side inductors in cases where the inductance value is larger enough to push the cross-coupling resonance low enough. In section 3.3.3, the

equations yielding the grid-side inductor value were presented. The *LC* and *LC+L* configurations do not have grid-side inductors. However, the cables connecting the filters in parallel presents some inductance, which can place the cross-coupling resonance over the switching frequency thereby causing destructive operating conditions. In the case of several inverters in parallel, it is possible that the cabling that connects inverters in parallel becomes longer, potentially increasing the inductance. However, compared with the *LCL* and *LLCL* cases, the *LC* and *LC+L* configurations lack some modularity considering this resonance and its potential problems.

The smaller the inverter-side current ripple is made by increasing the  $L_1$  inductor value, the less resonances are shifted. However, the smaller the ripple is, the larger losses are caused in the inductors itself. On the other hand, the larger the ripple can be, the more losses are caused in the inverter bridge by switching of larger currents. The effect of  $L_1$  on the modularity is part of a larger optimization problem, which involves aspects not studied in this dissertation.

Considering the energies of the components, compared with the *LCL* case, the *LLCL* configuration presents a slightly larger total energy. This difference is due to the additional capacitor branch inductor. The difference in the calculations was minimal partly because the calculations were made at the fundamental frequency. Assuming a maximum ripple current flowing into the capacitor branch, the energy of the inductor is in the range of 0.001 pu with the nominal filter values used in the calculations. Moreover, when taking the switching frequency ripple account, the other components such as the inverter-side inductor store a significantly larger proportion of energy rendering the additional inductor energy insignificant.

When comparing the total energies, the *LC* configuration changes least as  $n$  increases. The *LCL* and *LLCL* ones are close to the *LC* configuration, whereas the *L* and *LC+L* configurations have the second largest and largest energies. In the weak grid case, where the grid-side inductor and capacitor values are smaller, the *LCL* and *LLCL* experience less change than the *LC* but the *L* and *LC+L* configurations remain the least modular.

Both the resonance shift and energy and their change can be influenced by component changes. However, the inverter-side inductor is a fixed design married normally to the inverter, being seldom a component that can be changed. Moreover, in many cases the whole filter is an integrated structure, which means that single components cannot be changed for retrofit or maintenance reasons. This holds for the *LCL*, *LLCL*, *LC*, and *LC+L* configurations with the exception that the common grid-branch inductor of the *LC+L* can be changed as it is an individual component.

In the *L*-configuration, the capacitor and the grid-side inductor can both be individual components, or they can be integrated into one unit. Regardless of which of these options is the basis for the design of the *L*-configuration, the modularity of the configuration is very high, especially from the perspectives of retrofit and maintenance. The inverter-side inductor can be integrated into the inverter module while for a particular number of

parallel-connected inverters, either the capacitor, grid-side inductor, or both can be changed to accommodate the requirements of the application. Of course, the integrated *CL* circuit option would be better from the viewpoint of component optimization because the connections between the components can be minimized or at least optimized. The capacitor and the grid-side inductor can be designed in such a way that the resonances and attenuation stay within the designed range for a few paralleled inverters. When more inverters are added in parallel, a new *CL* circuit will be chosen, which will work again for a few more paralleled inverters.

For the other configurations, the filters can be designed in such a way that they provide adequate attenuation and resonances are kept within the desired range for instance by using a capacitor value that suits for a range of paralleled inverters. In section 3.4.2 this was referred to as ‘average filter design’ or ‘average capacitor’ to be accurate. The capacitor value can be chosen as an average over a certain range of numbers of parallel-connected inverters. In this way, the resonances can be kept within a chosen range while the attenuation is not compromised. If the average capacitor is used for a number of paralleled inverters at the low end ( $n = 2\text{--}3$ ) of the range, the resonances are higher and the attenuation is less than in the middle of the range. Similarly, at the high end ( $n = 4\text{--}6$ ) of the range, the resonances are lower but the attenuation is greater than in the middle.

The best configuration for the average filter design is the *LLCL* one because of its additional resonance, which should be placed at the switching frequency. Although this third resonance changes the increase rate of the attenuation to 20 dB/dec after the resonance, it ensures that the attenuation around the switching frequency and above it is not lost with the average capacitor at the low end of the range of paralleled inverters. When the capacitor is changed, the series inductor also has to be changed. However, with the average capacitor being fixed, the inductor is also fixed and it evens out the shift.

Because of the lack of a grid-side inductor, the *LC* configuration generally requires a larger capacitor to achieve  $f_{r2} \leq f_{sw}/2$ . Generally, the average capacitor is smaller than it would be for a single filter, which means that the applicability of the average capacitor design for this configuration is more limited than for the *LLCL*, *LCL*, and *LC+L* cases, where the grid-side inductor allows the use of smaller capacitances.

From the perspective of maintenance, the *L*-configuration is the best one. This is naturally due to the fact that it presents more components that can be changed if broken, or even better, which are about to break. The common capacitor can be replaced or both capacitor-inductor on the grid side can be replaced. For the other configurations, all filter components of a single filter are more likely to be changed in case of failure. Of course, the filters can be designed in such a way that for instance capacitors can be changed from the integrated design, but this may not be the best solution as it most certainly will take more time than changing the whole filter. The *LC* and *LC+L* configurations can present better modularity by maintenance compared with the *LCL* and *LLCL* configurations. Considering a situation where  $L_1$  or  $C_f$  (which can be assumed to be integrated components) fail, the module is replaced, leading to a maximum of two components to

be replaced at a time. With the *LCL* and *LLCL* configurations, the filter as a whole is replaced because it is often integrated into one unit.

However, both the common capacitor and the common grid-side inductor are crucial components for the operation of the whole system. If one of them fails, all inverters with individual inductors are down, whereas in the other configurations, only the failed inverter is off-line while the others can operate at least with partial power.

To summarize the discussion on the modularity of each configuration, the following observations were made

- The *L*-configuration presents great modularity from all aspects discussed above, especially from the perspectives of retrofit and maintenance. Furthermore, the *L*-configuration does not present cross-coupling resonance, which does not have to be taken into account when changing components.
- The common capacitor and grid-side inductor make the *L*-configuration least redundant. If either of them fails, none of the inverters can feed power to the grid. Similarly, the *LC+L* configuration suffers from decreased redundancy caused by the common grid-side inductor.
- The *LLCL* configuration is the most modular one because of its third resonance frequency at the switching frequency, which keeps the high-frequency attenuation at a good level even if the capacitor was designed for a broader range of paralleled inverters.
- The *LC+L* configuration benefits from the grid-side inductor compared with the *LC* configuration. However, the grid-side inductor leads to more energy stored in the filter components, and thus, a larger filter configuration.
- The *LC* configuration needs a larger capacitor to place the filter resonance low enough, which limits the modularity of this configuration to a narrower range of paralleled inverters.

### **3.8 Discussion and Conclusion – Chapter 3**

For parallel-connected inverters, several different filter topologies can be used to implement the high-order filtering needed in grid-connected inverters. Five configurations, *LCL*, *LLCL*, *LC*, *LC+L*, and *L*, were studied and compared in this chapter. The *LCL* and *LC* configurations are formed of the well-known and widely used filter topologies. The *LLCL* has been gaining more attention in recent years, and the *L* configuration is practically an *LCL* filter but with divided inverter-side inductors. Finally, the *LC+L* configuration includes a common grid-side inductor, which makes this configuration different from the *LC* configuration.

### 3.8.1 Components and modularity

First, the main difference between the configurations is of course the different number of components in the configurations. The *LCL* filters in the paralleled configuration make a total of  $2n$  inductors and  $n$  capacitors. The *LLCL* configurations have  $n$  inductors more, but the *LC*, *LC+L* and *L*-configurations have fewer components. The *LC* filters have only one *L* and *C* per inverter making  $n$  of both, which is less than with the *LCL* and *LLCL*. The *LC+L* configuration includes an additional common grid-side inductor, which increases the number of inductors by one. The *L*-configuration has the lowest number of components with  $n+1$  inductors and one capacitor, being thus the configuration that provides the greatest modularity from the perspective of maintenance. Furthermore, the *L*-configuration has a common *CL* circuit, which can be designed so that one *CL* circuit works for a few paralleled inverters and when more inverters should be added in parallel, only the *CL* circuit as a module or either of the components have to be changed. In the case of a very high power application, the common grid-side inductors can be removed as the capacitor is designed large. The component number is decreased, which narrows/limits modularity from the perspectives of retrofit and maintenance.

If the inverters have their individual filters, which would work alone, such as the *LCL*, *LLCL*, and *LC* filters, the modularity would be high. Inverters and filters could easily be connected together if the filters and inverter control were dimensioned to suit a possible parallel connection. For the *LC+L* configuration, the common grid-side inductors decrease the modularity by design because in the case of a high power application its energy increases significantly rendering the configuration impractical after a few MW of power. The *LC* configuration itself possesses a disadvantage of having an originally larger capacitor than the *LC+L* configuration. The originally large capacitor decreases the range of paralleled inverters for which the filter can be designed compared with the other configurations.

### 3.8.2 Resonances

In parallel-connected setups, the filter resonances are not those of a single inverter and filter. The resonance frequencies are shifted depending on the number of paralleled inverters, which if not considered in the filter design, and this can lead to destructive conditions when power is driven and load variations occur. Assuming identical components for design purposes, the paralleled inverters see the grid branch impedance multiplied by the number of parallel-connected inverters. In weak grids, which have a high inductance, the difference in the impact of grid branch multiplication is less significant amongst the configurations. This is due to the fact that with a large grid inductance, less inductance has to be added on the grid side as a discrete filter component.

In stiff grids, the individual or common grid-side inductors cause larger differences in reactions against the number of paralleled inverters. The *LLCL* configuration clearly benefits from the third inductor connected to the capacitor branch. The resonance frequencies of the *LLCL* filter are close to the *LCL* filter when the capacitor branch

inductance is small. This similarity means that with *LLCL* filters there will be no significant differences in the control design compared with the *LCL* filter. Further, an extra component leads to resonance frequencies that are shifted less with the *LLCL* configuration than with the *LCL* configuration.

Comparing the *LC+L* and *LC* configurations, the common grid branch inductor decreases the impact of resonance shift. This means that for a lower number of paralleled inverters, using a common inductor in the grid branch would bring some benefits against the resonance shift and grid inductance variations, the effect of which is also multiplied by  $n$ . Normally, of course, the grid inductance variations from the other side of the transformer are too small compared with the transformer inductance to be seen at all at the PCC. However, with high-power inverters, using a common grid-side inductor may be impractical as the current flowing through it is also increased with the number of paralleled inverters. This practical issue limits the applicability of the *LC+L* configuration around 3–4 MW powers.

The *L*-configuration benefits from a constant lower resonance frequency. This allows the resonance frequency to be already dimensioned to be as low as possible in order to yield the best possible attenuation. Adding inverters in parallel to increase the application power would not shift the resonance frequency any lower. If the capacitor and the possible common grid-side inductor are not changed, the higher resonance frequency is shifted towards higher frequencies. This can cause problems with applications that have a low switching frequency as the suitable area to place the resonance peak is not very wide to begin with. If the capacitance is increased along with the number of paralleled inverters, the higher resonance can be kept constant at the design point. By designing the capacitor larger than needed, the modularity of the *L*-configuration for retrofitting the application for a larger power is increased. The required capacitance to keep the higher resonance frequency constant does not directly increase proportionally to the number of paralleled inverters. If conventional design guidelines were employed, the capacitor starting from the nominal value would have to be multiplied by  $n$  to match the capacitance to the power, which now would be multiplied by  $n$ . However, for the stiff grid values, the capacitance for the *L*-configuration would be increased by the ratio of [1.3567, 1.7100, 2.0667, 2.4233, 2.7767] for  $n = 2\text{--}6$ , respectively. This suggests that the *L*-configuration as a greater retrofit capacitor would be a very good filter solution for paralleled inverters. Furthermore, if properly considered in the filter design, the *L*-configuration may also be suitable for up to 3–4 paralleled inverters even with the same capacitor regardless of the fact that the higher resonance frequency is pushed towards the switching frequency.

The *L*-configuration also benefits from the fact that it lacks the cross-coupling resonance between the inverters. The parallel-connected filters have an interactive cross-coupling resonance, which only depends on the filter parameters, which places it higher than the higher filter resonance frequency. For the *LCL* and *LLCL* configurations, the individual grid-side inductor is often large enough to place the cross-coupling resonance low and away enough from the switching frequency. Comparing the filter design constraints for a

single inverter and paralleled inverters, the cross-coupling resonance adds one design constraint to the parallel-connected case.

The cross-coupling resonance can cause serious problems in the *LC* and *LC+L* configurations. Both of them experience this resonance frequency similarly. Since there are no individual inductors after the capacitors, it is possible that the cross-coupling resonance is set to close or over the switching frequency. If the resonance placement is done according the normal guidelines for single inverters by placing the resonance close to  $f_{sw}/2$ , even a small cable inductance can place the cross-coupling resonance over the switching frequency when paralleled *LC* filters are used. The higher the switching frequency is, the smaller cable inductance is needed.

In parallel-connected inverters, different components, measurement errors, and asynchronous control with time delays can cause high-frequency circulating current between the inverters. This current is driven by the common-mode voltage produced by PWM modulation and has the frequency of the switching frequency. If *LC* and *LC+L* configurations are to be used, great attention has to be paid to prevent this circulating current. Of course, the circulating current should always be minimized because it causes additional losses in the inverter stage and the filter components. The *LCL* and *LLCL* configurations benefit from the individual grid-side inductors, which are in the path of the circulating current.

When considering the effect of component value changes over time or tolerances in them, the effects are quite similar to a single inverter case. However, in paralleled inverters, the other resonance circuits can produce additional resonances around the cross-coupling resonance, which have to be taken account of in the design. Placing some resistance seems to damp those resonances quite well, leaving only the stiffest cross-coupling resonance to be considered in the design.

### 3.8.3 Energy

Energy being a good measure of relative component physical sizes, it was used to compare the filter configurations. Generally, the *LC* configuration has the least amount of energy stored in the filter components, whereas *LCL* and *LLCL* are very close to each other, both storing around 23 % more energy than the *LC* configuration. The reason for this is that there are grid-side inductors in the *LCL* and *LLCL* configurations. The *LC+L* configuration presents the highest amount of energy mainly because of the common grid-side inductor. In addition, the common grid-side inductor can increase the energy stored in the *LC* parts of the *LC+L* configuration compared with the *LC* configuration even though the component values were the same. This is mainly due to the different capacitor voltages between the configurations. Like the *LC+L* configuration, the *L*-configuration suffers from the common grid-side inductor. However, if this component can be made smaller or even got rid of, the *L*-configuration will present very small energies compared with the other configurations, making it a more attractive choice for filter configuration.

Using a smaller capacitor generally leads to a smaller total energy because the capacitor voltage is close to the grid voltage in all operating points under consideration. By designing the filters so that the resonances are kept above certain limits or within a specific range, the capacitor could be designed small. This leads to less energy stored in the filter arrangement, but the filter performance would not be compromised at a small number of paralleled inverters. Practically, this kind of averaging of component values would work only on a small range of paralleled inverters, such as  $n = 2\text{--}4$  or  $n = 4\text{--}6$  without compromising the attenuation and control system stability at lower numbers of paralleled inverters.

The *LLCL* configuration, especially compared with the *LCL* configuration, provides interesting results for using average capacitor values. Because the third resonance frequency of the *LLCL* filters has to be placed over the switching frequency, constant values for the capacitor and capacitor branch inductors have to be used. This would also lead to filter resonances that remain closer to the design values even though the number of parallel-connected inverters were changed. For both the *LCL* and *LC* configurations, the resonances shift more compared with the *LLCL* configuration, which makes the *LLCL* configuration a more attractive choice for paralleled inverters, especially compared with the *LCL* configuration.

### 3.8.4 Open-end inverter

An open-end inverter can be considered a special case of two paralleled inverters. It consists of two inverters that drive each phase from both ends. For instance, phase A of inverter 1 is connected to A+ of the transformer, whereas phase A of inverter 2 is connected to A- of the transformer. The filters suitable for this configuration are *LC* or *LCL* filters. The *LLCL* filter would not work because there is already a series *LC* loop in the filter circuit, which removes the effect of an additional capacitor inductor. Ideally, the open-end inverter allows the use of smaller filter components because the inverter can produce three-level voltage compared with the two-level voltage of normally parallel-connected inverters. However, this topology has some practical limitations, which remove the advantage of smaller components.

For instance while using three-level modulation, a common-mode circulating current is included in the open-end system. The main path of this current is through the capacitor connected over the transformer phase, whereas the impedance of the transformer and possible filter inductors in series with it is much larger compared with the capacitor branch. To mitigate this current, either the inverter-side inductors or the capacitor have to be increased. Preferably, the capacitor should not be increased because it would cause more current to circulate through the transformer, which could saturate the transformer in the worst case.

Because there is no cancellation for the zero-sequence voltage, space-vector modulation or similar harmonic injection techniques cannot be used in open-end inverters. The zero-sequence current can flow through the transformer, easily saturating it. There is also

always some common-mode circulating current flowing through the capacitors. This can be removed by placing the modulator carriers in the same phase. However, this action leads to a loss of higher apparent switching frequency, which, in turn, leads to a need for larger filter inductors. The proper use of the open-end topology would require a special transformer design. Perhaps a transformer consisting of separate single-phase transformers could provide a large enough magnetizing inductance to allow the use of common-mode minimization techniques in the voltage generation of an open-end inverter system. Although this transformer study would be an interesting task, it is outside the scope of this dissertation. The open-end inverter system is presented and analysed as a special case of paralleled inverters to demonstrate that there are also topology-dependent possibilities to use smaller filter components.

### 3.8.5 Conclusion

In conclusion, the *LLCL* configuration has some interesting and advantageous qualities from the viewpoint of filter design for parallel-connected inverters; it yields the best attenuation for switching frequency harmonics, and designing an *LLCL* configuration over a range of values of  $n$  does not compromise the high-frequency attenuation. Compared with the *LCL* configuration, the stored energy and frequency characteristics are very close to each other, although *LLCL* filters have one extra component. Furthermore, the *LLCL* configuration resonances seem to suffer from the smallest impact by the number of paralleled inverters. If the modularity is the primary criterion, the *LLCL* and *LCL* filters are the safest choice because they both provide the grid-side inductor to keep the cross-coupling resonance away from the switching frequency range.

When *LC* filters are used, special attention has to be paid to the minimization of the circulating current. If this is achieved, the *LC* configuration will be a very good choice considering the number and sizes of the filter components. The downside of the *LC* configuration is that it is more susceptible to variations in grid inductance compared with the other configurations. The common grid-side inductor mitigates this problem but becomes impractical when the power levels of the application are increased.

The *L*-configuration is a very attractive choice for filtering when the application power level is set and the inverter would not be added in parallel after the installation. However, with small changes in the capacitor and the grid-side inductor, the *L*-configuration can also be used in a modular fashion. Moreover, the *L*-configuration does not suffer from the cross-coupling resonance because the capacitor is a common component.

The common design guidelines for a single component work for paralleled inverters in general. However, the cross-coupling resonance requires a minimum value for the grid-side inductor of the *LCL* and *LLCL* configurations, which were derived in section 3.3.3. The inverter-side inductor should also be considered from the viewpoint of resonance shift in paralleled inverters, whereas for a single inverter, the issue is commonly addressed only by focusing on the inverter-side current ripple.



## 4 Simulations and experimental tests

In this chapter, simulations are made to verify the results and issues presented and analysed in Chapter 3. Furthermore, experimental tests with a low-power prototype setup are presented and discussed in brief.

### 4.1 Closed-loop system stability

#### 4.1.1 Parallel-connected inverters

In the simulations, synchronous reference frame PI controllers are used. The controller design is made as presented in Chapter 2. Normally, the grid-connected inverter control is designed according to the total forward path inductance of the filter. However, for high-power inverters with a large current, even a small inductance interacting with harmonic current can produce voltage over filter impedances, being then amplified by the control system. A conservative option is to dimension the current control according to the inverter-side inductance. By doing this, the controller bandwidth is kept low, assuming a proper design otherwise, and the harmonic frequencies are not excessively amplified by the control. This conservative design holds also for low-power applications where the inductances may be large and even a small current can produce a significant voltage over a large impedance. The benefit of this design is better disturbance rejection.

The controlled current is the inverter-side current. For  $n$  paralleled identical inverters, the system in general is an MIMO system of the form

$$\mathbf{I}_1 = \mathbf{Y}_1 \mathbf{U}, \quad (4.1)$$

which, with the simplified notation, is written as

$$\begin{bmatrix} i_{11} \\ i_{12} \\ i_{13} \\ \dots \\ i_{1n} \end{bmatrix} = \begin{bmatrix} Y_{11} & -Y_{12} & -Y_{12} & -Y_{12} & -Y_{12} \\ -Y_{12} & Y_{11} & -Y_{12} & -Y_{12} & -Y_{12} \\ -Y_{12} & -Y_{12} & Y_{11} & -Y_{12} & -Y_{12} \\ \dots & \dots & \dots & \dots & \dots \\ -Y_{12} & -Y_{12} & -Y_{12} & -Y_{12} & Y_{11} \end{bmatrix} \begin{bmatrix} u_{11} \\ u_{12} \\ u_{13} \\ \dots \\ u_{1n} \end{bmatrix}, \quad (4.2)$$

where  $Y_{11}$  on the diagonal are transfer functions from the inverter's own voltage to its own current and  $Y_{12}$  on the off-diagonal are the transfer functions from other inverter voltages to a particular inverter current. The PI controller is a diagonal matrix of the PI controller transfer functions as follows

$$\mathbf{K} = \begin{bmatrix} (K_p + K_i/s) & 0 & 0 & 0 & 0 \\ 0 & (K_p + K_i/s) & 0 & 0 & 0 \\ 0 & 0 & (K_p + K_i/s) & 0 & 0 \\ \dots & \dots & \dots & \dots & \dots \\ 0 & 0 & 0 & 0 & (K_p + K_i/s) \end{bmatrix} \$. \quad (4.3)$$

The controller gains can be selected with (2.70) and (2.71).

Because the inverters are digitally controlled, the computational and sampling delays have to be incorporated into the controller  $\mathbf{K}$ . A common method used in pulse-width-modulated converters for sampling is the zero-order hold (Liserre et al., 2005), (Wu and Lehn, 2006), which, together with the computational delay and the sampling delay, forms a delay function of

$$G_d = \underbrace{e^{-sT_s}}_{\substack{\text{Computation} \\ \text{delay}}} \times \underbrace{\frac{1}{1.5T_s}}_{\substack{\text{Sampling} \\ \text{delay}}} \times \underbrace{\frac{1 - e^{-sT_s}}{s}}_{\substack{\text{Zero-order hold} \\ \text{delay}}} = \frac{e^{-sT_s}(1 - e^{-sT_s})}{1.5sT_s}. \quad (4.4)$$

The delay terms of type  $e^{-Ts}$  cannot be represented by rational functions. To overcome this limitation, a common approach is to approximate the terms by the *Padé* approximation, as was done in (Agorreta et al., 2011). The resulting delay emulator is of the form

$$G_d = \frac{Padé_1(1 - Padé_1)}{1.5sT_s} = \frac{2(4 - 2sT_s)}{3(2 + sT_s)^2}. \quad (4.5)$$

For simplicity, the diagonal elements in  $\mathbf{K}$  are substituted with  $K = G_d(K_p + K_i/s)$  in the following equations, where the delay emulator is incorporated into the controller  $K$ .

The open-loop transfer function matrix is now

$$\mathbf{L} = \mathbf{Y}_1 \mathbf{K} = \begin{bmatrix} KY_{11} & -KY_{12} & -KY_{12} & -KY_{12} & -KY_{12} \\ -KY_{12} & KY_{11} & -KY_{12} & -KY_{12} & -KY_{12} \\ -KY_{12} & -KY_{12} & KY_{11} & -KY_{12} & -KY_{12} \\ \dots & \dots & \dots & \dots & \dots \\ -KY_{12} & -KY_{12} & -KY_{12} & -KY_{12} & KY_{11} \end{bmatrix}. \quad (4.6)$$

The closed-loop current controlled system can be written as

$$\mathbf{I}_1 = \mathbf{T} \mathbf{I}_{ref}, \quad (4.7)$$

where  $\mathbf{I}_{ref}$  is the column vector containing all the current references, and  $\mathbf{T}$  is the closed-loop transfer function matrix computed from  $\mathbf{L}$  by

$$\mathbf{T} = \mathbf{L}[\mathbf{I} + \mathbf{L}]^{-1} = \mathbf{Y}_1 \mathbf{K} [\mathbf{I} + \mathbf{Y}_1 \mathbf{K}]^{-1}. \quad (4.8)$$

The closed-loop system of (4.7) is

$$\begin{bmatrix} i_{11} \\ i_{12} \\ i_{13} \\ \dots \\ i_{1n} \end{bmatrix} = \begin{bmatrix} T_{11} & T_{12} & T_{12} & T_{12} & T_{12} \\ T_{12} & T_{11} & T_{12} & T_{12} & T_{12} \\ T_{12} & T_{12} & T_{11} & T_{12} & T_{12} \\ \dots & \dots & \dots & \dots & \dots \\ T_{12} & T_{12} & T_{12} & T_{12} & T_{11} \end{bmatrix} \begin{bmatrix} i_{11,\text{ref}} \\ i_{12,\text{ref}} \\ i_{13,\text{ref}} \\ \dots \\ i_{1n,\text{ref}} \end{bmatrix} \quad (4.9)$$

The elements of  $\mathbf{T}$  after some serious manipulation are of the form

$$T_{11} = \frac{K^2 n (Y_{11} + Y_{12})(Y_{11} - (n-1)Y_{12}) + KY_{11}n}{(1 + K(Y_{11} - (n-1)Y_{12}))(1 + K(Y_{11} + Y_{12}))} \quad (4.10)$$

and

$$T_{12} = -\frac{KY_{12}n}{(1 + K(Y_{11} - (n-1)Y_{12}))(1 + K(Y_{11} + Y_{12}))}. \quad (4.11)$$

Here, it is noteworthy that the negative of  $Y_{12}$  is now embedded into  $T_{12}$ .

The zeros and poles of  $\mathbf{T}$  are complex to compute. However, as it can be seen from (4.10) and (4.11), the poles of all elements of a multivariable system are the same, it is sufficient to compute the poles of only either  $T_{11}$  or  $T_{12}$ . The poles of  $T_{11}$  and  $T_{12}$  can be divided into two sets as can be seen from (4.10) and (4.11). These two pole sets are called cross-coupling stability poles and external stability poles. In (Agorreta et al., 2011), similar pole sets as in (4.10) and (4.11) are called internal stability and external stability poles. However, part of the cross-coupling stability poles of (4.9) include the interactive cross-coupling resonance and its poles, hence the name, and they are found as the zeros of

$$P_{\text{cross}} = (1 + K(Y_{11} + Y_{12})). \quad (4.12)$$

The external stability poles of (4.9) are found as the zeros of

$$P_{\text{ext}} = (1 + K(Y_{11} - (n-1)Y_{12})). \quad (4.13)$$

Since each of the configurations has the same inverter-side inductor values, the controller design becomes the same, as a result of which only  $Y_{11}$  and  $Y_{12}$  have to be changed to correspond to a particular filter configuration.

From (4.12) and 4.13) we can see that the equivalent model (3.15) describing a single inverter in a multi-parallel-inverter system defines the external stability poles. The equivalent model is based on the assumption of zero circulating current between the parallel-connected inverters. However, as can be seen from above, there are still some poles that are not present in (4.13). For this reason, the equivalent model alone is not sufficient for analysing stability of the control system of a multi-parallel-inverter system

because in real applications, there are always some differences for instance in switching instants as well as measurement errors, which lead to different current references for the paralleled inverters even though they would drive the same power to the grid.

Lu et al. (2017) point out that the control stability study in (Argorreta et al., 2011) cannot describe the transient behaviour of the multi-inverter system because it is based on the equivalent model derived in the publication. Agorreta et al. derived an equivalent model from the closed-loop transfer function matrix. This equivalent model, where the grid impedance is multiplied by  $n$ , is based on the assumption that the current references for all inverters are the same, which is seldom the case in a real application. This assumption effectively removes the cross-coupling resonance from the analysis, which can lead to an unstable system if not considered in the analysis. In this dissertation, the controller stability is obtained analysing a closed-loop system where the current references are not assumed to be identical. There is cross-coupling resonance in both  $Y_{11}$  and  $Y_{12}$ , and thus, it is incorporated into the closed-loop transfer functions.

Figure 4.1 presents the pole-zero maps plotted for (4.12) on the top row and for (4.13) on the bottom row for the *LCL* configuration with no damping. The pole-zero maps are plotted for  $n = 2\text{--}10$ . The left-hand figures are close-ups on the imaginary axis. The cross-coupling poles and zeros located around the real axis between  $-15000$  1/s and  $-10000$  1/s change as  $n$  changes, but the rest remain the same. There is a complex pole pair in the right half plane (RHP), which renders the system unstable. This pole pair does not move as  $n$  increases, and it is dependent on the filter and grid parameters only; in fact, it is caused by the cross-coupling resonance. Similarly, there is an unstable pole pair in the external stability pole equation. This pole pair moves towards the stable LHP as  $n$  is increased. However, the unstable cross-coupling pole pair would still render the system unstable should the external stability poles lie in the LHP. The system clearly has to be damped by some means.

There are several different methods to damp the filter resonances either passively or actively. In passive damping, resistance is added to the filter circuit. The simplest method is to add the damping resistor in series with the capacitor. However, this solution suffers from two disadvantages; relatively large losses and degraded attenuation in the high-frequency range. To overcome these problems, the capacitor can be split into two parts, where the larger part is added with a damping resistor whereas the smaller part is left undamped (Balasubramanian and John, 2013) (Wu et al., 2013). The resulting resistor may be larger than in conventional capacitor damping, but the losses caused by the resistor are decreased (Beres et al., 2014). Furthermore, as shown in Wu et al., the damping resistor in the same branch as the additional inductor of the *LLCL* filter will also damp the third resonance frequency supposed to mitigate the switching frequency.

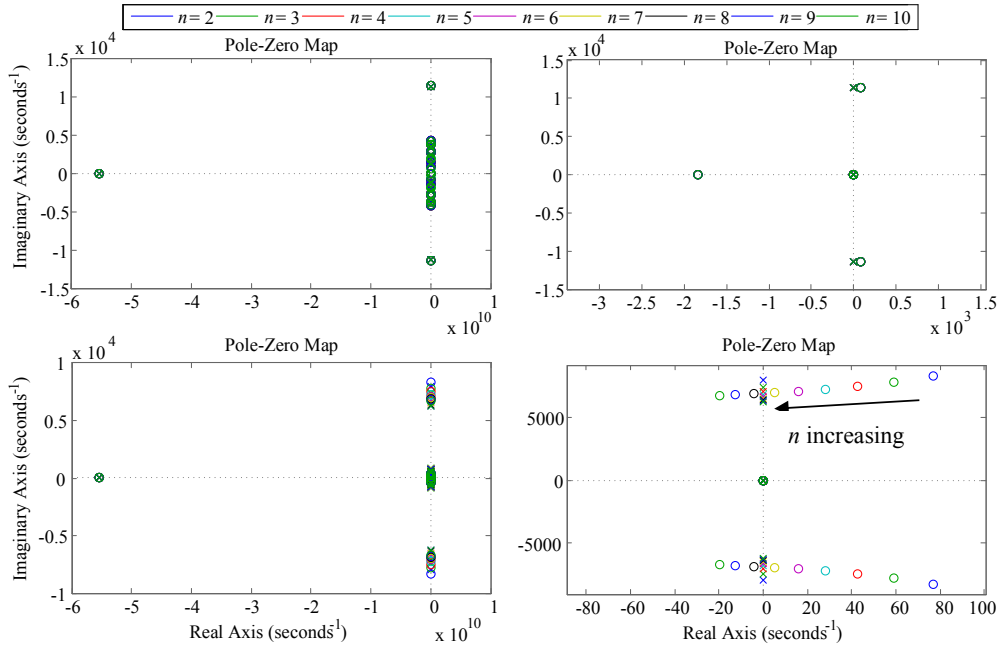


Figure 4.1 Undamped *LCL* configuration cross-coupling poles (top row) and external stability poles (bottom row) with  $n = 2\text{--}10$ . The right-hand figure is an enlargement showing the unstable poles. Note that the zeros of these figures are the poles of the closed-loop system.

For this reason, much better attenuation is achieved by splitting the capacitor for the *LLCL* filter. A third option for passive damping would be to add a series *RL* damping circuit in parallel with the grid-side inductor or a parallel *RL* damping circuit in series with the grid-side inductor (Hiltunen et al., 2014). Beres et al. (2016) present an optimal design for a passive-damped filter to minimize the resonance peak. They analyse several different damping methods including multiple trap filters in parallel with the damped capacitor branch to overcome the limited attenuation in the high-frequency range. In (Rockhill et al., 2011), a selective passive damping to limit the damping losses was presented.

In the case of active damping, the filter is not equipped with extra components to cause losses. Instead, the control system is augmented in order to damp the resonances. Dahono (2002) presents and analyses a virtual resistor method, where the controller is provided with a feedback loop to implement a closed-loop system which is the same as if the original system included a real resistor. Virtual resistor active damping is used for instance in (Wessels et al., 2008), (He et al., 2013), and (Alemi and Lee, 2014). Another implementation of active damping can be achieved with capacitor current or voltage feedback (Dannehl et al., 2010) (Parker et al., 2014). In (Dannehl et al., 2011), filter-based active damping that requires no extra sensors was studied, and in (Miskovic et al., 2014) and (Abdeldjabar et al., 2016), observer-based active damping was investigated.

Because the optimization of the filter and system efficiency are outside the scope of this dissertation, active damping methods are not studied in this work. The split-capacitor passive damping is selected because it preserves the high-frequency attenuation and does not damp the *LLCL* filter third resonance. Furthermore, the attenuation after the third resonance of the *LLCL* filter is increased to -40 dB/dec from -20 dB/dec. All of the filter configurations will have a similar damping method.

The cross-coupling stability poles become stable with a fairly low amount of damping resistance, whereas the external stability poles need more damping. Figure 4.2 presents the damped external stability poles for the *LCL* configuration with four different damping resistor values for  $n = 2\text{--}10$ . The damping resistor  $R_d$  is in series with the damping capacitor  $C_d = 0.9C_f$ . The rest of the capacitance is in the undamped  $C_1 = 0.1C_f$ . With no  $R_d$ , the poles move towards the LHP when  $n$  increases in a similar manner as with  $R_d = 20\text{ m}\Omega$  in the top left corner in Figure 4.2.

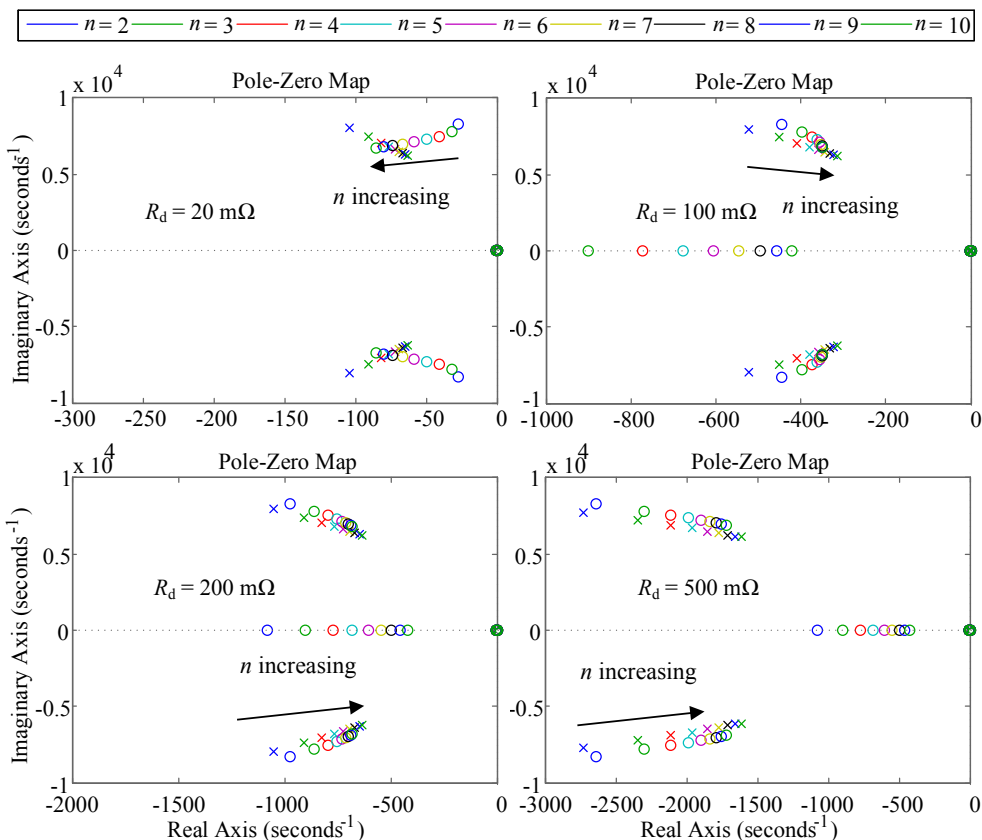


Figure 4.2 Damped external stability poles for the *LCL* configuration with  $n = 2\text{--}10$  with four different damping resistances;  $20\text{ m}\Omega$ ,  $100\text{ m}\Omega$ ,  $200\text{ m}\Omega$ , and  $500\text{ m}\Omega$ .

Increasing the damping resistor changes the direction of the pole movement as can be seen from the rest of Figure 4.2. Increasing the resistor makes the margin larger, but too high a value would only result in extra losses without any advantages.

For the *LLCL* configuration, the additional inductance in series with the capacitor has to be added to the undamped capacitor to yield a resonance sag over the switching frequency. While the capacitor is now 10 % of the original, the required inductance is tenfold to the original value used previously in the dissertation. Because the capacitor branch differs between the *LCL* and *LLCL* configurations, there is an insignificant difference in the poles and damping of them. There is an additional imaginary pole pair resulting from the additional capacitor branch inductor for the *LLCL* configuration. However, this pole pair is deeper in the LHP than the lower frequency pole pairs. While in the case of the *LCL* configuration, already a 20 mΩ resistor damps the unstable poles, for the *LLCL* configuration, a larger resistor is needed.

Considering the *LC*, *LC+L*, and *L*-configurations, the damping effect of the same resistance values results in a similar outcome as for the *LCL* configuration, given that the poles are placed in slightly different locations and the *L*-configuration lacks the cross-coupling poles. The value of  $R_d = 200\text{m}\Omega$  is chosen for all configurations.

#### 4.1.2 Open-end inverter

The controller stability for the open-end inverter systems is very similar to the single grid-connected inverter. Figure 4.3 presents the equivalent circuit for the control design of the open-end inverter based on a single inverter with doubled filter inductors. The control system designed with the doubled inductor value for the  $L_1$  inductor, as indicated by Figure 4.4, shows the effect of the split-capacitor damping for the open-end system. As can be seen, even a small value of  $R_d$  can damp the unstable poles. The value of  $R_d = 200\text{m}\Omega$  similarly as for normal paralleled inverters is chosen for the open-end system. However, as the capacitor shorts the phase conductors, there is a current path especially for a high-frequency current, the value may have to be revised after verifying the losses of the damping resistor.

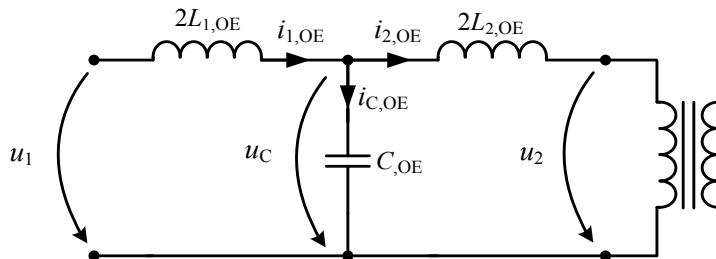


Figure 4.3 Single-phase circuit for an open-end inverter system.

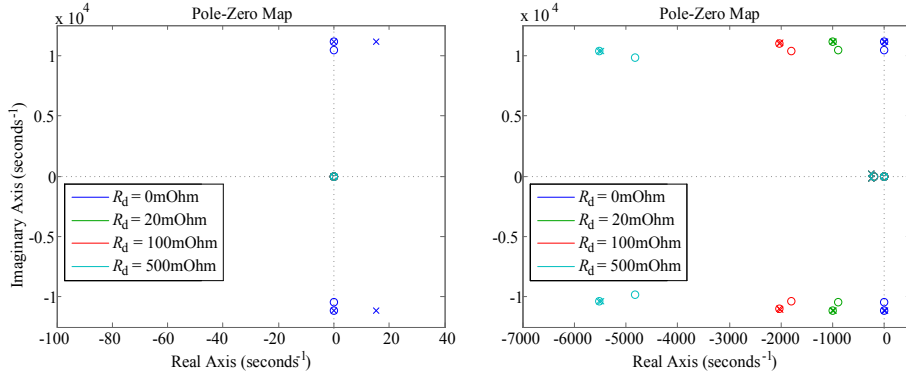


Figure 4.4 Open-end system unstable poles being damped with an increased damping resistor  $R_d$ .

## 4.2 Simulations

Simulation models of the parallel-connected inverters and the open-end inverter system were created in *Simulink* with the SimPowerSystems toolbox components. The parallel-connected inverters were simulated with the number of paralleled inverters applying  $n = 2\text{--}6$ . The upper limit is due to practical issues such as the size of the computer memory. A basic description of the simulation models and the applied filter parameters is given in Appendix H.

The inverter bridges were modelled with the universal bridge block with the IGBT and diode option for the power semiconductor devices. Forward voltages of 0.5V for both the IGBTs and diodes were used. A fall time of 400 ns and a current tail time of 900 ns were used for the IGBT switches. A resistance of 0.1 mΩ was used for conduction resistance. The snubber circuit required by the IGBT diode bridge was designed according to Simulink's advice to limit the leakage current of the snubber circuit to less than 0.1 % of the nominal current.

The grid was modelled as an inductive grid with a controlled voltage source and inductive grid impedance. Table 4.1 presents the harmonics included in the grid voltage in simulations. The harmonics were added up to the 50<sup>th</sup> harmonic, which is the upper limit for the THD calculation for a 50 Hz system as in the simulations. The values result in  $THD = 2.6372 \%$ , which is below the 3 % limit required by the Finnish TSO Fingrid (Fingrid, 2015). The actual limits per each harmonic allowed in the Finnish 110 kV grid are higher, but in practice, the voltage distortion in the high-voltage grid is less than allowed. For instance, harmonics measured from the Polish high-voltage grid include mainly the fifth, seventh, and eleventh harmonics. Moreover, small quantities of second, third, fourth, sixth, ninth, thirteenth, and twenty-fifth harmonics are present in the measurements but all of them are less than 0.25 % (Pawełek and Wasiak, 2014). Figure 4.5 presents the grid voltage waveforms illustrating the distortion caused by the harmonics.

Table 4.1. Harmonics included in the grid voltage in simulations.

Odd harmonics	Relative amplitude [%]	Even harmonics	Relative amplitude [%]
3 <sup>rd</sup>	0.50	2 <sup>nd</sup>	0.40
5 <sup>th</sup>	1.25	4 <sup>th</sup>	0.30
7 <sup>th</sup>	1.05	6 <sup>th</sup>	0.10
9 <sup>th</sup>	0.30	8 <sup>th</sup>	0.10
11 <sup>th</sup>	1.10	10 <sup>th</sup>	0.20
13 <sup>th</sup>	0.80	12 <sup>th</sup>	0.20
15 <sup>th</sup>	0.50	14 <sup>th</sup>	0.20
17 <sup>th</sup>	0.40	16 <sup>th</sup>	0.20
19 <sup>th</sup>	0.40	18 <sup>th</sup>	0.20
21 <sup>st</sup>	0.50	20 <sup>th</sup>	0.20
23 <sup>rd</sup>	0.20	22 <sup>nd</sup>	0.20
25 <sup>th</sup>	0.20	24 <sup>th</sup>	0.20
≥27 <sup>th</sup>	0.20	≥26 <sup>th</sup>	0.10

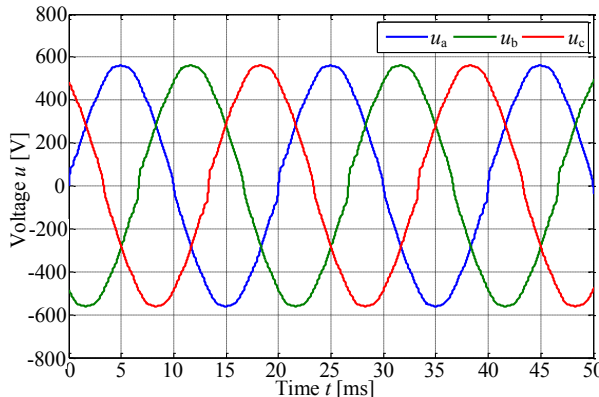


Figure 4.5 Distorted grid voltage used in the simulations.

The supply for each inverter was modelled as a controlled direct current source, whose DC value was added with white noise with a maximum value around  $\pm 15\%$  sampled with a 5 kHz frequency to make the simulations closer to real-life applications, such as photovoltaic and wind power generation. The noise in the supply current simulates partial shading of solar power, wind gusts, and noise caused by the mechanical system in wind power plants. Figure 4.6 presents the DC link input current with a mean value of approximately 914 A.

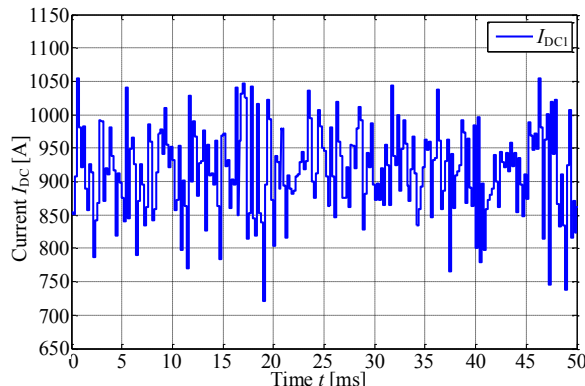


Figure 4.6 DC link input current with white noise added to it.

#### 4.2.1 Control system

Typically, the control system of a parallel-connected inverter is designed as individual controllers kept in line with droop controllers or as a master controller where all of the parallel inverters use the same gate signals generated by the control of one inverter control. The choice of the control system design is application dependent and there are differences in the operation between the two designs.

For instance, using individual controllers for each parallel-connected inverter leads to a situation where the differential-mode circulating current is controlled ideally to zero. Naturally, because of differences in the measurements, switching times of semiconductor devices, and component tolerances, there is always some difference in the grid-side currents. However, assuming that there are tolerances in components and the filters are not identical, the controllers will produce a different voltage to drive the same power to the grid resulting in a different common-mode voltage produced by the inverters. This common-mode voltage difference will drive a circulating current between the inverters.

The individual control electronics of the parallel-connected inverters will have small differences in the clock frequencies, which results in time asynchronous carriers. This asynchronous operation will cause a circulating current, which has to be minimized by continuously resynchronizing the carriers (Purhonen, 2014). With  $LC$  configuration, where there is no  $L_2$ , even a small cable inductance can set the cross-coupling resonance close this circulating current frequency. Yang et al. (2018) also present how the asynchronous carriers can lead to sideband harmonic instability in paralleled inverters. In addition, the IGBT switching instants have some time deviation, and they differ between the paralleled inverters. These differences in switching instants can result in a voltage difference, which would also drive circulating current.

Using a master controller and the same gate signals for all of the parallel-connected inverters results in different powers injected to the grid but a minimized common-mode voltage difference between the paralleled inverters. Of course, because of the different

powers injected to the grid, a differential-mode current will circulate between the inverters.

Control system design of master control type was employed in the simulations because of its simplicity and the ability of implementing the design. Using only one modulator carrier signal would ensure synchronized operation for all inverters. Moreover, using only one controller would free memory for other variables in the simulation, helping to simulate more inverters in parallel. Further, including minuscule nanosecond level differences in the switching instants would also require sample times of a nanosecond scale. This would result in very high memory usage and a long simulation time. For these reasons, the IGBT switching deviation was not modelled.

The simulation control system was triggered at the peaks of the carrier wave of the modulator. To generate the computational delay that is present in real applications, the modulator used the control input from the previous calculations. This delay of half a switching period was produced by updating the control output registers in the middle of the carrier wave.

#### 4.2.2 Identical filters

First, the simulations were made with identical filter values as was the case in the theoretical studies. The filters were designed as stiff grid nominal designs used in the this dissertation  $L_g = 173 \mu\text{H}$ ,  $C_f = 200.57 \mu\text{F}$ ,  $L_2 = 50 \mu\text{H}$ , and the grid inductance was  $L_g = 45.465 \mu\text{H}$ .

##### ***LCL* and *LLCL* configurations**

Figure 4.7 presents the first 50 harmonics for one inverter (a), two paralleled inverters (b), three inverters (c), four inverters (d), five inverters (e), and six inverters (f) with *LCL* filters simulated with 1 MW power per inverter with a power factor of  $PF = 1$ . In addition, the harmonic limits from Table 2.2 in section 2.5.1 are shown in the figures. As it can be seen, with the one inverter system, not all of the harmonics are below the limits. The 38<sup>th</sup>, 40<sup>th</sup>, 46<sup>th</sup>, and 50<sup>th</sup> harmonic are slightly larger than allowed, which would require some adjustment in the filter component dimensioning with this particular grid condition and in a case where the filter is used in a single inverter application. Increasing the grid-side inductor from 0.033 pu ( $50 \mu\text{H}$ ) to 0.0396 pu ( $60 \mu\text{H}$ ) would result in low enough harmonics. The higher resonance frequency and the cross-coupling resonance would still be very close to the original design value. The simulations are made with a probably worse grid voltage than it normally is, which suggests that the filtering is properly designed. The grid voltage in the simulation included 0.2 % of each odd harmonic above the 25<sup>th</sup> and 0.1 % of each even harmonic from the 26<sup>th</sup> onwards.

Subfigures (a)–(f) in Figure 4.7 show that as the theoretical calculations suggested, the attenuation is increased as  $n$  increases, which is shown by the improved harmonic content *THD*. Figure 4.7 indicates a general trend that the harmonics decrease when  $n$  increases.

However, some deviation especially in the second and fourth harmonics can be seen. There are two reasons for this: both the random noise added to the measurements and the noise added to the DC supply vary with every simulation.

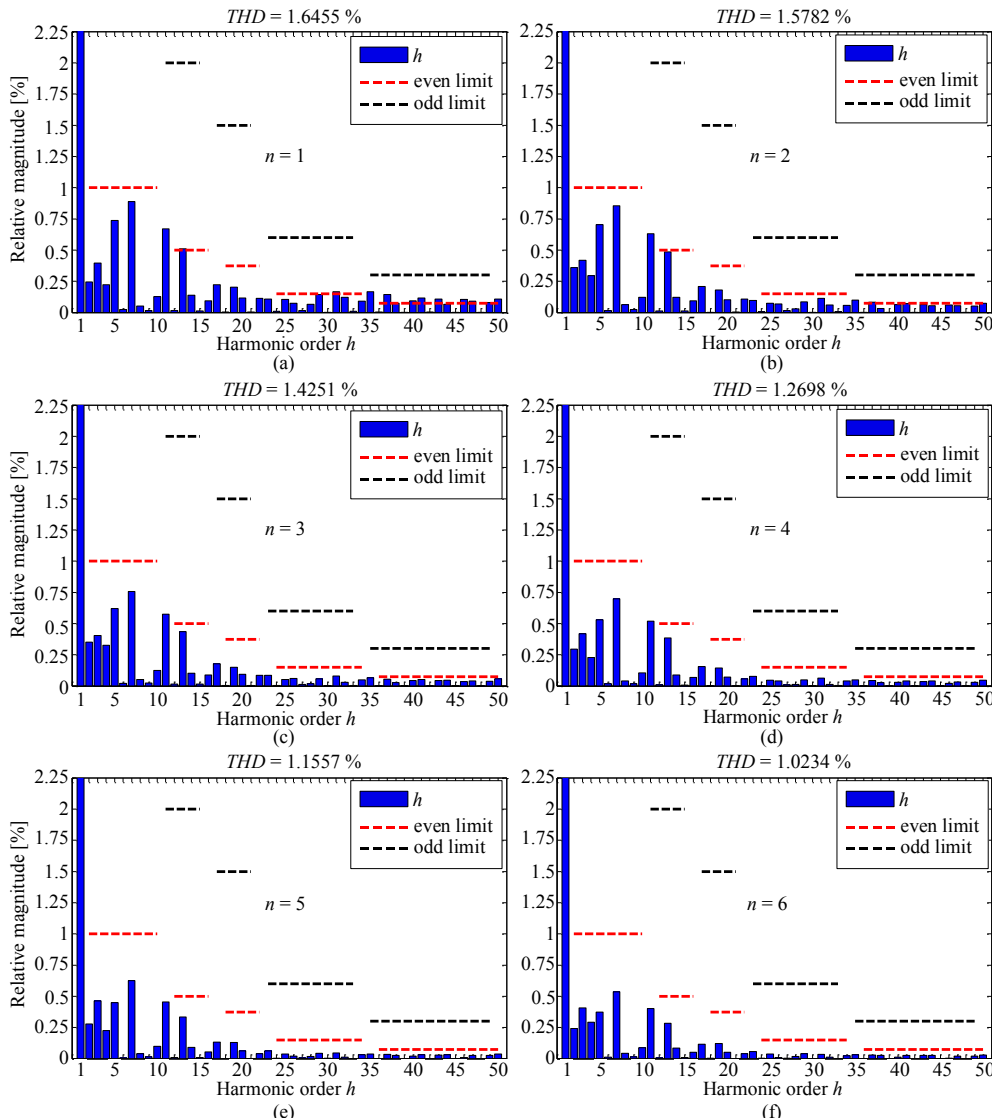


Figure 4.7 First 50 harmonics of inverter 1 with the one inverter system (a) and two (b), three (c), four (d), five (e), and six parallel-connected inverter system (f) equipped with identical  $LCL$  filters. The power factor was  $PF = 1$ , and the red and black dashed lines indicate the harmonic limits from Table 2.2.

Figure 4.8 and Figure 4.9 present the harmonic content of the  $LCL$  configuration with  $PF = 0.9_{cap}$  and  $PF = 0.9_{ind}$ , respectively.

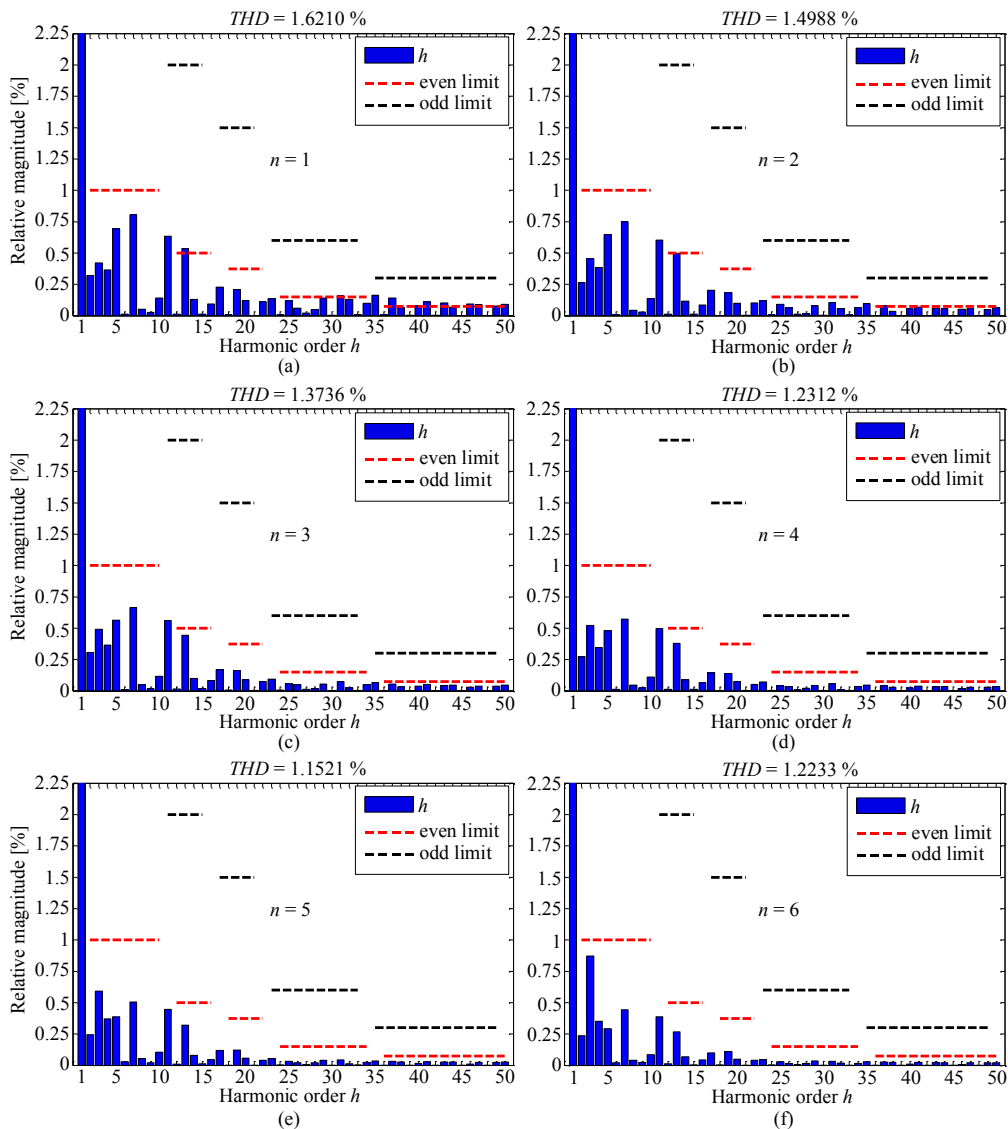


Figure 4.8 First 50 harmonics of inverter 1 with one inverter system (a) and two (b), three (c), four (d), five (e), and six parallel-connected inverter system (f) equipped with identical  $LCL$  filters. The power factor was  $PF = 0.9_{cap}$  and the red and black dashed lines indicate the harmonic limits from Table 2.2.

As can be seen from the figures, the  $THD$  is reduced when  $n$  increases except for both the capacitive and inductive power factors. With the capacitive power factor, the third harmonic seems to increase somewhat when the simulations are made with six inverters in parallel. The fifth harmonic seems to stay around the 0.75 % level for the inductive power factor when the number of paralleled inverters is increased to five and six. Similarly to the unity power factor, the single inverter results show that some of the

higher-end harmonics are over the limits, suggesting that if these harmonics existed in the grid as they were included in the simulations, the filter design would have to be adjusted for a single inverter use. However, as  $n$  increases, the filtering is improved and no harmonics exceed the limits.

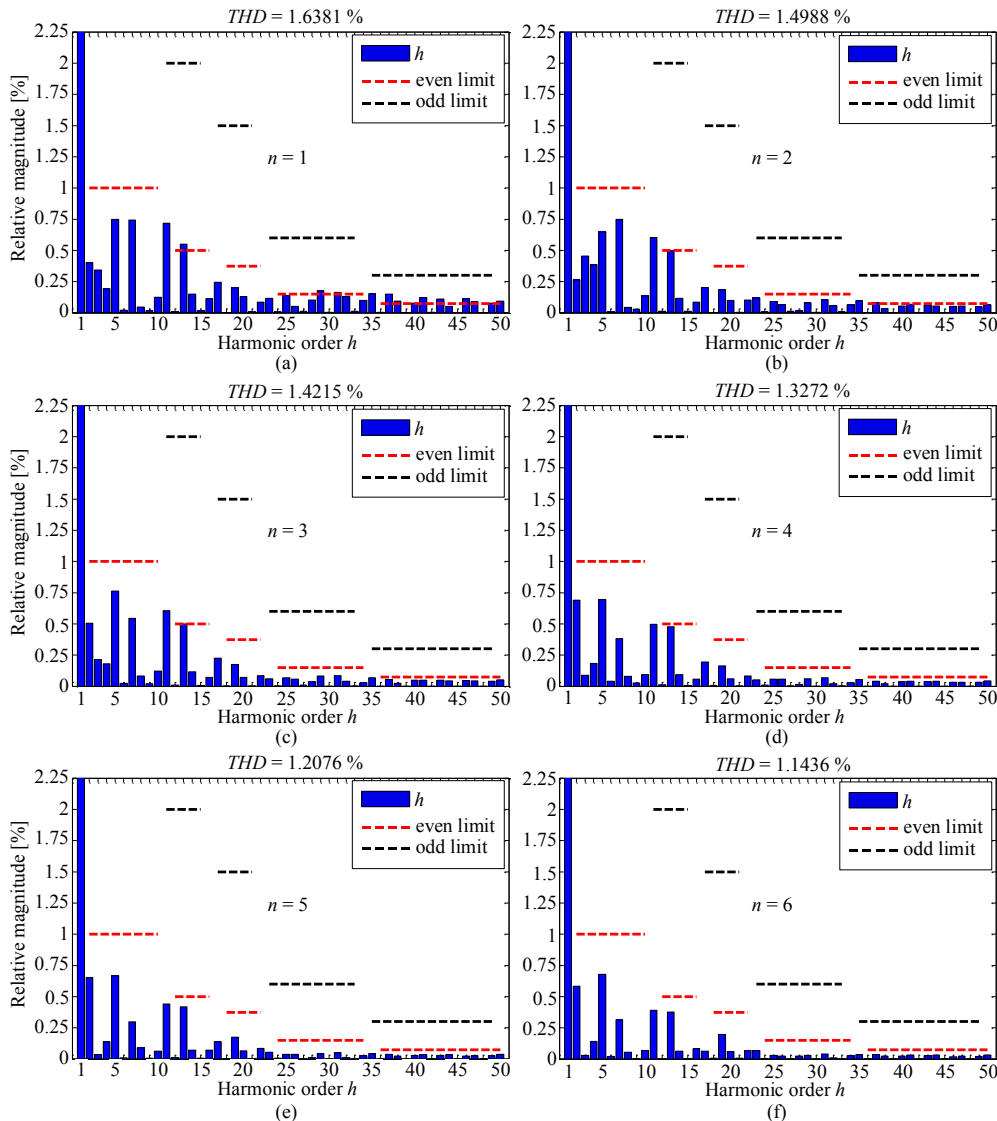


Figure 4.9 First 50 harmonics of inverter 1 with one inverter system (a) and two (b), three (c), four (d), five (e), and six parallel-connected inverter system (f) equipped with identical  $LCL$  filters. The power factor was  $PF = 0.9_{ind}$  and the red and black dashed lines indicate the harmonic limits from Table 2.2.

The harmonic content of the  $LCL$  configuration looks very similar to the  $LCL$  configuration presented in Figure 4.7, Figure 4.8, and Figure 4.9 making it more

worthwhile to look at the *THD* itself for comparison. Figure 4.10 presents the *THD* of the inverter 1 current after the filter  $i_{21}$  for both configurations with the three simulated power factors. As it can be seen, the *THDs* are very similar for both. The *LLCL* configuration presents a slightly better *THD* over the whole range of  $n$ . Furthermore, for the *LLCL* configuration, the inductive power factor case does not exceed the capacitive power factor case in the low range of  $n$  as it does with the *LCL* configuration. The *LLCL* configuration generally presents a better *THD*, but both configurations can be determined to be close to each other and well below the limits in the standards.

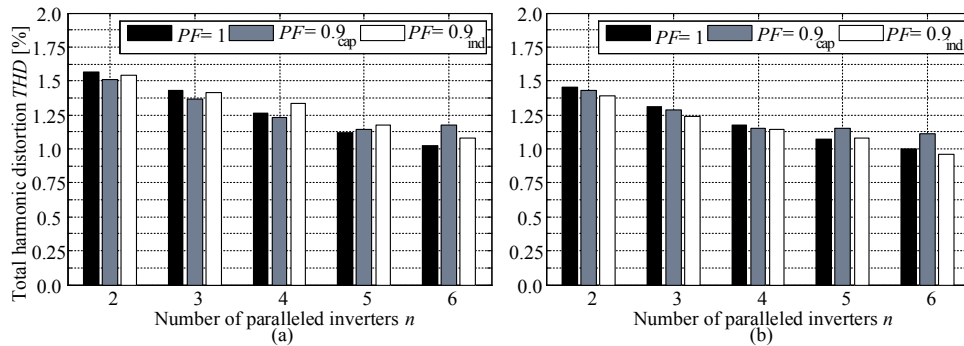


Figure 4.10 THD of the inverter 1 current  $i_{21}$  after the filter in the *LCL* configuration (a) and *LLCL* configuration (b) while  $n$  goes from  $n = 2-6$  with the three different power factors used in the study.

As the main difference between the two configurations considered here is the switching frequency attenuation, these frequencies should also be observed even though the standard *THD* calculation does not require it. Figure 4.11 presents the first 65 harmonics of the grid-injected current of the single inverter with the *LCL* filter (a) and the *LLCL* filter additional resonance damped and undamped overlapped (b) with the unity power factor driving nominal power to the grid. As it can be seen, around the 60<sup>th</sup> harmonic the

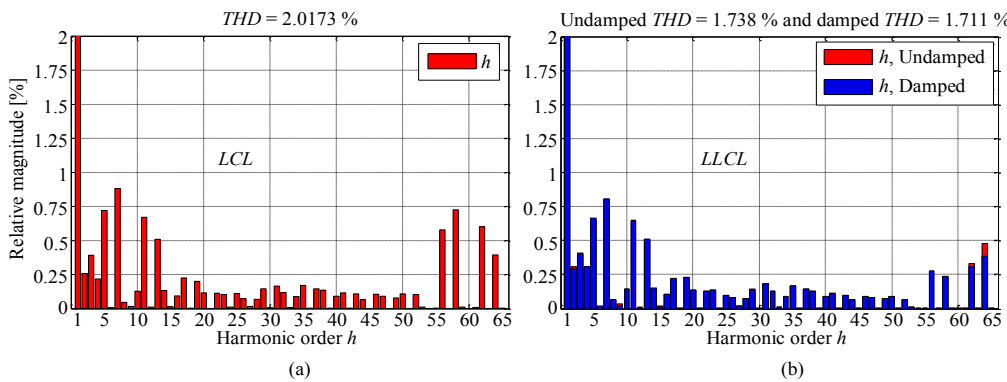


Figure 4.11 First 65 harmonics of the single inverter grid-side current with the *LCL* filter (a) and with the *LLCL* filter (b) with the unity power factor and 1MW power. The switching frequency was 3 kHz =  $60f_1$ . The *LLCL* filter  $L_C$  included a 100 mΩ damping resistor in the damped case.

switching frequency sideband harmonics 56<sup>th</sup>, 58<sup>th</sup>, and 62<sup>nd</sup> are attenuated more with the *LLCL* filter. The 64<sup>th</sup> harmonic is larger with the undamped *LLCL* filter, because after the third resonance frequency of the filter, the attenuation becomes lower compared with the *LCL* filter, whose attenuation increases at the rate of 60 dB/dec, whereas the *LLCL* filter attenuation increases with the rate of 40 dB/dec after  $f_{r3}$ . This can be seen from Figure 4.12 presenting the current harmonic attenuation Bode magnitude plot of the *LCL* filter and the *LLCL* filter without and with additional *LC* circuit damping. As it can be seen, without damping the resonance frequency  $f_{r3}$ , the *LLCL* filter attenuation around the 64<sup>th</sup> harmonic is larger compared with the *LLCL* filter than with the *LCL* filter with the same parameters. In addition to the better attenuation around the switching frequency, it can be stated that the *LLCL* configuration presents a slightly better attenuation in the lower frequency range, which can be seen from the better THD calculated with the first 50 harmonics shown in Figure 4.10.

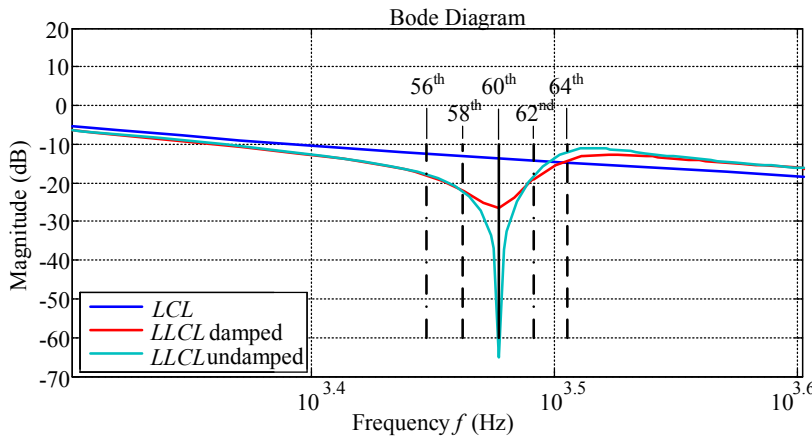


Figure 4.12 Current harmonic attenuation  $i_2/i_1$  around the switching frequency of the *LCL* and *LLCL* filters with the slightly damped  $f_{r3}$  resonance (red) and the undamped  $f_{r3}$  resonance (cyan). The additional damping resistor value was set to 100 mΩ. The switching frequency and its sideband harmonics are also shown in the figure.

As already shown by Figure 4.8, with the capacitive power factor, the third harmonic increases with  $n = 5$  with the capacitive power factor. The reason for this can be found from the modulator used and the decline of the modulation index with the capacitive power factor.

Figure 4.13 presents the vector diagram of the grid-connected inverter with the *LCL* filter driving power to the grid with a power factor of  $PF = 0.9_{cap}$ . The PCC voltage  $u_2$  is at an angle of 0° with an amplitude of 1 pu. The grid-injected current  $i_2$  has an amplitude of 1 pu and the angle of  $\text{acos}(0.9) = 25.8419^\circ$ . The nominal *LCL* filter parameters are used to calculate the voltage drops over the inductors. As it can be seen, driving capacitive reactive power to the grid forces the inverter terminal voltage  $u_1$  to be smaller compared

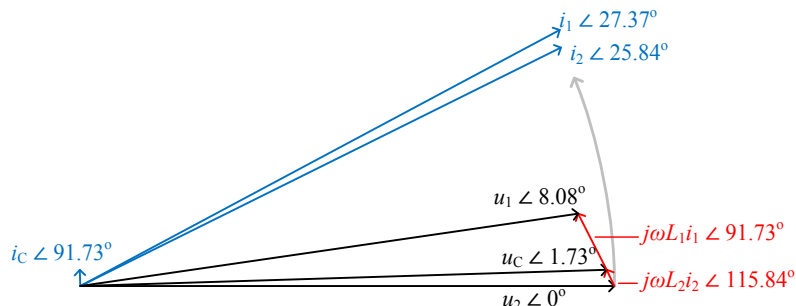


Figure 4.13 Vector diagram of the grid-connected inverter equipped with an  $LCL$  filter supplying current to the grid with a power factor of  $PF = 0.9_{cap}$ . The PCC voltage  $u_2$  and the grid-injected current  $i_2$  are 1 pu. The grey arch is a section of the full circle drawn with a radius of  $|u_2|$ . The figure is not made completely accurate but merely to illustrate the change in the voltage amplitude because of the capacitive power factor.

with the grid voltage. Calculating with  $L_1 = 0.1142$  pu and  $L_2 = 0.033$  pu, the length of  $u_1$  is around 94 % of the length of  $u_2$ . Further, the DC link injected current in the simulations included variation, which leads to variation in the DC link voltage. The increased DC link voltage together with the decreased reference voltage resulting from the capacitive power factor can lead to a situation where the modulation index becomes low enough to cause an increase in the produced harmonics.

Figure 4.14 presents the harmonics from the third to the 11<sup>th</sup> harmonic produced by the space vector modulator used in the simulations, the modulation index being  $m = 0.525 - 1.0$  with steps of 0.025. It is noteworthy that here the modulation index is a relation between the sinusoidal reference voltage amplitude and the carrier wave amplitude before the triangle wave of the space vector modulation is subtracted from the reference voltage.

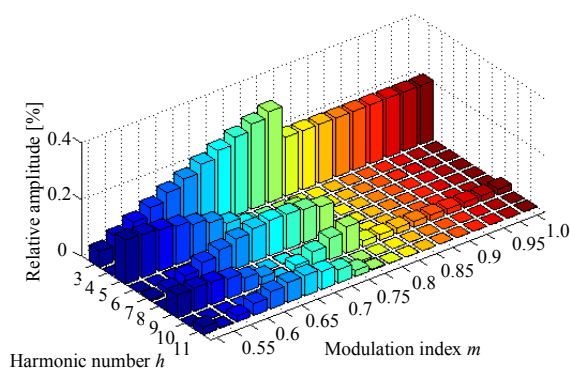


Figure 4.14 Voltage harmonics from the third to the 11<sup>th</sup> harmonic of the SVM used in simulations with the modulation index going from  $m = 0.525 - 1.0$  with steps of 0.025. The safe time and its compensation is included, and the current used in the compensation is the nominal current with the phase shift corresponding to  $PF = 0.9_{cap}$ .

As can be seen, the harmonics increase significantly when the modulation index is below 0.8. Even the third harmonic is increased, although it starts to decrease. However, at the low end of the range of  $m$ , the third harmonic becomes a high-amplitude component in the output of the modulator again.

Figure 4.15 presents the energies of the single filter in the *LCL* and *LLCL* configurations with identical filters. A comparison of the component energies shows that they are very similar between the two configurations. Computation of the difference shows that the *LLCL* configuration has a marginally larger energy stored in the filter components but the difference is of the magnitude of 0.0001. When the harmonics up to the 65<sup>th</sup> are considered, including the switching frequency side band harmonics, it can be seen that the energies are increased only slightly. Considering the operation of grid-connected inverters, this outcome is quite sensible; the most energy must be driven at the fundamental or the system efficiency will be poor. It can be seen from Figure 4.15 that the *LLCL* configuration does not benefit from the better attenuation over the switching frequency. On the other hand, it does not suffer from the additional capacitor branch inductor.

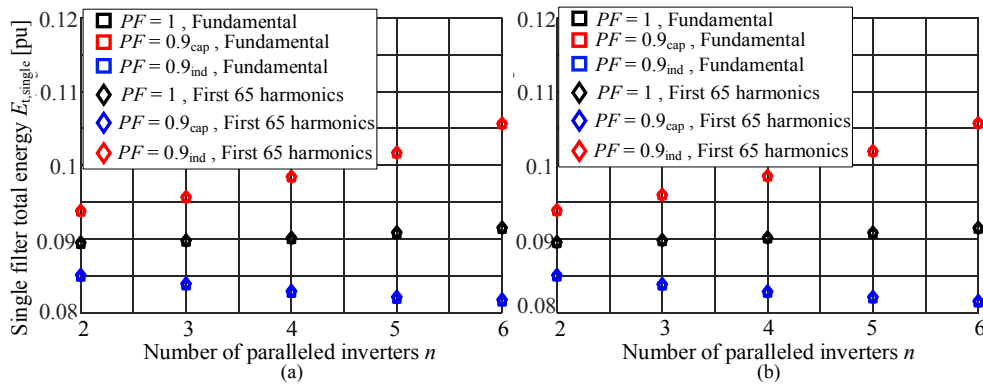


Figure 4.15 Simulated single inverter component total energies for the *LCL* configuration (a) and (b) and the *LLCL* configuration with the fundamental only (squares) and with the first 65 harmonics to include the switching frequency in the calculation (diamonds).

### LC and LC+L configurations

Figure 4.16 presents the simulated *THD* of current after the capacitor  $i_{21}$  of the *LC* configuration (a) and the *LC+L* configuration. As can be seen, the *LC+L* configuration presents a better *THD* compared with the *LC* configuration because of its additional grid-branch inductor. The *LC+L* configuration requires an increase in the DC link voltage for the inductive power factor. This is due to the common grid-side inductor, which in this identical filter case is multiplied by  $n$ . For this reason, the simulations with  $n = 3\text{--}6$  were performed with increased voltage levels; 1130 V, 1175 V, 1195 V, and 1220 V, respectively. As a result of these increases, the harmonics, especially the switching frequency harmonics, are increased, but as expected from the theory, the *THD* is

improved with all power factors when  $n$  is increased because of the multiplication of the grid branch. Furthermore, the inverter switching losses and the voltage stress over the semiconductor devices are increased with the DC link voltage, which would be a negative aspect.

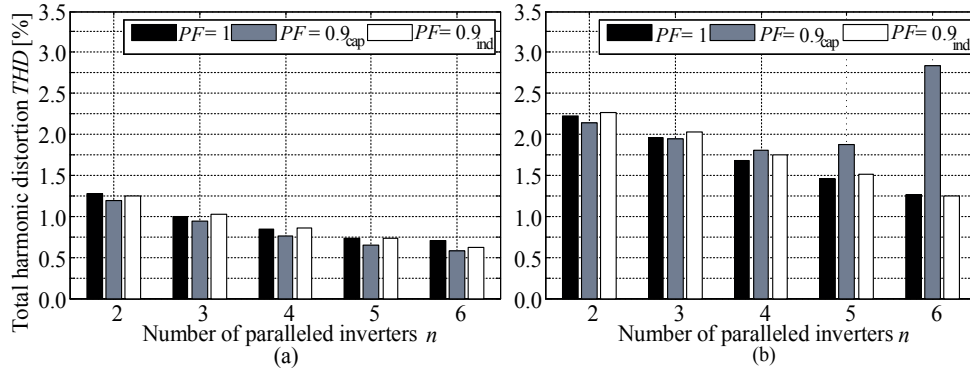


Figure 4.16 Simulated THD of the inverter 1 current  $i_{21}$  after the filter in the  $LC$  configuration (a) and the  $LC+L$  configuration (b) while  $n$  goes from  $n = 2\text{--}6$  with the three different power factors used in the study.

The  $LC$  configuration shows a decreasing THD for the unity power factor and the capacitive power factor, but with the capacitive power factor the THD starts to increase with  $n = 5$  and 6. This increase is due to the high DC link voltage and the low modulation index causing excess harmonics. Again, when looking at the THD of the grid-injected current, we can see that also the inductive power factor presents an increasing THD whereas the  $LC+L$  configuration presents a very similar THD for  $i_g$  as it shows for  $i_{21}$ .

Figure 4.17 presents the energies of the  $LC$  components of a single filter in the  $LC$  and  $LC+L$  configurations. As it can be seen, the plain  $LC$  filter stores more energy in  $L_1$  and  $C_f$  with the unity and capacitive power factors than the  $LC+L$  configuration  $LC$  part. This takes place even with the larger DC link voltages of the  $LC+L$  configuration. As with the  $LCL$  and  $LLCL$  configurations, including harmonics up to the 65<sup>th</sup> does not significantly increase the energies.

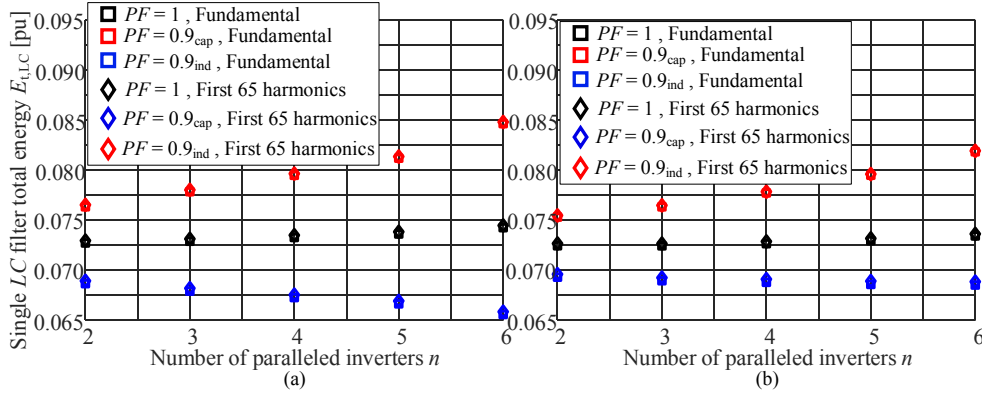


Figure 4.17 Simulated single LC filter total energies for the LC (a) and LC+L (b) configurations.

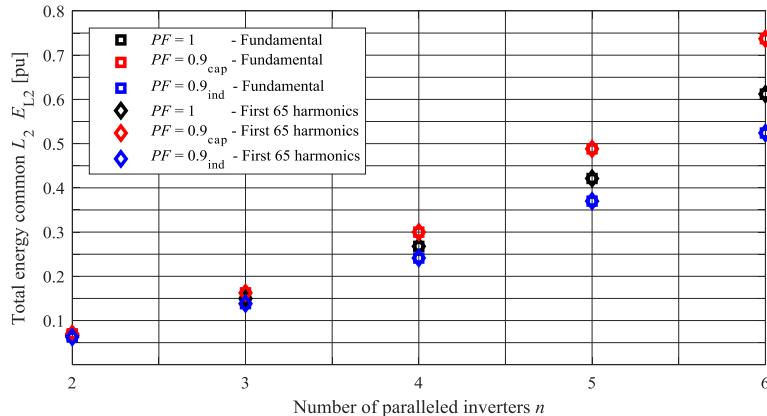


Figure 4.18 Simulated energy of the common grid-side inductor  $L_2$  of the LC+L configuration.

It has to be borne in mind that the  $LC+L$  configuration also has a common grid-side inductor, whose energy is huge compared with the rest of the components. This is naturally due to the summed current flowing through the inductor. Figure 4.18 presents the simulated energy of the common grid-side inductor of the  $LC+L$  configuration. The energy of the common grid-side inductor can be decreased by scaling it smaller by the factor  $1/n$  as was done in (Juntunen et al., 2015). By doing this, the energy of the common  $L_2$  increases ideally with the factor of  $n$  whereas with constant inductance, the increase is  $n^2$ . Scaling the inductance down on the grid side has an effect on the inverter-side inductor energy and the capacitor energy. As the grid-side inductor decreases, the filters, quite naturally, move towards the  $LC$  configuration. The outcome is more energy stored in the  $LC$  components of the  $LC+L$  configuration.

### L-configuration

Figure 4.19 presents the simulated *THD* of the grid-injected current of the *L*-configuration with the number of paralleled inverters being  $n = 2\text{--}6$ . When the switching frequency side bands are not included in the calculation in Figure 4.19(a), the *THD* decreases as  $n$  increases with the unity and  $0.9_{\text{cap}}$  power factors. However, with the  $0.9_{\text{ind}}$  power factor, the *THD* becomes worse as  $n$  increases. When the switching frequency side bands are added in Figure 4.19(b), the *THD* with the inductive power factor increases even more, and the *THD* increases also with the unity power factor, but with the capacitive power factor the *THD* decreases at  $n = 2\text{--}4$  and increases when the fifth inverter is added to the system. Finally, the *THD* seems to decrease again with the six inverters in parallel.

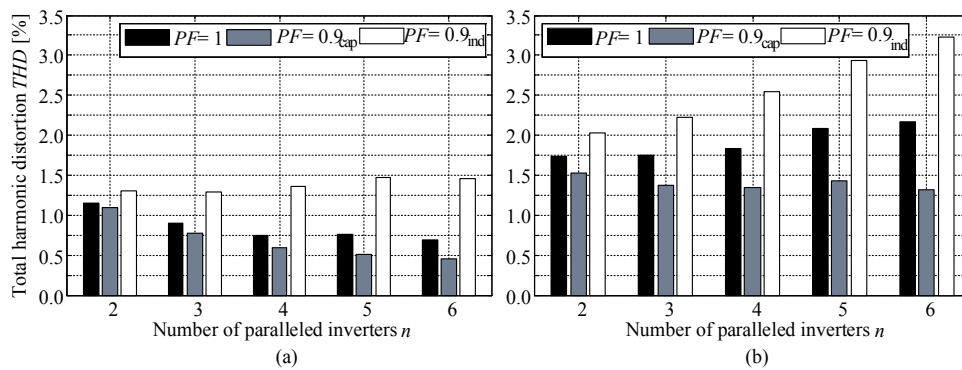


Figure 4.19 Simulated *THD* of the inverter grid-injected current  $i_g$  after the filter of the *L*-configuration with first 50 harmonics (a) and the first 64 harmonics (b) while  $n$  goes from  $n = 2\text{--}6$  with the three different power factors used in the study.

The main reason behind the *THD* getting worse is that the capacitor of the *L*-configuration remains the same leading to current harmonic attenuation staying the same. With the other configurations the attenuation after the higher resonance frequency  $f_{l2}$  becomes better when  $n$  increases. As more inverters are connected in parallel, the harmonics injected to the grid also increase and the original capacitor cannot handle all of the filtering needed in this case.

Figure 4.20 presents the first 65 harmonics of the *L*-configuration grid-injected current of the  $0.9_{\text{ind}}$  power factor with  $n = 6$  for both the original 0.03 pu capacitor (a) and the sixfold larger 0.18 pu capacitor (b). As can be seen, when the capacitor is small compared with the power of the application, the switching frequency harmonics injected to the grid are large. The 56<sup>th</sup> and 58<sup>th</sup> harmonics with the small capacitor are over 1.5 % and 2.0 %, respectively. From the harmonic limit tables in section 2.5.1, we can see that the standards do not present any limits for the harmonics above the 40<sup>th</sup> (IEC) or the 50<sup>th</sup> (IEEE) standards. However, high amounts of the switching frequency harmonics injected to the grid would not be a desired solution and also inconsistent with the idea of filtering in the first place. Instead, the switching frequency harmonics should be as small as possible. For

for this reason, the  $L$ -configuration naturally requires a capacitor that is increased proportionally to the value of  $n$ .

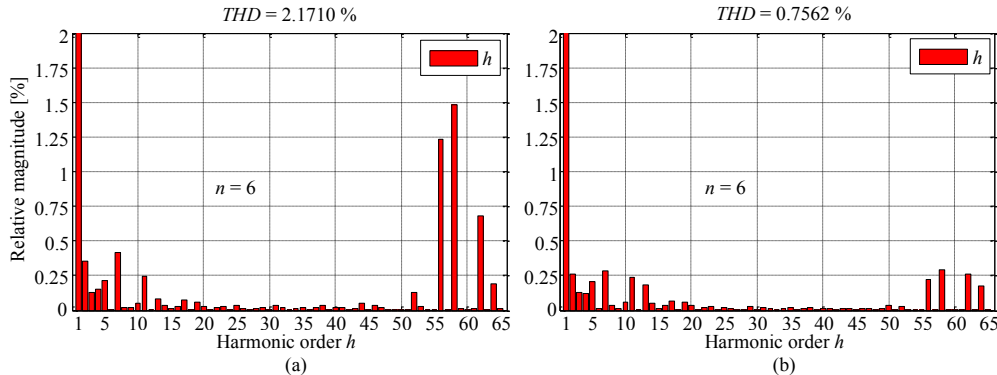


Figure 4.20 Simulated harmonics of the grid injected current  $i_g$  after the filter of the  $L$ -configuration with the original capacitor  $C_f = 0.03\text{pu}$  (a) and with the  $n$ -times larger capacitor  $C_f = 0.18\text{pu}$  (b) with  $n = 2\text{--}6$  and the power factor of  $0.9_{\text{ind}}$ .

Figure 4.21 presents the  $THD$  of  $i_g$  of the  $L$ -configuration with 50 harmonics (a) and with 65 harmonics (b) when the filter capacitor is increased with a relation of  $nC_f$  as  $n$  increases. As can be seen, the  $THD$  becomes better as the capacitor is increased, which is quite natural because an increase in the capacitor has a direct, proportional impact on the attenuation. Figure 4.21(a) shows that without the switching frequency harmonics, the capacitive power factor has always the lowest  $THD$ , whereas the difference between the unity power factor case and the capacitive power factor case becomes smaller when  $n$  increases. With the switching frequency harmonics included, the difference between these two power factor cases seems to remain more or less the same.

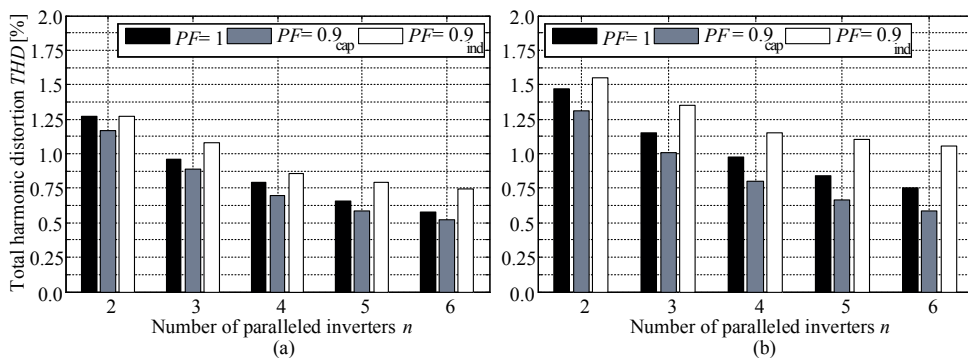


Figure 4.21 Simulated  $THD$  of the inverter grid-injected current  $i_g$  after the filter of the  $L$ -configuration whose capacitor increases with a relation of  $nC_f$  with the first 50 harmonics (a) and the first 65 harmonics (b) with  $n = 2\text{--}6$  and with the three different power factors used in the study.

The inductive power factor seems to decrease slightly less when the switching frequency harmonics are included in the calculation. In addition, the difference from the other two

power factor cases increases compared with the 50 harmonics case. An obvious reason why the inductive power factor shows a smaller decrease in the THD with 65 harmonics is that the DC link voltage had to be raised in the simulations similarly as for the  $LC+L$  configuration; 1130 V, 1175 V, 1195 V and 1220 V, respectively, for  $n = 3\text{--}6$ .

Figure 4.22 presents the simulated energies of the individual  $L_1$  inductors of the  $L$ -configuration with the capacitor staying at a constant value (a) and with the capacitor increased as  $nC_f$  (b). As can be seen, increasing the capacitor results in a larger energy stored in the  $L_1$  inductors. Further, when increasing the capacitor, the energy with the unity power factor increases, while with the constant capacitor it decreases. Similarly, with the inductive power factor case, the energy decreases more compared with the constant capacitor case. If the  $L$ -configuration is designed as a modular system where more inverters can be connected in parallel and only the capacitor (and perhaps the  $L_2$  inductor) is changed, the  $L_1$  inductors have to be designed keeping in mind the largest possible energy with respect to component optimization. A practical approach to this design would be to set a particular limit for the number of paralleled inverters for which the  $L_1$  design is sufficient.

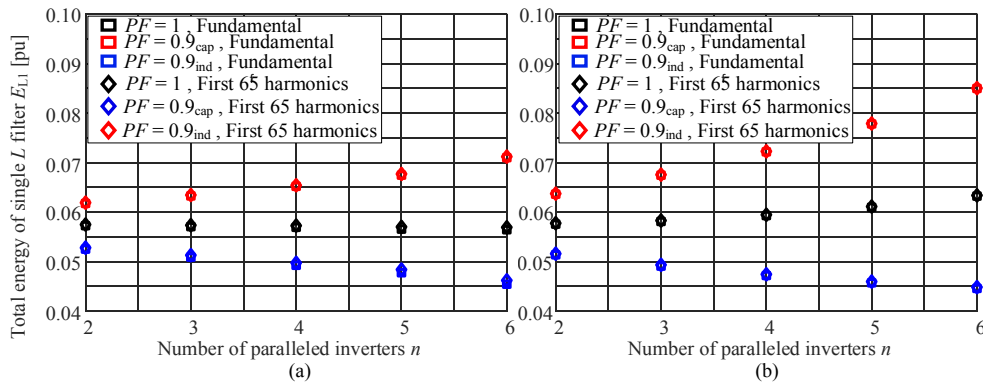


Figure 4.22 Simulated energy of the individual  $L_1$  inductors of the  $L$ -configuration; (a) energy with the original capacitor and (b) energy with the capacitor increased with the ratio of  $nC_f$ .

As with the  $LC+L$  configuration, the common grid-side inductor energy becomes very high as  $n$  increases. This component dominates the configuration energy especially with the larger number of paralleled inverters. Figure 4.23 presents the filter capacitor energies with the nominal capacitor (a) and with the  $nC_f$  capacitor (b). A comparison of the energies of the filter capacitor shows that when the capacitor is increased, the energy of the component increases, whereas the capacitor energy of the constant capacitor may even decrease along with  $n$ . The lower grid-side voltage of the capacitive power factor reduces the rate of capacitor energy increase for both scenarios.

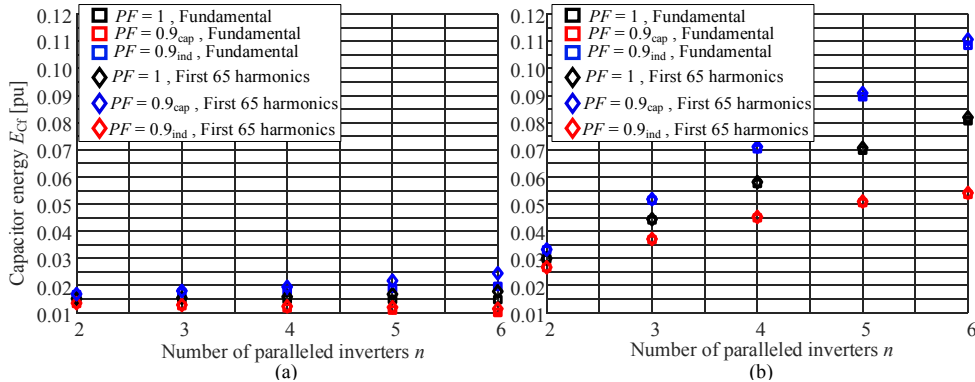


Figure 4.23 Simulated energy of the filter capacitor of the *L*-configuration; (a) energy with the original capacitor and (b) energy with the capacitor increased by the ratio of  $nC_f$ .

The comparison of the simulated and calculated energies shows that the varying PCC voltage and the grid-injected current in the power control mode applied cause an error between the simulated and calculated energies. Figure 4.24(a) shows that with the capacitive power factor the simulated energies are larger than the calculated ones, whereas with the inductive power factor the situation is the opposite. The unity power factor case is close to the calculated one. A similar error is present also in all the other filter configurations.

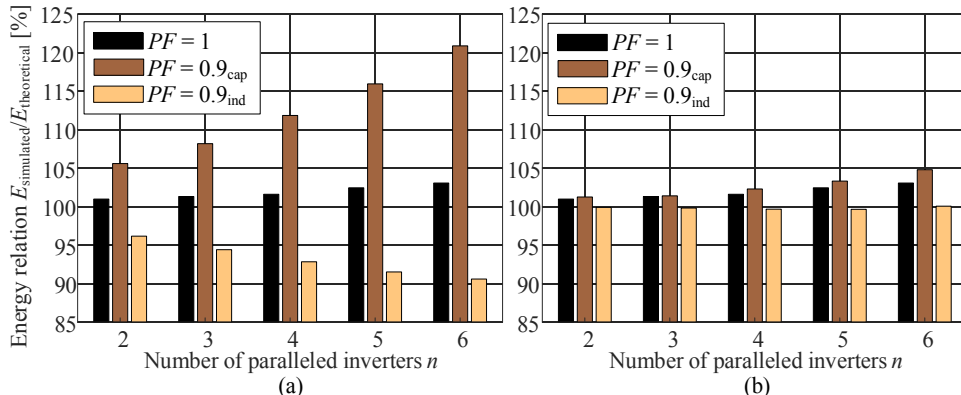


Figure 4.24 Simulated fundamental frequency energies of a single inverter in the *LCL* configuration compared with the calculated energies without any error compensation (a) and with error compensated in calculation (b).

If the voltage change at the PCC is compensated in the calculations, the difference between the simulations and the calculations becomes small. Figure 4.24(b) presents the simulated energy of a single filter in the *LCL* configuration compared with the voltage-compensated calculated energy. As can be seen, the difference is small and remains  $\leq 5\%$  for each case in the figure. However, there is still an error between the simulations and the calculations caused by the noise in the measurements, variation in the DC link input

currents, and harmonics in the grid voltage. If these are removed from the simulations, the difference is reduced to less than 1 %.

The voltage can be compensated for by using the factor of  $\sqrt{1 \pm L_g n}$ , depending on the power factor case used. This factor was found to work for all but the *L*-configuration, which required the use of  $(1 \pm L_g n)$  instead. For the *LLCL*, *LC*, and *LC+L* configurations, the effect of the compensation is similar to the *LCL* but with the *L*-configuration, the error increases towards a larger number of  $n$  as depicted in Figure 4.25.

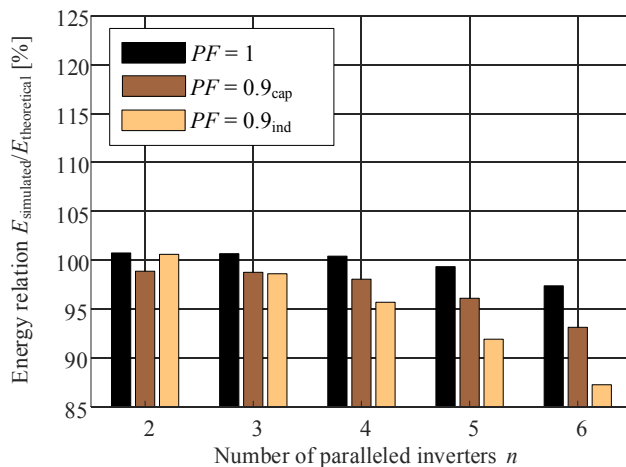


Figure 4.25 Simulated fundamental frequency energies of the *L*-configuration compared with the calculated energies with the error compensated in the calculation.

### Key findings

- The simulations show that the *THD* becomes better as the number of inverters increases.
- The *LLCL* configuration presents the best *THD* and the *LC* configuration the worst.
- The difference between the *LCL* and *LLCL* configurations is very small.
- The required DC link voltage is increased for the *LC*, *LC+L* and *L*-configurations, which lack the individual grid-side inductor.
- The *L*-configuration shows that to keep the switching frequency harmonics low enough, the capacitor has to be increased, for instance by the number of paralleled inverters.
- With the open-loop power control, the increased PCC voltage (inductive power factor case) causes a smaller current than in the calculations, whereas the decreased PCC voltage results in a larger current than in the calculations.

- The differences in the currents and voltages compared with the theoretical calculations result in different energies between the simulations and the calculations.
- If the voltage change is taken into account in the calculations, the simulated and calculated energies become very well aligned when empirically found factors are used.
- For the  $LCL$ ,  $LLCL$ ,  $LC$ , and  $LC+L$  configurations, the voltage compensation factor  $\sqrt{1 \pm L_g n}$  is appropriate, and for the  $L$ -configuration  $(1 \pm L_g n)$  is good.

#### 4.2.3 Distinct filter values

The filter configurations were simulated with random tolerances between  $\pm 20\%$  of the nominal value. The function *rand* generates pseudorandom numbers uniformly distributed in a certain interval. Numbers from the specified interval of  $(a,b)$  can be generated by computing

$$r = a + (b-a) * \text{rand}(N, 1),$$

where  $a$  is the start of the interval,  $b$  is the end of the interval, and  $N$  is the number of numbers generated (rows in a vector). Naturally, the equation works with  $a$  and  $b$  reversed. To achieve a high level of randomness, the tolerances for each component were calculated over 3 million times.

The tolerances were added by multiplying the component by its corresponding tolerance. Because the components had only  $1 \mu\Omega$ , the resistances were not added with any tolerance excluding the damping resistor  $R_d$  and the  $LLCL$  filter second damping resistor  $R_{d2}$ . In addition to the filter components, the DC link capacitors were provided with tolerance. For the common components such as the common  $L_2$  and  $C$  of the  $LC+L$  configuration and the  $L$ -configuration, the corresponding tolerances of inverter 1 were used. Table 4.2 presents the tolerances.

Table 4.2. Tolerances used in the simulations per component and inverter number.

Inverter	$\Delta_{L1}$	$\Delta_{L2}$	$\Delta_{Cf}$	$\Delta_{Cd}$	$\Delta_{Rd}$	$\Delta_{LC}$	$\Delta_{Rd2}$	$\Delta_{CDC}$
1	1.0033	0.8149	1.1705	1.1707	0.9036	0.8741	1.0886	0.8171
2	0.9579	1.1460	1.1439	0.8376	1.1255	0.8377	0.9812	1.0058
3	1.0133	1.1353	0.9481	0.8915	1.0909	1.1492	0.8170	0.8799
4	1.0246	1.1508	1.1261	0.8596	0.8048	0.8346	0.8140	1.1432
5	0.9030	0.8244	1.0216	0.8806	1.1366	0.9471	1.1370	1.0313
6	1.1465	0.8713	1.1611	0.8033	0.8225	1.1610	0.8118	0.8337

**LCL and LLCL configurations**

First, the simulations were made controlling all of the inverters with the inverter 1 control and with synchronized carriers to prevent circulating common-mode current from flowing between the inverters. Figure 4.26 presents the simulated *THD* of the current after the filter of the *LCL* and *LLCL* configurations with tolerances. The inverter 1 control and reference voltages were used for all inverters. The colour corresponds to the number of inverters in parallel. For instance, the inverter 1 current  $i_{21}$  is present in all simulations, whereas the inverter 6 current  $i_{21}$  is present only in the simulation with six parallel-connected inverters.

Two main observations can be made from the figures. First, the *THD* decreases like with the identical filters when  $n$  is increased. Second, the resulting *THD* differs between the inverters as was expected.

Even though the different filter values make the grid multiplication to vary from  $n$  like in the case of identical filters, the effect of tolerances is still small enough to cause an increase in the attenuation when more inverters are connected in parallel. Not only the different attenuation affects the *THD*, but also because the inverters were connected together from the DC link in the simulations, the powers fed to the grid, that is, the grid-side currents, are not equal either, and naturally, also not the inverter-side currents. For instance, for those inverters that drive a larger power than the reference to the grid than the nominal, the *THD* is smaller than for those that drive a smaller power than the reference.

The different powers in the simulation are a direct result of using only one controller and gate signals for all inverters. Figure 4.27 presents the simulated active and reactive powers of two parallel-connected inverters; inverter 1 and 5 and the respective references for both powers. The inverter 1 control was used to control both inverters, which also had their DC links connected together. Both the inverter DC links were fed with the same  $I_{DC} = 822.92$  A. The active power reference was  $P_{ref} = 900$  kW and reactive power reference  $Q_{ref} = 435.89$  kVAr resulting in a total of 1000 kVA of apparent power.

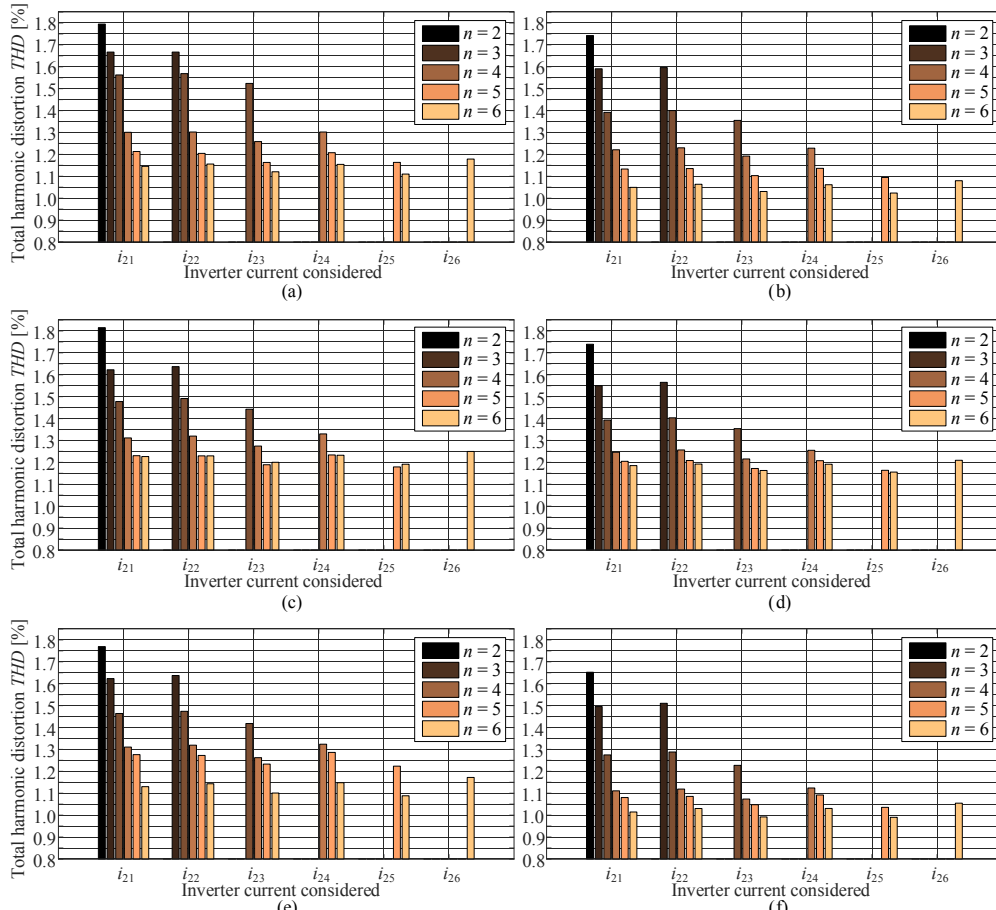


Figure 4.26 Simulated THD of the grid-injected current of the LCL and LLCL configurations with tolerances in the filter components and the DC link capacitors; (a) LCL with PF = 1, (b) LLCL with PF = 1, (c) LCL with PF = 0.9<sub>cap</sub>, (d) LLCL with PF = 0.9<sub>cap</sub>, (e) LCL with PF = 0.9<sub>ind</sub>, and (e) LLCL with PF = 0.9<sub>ind</sub>. The inverter 1 control was used for each inverter with synchronized carriers.

As can be seen from Figure 4.27(a), the powers are not equal, as expected. The different filter values result in greater active and reactive powers driven by inverter 5 when the inverters share a common DC link and are controlled with the inverter 1 control. Because the filters are not identical, the grid-side powers differ as can be seen from the figure. Because the inverters were connected in parallel from the DC link, the system balances it through this connection. The inverters can be controlled to drive the same power to the grid as Figure 4.27(b) depicts. The balancing control was performed by controlling the current differences to zero with PI controllers. It is assumed that the inverter control systems measure only the inverter-side currents, and thus, the balancing was carried out on the inverter side of the filters. Naturally, the different filters still cause different powers, and more precise balancing could be carried out by using the grid-side current should it be measured or estimated. However, with the maximum tolerances in the

components, the capacitors would draw reactive power between 2.5–3.75 per cent of the nominal power from the grid.

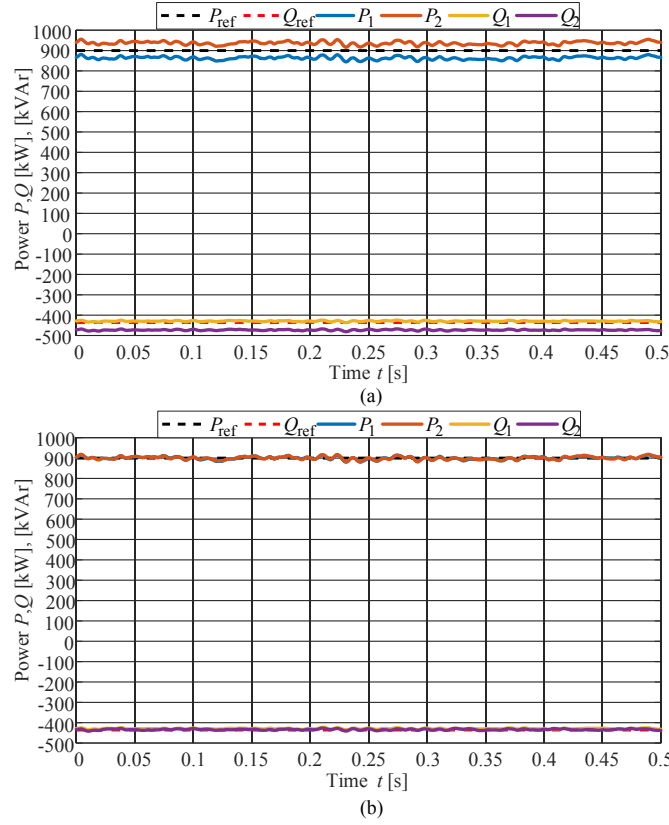


Figure 4.27 Simulated powers for two paralleled inverters with the  $LLCL$  filters; inverter 1 and inverter 5. (a) with inverter 1 control for both and (b) with inverter 1 control and output powers balanced. The power factor in the simulation was  $0.9_{\text{cap}}$ .

Figure 4.28 presents the circulating current rms mean value over 0.5 s for the  $LCL$  configuration with  $n = 2\text{--}6$ . The power factor was unity. In Figure 4.28(a), inverter 1 control was used for all directly, and in Figure 4.28(b) the output powers were balanced. It can be seen that without balanced powers, the circulating current remains very small, in any of the cases, less than 1 %. When the balancer is turned on, the circulating current becomes much larger. While inverter 6 shows the highest circulating current without the balancer, inverter 5 and its tolerances stand out in the balanced case.

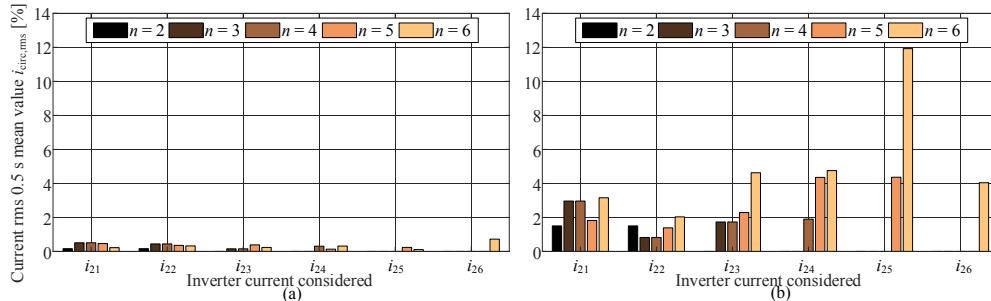


Figure 4.28 Simulated circulating currents with the *LCL* configuration with  $PF = 1$  and (a) no balancer and (b) with a balancer.

Owing to the tendency of the other inverters to drive circulating current into the inverter with the lowest impedance on the circulating current path, the inverter 5 output *THD* becomes the worst in the simulations. Figure 4.29 presents the *THD* of the *LCL* and *LLCL* configurations with tolerances when the output powers are balanced. It can be seen that the general trend is decreasing although inverter 5 suffers from the others. For the unity and capacitive power factors, the fifth inverter *THD* gets worse when inverter 6 is added to the system, whereas with the inductive power factor, the effect is opposite.

The influence of the circulating current clearly shows the importance of minimizing it. The use of one inverter control for all inverters, including a minimization algorithm for circulating current, is perhaps the most straightforward option. Because in the simulations the carriers were synchronized, the case with the inverter 1 control used for all inverters is close to this case. The circulating current both degrades the output *THD* and results in larger losses in the components if not controlled to be as small as possible. The filter components, especially the inductors, would have to be designed larger, which hardly is the aimed solution.

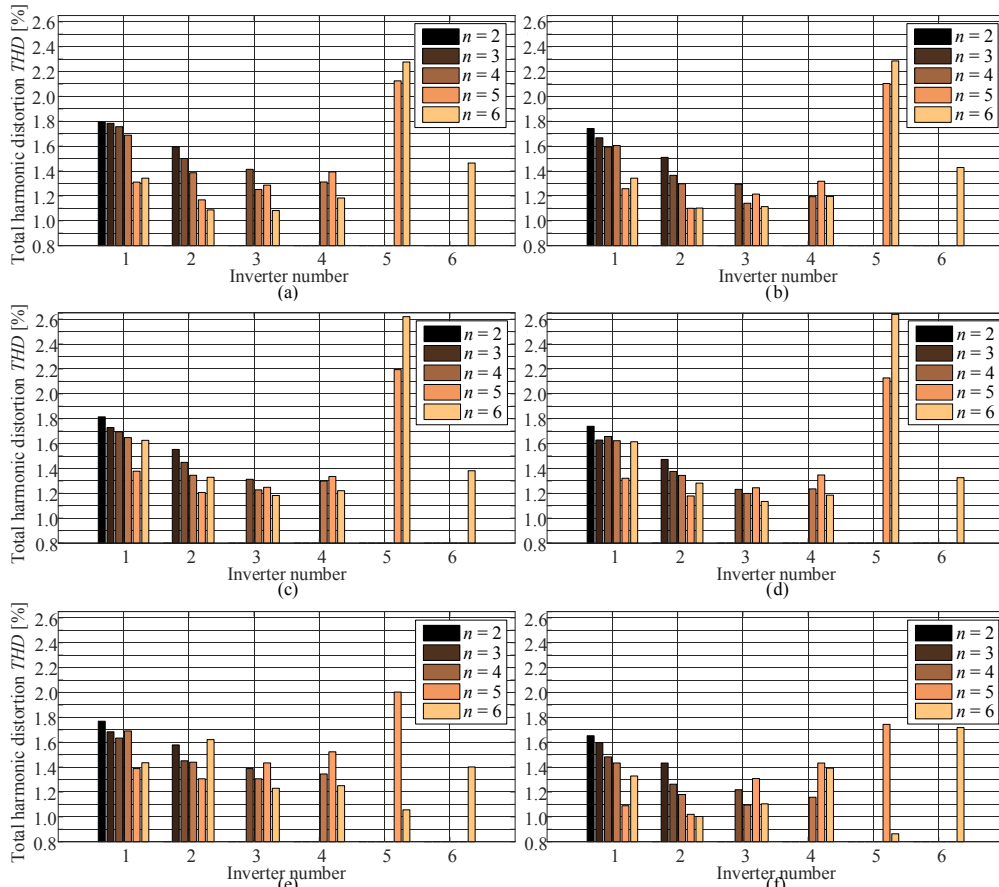


Figure 4.29 Simulated THD of the grid-injected current of the *LCL* and *LLCL* configurations with tolerances in the filter components and the *DC* link capacitors; (a) *LCL* with  $PF = 1$ , (b) *LLCL* with  $PF = 1$ , (c) *LCL* with  $PF = 0.9_{cap}$ , (d) *LLCL* with  $PF = 0.9_{cap}$ , (e) *LCL* with  $PF = 0.9_{ind}$ , and (f) *LLCL* with  $PF = 0.9_{ind}$ . The inverter 1 control was used for each inverter with synchronized carriers, and the output powers were controlled to be equal.

Figure 4.30 and Figure 4.31 present the THDs with tolerances normalized to the identical inverter case without and with a power balancer, respectively. When the powers are not controlled to be equal, the THDs of both the *LCL* and *LLCL* configurations are mainly increased and close to each other. With the inductive power factor case, clear differences emerge, and for some inverters the THD may be reduced below the identical filters case.

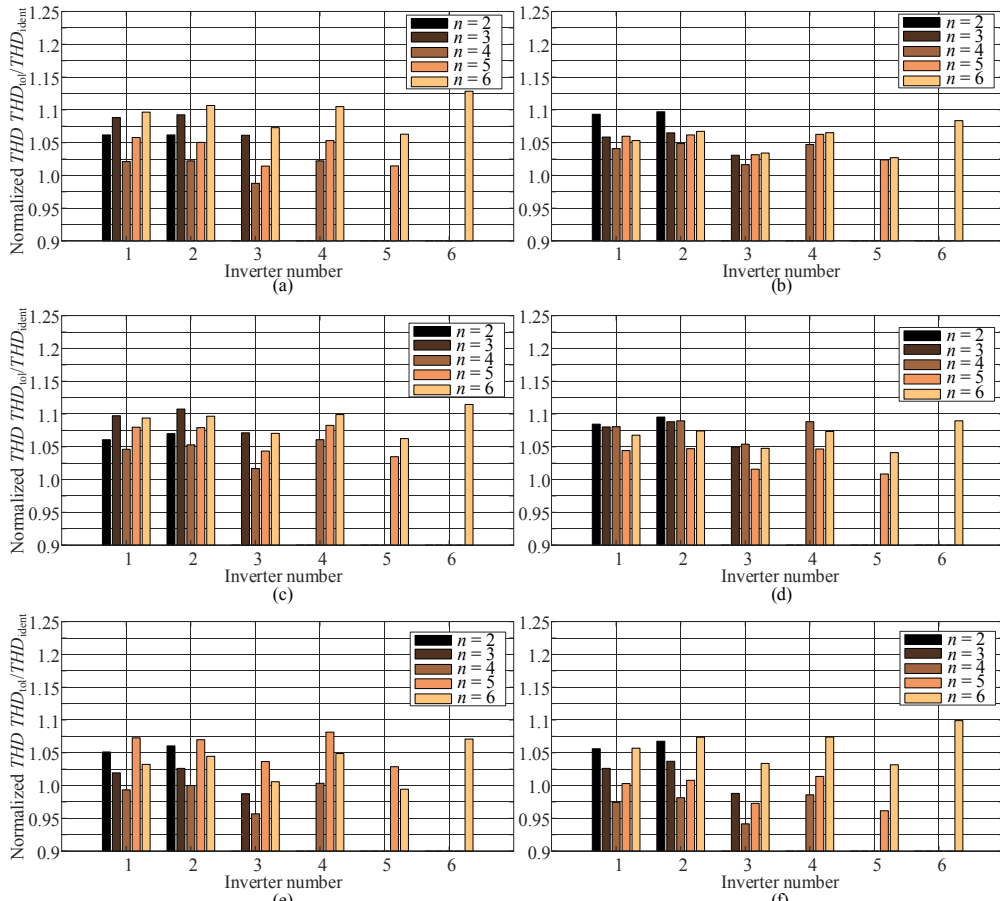


Figure 4.30 Normalized simulated THD of the grid-injected current of the *LCL* and *LLCL* configurations with tolerances in the filter components and the *DC* link capacitors; (a) *LCL* with  $PF = 1$ , (b) *LLCL* with  $PF = 1$ , (c) *LCL* with  $PF = 0.9_{cap}$ , (d) *LLCL* with  $PF = 0.9_{cap}$ , (e) *LCL* with  $PF = 0.9_{ind}$ , and (f) *LLCL* with  $PF = 0.9_{ind}$ . The inverter 1 control was used for each inverter with synchronized carriers. The grid-injected powers were not controlled equal.

Controlling the power equal causes more differences between the inverters, and as can be seen, the fifth inverter THD is more than doubled compared with the identical case. Further, the general trend seems to be that the THD increases compared with the identical case when more inverters are introduced in parallel, whereas without power balancing, the fourth inverter tolerances cause a dip in the normalized THD.

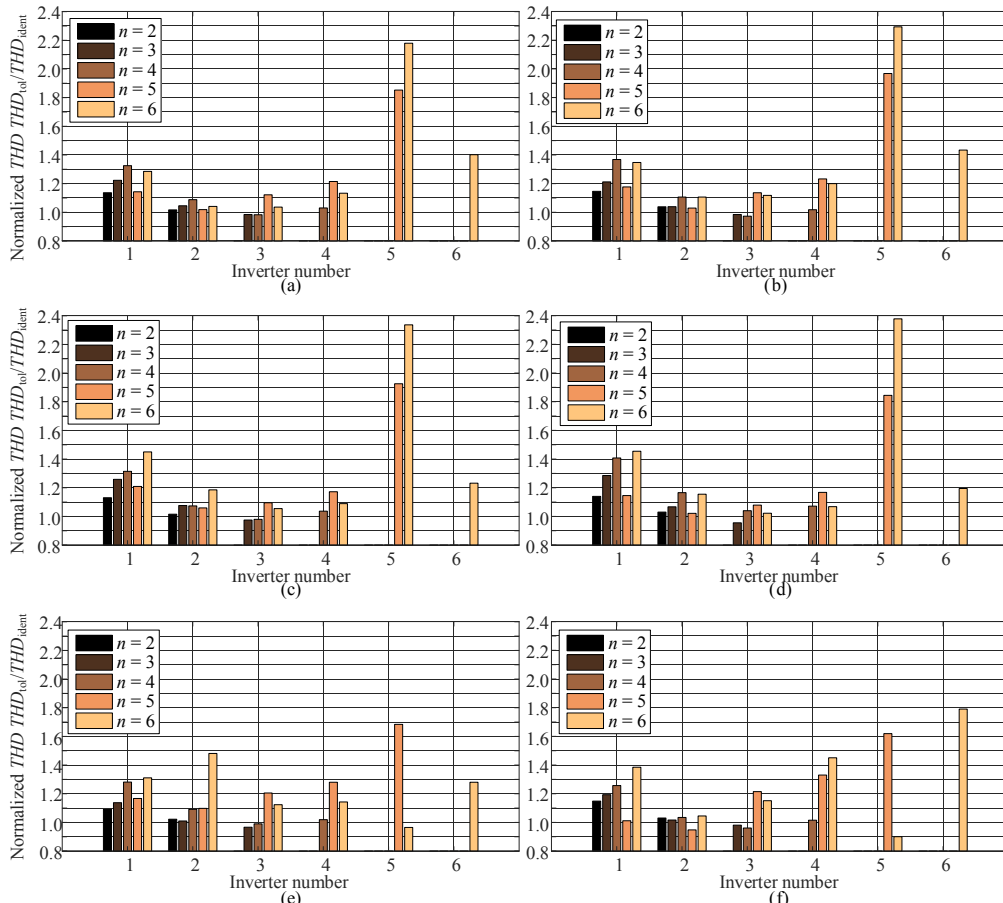


Figure 4.31 Normalized simulated THD of the grid-injected current of the *LCL* and *LLCL* configurations with tolerances in the filter components and the DC link capacitors; (a) *LCL* with  $PF = 1$ , (b) *LLCL* with  $PF = 1$ , (c) *LCL* with  $PF = 0.9_{cap}$ , (d) *LLCL* with  $PF = 0.9_{cap}$ , (e) *LCL* with  $PF = 0.9_{ind}$ , and (f) *LLCL* with  $PF = 0.9_{ind}$ . The inverter 1 control was used for each inverter with synchronized carriers, and the power balancing control was used.

Behind the THD lie the individual harmonics, which have to be below the corresponding limits set by the standards. The simulated harmonics from the fundamental to the 50<sup>th</sup> for each inverter in the simulated cases were compared with the IEEE 519-1992/2014 limits. For the *LCL* configuration with tolerances with unbalanced grid-injected powers, only inverter 5 exceeded the harmonics limits. The specific cases were:  $n = 5\text{--}6$  with the unity and inductive power factor cases. For five inverters in parallel, the exceeded harmonic was the 50<sup>th</sup> harmonic, while with six paralleled inverters also the 44<sup>th</sup> harmonic exceeded the limits for the inductive power factor case.

When the power balancing control was turned on, the outcome was that inverter 3 exceeded the 50<sup>th</sup> harmonic with  $n = 3$  and the unity power factor. With  $n = 5$ , inverter 5 exceeded the 50<sup>th</sup> harmonic with all power factor cases. With  $n = 6$ , the 50<sup>th</sup> harmonic was exceeded with all three power factors, and further, for the unity and inductive power factor cases, the 44<sup>th</sup> and 46<sup>th</sup> harmonics exceeded, respectively.

The *LLCL* configuration results were very similar to the *LCL* configuration. Without the power balancing control, also inverter 6 exceeded the 50<sup>th</sup> harmonic with the unity power factor, whereas the other failures were the same as for the *LCL* configuration. With the power balancing control, inverter 5 exceeded the 50<sup>th</sup> harmonic for the unity and inductive power factor with  $n = 5$ , and with  $n = 6$  only inverter 5 exceeded the 44<sup>th</sup> and 50<sup>th</sup> harmonics with the unity power factor.

Figure 4.32 presents the simulated energies of the *LCL* and *LLCL* configurations with tolerances normalized to the identical filter cases. Because the tolerances in the filter components are usually unknown, the calculations were made with the nominal filter component values for all the inverters.

The inverter 5 energies are clearly increased by the circulating current; this applies to both the *LCL* and *LLCL* configurations. When comparing the inverter 6 energies, we can see that for the *LCL* configuration, the energy with tolerances is increased by more than 20 % compared with the identical case, whereas with the *LLCL* configuration the energy is decreased to around 85 % of the identical filters case. The *LLCL* configuration generally presents a smaller increase in the energies associated with the tolerances than the *LCL* configuration.

The different powers of the inverters are the main result when considering the different energies. Figure 4.33 presents the filter energies when the grid-injected powers were controlled equal. As it can be seen, the energies are virtually the same with tolerances than with identical filters. When comparing the *LCL* configuration with the *LLCL* configuration, we can see that the *LLCL* filters store slightly less energy than the *LCL* filters.

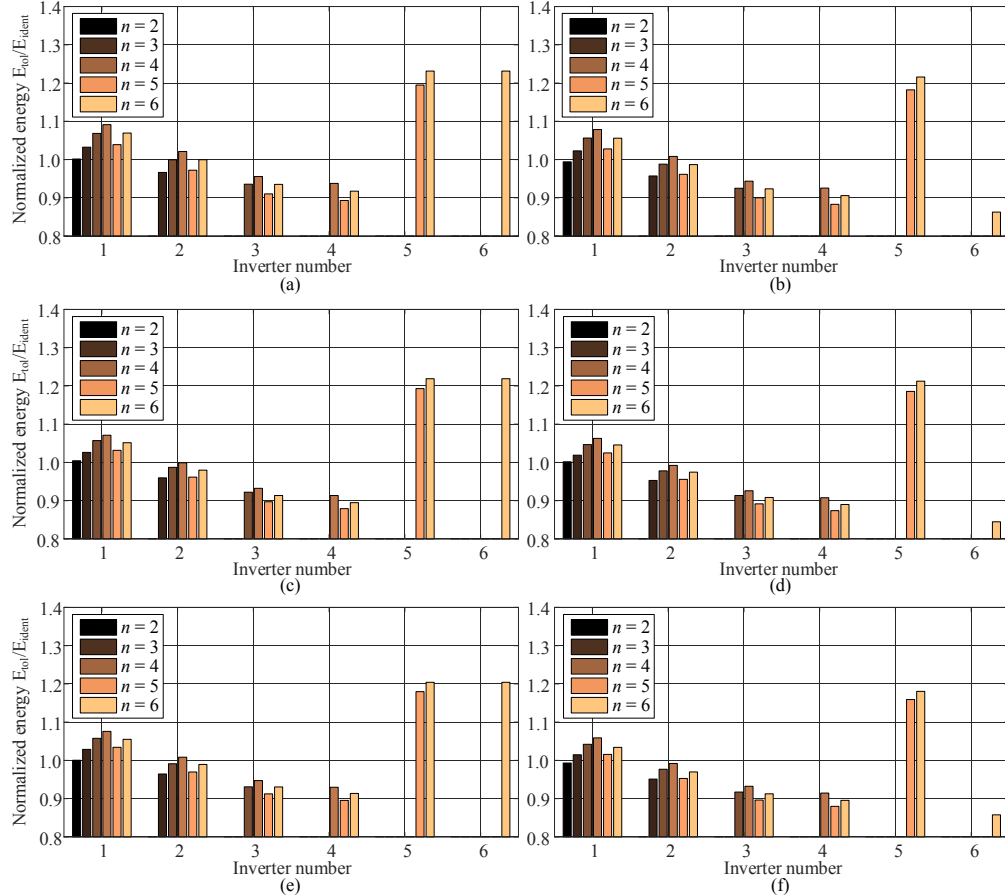


Figure 4.32 Simulated energies of the filter with tolerances normalized to the identical filters case.  
 (a)  $LCL$  configuration with  $PF = 1$ , (b)  $LLCL$  configuration with  $PF = 1$ , (c)  $LCL$  configuration with  $PF = 0.9_{\text{cap}}$ , (d)  $LLCL$  configuration  $PF = 0.9_{\text{cap}}$ , (e)  $LCL$  configuration with  $PF = 0.9_{\text{ind}}$ , and (f)  $LLCL$  configuration with  $PF = 0.9_{\text{ind}}$ . Inverter 1 control was used for all the inverters, and the powers were not controlled equal.

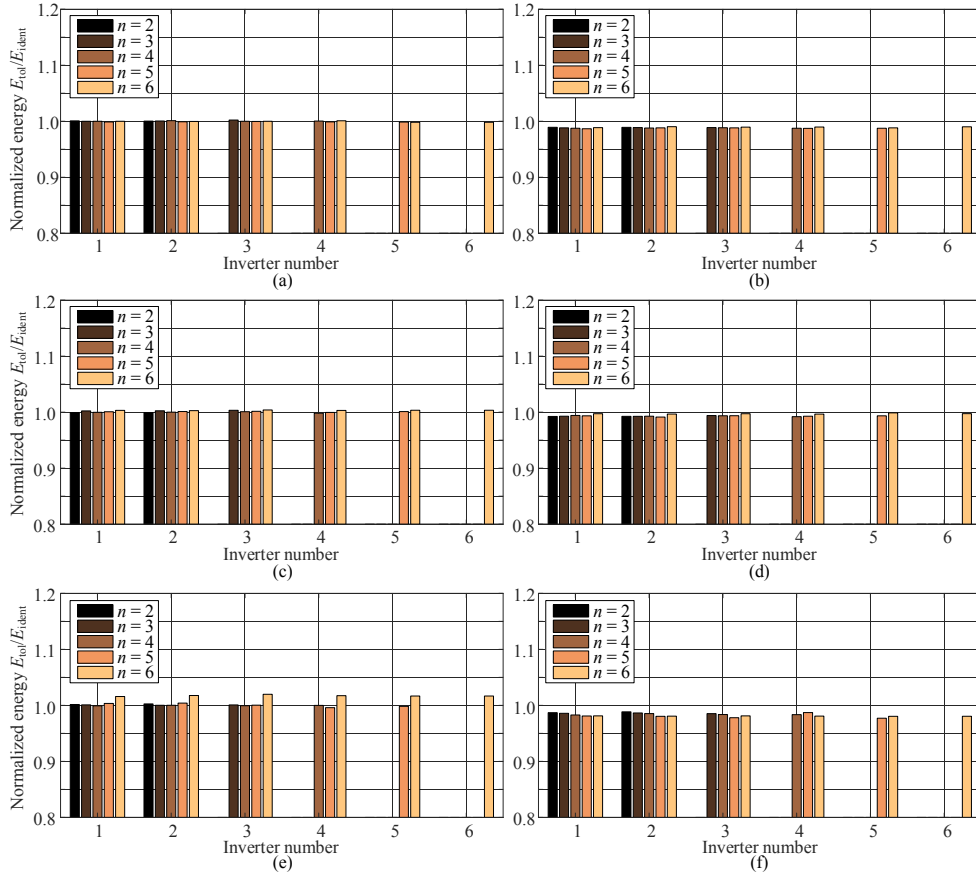


Figure 4.33 Simulated energies of the filter with tolerances normalized to the identical filters case. (a)  $LCL$  configuration with  $PF = 1$ , (b)  $LLCL$  configuration with  $PF = 1$ , (c)  $LCL$  configuration with  $PF = 0.9_{cap}$ , (d)  $LLCL$  configuration  $PF = 0.9_{cap}$ , (e)  $LCL$  configuration with  $PF = 0.9_{ind}$ , and (f)  $LLCL$  configuration with  $PF = 0.9_{ind}$ . The grid-injected powers were controlled equal.

### LC and LC+L configurations

Figure 4.34 presents the simulated  $THD$  of the  $LC$  and  $LC+L$  configurations with tolerances and unbalanced powers. As can be seen, the  $THD$  decreases, and like with identical components, the  $LC$  configuration  $THD$  is much larger compared with the  $LC+L$  configuration, which from the  $THD$ 's perspective benefits from the common grid-side inductor. The difference between the two configurations is around 0.8 %-unit in the  $THD$ . However, it should be remembered that the common grid-side may be impractically large with many paralleled inverters if it is not designed with a smaller inductance value when the number of inverters increases. If the common  $L_2$  is designed to a smaller value, the difference between the  $LC$  and  $LC+L$  configurations becomes smaller.

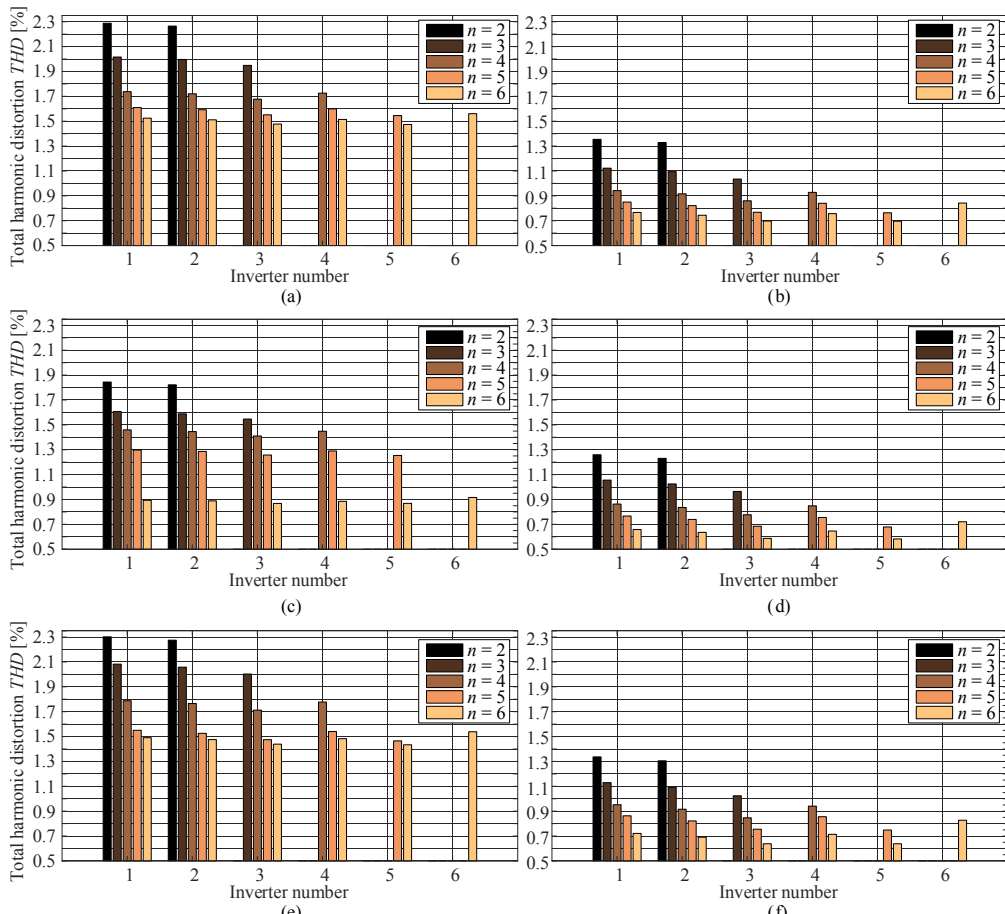


Figure 4.34 Simulated THD of the grid-injected current of the LC and LC+L configurations with tolerances in the filter components and the DC link capacitors; (a) LC with  $PF = 1$ , (b) LC+L with  $PF = 1$ , (c) LC with  $PF = 0.9_{cap}$ , (d) LC+L with  $PF = 0.9_{cap}$ , (e) LC with  $PF = 0.9_{ind}$ , and (e) LC+L with  $PF = 0.9_{ind}$ . The inverter 1 control was used for each inverter with synchronized carriers.

Figure 4.35 presents the simulated THD when the powers of each inverter are controlled to be equal. Especially for the LC configuration, the THD increases similarly to the LCL or LLCL configurations. However, the LC+L configuration does not suffer so much from the power balancing control except for the fifth and sixth inverters, whose THD increases because of the circulating current. The difference between the two configurations is increased for inverters 2 and 5 but decreased for inverters 1, 3, 4, and 6.

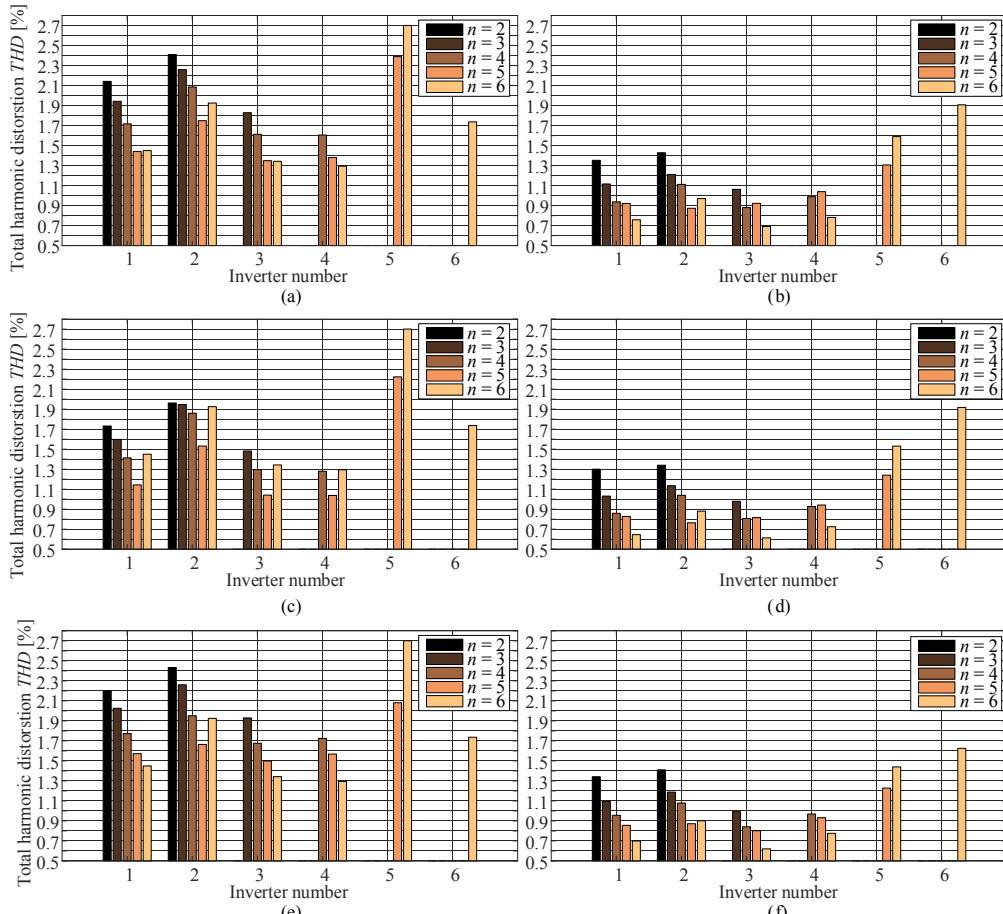


Figure 4.35 Simulated THD of the grid-injected current of the  $LC$  and  $LC+L$  configurations with tolerances in the filter components and the DC link capacitors; (a)  $LC$  with  $PF = 1$ , (b)  $LC+L$  with  $PF = 1$ , (c)  $LC$  with  $PF = 0.9_{cap}$ , (d)  $LC+L$  with  $PF = 0.9_{cap}$ , (e)  $LC$  with  $PF = 0.9_{ind}$ , and (e)  $LC+L$  with  $PF = 0.9_{ind}$ . The inverter 1 control was used for each inverter with synchronized carriers, and the output powers were controlled to be equal.

The normalized THD shows similar results for both the  $LC$  and  $LC+L$  configurations as for the  $LCL$  and  $LLCL$  configurations. Figure 4.36 and Figure 4.37 present the normalized THD without and with the balancer, respectively. Without the balancer, the general trend is that the THD compared with the identical case increases for both the  $LC$  and  $LC+L$  configurations. However, with the  $LC$  configuration, the THD seems to decrease as  $n$  increases especially for the inductive power factor case. For the  $LC+L$  configuration the THD tends to increase more as  $n$  increases.

While the powers are controlled to be equal, the inverter 5 THD stands out for the  $LC$  configuration. With the capacitive power factor, the inverter 6 THD is much higher compared with the other simulations. The  $LC+L$  configuration has a higher normalized

*THD* compared with the *LC* configuration especially considering inverters 5 and 6 rendering the *LC* configuration more robust against random tolerances from the *THD* perspective, especially with a higher number of  $n$ .

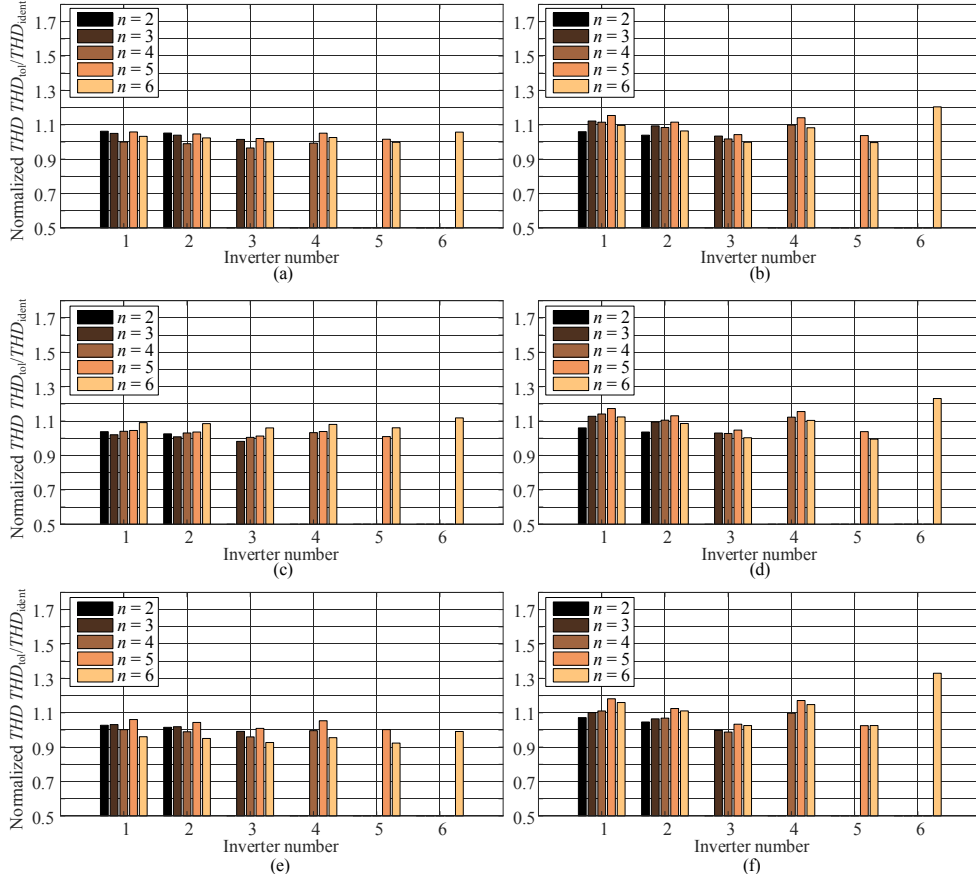


Figure 4.36 Simulated *THD* of the filter with tolerances normalized to the identical filters case. (a) *LC* configuration with  $PF = 1$ , (b) *LC+L* configuration with  $PF = 1$ , (c) *LC* configuration with  $PF = 0.9_{cap}$ , (d) *LC+L* configuration  $PF = 0.9_{cap}$ , (e) *LC* configuration with  $PF = 0.9_{ind}$ , and (f) *LC+L* configuration with  $PF = 0.9_{ind}$ . The grid-injected powers were controlled equal.

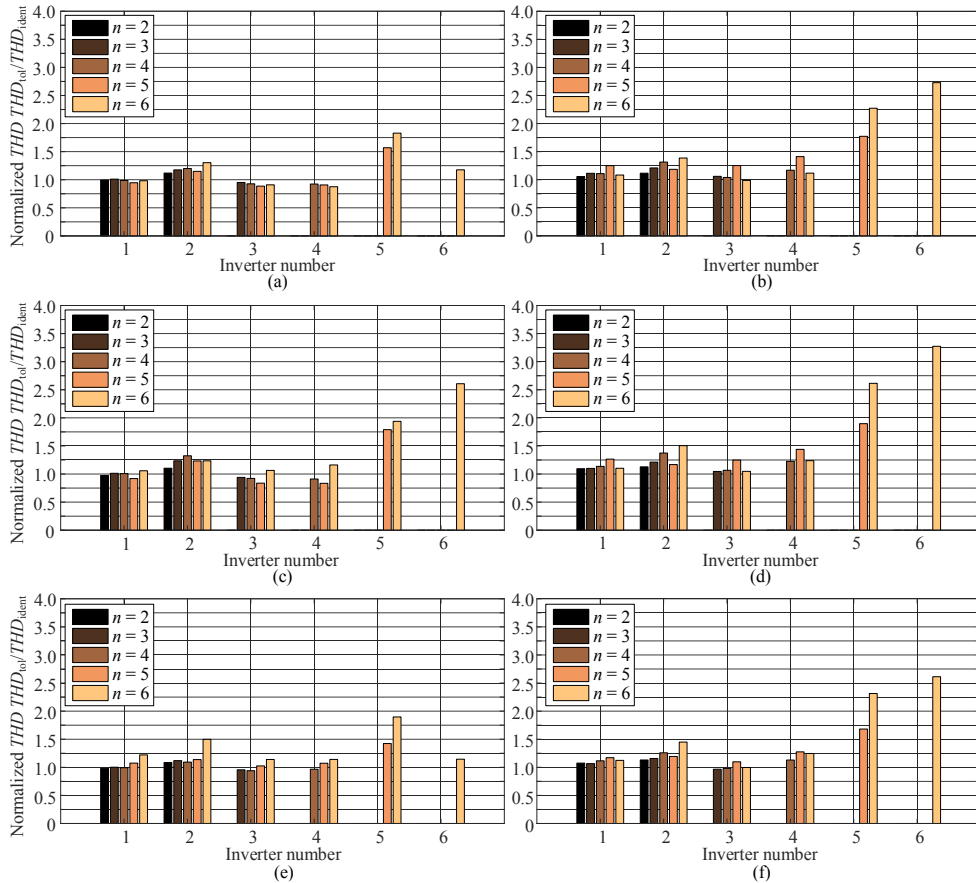


Figure 4.37 Simulated THD of the filter with tolerances normalized to the identical filters case. (a) LC configuration with  $PF = 1$ , (b) LC+L configuration with  $PF = 1$ , (c) LC configuration with  $PF = 0.9_{cap}$ , (d) LC+L configuration  $PF = 0.9_{cap}$ , (e) LC configuration with  $PF = 0.9_{ind}$ , and (f) LC+L configuration with  $PF = 0.9_{ind}$ . The grid-injected powers were controlled equal.

Figure 4.38 presents the simulated energies with tolerances normalized to the identical cases for the LC and LC+L configurations. The LC configuration shows similarly varying results as the LCL and LLCL configurations. However, a clear difference is that while the normalized energies of the LCL and LLCL configurations decreased along with the inverter number, the LC configuration shows the same level of normalized energies for inverters 1, 3, and 4, whereas inverter 2 is larger than the three aforementioned inverters. Inverter 5 has the highest energies and inverter 6 the lowest. The low energy of inverter 6 is a result of the larger inverter-side inductor, which is 1.1465 times the nominal. This increased inductor combined with the inverter 1 control results in less power (i.e., current) driven through the inverter 6 filter, which, in turn, is shown as a smaller energy. For instance, without the power balancing control, inverter 6 drives around 880 kW power to

the grid, while inverter 1 drives 1000 kW. This power difference results in over 150 A peak current difference between these two inverters.

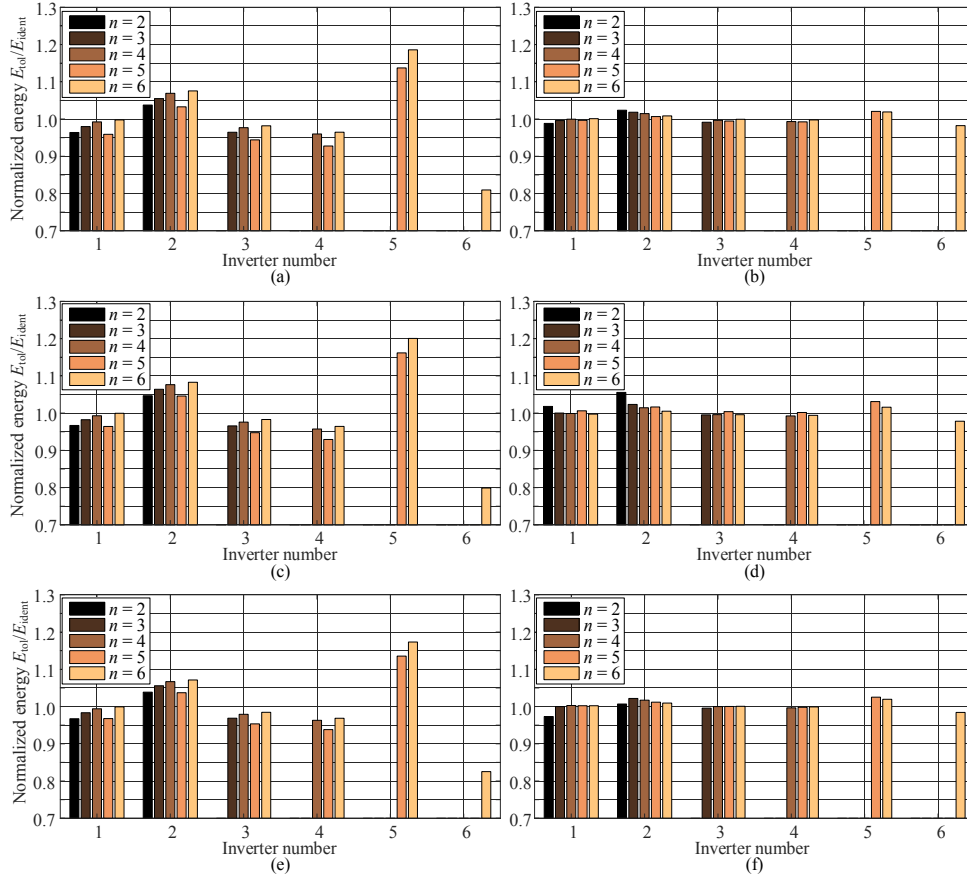


Figure 4.38 Simulated energies of the filter with tolerances normalized to the identical filters case. (a)  $LC$  configuration with  $PF = 1$ , (b)  $LC+L$  configuration with  $PF = 1$ , (c)  $LC$  configuration with  $PF = 0.9_{\text{cap}}$ , (d)  $LC+L$  configuration  $PF = 0.9_{\text{cap}}$ , (e)  $LC$  configuration with  $PF = 0.9_{\text{ind}}$ , and (f)  $LC+L$  configuration with  $PF = 0.9_{\text{ind}}$ . The inverter 1 control was used for all the inverters, and the powers were not controlled equal.

With the  $LC+L$  configuration, the common grid-side inductor dominates the filter energies, resulting in less variation from the identical cases. Inverters 5 and 6 do not stand out from the others with the  $LC+L$  configuration. When the energies are controlled to be equal, the situation for both configurations becomes similar to the  $LCL$  and  $LLCL$  configurations; the energies are virtually the same as for the identical cases.

### **L-configuration**

Figure 4.39(a) presents the simulated grid-injected current  $THD$  for the  $L$ -configuration with tolerances without the power balancing control. Similarly as for the identical case

simulations, the DC link voltage references were set to 1130 V, 1175 V, 1195 V and 1220 V, respectively, for  $n = 3\text{--}6$ . As the capacitor was increased according to  $n$ , the attenuation improved decreasing the grid-injected current  $THD$ . The case in Figure 4.39(a) was simulated with the inverter 1 capacitor tolerances, which caused both the undamped and damped capacitor to be around 17 % larger than nominal. However, even an extreme tolerance in the opposite direction would still result in a decreasing  $THD$ , although the change would of course be smaller. Further, the common grid-side inductor was 81.4 % of the nominal, balancing out the effect of capacitor tolerances almost completely; the current harmonic attenuation function resonance peak frequency  $f_{r1}$  is increased by around 2.5 %, resulting in a slightly reduced harmonic attenuation than for the nominal case.

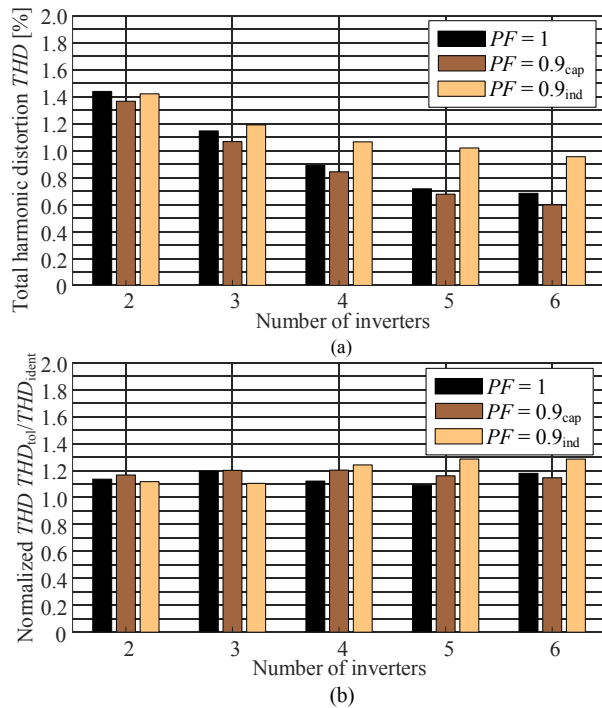


Figure 4.39 (a) Simulated  $THD$  of the grid-injected current of the  $L$ -configuration with tolerances in the filter components and the  $DC$  link capacitors without power balancing control and capacitor increased as  $nC_1$ . (b) Simulated  $THD$  normalized of the grid-injected current of the  $L$ -configuration with tolerances normalized to the identical case. The inverter 1 control was used for each inverter with synchronized carriers.

Using the power balancing controller was not found to have virtually any effect on the output  $THD$ . The result was expected as the attenuation in the  $L$ -configuration is not affected by the number of paralleled inverters because they all share a common capacitor and a grid-side inductor, which determine the attenuation.

Figure 4.39(b) presents the simulated *THD* normalized to the corresponding identical case. As can be seen, the *THD* is very similar to the identical case in the case of the decreasing *THD*, which can be seen from Figure 4.39(b) where the *THDs* remains around the same level. The effect of the tolerances can be seen in the slightly increased level of the *THD*, which was 15–30 % higher than in the identical case.

Because the *L*-configuration has a common *CL* circuit on the grid side, the circulating current does not have a direct effect on the grid-injected current as it has with the other configurations. Of course, the circulating current affects the inductor dimensioning as the circulating current flows through the inductors increasing the energy of the components. The inverter with the lowest inverter-side inductor value tends to draw more circulating current from the others. However, in case the output powers are balanced by control, the output currents are very close to each other. Naturally, with different inductor values the component energy differs between the inductors with tolerances. Because the assumption here is that the tolerances are not known in the calculations, the normalized energies for the inverter-side inductors are very close to the identical situation. This is also applied to the other filter configurations.

Subfigures (a)–(c) in Figure 4.40 present the inverter-side inductor energies of the *L*-configuration with tolerances without power balancing control with  $PF = 1$ ,  $PF = 0.9_{cap}$ , and  $PF = 0.9_{ind}$ , respectively. The inverter 1 controls used for each inverter resulted in different currents for each inverter, which, in turn, resulted in different energies as can be seen subfigures (a)–(c) in Figure 4.40. A vague general trend of decreasing energy can be seen in Figure 4.40(a) of the unity power factor, while with the capacitive power factor the decrease is clearer. With the inductive power factor, the trend is increasing.

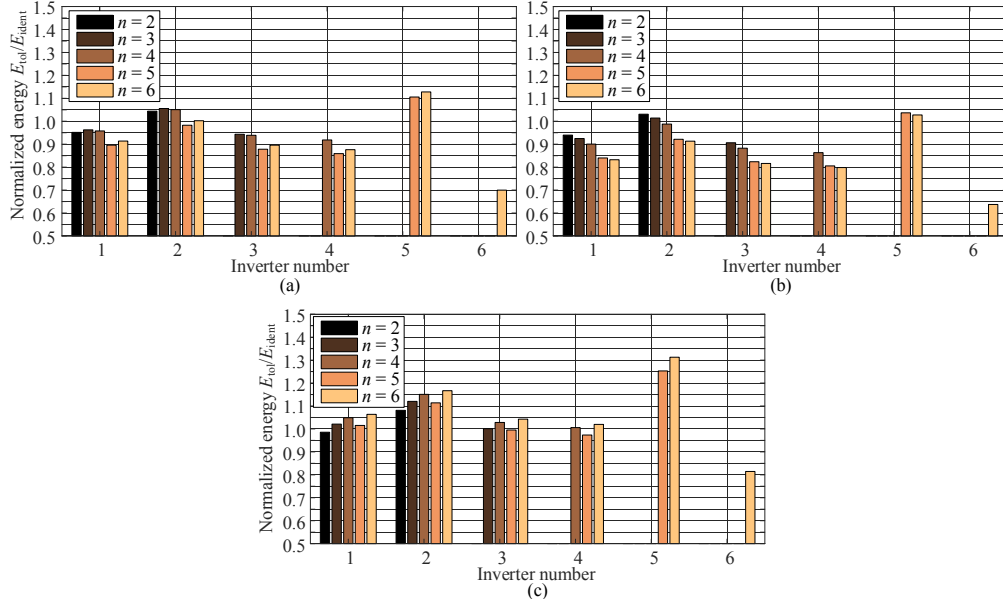


Figure 4.40 Simulated inverter-side inductor  $L_1$  energies normalized to the identical case energies of the  $L$ -configuration with tolerances in the filter components and the DC link capacitors without power balancing control and capacitor increased as  $nC_f$ . The inverter 1 control was used for each inverter with synchronized carriers. (a)  $PF = 1$ , (b)  $PF = 0.9_{\text{cap}}$  and (c)  $PF = 0.9_{\text{ind}}$ .

Subfigures (a)–(b) Figure 4.41 present the normalized energies for  $L_2$  without and with power balancing control, respectively, and subfigures (c)–(d) in Figure 4.41 present the normalized energies of  $C_f$  without and with power balancing control, respectively. As can be seen, there was virtually no difference between the cases without and with a balancer because in both cases  $C_f$  and  $L_2$  determining the attenuation were the same. After the inverter-side inductors, the powers in both simulation cases were the same even though without power balancing the currents fed by each inverter were different.

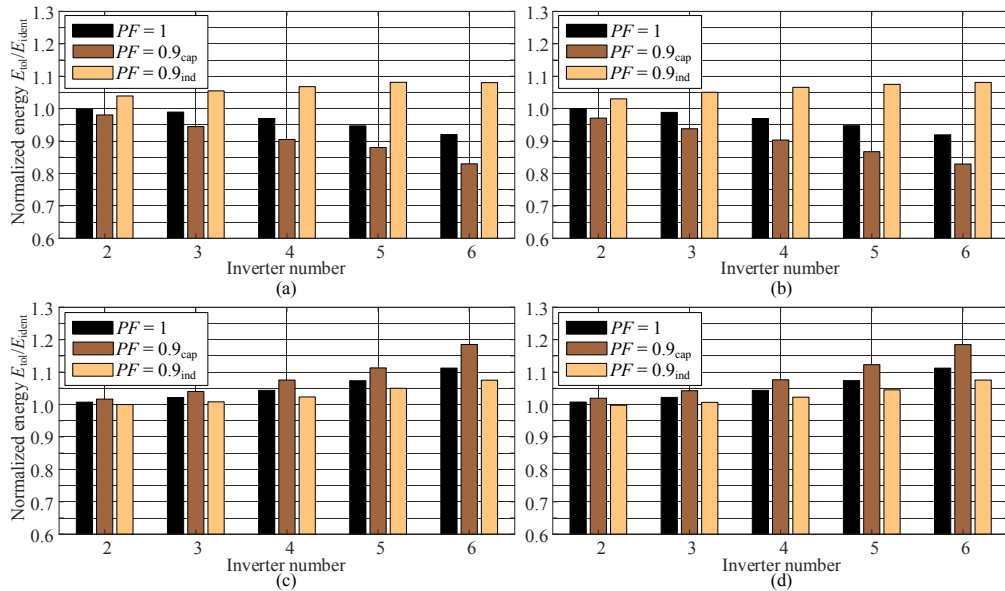


Figure 4.41 Simulated grid-side inductor  $L_2$  and capacitor energies normalized to the identical case energies of the  $L$ -configuration with tolerances in the filter components and the DC link capacitors capacitor increased as  $nC_f$ . The inverter 1 control was used for each inverter with synchronized carriers. (a)  $L_2$  energy without power balancing control, (b)  $L_2$  energy with powers balanced, (c)  $C_f$  energy without power balancing, and (d)  $C_f$  energy with powers balanced.

### Key findings

- The simulations show that with tolerances the effect of the grid multiplication is similar to the case of identical filters, and the  $THD$  becomes better as  $n$  increases.
- Using the same control for all inverters minimizes the common-mode circulating current but causes high deviation in both the  $THD$  and component energies.
- Balancing the output powers results in component energies close to the identical case.
- Circulating current is minimized with the same controls for each inverter but maximized when powers are balanced. Some additional circulating current minimization control could be suggested.
- The  $L$ -configuration grid-injected  $THD$  is virtually the same whether the inverter powers are balanced or not, whereas an individual inverter  $THD$  may differ considerably with the other configurations driving balanced power to the grid.

#### 4.2.4 Open-end inverter

The open-end inverter was simulated in Simulink. The simulation models were based on conventional parallel-connected inverter models to add a similar level of noise and other disturbances to the simulations. The two cases from section 3.5 and a further, third case with the zero-sequence current minimizing modulation method were simulated and compared with the conventional two parallel-inverter system. For the first two cases, the unipolar modulation method was used to double the output voltage of each phase H-bridge, whereas with the zero-sequence current minimizing modulation, the output voltage was not doubled.

If a three-phase transformer is used, the transformer can easily become saturated by the zero-sequence current. When all phase windings share a common core, the leakage flux between the phase windings increases the saturation effect because the magnetizing inductance collapses. One solution to tackle this particular problem is to use separated single-phase transformers for each phase so that in an actual application they are also isolated from each other to mitigate the leakage flux problem. The open-end transformer in the simulations was constructed by using three single-phase transformers, which were connected to wye on the grid side.

Table 4.3 presents the transformer parameters used in the simulations. The nominal power of the open-end system is 2000 kVA so that it can be compared with the 2par system. For Case 2 with the same DC link voltage as for the 2par system, the transformer secondary voltage was 1.38 kV. The transformer short-circuit resistance and reactance were distributed equally between the primary and the secondary, and the magnetizing parameters were calculated on the primary side.

Table 4.3. Transformer parameters used in the open-end and 2par simulations.

Symbol	Quantity	Value
$S_n$	Nominal power	2000 kVA
$u_{\text{pri}}$	Primary voltage	3300 V <sub>L-L,rms</sub>
$u_{\text{sec}1}$	Secondary voltage 1	690 V <sub>L-L,rms</sub>
$u_{\text{sec}2}$	Secondary voltage 2	1380 V <sub>L-L,rms</sub>
$u_k$	Short-circuit voltage	6.0%
$P_0$	No-load losses	14 kW
$P_{\text{Cu}}$	Copper losses	12 kW
$R_{\text{pri,sec}}$	Winding resistance primary and secondary	0.003 pu
$L_{\text{pri,sec}}$	Winding inductance primary and secondary	0.02985 pu
$R_m$	Magnetizing resistance, primary	4722.152 pu
$L_m$	Magnetizing inductance, primary	3554.593 pu

As it was discussed in section 3.5.2, the zero-sequence component injected into the reference voltages of the SVM is not cancelled at the transformer. For this reason, the low-frequency zero-sequence voltage injected into SVM drives current through the transformer windings. On the grid side, the winding can be in wye or delta, thereby removing the component from the grid-injected current, but this extra component has a significant effect on the transformer design. For instance, in the SVM, the injected zero-sequence component amplitude is one-fourth of the fundamental amplitude, which at the 690 V voltage level corresponds to 140 V<sub>peak</sub> and 81 V<sub>rms</sub>, respectively.

The transformer saturation can be simulated by decreasing the magnetizing branch parameter. Figure 4.42 presents the transformer current with normal transformer parameters (a) and with the magnetizing branch multiplied by 0.0001 (b). When the magnetizing branch values are very small, the zero-sequence component of the SVM is fed to the transformer, which can be seen at  $t = 0\text{--}0.04\text{ s}$  in subfigure (b). The transformer current in subfigure (b) contains 16 % of the third harmonic.

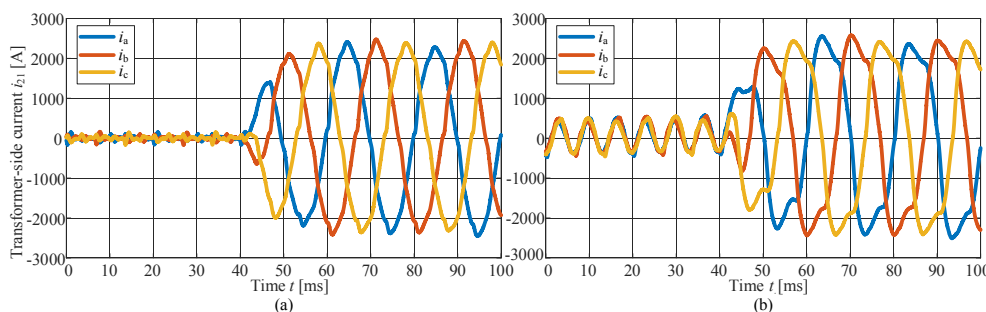


Figure 4.42 Simulated transformer current with the open-end inverter with space vector modulation; (a) with normal transformer parameters and (b) with magnetizing branch parameters multiplied by 0.0001.

### Case 1

In Case 1, the DC link voltage was nominally set as half of the 2par system DC link voltage,  $U_{DC,OE} = 550\text{ V}$ . The inverter-side inductor value for the open-end inverter was designed to limit the current ripple at a maximum of 15 % of the base current, which makes  $L_{1,OE} = 44\text{ }\mu\text{H}$ , roughly one-fourth of  $L_{1,2\text{par}}$ . For the SPWM, the DC link voltage was set 15.47 % higher leading to an inverter-side inductor of  $L_{1,OE} = 60\text{ }\mu\text{H}$ . The capacitor value was set similarly for 3 % of the base capacitor resulting in  $C_f = \sim 401\text{ }\mu\text{F}$ , while the grid-side inductor was chosen as  $L_{2,OE} = 25\text{ }\mu\text{H}$ , which is half of  $L_{2,2\text{par}}$ . These values result in resonance frequencies of  $f_{r1} = 932.4\text{ Hz}$  and  $f_{r2} = 1259.8\text{ Hz}$  for the open-end system with the SVM and  $f_{r1} = 932.5\text{ Hz}$  and  $f_{r2} = 1225.1\text{ Hz}$  for the open-end system with the SPWM. The 2Par system resonance frequencies accounting for the resonance shift were  $f_{r1} = 1151.5\text{ Hz}$  and  $f_{r2} = 1433.9\text{ Hz}$ . The open-end system resonances are naturally lower because of the larger capacitor  $C_{f,OE} = 2C_{f,2\text{Par}}$ , because the open-end system drives double the power compared with a single inverter in 2Par system drives.

When the SVM is used, the open-end inverter drives zero-sequence current with a fundamental frequency of 150 Hz. The zero-sequence current also contains a large amount of the third and fifth multiples of this fundamental frequency, that is, the ninth and 15<sup>th</sup> harmonics of the fundamental grid frequency. The average rms value calculated over 0.5 s from the simulations was around 58–75 A depending on the power factor. A great majority of the switching frequency components of the circulating current flow through the filter capacitors and not through the transformer. However, with the low-frequency components there is still a small amount of zero-sequence current also in the transformer. As the nominal rms current in the simulations was 1674 A, this zero-sequence current was around 3.5–4.5 % of the nominal current.

Subfigures (a)–(f) in Figure 4.43 present the first 50 harmonics of the inverter-side and grid-side current; the open-end inverter with the space vector modulation in (a)–(b), the open-end inverter with the sinusoidal PWM in (c)–(d), and the 2Par system in (e)–(f). Two main differences can be observed between the open-end system and the 2Par system grid-injected currents; the fifth, seventh, thirteenth, and fifteenth harmonics have a much higher value in the open-end systems, and their *THD* is also worse. A comparison of the open-end systems shows that removing the zero-sequence injection from the modulator results in decreased low-order harmonics in the inverter-side current but increased low-order harmonics in the grid-injected current.

With the space vector modulation, the inverter-side current contains more harmonics than with the sinusoidal PWM. Especially, the third harmonic from the zero-sequence current of the SVM and its multiples, the ninth and fifteenth, are clearly seen in Figure 4.43. These harmonics are not present in the inverter-side current of the open-end system with the sinusoidal PWM. However, because of the dead time, some zero sequence voltage is always produced (Baiju et al., 2004). Removing the injected zero-sequence from the modulator results in a worse harmonic content in the inverter voltage. In addition, increased DC link voltage is needed, which increases the inverter-side inductor value.

The grid-injected current shows that the eleventh harmonic for the open-end system with the SWPM is at the allowed limit, which would require additional iteration in the filter dimensioning to keep all harmonics below the limits. Generally, increasing the inverter-side inductor and, if necessary, decreasing the capacitor would result in a better situation with the harmonics.

Subfigures (a)–(d) in Figure 4.44 illustrate the open-end system inverter-side current harmonics and grid-injected current harmonics with an ideal grid voltage. The open-end system with the SVM presents much more low-order harmonics in the inverter-side current compared with the SPWM case, which is of course due to the injected zero-sequence signal. A difference in the grid-injected current can also be seen; the third harmonic is present in the current with the SVM, and also the seventh, eleventh, and thirteenth harmonics are larger compared with the SPWM case.

With similar control systems and with the same basic filter dimensioning principles, the open-end inverter seems to be more sensitive to the grid harmonics than the 2Par system. Of course, it should be remembered here that as the apparent switching frequency of the open-end system is doubled compared with the 2Par system switching frequency, the control sampling frequency was also doubled in the simulations. This may have an effect on the performance of the control and thereby on the current harmonics, but it cannot explain the significant differences seen in Figure 4.43.

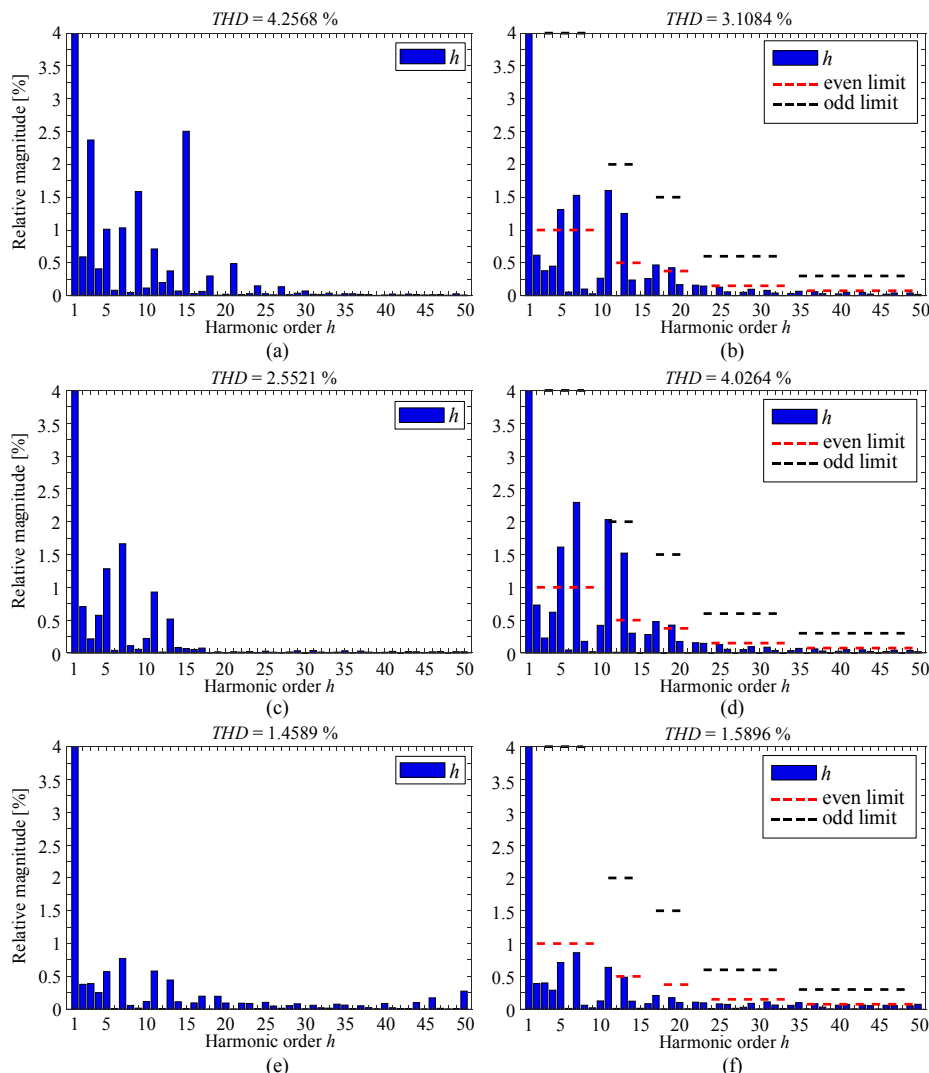


Figure 4.43 Simulated harmonic content of the inverter-side and grid-injected current of the open-end system with the SVM (a)–(b), with the SPWM (c)–(d), and the 2Par system (e)–(f), respectively. The power factor  $PF = 1$ .

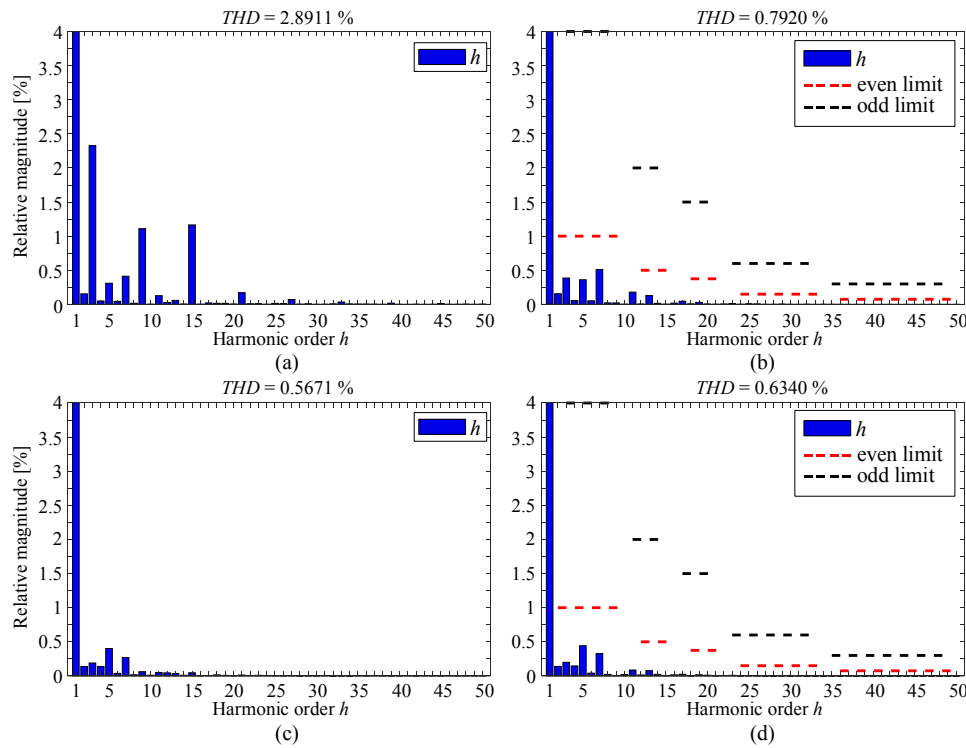


Figure 4.44 Simulated harmonic content of the inverter-side and grid-injected current of the open-end system with the SVM (a)–(b) and with the SPWM (c)–(d), respectively. The grid harmonics were excluded and the power factor  $PF = 1$ .

Subfigures (a) and (b) in Figure 4.45 depict the simulated grid-injected current  $THD$  for the open-end system with the SVM and with the SPWM and the 2Par system for all three power factor cases. Subfigure (a) illustrates the results with identical components and subfigure (b) with tolerances. Additionally, the 2Par system was simulated with balanced output powers as a fourth case.

Figure 4.45 shows that both open-end scenarios suffer from the tolerances, yet the 2par system less so. A minor difference between the two grid-side currents was seen in the simulations, but the grid-injected current at the transformer primary (grid side) remains virtually the same. Balancing the output powers had also virtually no effect on the transformer primary side either. In addition, the open-end system shows much more variation in the  $THD$  depending on the power factor.

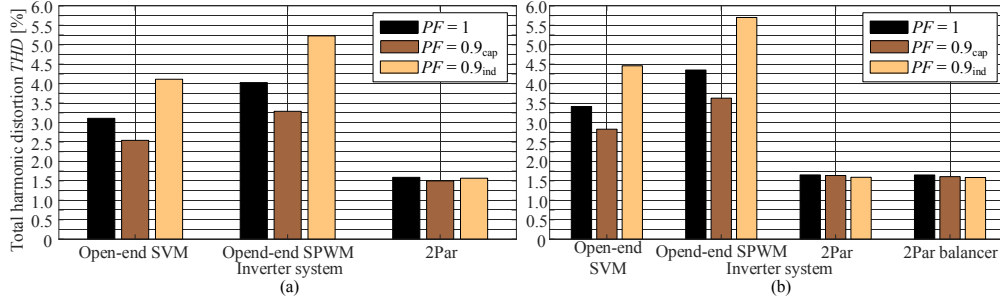


Figure 4.45 Simulated grid-injected current  $THD$  for the open-end system with the SVM, the open-end system with the SPWM, and for the 2Par system; (a) with identical components, (b) with inverter 1 and inverter 2 tolerances.

Subfigures (a) and (b) in Figure 4.46 present the open-end and 2Par system filter energies with identical components and components with tolerances, respectively. The difference between the SVM and SPWM schemes can mainly be explained by the fact that the increased DC link voltage of the SPWM scheme requires a larger inverter-side inductor. The tolerances applied here had virtually no effect on the filter energies for any of the simulated scenarios. It is emphasized that the energies were calculated with the nominal filter component values and the current driven by the open-end system to the grid remains the same regardless of the inductor values, whereas the 2Par system inverters can drive different currents to the grid when the master inverter controls are used for both inverters. Of course, the actual energy in the open-end system would be smaller with smaller inductor values.

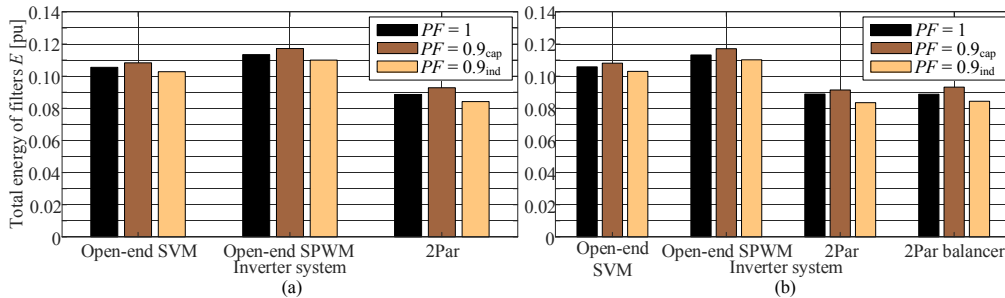


Figure 4.46 Simulated filter energies of the fundamental frequency component for the open-end system with the SVM, the open-end system with the SPWM and for the 2Par system; (a) with identical components, (b) with inverter 1 and inverter 6 tolerances.

In Figure 4.46, the difference in the 2Par system cannot be seen because the energies shown in the figure are the total energy of the filter configuration and balancing of the output power only balances the energy stored in the filter configuration when the total output power remains the same. Tolerances have an effect on the individual component energies yet the total energy is approximately the same. The 2Par system was also tested by changing the other tolerances to inverter 2 tolerances instead of the originally applied

inverter 6 tolerances. Now, without balancing the output powers, the total energies compared with the original simulation were  $E = [0.9955, 1.0088, 1.0048]$  for the unity, capacitive, and inductive power factors, respectively. The individual inverter energies were  $E_{inv1} = [0.9346, 0.9444, 0.9454]$  and  $E_{inv2} = [1.0700, 1.0878, 1.0769]$ . The change in the inverter energies was noticeable, whereas the whole filter configuration energy remained more or less the same.

When the *THD* of the grid-injected current of the open-end and 2Par systems is compared with similar filter designs, we can see that the same design principle used for both systems does not provide a similar filtering action. By designing the capacitor of the open-end system according to the application power, as was done here, the resonance frequencies are close to each other with the both systems. However, the apparent switching frequency of the open-end system  $f_{sw,OE} = 2f_{sw,2Par}$ , doubled the switching frequency of an individual inverter arm. This higher frequency allows the filter resonance frequencies to be placed higher, thereby yielding better reference tracking for the control. This can be done by dimensioning the filter capacitor smaller than the  $C_{2Par}$  value. The grid-side inductor value could also be decreased to make the resonances higher. However, this was found to have a much smaller impact on the attenuation and inverter performance than the capacitor. Additionally, the *THD* can be made slightly better by increasing the inductances, but this is not a preferred solution because with the MW-scale applications, the filter design becomes more difficult and larger inductors can cause more disturbances to the control through the measurement of the harmonic current and their voltage drops in the large inductors.

In the inverter-side current, the triple multiples of the zero-sequence current with the fundamental frequency of 150 Hz are more attenuated, but additionally, some clear peaks of the 21<sup>st</sup>, 24<sup>th</sup>, 27<sup>th</sup>, and 30<sup>th</sup> harmonics can be introduced depending on the filter values. The smaller the capacitor is made, the higher peaks are introduced into  $i_{11}$ . However, these are filtered from the grid-injected current.

Figure 4.47 shows the simulated *THD* of the open-end systems without and with tolerances when the inductors were kept as previously and the capacitor was decreased to one-fourth of the original. The resonance frequencies were now  $f_{r1} = 1865.0$  Hz and  $f_{r2} = 2519.6$  Hz for the SVM and  $f_{r1} = 1864.7$  Hz and  $f_{r2} = 2450.1$  Hz for the SPWM. As can be seen, the *THD* is decreased when the capacitor is smaller. Compared with the original design, the *THDs* are now reduced to  $THD_{SVM} = [82.09\%, 88.30\%, 80.87\%]$ ,  $THD_{SVM,tol} = [76.60\%, 83.56\%, 77.38\%]$ ,  $THD_{SPWM} = [79.93\%, 94.59\%, 73.79\%]$ , and  $THD_{SPWM,tol} = [76.92\%, 91.47\%, 70.14\%]$  of the original design *THD* for  $[PF = 1, PF = 0.9_{cap}, PF = 0.9_{ind}]$ , respectively.

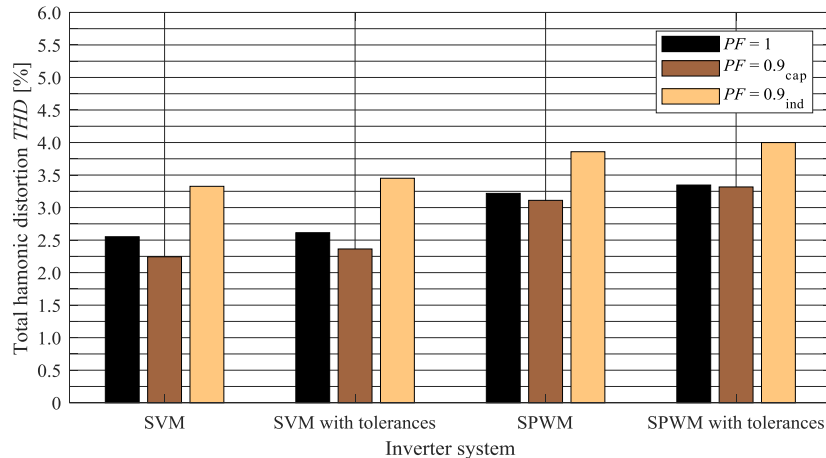


Figure 4.47 Simulated THD of the grid-injected current of the open-end system with the filter capacitor decreased to one-fourth of the original.

Increasing the inverter-side inductor would result in an even better THD and harmonic content, which can be seen from Figure 4.48.

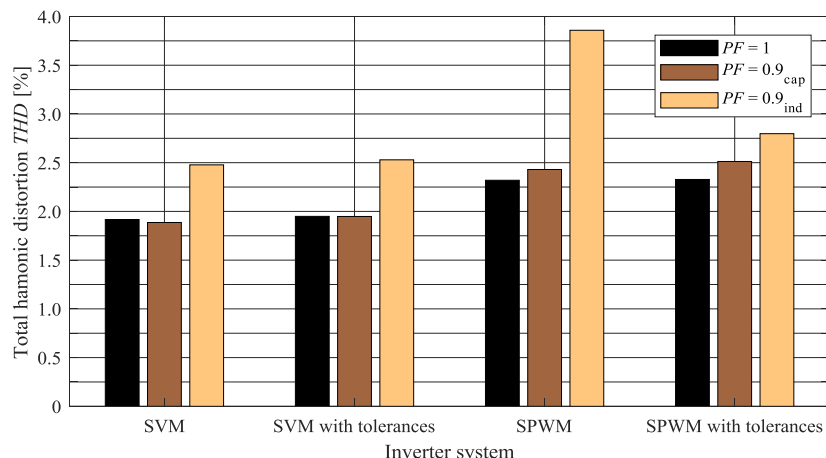


Figure 4.48 Simulated THD of the grid-injected current of the open-end system with the filter capacitor decreased to one-fourth of the original and the inverter-side inductor value increased by 50 %.

The THD in the inductive power factor case is much larger compared with the two other power factors. Interestingly, the SPWM seems to benefit from the tolerances as the inductive power factor and the THD do not seem to be as large as in the other cases. The tolerances increased the other  $L_{1,OE}$  by  $\sim 14.5\%$  and  $C_f$  by  $\sim 17\%$ .

In general, decreasing the capacitor results also in a decreased total energy of the filter arrangement. The inverter sees the filter as an inductance at the fundamental frequency,

and a majority of the energy is transferred at this frequency. This means that decreasing the capacitor has no real effect on the current amplitude. The revised filter component energy relation to the nominal case was  $E_{\text{revised}}/E_{\text{nom}} = [0.8906, 0.9095, 0.8739]$ . However, increasing the inductors would result in an increase in the energy in those components cancelling out the effect of the capacitor energy change. The energy for the revised filter with the increased inverter-side inductor in addition to the decreased capacitor results in  $E_{\text{revised}}/E_{\text{nom}} = [1.1625, 1.1887, 1.1405]$ .

### Case 2

In Case 2, the DC link voltage was nominally set as the same of the 2par system DC link voltage;  $U_{DC,OE} = 1100$  V. The transformer equivalent phase-to-phase voltage was 1380 V, which corresponds to two times the 2Par system voltage. The inverter-side inductor value for the open-end inverter was designed to limit the current ripple at a maximum of 15 % of the base current, which makes  $L_{1,OE} = L_{1,2\text{par}}$ . The  $L_{1,OE}$  value for the SPWM system was 199  $\mu\text{H}$ . The capacitor value was set similarly for 3 % of the base capacitor, resulting in  $C_f = \sim 100.3\mu\text{F}$  while the grid-side inductor was chosen again as  $L_{2,OE} = 25\mu\text{H}$ . The transformer phase inductance was  $L_g = \sim 90.5\mu\text{H}$ . These values result in resonance frequencies of  $f_{r1} = 1340.5$  Hz and  $f_{r2} = 1590.0$  Hz for the SVM and  $f_{r1} = 1340.5$  Hz and  $f_{r2} = 1559.4$  Hz for the SPWM.

Subfigures (a)–(b) in Figure 4.49 depict the simulated first 50 harmonics of the inverter-side and grid-side current of the open-end system with the SVM, and subfigures (a)–(b) in Figure 4.50 the same figures for the SPWM. A very high amount of the fifteenth harmonic is present in the inverter-side current of the space-vector-modulated open-end system. In addition, the third, fifth, seventh, ninth, eleventh, and thirteenth harmonics are produced. A comparison of the SVM system with the SPWM system shows that the SPWM system produces a larger amount of lower harmonics. In the grid-injected current, a benefit in the harmonic content of the space vector modulation is demonstrated, and the THD is much better than with the SPWM.

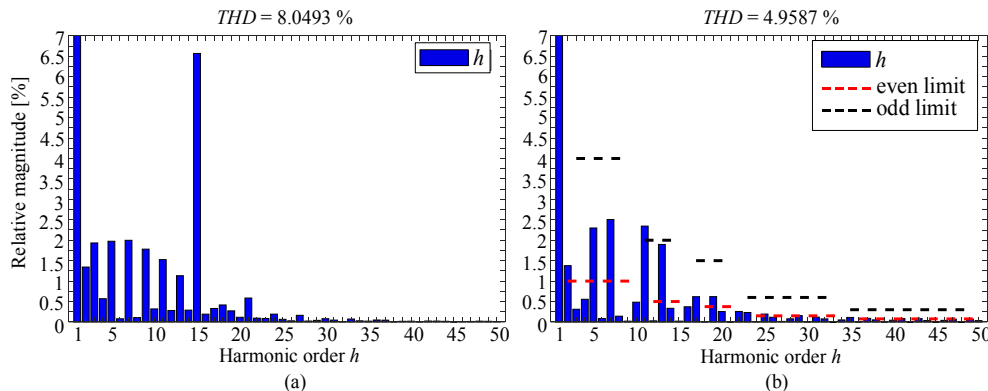


Figure 4.49 Simulated harmonic content of the open-end system. (a) Inverter-side current with the SVM, (b) grid-side current with the SVM. The power factor  $PF = 1$ .

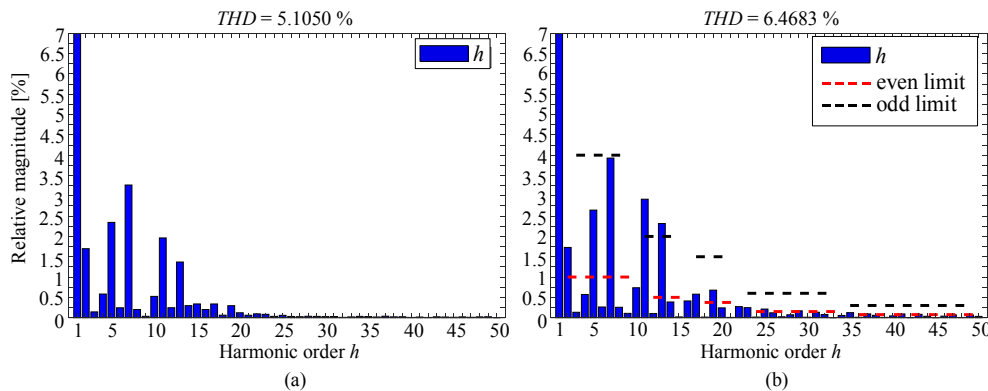


Figure 4.50 Simulated harmonic content of the open-end system. (a) Inverter-side current with the SPWM, (b) grid-side current with the SPWM. The power factor  $PF = 1$ .

Subfigures (a)–(d) in Figure 4.51 show the simulated first 50 harmonics of the inverter-side and grid-side currents of the open-end system with the modified filter design. The filter capacitor value was decreased to one-fourth of the original as was done in Case 1. In addition, the inverter-side inductor had to be increased to ensure good attenuation and THD for the case 2 system. The THD of the grid-injected current was now reduced to half of the original filter design, and the fifteenth harmonic in the inverter-side current of the SVM system was also decreased.

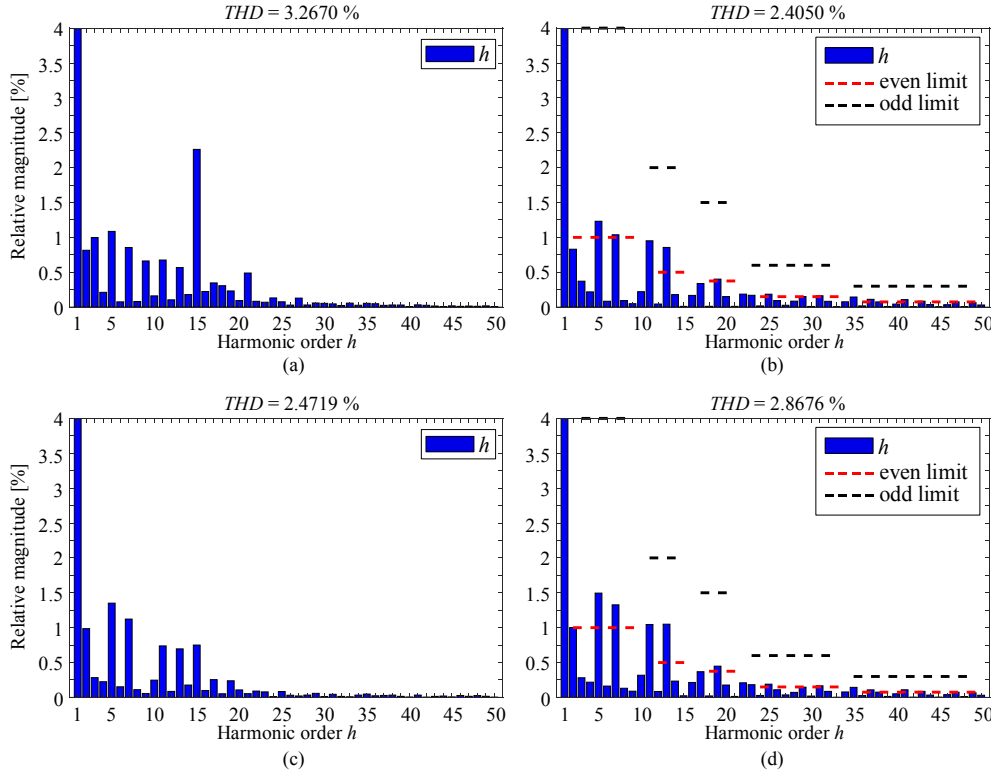


Figure 4.51 Simulated harmonic content of the open-end system with iterated filter parameters to improve the attenuation. (a) Inverter-side current with SVM, (b) grid-side current with SVM, (c) inverter-side current with the SPWM, and (d) grid-side current with the SPWM. The power factor  $PF = 1$  in all subfigures.

The zero-sequence current in the case 2 system has approximately the same rms value as the zero-sequence current in Case 1. Although the voltage of the case 2 system is larger, the inverter-side inductor is also larger limiting the increase in the current. However, the open-end system with the higher DC link voltage still seems to need the modified filter more than the Case 1 system in order to provide adequate grid-injected current. One key difference that can have an effect on this is the relation between the capacitor branch impedance, which is on the zero-sequence current path, and the transformer branch impedance. This relation is depicted in Figure 4.52.

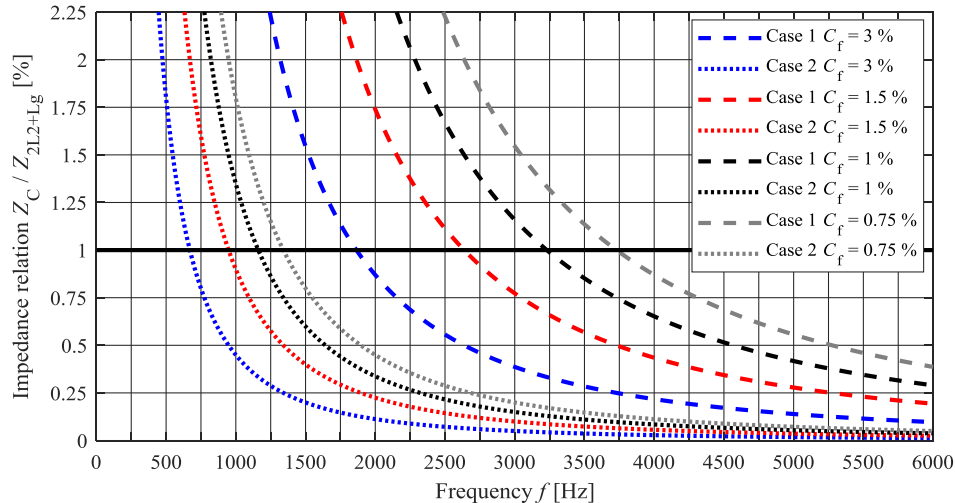


Figure 4.52 Relation of the capacitor branch impedance  $Z_C$  to the transformer branch impedance  $Z_{2L2+Lg}$  for Case 1 (dashed) and for Case 2 (dotted) as a function of frequency with four different capacitor values. The black line depicts the point where the impedances are equal.

As can be seen, the case 1 capacitor branch impedance is lower than the transformer branch impedance in a much lower frequency range than with the case 2 system. A faster reduction in the capacitor branch impedances results in more low-order harmonics trapped in the loop formed by the filter capacitors and not driven into the transformer, and which are thus not seen in the grid-injected current. In addition, if the zero-sequence loop is considered, there is an  $LC$  circuit formed by the two inverter-side inductors and the capacitor, which can have a resonance frequency not seen by the control system. Resistances, such as the capacitor equivalent series resistance  $ESR$  or the damping resistor  $R_d$ , make the resonance peaks of the series resonance wider meaning that this resonance frequency of the zero-sequence loop does not have to be at the driven frequency to have an effect on the frequencies adjacent to the resonance frequency.

Subfigures (a)–(d) in Figure 4.53 illustrate the aggregated filter component energy of the open-end system with the SVM and the SPWM and the 2Par system with and without tolerances. When the filter is designed with the same principles for the open-end system and the 2Par system with the DC link voltage being the same, the energy stored in the filter components of the open-end system with the SVM is slightly smaller than in the filter component of the 2Par system. Using the SPWM with the open-end inverter resulted in approximately the same energy in both systems. Modifying the filter by decreasing the capacitor to one-fourth of the original and increasing the inverter-side inductor by 50 % results in an increased energy of the open-end system. Now, the 2Par system filter components stored less energy compared with the open-end system.

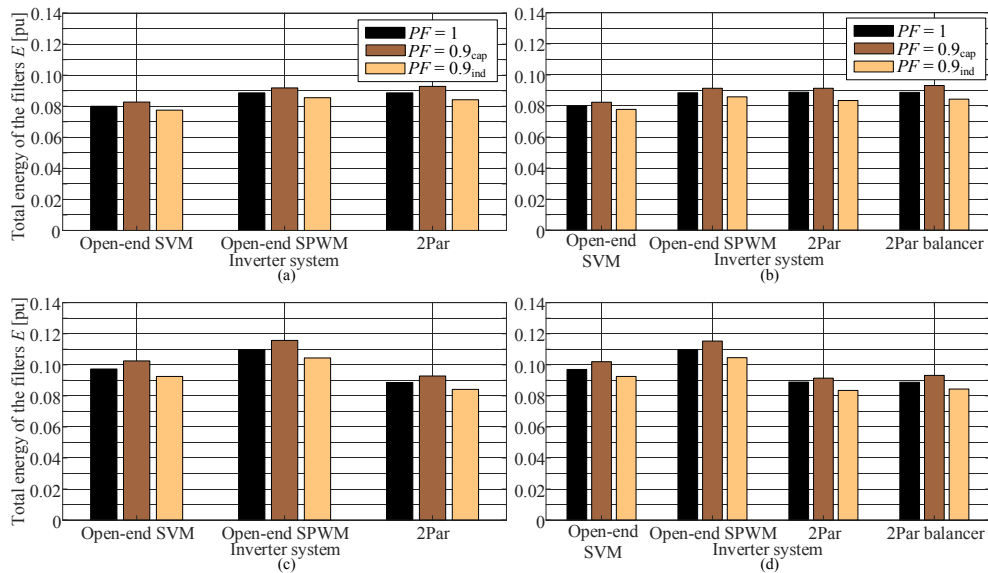


Figure 4.53 Simulated aggregated energy of the open-end system filter components and the 2Par system (a) with the nominal filter design and identical components, (b) with the nominal filter design and tolerances in components, (c) with the modified filter design with identical components, and (d) with the modified filter design with tolerance in components.

Remembering that the *THD* was better for the 2Par system even when compared with the open-end system with a better filter, we may state that from the viewpoint of the component energy, the open-end system with a doubled grid voltage does not offer much benefits when used instead of the 2Par system. However, there are no significant disadvantages either. Considering the number of components, the open-end system, in general, requires one capacitor less than the 2Par system. In addition, the larger output voltage may give some leverage in the transformer design, and the higher apparent switching frequency provides more room to optimize both the filter design and the controller design, which is not studied in detail in this dissertation.

### Zero zero-sequence modulation

Obviously, using the SPWM only with the open-end inverter results in an unfavourable outcome considering both the grid-injected current *THD* and the energy stored in the filter components compared with the 2Par system. Using the SVM results in a better *THD* and a smaller energy stored in the filter component, which, however, is still larger compared with the 2Par system. Of course, the inverter switching losses were not considered here. These losses are lower for the open-end system, which has half the DC link voltage compared with the 2Par system.

Naturally, if the SVM is used, the zero-sequence current has to be taken into account in the component design if it is not minimized or removed. Subfigures (a–d) in Figure 4.54

present the simulated zero-sequence current of Case 1 with the SVM, Case 1 with the SPWM, Case 2 with the SVM, and Case 2 with the SPWM, respectively. Nominal filter values were used. With the modified filter values, that is, the increased inverter-side inductor and the decreased capacitor, the  $i_0$  amplitude would be lower especially for the case 2 system. The current amplitude in subfigure (c) corresponds to around 10 % of the nominal output current.

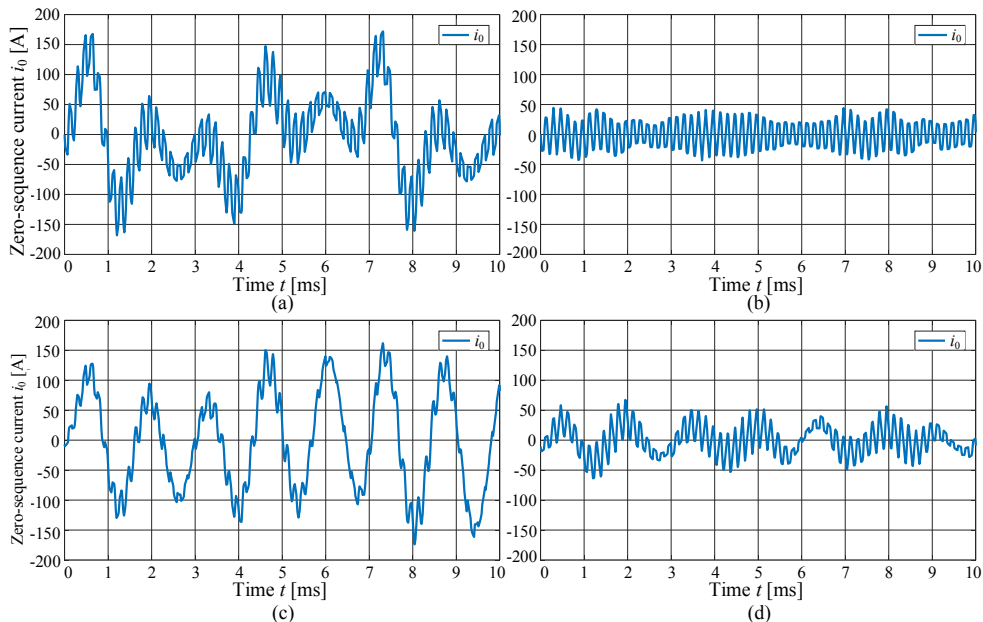


Figure 4.54 Simulated zero-sequence current  $i_0$  of the case 1 and case 2 open-end inverters with  $PF = 1$ ; (a) Case 1 with the SVM, (b) Case 1 with the SPWM, (c) Case 2 with the SVM, and (d) Case 2 with the SPWM.

The zero common-mode modulator from Korhonen et al. (2017) was used in the simulations. In this modulation method, the zero-sequence signal is injected into the reference voltages to produce the SVM. Cancellation of the zero sequence is done by generating the actual reference voltage of each phase by using two reference voltages with a  $120^\circ$  phase shift (Korhonen et al., 2017). The benefit of the zero common-mode modulator is that the resulting zero-sequence current is minimized without any additional control loops. Ideally, the modulation method with dead time compensation can practically totally remove the zero-sequence current. In reality, there is a small amount of zero-sequence current, the removal of which would require a specific zero-sequence control. The zero common-mode modulator does not allow voltage doubler operation, which leads to an inverter-side inductor of  $L_{1,ZCM} = 87 \mu\text{H}$ . Otherwise, the nominal component designs from Case 1 are the same. The resonance frequencies with nominal values were  $f_{r1} = 932.5 \text{ Hz}$  and  $f_{r2} = 1110.2 \text{ Hz}$ .

A comparison of the zero-common mode modulator simulation results with the case 1 and case 2 open-end results shows that the zero-sequence current is much larger when the conventional SVM and SPWM with unipolar modulation are used. The fundamental component frequency is highly dependent on the filter capacitor value. For instance, with the nominal capacitor, the fundamental of the  $i_0$  is 450 Hz while with one-fourth of the capacitor the fundamental is 1050 Hz. The zero-sequence current also contains a clear spike, which occurs at the frequency of 150 Hz. This spike occurs during zero crossing of the phase currents. The circulating zero-sequence current flows through the path formed by the inverter-side inductors and the filter capacitors.

Subfigures (a), (c), and (e) in Figure 4.55 show the zero-sequence current  $i_0$  calculated from the inverter-side current  $i_{11}$  with three different damping resistor values, 200 mΩ, 600 mΩ, and 1 Ω, respectively. Subfigures (b), (d), and (f) present the corresponding harmonic content of the grid-injected current  $i_g$ . With a lower damping resistor value the zero-sequence current contains 450 Hz as the strongest component. The 150 Hz spikes are also seen. Increasing the damping causes the higher frequency components to decrease while the 150 Hz spiking becomes dominant. Even though the zero-common mode modulator is not perfect, the circulating current is certainly at a better level compared with the SMV and SPWM.

Increasing the damping resistor results in a worse *THD* in the grid-injected current, and for instance, the fifth harmonic was clearly higher in amplitude. In addition, with a larger damping resistor value the resistor losses tend to increase. Using only one capacitor damped with  $R_d = 1 \Omega$ , the power loss in the resistor was around 3.1 kW calculated with the first 65 harmonics to include the switching frequency components. This power corresponds to 0.15 % of the nominal power of the open-end inverter. The grid-injected current *THD* was 2.1657 % with  $PF = 1$ , whereas the split-capacitor damping with the same damping resistor value resulted in 2.7892 % *THD*. The damping resistor losses were 2.79 kW. If a single capacitor was used with an even larger, for instance 2 Ω resistor, the *THD* would be even better yet the losses would be over 5 kW. To put these losses into a better perspective, they correspond to common single and three phase electric sauna heater power levels, respectively.

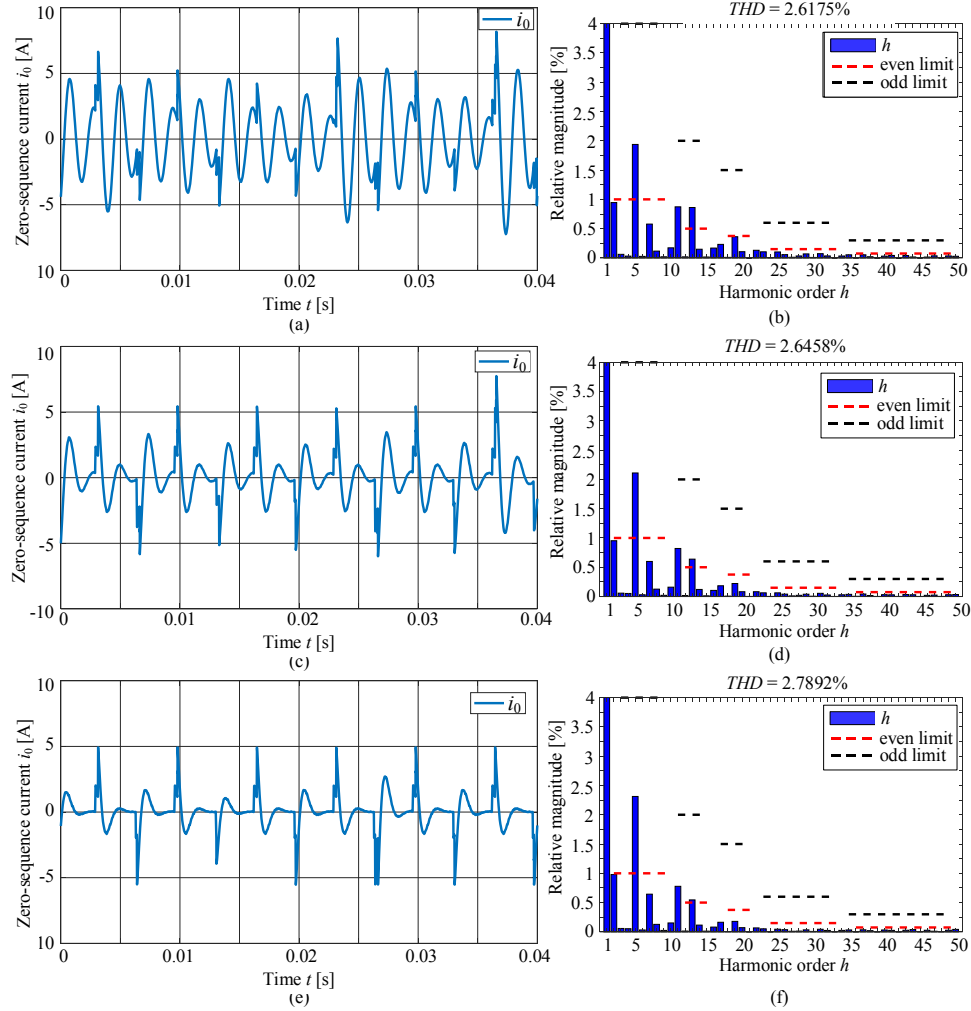


Figure 4.55 Simulated zero-sequence current  $i_0$  ((a), (c), and (e)) calculated from the inverter-side current and the corresponding grid-injected current harmonic content ((b), (d), and (f)) with  $PF = 1$  with three different damping resistor values  $R_d = 200 \text{ m}\Omega$ ,  $R_d = 600 \text{ m}\Omega$ , and  $R_d = 1 \Omega$ , respectively.

Figure 4.56 presents the simulated THD of the grid-injected current (a) with identical components and (b) with tolerances in components. The simulations were performed with the nominal filter, with the filter with  $1.5L_{1,\text{OE}}$ ,  $C_f/4$ , and  $2L_{2,\text{OE}}$ , and with filters having only the capacitor  $C_f/4$  or the grid-side inductor  $2L_{2,\text{OE}}$ , respectively. Increasing the inductors and decreasing the capacitor yielded the best THD, whereas decreasing only the capacitor had only a marginal effect. Additionally, with the smaller capacitor, some of the higher harmonics, such as the 44<sup>th</sup>, were increased above the limits. Increasing only the grid-side inductor made also the THD smaller.

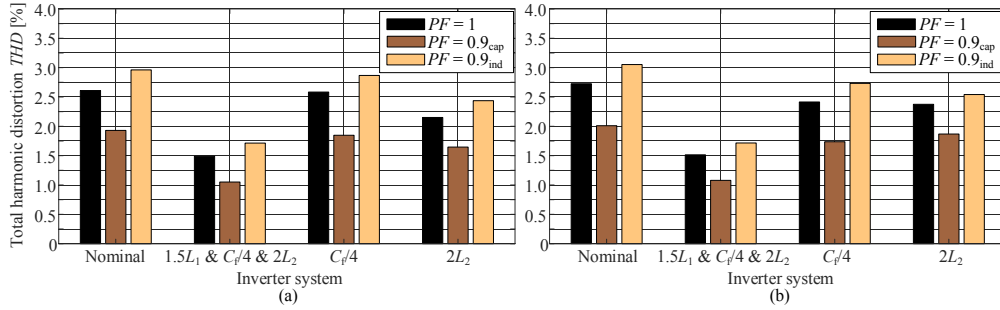


Figure 4.56 Simulated THD of the grid-injected current with the open-end inverter employing the zero common-mode modulator. The nominal filter and four different filter values are shown here. (a) with identical filter components and (b) with tolerance in component values.

Consequently, the best way to achieve a better THD with the open-end system (including the conventional SVM and SPWM) is to increase the inductor values. However, this leads to larger components as the energy stored in the components is also increased. Figure 4.57 presents the simulated total energies of the filter components with the open-end inverter using the zero common-mode modulator. In subfigure (a), the components were identical, whereas in subfigure (b) tolerances were added to the components.

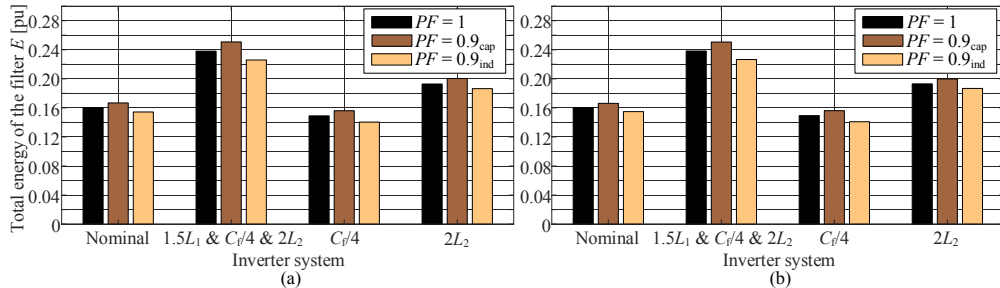


Figure 4.57 Simulated total energies of the filter components with the open-end inverter employing the zero common-mode modulator. The nominal filter and four different filter values are shown here. (a) with identical filter components and (b) with tolerance in component values.

As can be seen, with the 50 % larger inverter-side inductor and the doubled grid-side inductor, the energy was significantly increased compared with the nominal design. Even the fact that the capacitor was decreased to one-fourth did not have a significant effect. When only the capacitor was decreased, also the energy was only marginally decreased.

When comparing the THD and energies to the case 1 and case 2 open-end systems, we can see that minimizing the zero-sequence current leads to a better THD but larger components. Figure 4.58 presents a comparison of the zero common-mode modulator system and the Case 1 system. The energy of the zero common-mode modulator case with

the increased inductors and decreased capacitor results is approximately 2.25 times as high as in Case 1 with the SVM. At the same time, the *THD* is less than half.

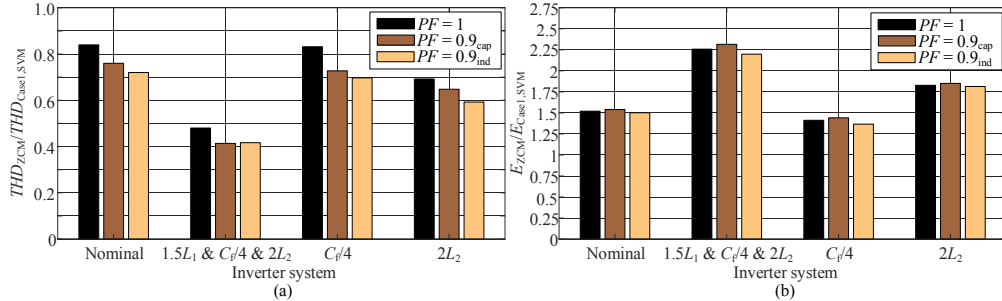


Figure 4.58 (a) Simulated *THD* of the grid-injected current of the open-end inverter employing the zero common-mode modulator normalized to the Case 1 system employing SVM. (b) Total energies of the filter components of the open-end inverter employing the zero common-mode modulator normalized to the Case 1 system employing SVM. The nominal filter and four different filter values are shown here.

### Key findings

- Open-end inverter is more susceptible to grid voltage harmonics than the 2Par system.
- With similar filter design rules, the grid-injected *THD* is larger for the open-end system.
- Decreasing the capacitor is the preferable option to enhance the filtering and grid-injected current *THD* of the open-end system. However, the 2Par system *THD* is still better than the open-end solutions.
- The open-end system has a significant zero-sequence current flowing through the loop formed by the filter capacitors.
- The zero-sequence current excites a resonance that is dependent on the  $L_1$  and  $C_f$  values
- A zero common-mode modulator can minimize the zero-sequence current.
- Zero common-mode modulator inherent 150 Hz pulse in the  $i_0$  excites resonances in the current path, thus requiring increased damping.

## 4.3 Experimental tests

An experimental test setup employing commercial inverters and a common transformer was used to test parallel inverters in operation. ABB ACSM1 inverters with WFU-02 *LCL* filters were controlled with the Xilinx Kintex KC705 FPGA. Gate signals were fed directly to the ACSM1s, the current and DC link voltage measurements of which were used in the control system. Figure 4.59 presents the parallel-inverter test setup and its

main components. The grid-side voltage for grid synchronization was measured after the filter by using three LEM DVL 1000 voltage transducers. In addition, similar voltage transducers were used in the setup to measure DC link voltages. All inverters were supplied by the same autotransformer and a six-pulse rectifier.

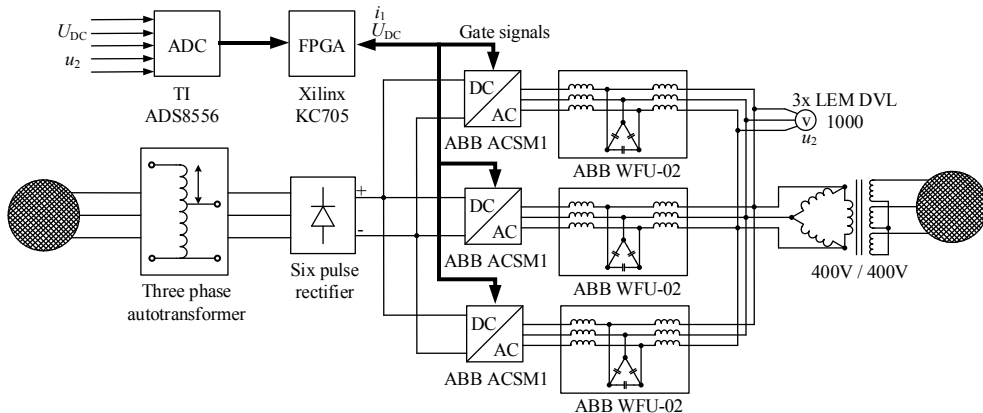


Figure 4.59 Hardware of the parallel-inverter test setup with main components and measurements. The test setup was essentially the same as the one used in (Purhonen, 2014).

The synchronous reference frame PI control was used for the inverter currents. Moreover, the DC link voltage controller was implemented in the control system. However, as the supply provided constant voltage, which would lead the DC link voltage controller winding to the upper limit, the output current was set by limiting the current reference value given as the DC link voltage controller output.

Two Agilent DSO6104A 1GHz 4GSa/s oscilloscopes were used to store the measurements. Two Agilent N2774A 15Apeak and Two Agilent 2781A 150Apeak current probes were employed for current measurements, and Tektronix p5120 HV differential probes were used to measure the voltages. Both oscilloscopes were triggered with the same signal generated by the Tektronix AFG3252 function generator. Subfigures (a)–(c) in Figure 4.60 present the inverters, filters, and the measuring equipment, respectively. The inverters had a specially designed interface board (green) illustrated in subfigure (a). This interface board allowed feeding in of the gate signals and retrieving the inverter current and DC link voltage measurement data.

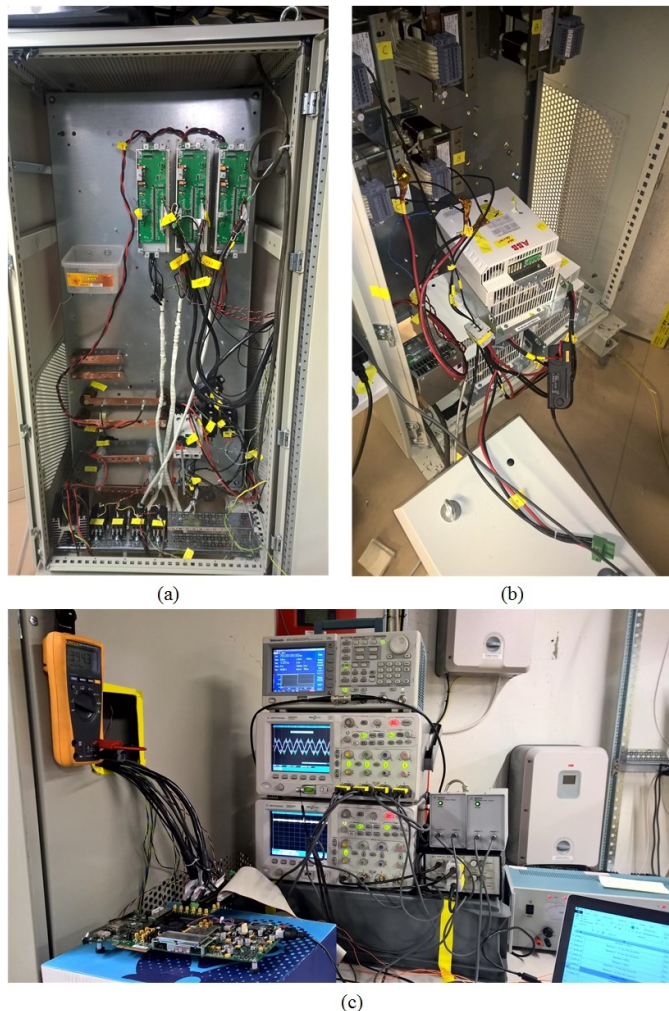


Figure 4.60 Hardware of the parallel-inverter test setup; (a) the inverters and the DC input inside the cabinet, (b) the *LCL* filter and the transformer, and (c) the KC705 control board (in front) and the oscilloscopes and the function generator.

The grid-injected current of the inverters with the *LCL* and *LC* filters and the open-end inverter with the *LCL* filter was measured. In addition, the grid-side voltage and the inverter-side current were stored. In some cases, inductor currents and capacitor voltage was measured from one phase for energy calculations.

#### 4.3.1 Measurement of parallel-connected inverters

It turned out to be quite difficult to perform measurements in such a way that the results were actually comparable. The supply power and grid transformer nominal power of the

test setup matched but as the grid inverter power, particularly the filter nominal power, was around the nominal power of the grid transformer, the filtering was not as good as it should have been.

If the grid inverter operates with a much lower power than the nominal power (i.e., nominal current) of the filter, the filtering will not work as well as it should. For instance with  $PF = 1$ , the voltage amplitude remains the same regardless of the current amplitude. The pulse-width modulator still produces the same harmonics that cause the harmonic current to flow, thereby resulting in a larger proportion of harmonics in the output current. This relatively high amount of harmonics makes the output  $THD$  to deteriorate.

Figure 4.61 presents the inverter-side current in subfigures (a) and (c) and the grid-side current in subfigures (b) and (d) of the single inverter with an  $LCL$  filter and inverter 1 of the two-inverter system driving around 3.4 kW of power to the grid. The measured currents were filtered with a 200 sample moving-average filter to get rid of the measurement noise. As can be seen, the inverter-side current includes a very high amount of switching frequency ripple while the filtered grid-side current also shows a distorted waveform. With two inverters in parallel, employing their own controls, the grid-side current is slightly better in terms of its waveform. For the single inverter, the current ripple around zero crossing is around 30.2 % of the peak value, and for the inverter 1 of a two parallel-inverter system, the current ripple is around 32 %. Naturally, the inductor still limits the current ripple to the original maximum value, but with a lower current amplitude, the ripple is larger and results in an undesirable current waveform as can be seen in Figure 4.61.

Figure 4.62 presents the grid-injected current harmonics for the single inverter case (a) and for the two inverters in the parallel case inverter 1 current (b). Both currents include a fairly high amount of harmonics around the 10<sup>th</sup>–20<sup>th</sup> harmonics. The  $THD$  is slightly better for the two inverters case, and many of the harmonics between the tenth and twentieth are lower. However, as the inverter 2 current apparently was not stored and it was not possible to make comparable measurements with three inverters, this measurement cannot be considered a reliable proof of the grid multiplication. Measurements with the  $LC$  filters were also done by bypassing the grid-side inductor of the  $LCL$  filters. Of course, by doing this, the current harmonic attenuation was made worse, which resulted in poorer current waveforms,  $THD$ , and harmonic content in general.

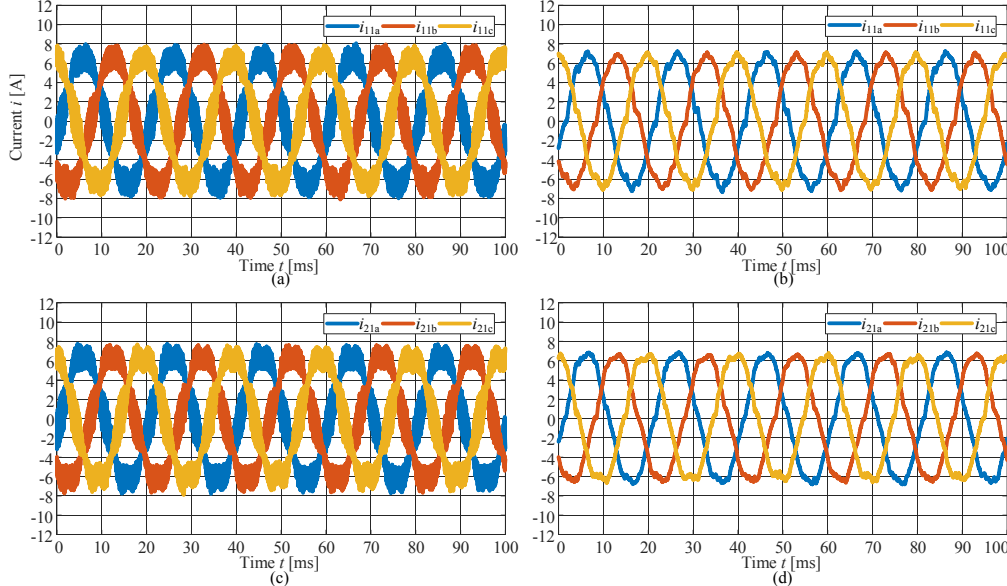


Figure 4.61 Inverter-side current of the single inverter with an  $LCL$  filter (a), the filtered grid-side current (b), the inverter-side current of inverter 1 of a two-inverter system (c), and the grid-side current of the inverter 1 of the two-inverter system (d). Both currents were digitally filtered with a 200 sample moving-average filter to remove the measurement noise. The measurements consisted of 4 million data points, i.e., the sampling frequency was 250 MSa/s.

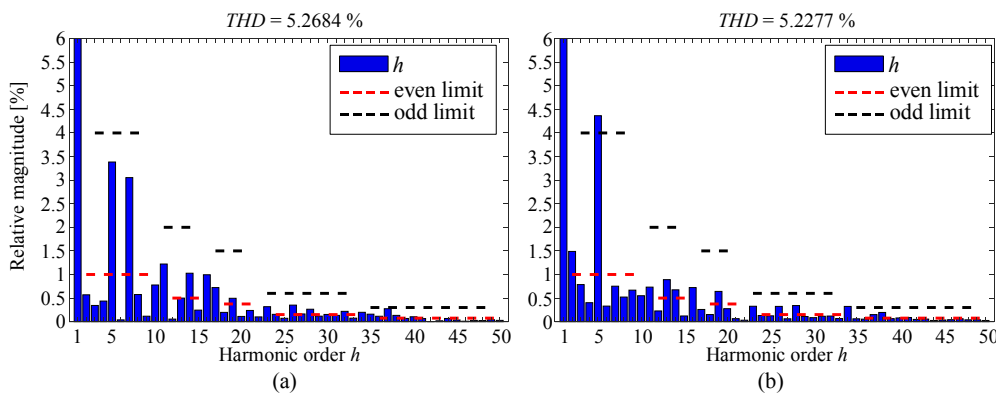


Figure 4.62 Grid-injected current harmonics of the single inverter with an  $LCL$  filter (a) and inverter 1 of the two-inverter system (b).

#### 4.3.2 Open-end grid inverter

The test setup was also transformed into an open-end inverter system. The transformer was turned around to have a delta connection on the grid side, and the wye windings were

opened and connected to the open-end inverter. The nominal voltage of each open winding was now 230 V. The inverter-side inductor and capacitor  $LCL$  circuit was built from scavenged components taken from inverters disassembled from some older test setups. Figure 4.63 illustrates the open-end test setup.

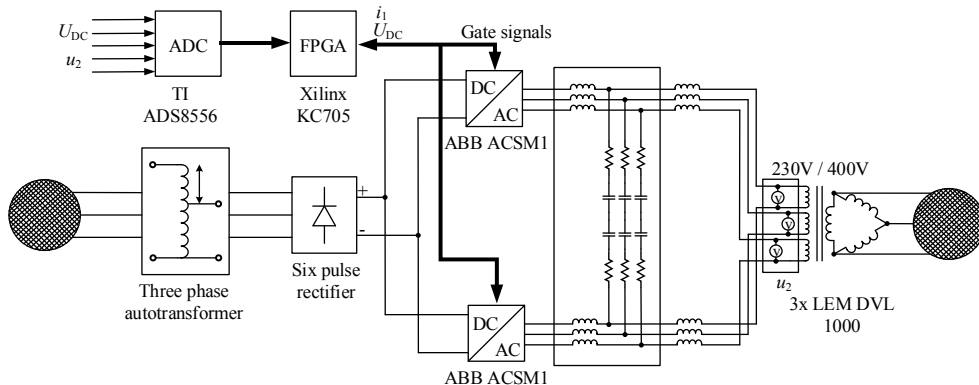


Figure 4.63 Schematic of the open-end inverter test setup.

Figure 4.64 presents the inverter-side inductor and filter capacitor part of the open-end inverter filter. For both inverter bridges in the open-end system, the inverter-side inductor was constructed by connecting two 1.5 mH ferrite core inductors in series. Between the inductors, two capacitors in series per phase were connected. The capacitors were  $C_f = 1.2 \mu\text{F}$  and had their own 1  $\Omega$  damping resistors, resulting in the total damping of 2  $\Omega$ . The transformer inductance was estimated from the transformer plate values to be  $L_g = 1.1 \text{ mH}$ , and separate 600  $\mu\text{H}$  inductors were used as the grid-side inductors. With these values, the resonance frequencies were  $f_{r1} = 4268.1 \text{ Hz}$  and  $f_{r2} = 5025.2 \text{ Hz}$ . The apparent switching frequency was  $f_{sw} = 20 \text{ kHz}$ .

Sinusoidal PWM was used in the modulator for the test setup. Originally, the idea was to use both the SVM and a special clamping modulator, but problems were soon detected with the zero-sequence. The only measurements in which power was fed to the grid were made with the SPWM modulator.

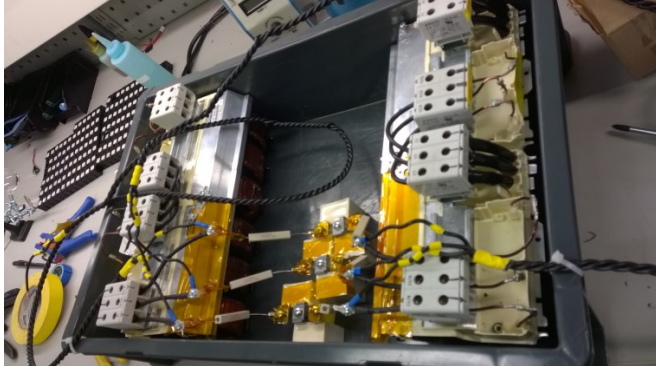


Figure 4.64 Open-end inverter inverter-side inductors and filter capacitor made from scavenged components.

Subfigures (a)–(b) in Figure 4.65 present the inverter-side and grid-side currents of the open-end system, respectively. As can be seen, the current waveform is not a sinusoidal waveform as was expected. The currents include a high amount of the third harmonic; approximately 5.9 % in the inverter-side current and 5.5 % in the grid-side current. The probable cause for the third harmonic is the dead time compensation in the modulator, which may not have been most accurate. Subfigures (a)–(b) in Figure 4.66 represents the transformer voltage, the DC link voltage, and the zero-sequence current in the inverter-side current, respectively, for (a) and (b). The transformer voltage was measured when approximately 3.7 kW of power was injected to the grid. As can be seen, the voltage waveform appears to be normal. The voltage itself contains approximately 0.6 % of the fifth harmonic, 1 % of the seventh, and 0.3 and 0.1 of the eleventh and thirteenth harmonics, respectively. The THD of the grid voltage was 1.3072 %. If there was slight saturation in the transformer, it could be determined from the measured voltages. The voltages were the same also without any current injected into the grid.

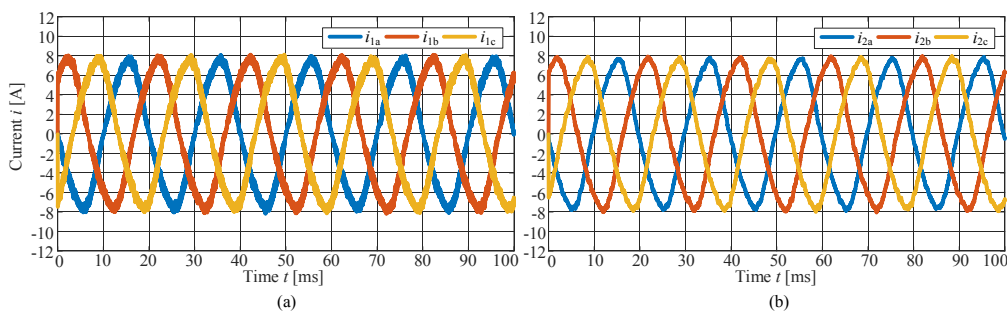


Figure 4.65 Open-end inverter inverter-side currents (a), and grid-side currents (b). The currents were filtered with a 200 sample moving average to get rid of the measurement noise.

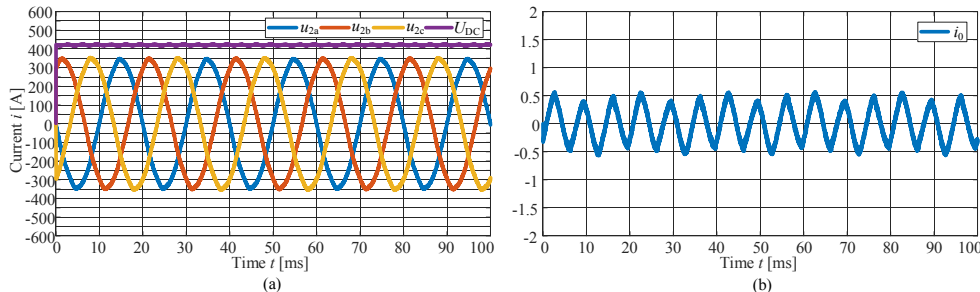


Figure 4.66 Open-end transformer winding voltages and the DC link voltage (a) and the zero-sequence current fed by the inverter calculated from the inverter-side current.

The arithmetic mean value of the DC link voltage was 421.4 V, which shows that the open-end inverter requires a lower voltage on the DC side compared with the 2Par system. Of course, the applied voltage was higher than the theoretically needed 0.5774 times the 2Par system, when the 2Par system uses SVM. However, this 421 V is still 25 % lower, which results in lower inverter bridge losses.

Tests were also carried out using a resistive load instead of the grid. The current waveforms presented the same third harmonic while the voltage measured on the load side of the transformer was of a sinusoidal waveform.

#### 4.4 Discussion and Conclusion – Chapter 4

In order to make the simulations closer to real applications, the simulation models were included with noise in the DC link input currents to model partial shading or wind gusts and mechanical oscillations that would be present in photovoltaic and wind power plants. Further, the measurements were added with noise around 5 % of the corresponding base values to make the simulation more realistic. Digital delay was also included in the control system. As the measurements were triggered in the peaks of the carrier wave, the control output that was used at the modulator was updated in the middle of the carrier wave, which meant that the modulator always used the previous values as in a real application. This ensured that digital delay was present in the simulations.

Especially the noises in the measurements caused much of the low-frequency harmonics in the output current of the inverters. The effect of noise could have been mitigated by employing a higher sampling rate and using a median filter to rule the noise out, but as this problem was already mitigated by the reduction in the controller bandwidth, it was not necessary in the simulations. Moreover, the measured grid voltage was chosen not to be filtered so that the feed-forwarded voltage would correspond to the actual grid voltage.

The simulations showed that the *THD* becomes better as more inverters are connected in parallel. This was true both for the identical filter case and for the filters with tolerance in the component values. Of course, if the inverters were truly identical, the effect of the

grid multiplication and thereby the decrease in the *THD* would be much stronger and shown equally in every inverter in the parallel-inverter system. Tolerances can cause deviation between the inverters, which can be seen as deviation in the inverter powers in the case where all inverters share a common DC link.

According to the simulations, the open-end inverter can also be operated with space vector modulation or some other modulation technique that includes a zero-sequence injection. However, it is required that the transformer is designed to also meet the extra zero-sequence current which is not cancelled in the transformer secondary. On the grid side, the transformer connection cancels the zero-sequence current and it is not fed to the grid.

#### 4.4.1 Identical filter parameters

When comparing the simulation results of the *LCL*, *LLCL*, *LC+L*, *LC*, and *L*-filter configurations, it could be seen that the *LLCL* configuration benefits from the third resonance frequency so that its grid-injected current *THD* is the best. However, this requires special attention in the capacitor branch *LC* circuit design. The *LLCL* filter also requires the split-capacitor damping to preserve the highest resonance frequency. However, the simulations showed that it was still beneficial to include a small amount of damping in the  $L_C C_1$ , where  $C_1$  was set as  $C_1 = 0.1 C_f$  and the  $L_C$  was dimensioned to place the  $f_{r3}$  over the switching frequency. Without damping in the  $L_C C_1$  branch, the higher switching frequency sideband harmonics were increased compared with the *LCL* filter. When the *THD* was calculated according to the standards, considering the first 50 harmonics, the difference between the *LCL* and *LLCL* configurations was small.

When comparing the *LC* and *LC+L* configurations, it was seen that including a common grid-side inductor in the filter configuration can lead to a significantly better output *THD* for the inverters. However, if the inductor value is not decreased in proportion to the number of parallel-connected inverters, the energy of this common inductor quickly becomes very high and renders the inductor impractical. Even though using the common inductor results in a lower energy in the *LC* part of the filter, the total filter energy is much larger with the *LC+L* configuration. As this grid-branch inductor is also multiplied by  $n$ , it has an effect on the DC link voltage needed for operation. The *LC* configuration requires less DC link voltage compared with the *LC+L* configuration.

The *L*-configuration requires a larger capacitor with more inverters when individual inverter-side inductors are in parallel. If the capacitor and the grid-side inductor were kept the same regardless of the number of paralleled inverters, the attenuation would remain the same but it would be inadequate to filter the harmonics from all of the paralleled inverters. The common grid-side inductor of the *L*-configuration also faces the same dilemma as the *LC+L* inductor; with a large number of high-power low-voltage parallel-connected inverters, the inductor design becomes very difficult if not impractical.

The  $LC$ ,  $LC+L$ , and  $L$ -configurations require larger DC link voltage compared with the  $LCL$  and  $LLCL$  configurations, which have individual grid-side inductors. This increased voltage not only causes greater harmonics in the output current thereby degrading the  $THD$ , but also makes the inverter bridge losses to increase. Furthermore, the individual switch voltage stress is larger. Commonly, low-voltage switching devices have voltage ratings of approximately 1.7 kV in applications with the DC link voltage around 1 kV. To have a 1.2 kV voltage at the DC link would require a fast and robust control, and most likely, special snubber circuits to ensure safe operating conditions. From the filter design perspective, the increase in the maximum DC link voltage should be considered as a design constraint. This, of course, applies to a single inverter facing a large grid inductance or having a large grid-side inductance, but with parallel-connected inverters, this voltage increase might take place with relatively low grid-side inductances.

The average filter designs were not covered in the actual simulation study of this dissertation for a simple reason. It became quite clear that in a situation where the grid voltage includes harmonics and the measurements contain noise, which may be difficult to filter out, the filter designed according to the conventional constraints may not provide adequate attenuation for a single inverter. When more inverters are connected in parallel, the attenuation becomes better and the harmonics more suppressed. From this perspective, making the capacitor smaller to provide higher resonance frequencies with a higher number of paralleled inverters results in poorer filtering with a lower end of the range of  $n$ . Should the filtering already be on the limits, making it even worse would not be a desired option.

The simulations performed with identical parameters also showed that calculations done in Chapter 3 deviate from simulations especially with respect to the capacitive and reactive power factors. With a single inverter, the voltage deviation would be low enough to be neglected, but the situation is different with parallel-connected inverters connected to the same point. To demonstrate the author's learning curve, the calculations in Chapter 3 were left as they are and the error caused by the voltage deviation was addressed in the simulation sections.

When simulations were compared with the computational study results, it was apparent that the error increased with a higher number of parallel-connected inverters the error. With the unity power factor, the error remained low, but of course, if there was significant resistance in the current path to the grid, the voltage would also change with  $PF = 1$ . When the voltage was compensated in the calculations, the simulated and calculated energies were closer to each other. Considering the  $\pm 5\%$  error margin appropriate, the voltage compensation factor  $\sqrt{1 \pm L_g n}$  was found to be suitable for the  $LCL$ ,  $LLCL$ ,  $LC$ , and  $LC+L$  configurations. With the  $L$ -configuration,  $(1 \pm L_g n)$  was found to work. When the noises from the measurements and the DC link current were excluded, these factors led to an error margin of  $\pm 1\%$ . Of course, the calculations did not include the effect of resistances, which also cause a small deviation between the calculations and simulations. However, in general, the resistances are small enough to be neglected.

A clear conclusion can be made; with parallel-connected inverters, the grid voltage deviation has to be taken into account by applying the presented factors when the filter component energies are assessed.

#### 4.4.2 Distinct filters

The filter components were included with tolerances on the scale of  $\pm 20\%$ . The simulations showed that similarly to the identical filter components, the general trend in the output current *THD* was still in decline especially when one master inverter control was used for all inverters and the powers were not controlled to be equal. Because of the tolerances in especially the inverter-side inductors and with the same control for all the inverters, different amounts of volt-seconds are lost in the inverter-side inductors. This difference in the inductive voltage losses resulting in unequal voltage phase shifts between the inverter voltage and the capacitor voltage is the cause for unequal powers for each parallel-connected inverters.

In practice, the unequal powers would not be problematic given that the tolerances are not very high. However, they are usually not known, and in the worst case, the parallel-connected inverters have tolerances in the opposite direction, which maximizes the effect of tolerances. In the simulations, the nominal power of each inverter was 1000 kVA, and with tolerances, the maximum energy of any inverter was approximately 1400 kVA. A 40 % larger power would need quite a large margin in the individual component designs requiring unnecessary large components. The powers, of course, should be balanced.

The power balancing control was implemented by adding extra current controllers to control the difference between the inverter 1 currents (in the dq frame) and the other parallel-inverter currents to zero. One controller per inverter and the output of these controllers were added to the reference voltages. This method proved to be effective enough even though the inverter-side current was used in the balancing control. The error in the grid-side powers was still much less than 1 %. If the grid-injected powers have to be more accurately controlled, the power balancing should perhaps be implemented by using the grid-side currents.

Balancing the output powers of the inverters has an impact on how the *THD* behaves with respect to the number of inverters in parallel. Now, the general trend was still decreasing, but depending on the tolerances, some inverters also presented a greatly increased *THD* when connected to the system. For instance with balanced powers, inverter 5 presented a much higher *THD* compared with the others and the case when the powers were not balanced. Additionally, adding inverter 5 in parallel with inverters 1–4 resulted in a larger decrease in the *THD* of inverters 1 and 2, but a slight increase in inverters 3 and 4.

Using the same control, that is, the same reference voltages for all inverters, leads to a situation where all inverters produce the same common-mode voltage. This minimizes the circulating zero-sequence current. Balancing the output powers leads to an opposite

outcome. The common-mode voltages become distinct and more current circulates in the system.

The inverter 5 tolerances were such that the inductance in the filter was smaller than that of the other inverter filters. This led to a situation where the other inverters were driving more circulating current into the inverter that had the least impedance in the current path. When operating without the power balancing control, the circulating current was small, but when the powers were balanced, the current became high especially in inverter 5. This high current would be problematic for the inductors that are in the current path, and in some cases, could ultimately lead to inductor saturation.

Considering the circulating current, the *LCL* and *LLCL* configurations benefit from their grid-side inductors as there is now more inductance in the circulating current path. With the *LC*, *LC+L*, and *L*-configurations, the circulating current is larger as they lack the grid-side inductor in the current path. The *L*-configuration actually benefits from the common *CL* circuit on the grid side; both with balanced and imbalanced inverter powers, the grid-injected current *THD* remains basically the same.

In general, the component energies with tolerances are larger than the component energies with identical filter components. However, depending on the tolerances, there may also be cases where the filter energy would be decreased because of the tolerances. The energies in the simulations were calculated with currents and voltages of each inverter but with the nominal filter component values. Without the power balancing control, the inverter 1 filter energy was in general larger than in the identical case, and the filters of inverters 2–4 stored less energy than in the identical case. The energies of inverters 5 and 6 were clearly larger than in the identical case for the *LCL* and *LLCL* configurations.

The *LC* configuration presented very similar energies normalized to the identical case energies compared with the *LCL* and *LLCL* configurations. The *LC+L* configuration, however, showed that the additional grid-branch inductor evens out the total energy of the filter configuration and its variation because of the tolerances. Of course, as the most energy, especially with a high number of  $n$ , is stored in the common grid-side inductor, the variation in the  $L_1$  and  $C_f$  values is not seen as clearly as in the *LC* configuration. With the powers balanced, the *LCL*, *LLCL*, *LC*, and *LC+L* configuration energies were very close to the identical case.

Compared with identical components, the *L*-configuration presented a very similar grid-injected current *THD* with tolerances. This is of course due to the fact that the current harmonic attenuation is only dependent on the common *CL* circuit, and its tolerances did not vary with respect to the number of parallel-connected inverters. Of course, when the *L*-configuration requires the capacitor to be increased as the number of paralleled inverters increases, the tolerance can change thus affecting the attenuation. However, the effect would be clear; a larger capacitor, that is, a positive tolerance, leads to better attenuation.

The normalized capacitor energy in the *L*-configuration tends to increase with  $n$  while the grid-side inductor energy increases with the capacitive power factor and increases with the inductive power factor as the PCC voltage changes with reactive current. The inverter-side inductor energy presents similar variation as the total filter energies with the other configurations.

Considering the grid-injected *THD*, the *L*-configuration presents the greatest robustness against the tolerances when the capacitor is increased with  $n$ . The *LLCL* configuration also benefits from the additional resonance frequency. Even though tolerances can shift this frequency farther from the switching frequency, the attenuation is very low around and after the third frequency. Compared with the *LCL* configuration, the *LLCL* configuration presented better grid-injected *THD*.

#### 4.4.3 Open-end inverter

The open-end inverter with three different cases was simulated and compared with the conventional two parallel-connected inverters system. Employing the SVM or some other zero-sequence injecting method causes additional zero-sequence current to flow in the inverter output current. If the transformer is designed with care to resist the zero-sequence current, some of this current can flow through the transformer windings causing no other problems than increased transformer losses. However, if the transformer is not designed to withstand the zero-sequence current, it can easily be saturated especially if a three-phase transformer design is used for the open-end transformer. When the transformer windings are wound on the same core, there is always leakage flux between the phase windings and between the primary and secondary windings. As there is no cancellation of the zero-sequence current on the secondary (inverter) side of the transformer, when using the SVM, a three-phase transformer would be saturated by the relatively large 150 Hz zero-sequence component.

In the simulations, three single-phase transformers were used. This was done to make sure that there would be no leakage flux problem between the windings and thus, no saturation. In an actual application, this might suffice especially if all of the phase transformers were protected with extra insulating material to prevent magnetic coupling. The saturation effect was, however, simulated with a very low value of magnetic branch impedance, which would correspond to the effect of core saturation in a transformer. As a result, the transformer current clearly included a great amount of the 150 Hz zero-sequence component.

It is pointed out here that the first time when the open-end inverter test setup was experimented, it was done with a space vector modulator. The result was that instead of driving approximately  $7.3 \text{ A}_{\text{rms}}$  50 Hz current per phase, the current seen on the oscilloscope was  $10 \text{ A}_{\text{rms}}$  of common-mode current with the frequency of 150 Hz. At first, the setup was mistakenly considered not to operate correctly.

Assuming that the transformer is designed to withstand the zero-sequence current without saturation and the leakage flux is minimized, an SVM modulator can be used with an open-end inverter. However, it will cause third-harmonic current and its integer multiples in the inverter-side current. The main path of this current is formed by the loop created by the inverter-side inductors and the filter capacitor. Depending on these circuit values and damping in the circuit, the zero-sequence current may produce some resonances around the multiples of the zero-sequence current.

The simulations showed that when designing the filter according to conventional design guidelines, the zero-sequence current may degrade the output current *THD*, especially for the Case 2 open-end system. With Case 2, the inverter-side inductor and filter capacitor impedance in relation to the transformer branch impedance decreased much faster compared with Case 1. This led to more zero-sequence current driven by the open-end inverter and worse transformer-side current. Decreasing the capacitor, thereby increasing the  $L_1C_F$  circuit impedance at lower frequencies, improves the transformer current and the grid-injected current *THD*. The same effect could be achieved by increasing the inductors, but this would lead to larger components and possibly more disturbance in the control.

Comparing the Case 1 and Case 2 simulations with the 2Par system showed that the 2Par has both a better grid-injected *THD* and less energy stored in the components. Additionally, the 2Par system presents greater redundancy than the open-end inverter, because if one inverter breaks in the 2Par system, there is still one inverter to drive at least partial power to the grid if necessary. If either of the open-end inverter bridges breaks, the system will be down. However, the open-end system presents other benefits, such as operation as a voltage doubler, which allows operation with a lower DC link voltage compared with the 2Par system when the output voltage levels are equal for both systems. The inverter bridge losses are proportional to the DC link voltage. Operating with the double output voltage (Case 2) would also be beneficial as the current of the open-end system would correspond to the individual inverter current of the 2Par system. Further, a lower current would allow a smaller transformer and lower conductive losses as less copper would be required in the transformer.

In motor applications, the zero-sequence current of the open-end inverter would cause problems because the motor inductances are usually much smaller than the filter and transformer inductances. The simulated zero-sequence-minimizing modulator proved to be helpful in mitigating the zero-sequence current in the open-end system. However, the modulator has an inherent pulse-like 150 Hz component, which may produce resonances leading to an increased current. However, it was found that the zero-sequence current with the minimizing modulator was still much less than with the conventional SVM and SPWM.

The zero-sequence minimizing modulator case also presented a greater grid-injected current *THD* than with the 2Par system. Increasing the inductors and decreasing the capacitor led to a situation where the *THD* of the open-end system was very close to the 2Par. Of course, the increased inductors caused an increase in the component energies,

which were now much larger than in the conventional paralleled inverter system. In addition, by minimizing the zero-sequence current, two of the benefits of the open-end system are lost; the output voltage is not doubled, and thus, the DC link cannot be halved, and the switching frequency of the line current is not doubled either. However, in applications where the common-mode voltage needs to be suppressed, the open-end inverter would be an interesting option.



## 5 Discussion and Conclusion

The design of a grid filter for parallel-connected inverters has some special features that distinguish it from the single inverter filter design. In order to provide both adequate attenuation and stable operation, these issues have to be taken into account in the filter design process. Otherwise, in the worst case, the outcome can be destructive for the filter components.

The main difference between the single inverter design and the parallel-connected inverters case is the resonance frequencies. Assuming identical filter components, the grid branch impedance is seen as multiplied by the number of parallel-connected inverters. This shifts the resonances lower than with the single inverter meaning that the resonance frequencies have to be determined with (3.34)–(3.42). Although the attenuation becomes better with the resonance shift, resonances at wrong frequencies can cause stability issues and potentially destructive operating conditions. This potential problem becomes more severe in applications operating with low switching frequencies where the space for resonance placement is narrow to begin with.

As in the single inverter case, the main driver of the inverter-side inductor  $L_1$  dimensioning is the aim to limit the inverter-side current ripple to a specified maximum value. The higher the ripple current is, the higher are the losses that the inverter bridge can experience, while inductor losses will correspondingly be lower. This, of course, works also in the opposite case. In parallel-connected inverters, the  $L_1$  value also affects the resonance shift. Increasing the  $L_1$  value leads to a larger resonance shift. For the  $LCL$ ,  $LC$ , and  $LC+L$  configurations, the limit value where  $f_{r2}$  converges when  $n$  approaches infinity is set by  $L_1$  and the filter capacitor  $C_f$  values. For the  $LLCL$  configuration, the limit value is also affected by  $L_C$  meaning that for the  $LLCL$  configuration the resonances are always lower than those of the  $LCL$  filter. However, comparing the resonance shift, the  $LLCL$  resonances change less with respect to the nominal (single inverter) frequencies than the other configuration frequencies.

The  $L$ -configuration experiences the resonance shift at the higher resonance frequency, which has no upper limit. However, the lower resonance remains unchanged because it is defined only by the capacitor and grid-side inductor values in addition to the grid inductance itself. The higher resonance frequency increases more with a larger  $L_1$ . Therefore, in a filter design process for the parallel-connected inverters, the  $L_1$  should also be considered from the viewpoint of the resonance shift and perhaps revised in order to find a good balance between the resonance frequency and inverter bridge losses.

In addition to the resonance shift, the parallel-connected inverters with individual filters are included with cross-coupling resonance, which has to be taken into account in the filter design. This resonance frequency is determined by the filter parameters, and it is not affected by the grid inductance. By designing the filter with the conventional design constraints of the single inverter and setting  $f_{r2} \leq f_{sw}/2$ , the cross-coupling resonance can be very close to the switching frequency especially with high-inductive grid connection.

In this case in particular, the cable inductances after the capacitors of the *LC* configuration can cause destructive operating conditions if the inverter synchronization is not performed well. A design constraint for the parallel-connected inverter filters, which differs from the single inverter, would be that the  $L_2$  dimensioning has to take into account the cross-coupling frequency. Equations (3.52) and (3.53) can be used to calculate the  $L_2$  value for a specific frequency, and (3.54) and (3.55) to assess the difference between  $f_{l2}$  and  $f_{rc2}$ .

The *L*-configuration benefits from the fact that there is no cross-coupling resonance. However, the filter capacitor must be dimensioned according to the total power level of the application to ensure proper attenuation.

Assessing the filter design with respect to the inverter DC link voltages, the *LC*, *LC+L*, and *L*-configurations need more attention especially with the common grid-side inductor dimensioning. If the total grid-side inductance ( $L_2 + L_g$ ) is large, the inverter DC link voltage may have to be raised from the intended value.

Component energy as a design constraint for the component optimization is outside the scope of this doctoral dissertation. However, at the system level, the total filter configuration energies were also analysed. The analysis showed that an increase in the inverter-side inductor value reduces the rise of energy when the number of parallel-connected inverters is increased.

A clear difference between the filter configurations can be found in the number of components. The *L*-configuration has the lowest and the *LLCL* configuration the highest number of components. A benefit of having fewer components is obviously that there are fewer components to fail. However, the *LLCL* configuration and its great attenuation at the switching frequency is also a benefit. The *LCL* configuration has  $n$  inductors less than *LLCL*, but still more components than the *LC+L* and *LC* configurations.

In spite of having more components than the *L*-configuration, the *LC* configuration generally stores the least amount of energy, but if the *L*-configuration is designed without the grid-side  $L$ , it is close to the same filter design. However, the question would be which one is easier to optimize; one capacitor or several of them. To achieve adequate attenuation, the *L*-configuration requires a capacitor that is increased by the number of parallel-connected inverters. Increasing the capacitor also results in more energy stored in the component. Similarly, if the *LC+L* configuration was designed with a common grid-side inductor divided by the number of parallel-connected inverters, the configuration would resemble the *LCL* configuration. The *LCL* and *LLCL* configurations store more energy than the *LC* configuration, but as they benefit from the individual grid-side inductor by having no problem with respect to the cross-coupling frequency, the additional energy can be considered an investment in safer operation.

The simulations showed that while setting the PCC voltage and current for the energy calculation works for a single inverter, with parallel-connected inverters this kind of a

method produces error as  $n$  increases. For this reason, variation in the PCC voltage has to be taken into account in the calculations with the suitable factors presented in the simulation section. By doing this, the difference between the calculations and the simulations was below 5 % even with the larger  $n$ , and most of the difference was caused by varying powers and noise in the measurements used in the simulations.

The simulations showed that the grid multiplication and its effect of increased attenuation are present also with filters having tolerances in them. Of course, the *THD* is also highly dependent on the possible circulating current. The inverters have a tendency to drive the circulating current into the inverter that has the smallest inductances if not dealt with properly.

The control design of parallel-connected inverters has to take into account the additional cross-coupling frequency, which can cause destructive operation. If an equivalent model was used in controller tuning, the resulting control system could be unstable as the equivalent model removes the cross-coupling resonance from the controlled plant. One should not assume all inverters to have an identical current reference in order to avoid accidentally use of the equivalent model.

The use of one master inverter to provide the control voltages for all inverters was found to be a good option. In the case of tolerances in the components, the circulating current is low because the inverters will produce ideally the same differential-mode and common-mode voltage. However, using a common-voltage reference will lead to differing powers driven by the inverter, which, in turn, may cause overheating and breakdown in the inverter driving larger than the nominal power. Balancing of the output powers leads to more even energy distribution amongst the filter components. Additionally, the common-mode circulating current is increased, which causes degradation in the *THD* of those inverter output currents that have the least inductance. Of course, by applying a circulating current minimizing control, problems of this kind could be avoided.

The open-end inverter analysed in this doctoral dissertation as a special case of the parallel-connected inverters is an interesting option for the conventional two parallel-inverter system. Ideally, the open-end inverter can use half the DC link voltage or have a doubled line-to-line voltage compared with the 2Par inverter system. In practice, this is difficult to achieve as the open-end connection provides no cancellation of the zero-sequence current on the inverter side of the transformer. This results in zero-sequence current flowing in the filter circuit, and depending on the component designs, also in the transformer requiring an even more special transformer. However, with modulation methods that remove the common-mode voltage, the open-end inverter presented a similar kind of *THD* as the 2Par grid-injected current. The price of this was to give up the higher apparent switching frequency and voltage doubler operation, and to use slightly larger components than in the 2Par system. In addition, the open-end system presents less redundancy than the 2Par system because a failure of either of the inverter bridges will cause complete inverter malfunction.

A comparison of the filter configurations from the perspective of modularity revealed that the *L*-configuration presents great modularity especially from the perspective of retrofit and maintenance. However, the redundancy of this configuration is lower than with the other configurations because of the common *CL* circuit on the grid side. If one of them fails, the whole inverter will be inoperable. With the other configuration, the level of redundancy is high and a failure of one inverter may not mean that all of them have to be shut down. In the *LC+L* configuration, the common grid-side inductor also decreases the redundancy compared with the *LCL*, *LLCL*, and *LC* configurations.

The *LLCL* configuration benefits clearly from the third resonance frequency, which is not affected by the grid multiplication. The switching frequency attenuation remains the same regardless of the number of parallel-connected inverters. Assuming that the grid does not contain much harmonic voltages and proper filtering is implemented, the *LLCL*, owing to its very good switching frequency harmonic attenuation, could perhaps be designed following the average capacitor idea discussed in this doctoral dissertation.

Considering the future work, proper measurements especially for the open-end inverter system would be required. As modelling of the minuscule differences in the switching instants is extremely difficult and time consuming, it would be an easier task to study them by measurements. In addition, by implementing the control system on the same controller would provide a means to study the circulating currents and their minimization, and possible differences between the filter configurations.

A comparative study of the resistive losses in the parallel-connected inverter systems would be an interesting task. The filter configurations present a distinct number of components that are in series, which, of course, has an effect on the applicability of the configurations.

Another interesting research question would be to investigate further the transformer design for a parallel-connected inverter, especially for the open-end inverter, which produces quite a lot of circulating current in the system.

## References

- Abdeldjabar, B., Huaiyuan, L., Jian, W., and Dianguo, X. (2016). Robust observer based active damping control for LCL filtered grid connected converters using LMI criterion. In: *2016 18th European Conference on Power Electronics and Applications*, pp. 1–6. Karlsruhe: IEEE. doi: 10.1109/EPE.2016.7695376.
- Abu-Rub, H., Holtz, J., Rodriguez, J., and Baoming, G. (2010). Medium-Voltage Multilevel Converters - State of the Art; Challenges and Requirements in Industrial Applications. *IEEE Transactions on Industrial Electronics*, vol. 57, no. 8, pp. 2581–2596.
- Agorreta, J.L., Borrega, M., López, J., and Marroyo, L. (2011). Modeling and Control of N-Paralleled Grid-Connected Inverters With LCL Filter Coupled Due to Grid Impedance in PV Plants. *IEEE Transactions on Power Electronics*, vol. 26, no. 3, pp. 770–785.
- Alemi, P. and Lee, D.C. (2014). Active damping control of LLCL filters based on virtual resistor for T-type three-level PWM converters. In: *2014 IEEE Energy Conversion Congress and Exposition (ECCE)*, pp. 2241–2248. Pittsburgh, PA: IEEE. doi: 10.1109/ECCE.2014.6953702.
- An, Q., et al. (2016). Dual-Space Vector Control of Open-End Winding Permanent Magnet Synchronous Motor Drive Fed by Dual Inverter. *IEEE Transactions on Power Electronics*, vol. 31, no. 12, pp. 8329–8342.
- Argorreta, J.L., Borrega, M., López, J., and Marroyo, L. (2011). Modeling and Control of N-Paralleled Grid-Connected Inverters with LCL Filter Coupled Due to Grid Impedance in PV Plants. *IEEE Transactions on Power Electronics*, vol. 26, no. 3, pp. 770–785.
- Asiminoaei, L., et al. (2006). An Interleaved Active Power filter with Reduced Size of Passive Components. In: *Twenty-First Annual IEEE Applied Power Electronics Conference and Exposition (APEC)*, pp. 29–35. IEEE. DOI: 10.1109/APEC.2006.1620656.
- Aura, L. (1986). *Sähkömiehen käskirja 2, Sähkökoneet [Electrician's Handbook 2, Electrical Machines]*, 1st edn. WSOY. 9510134791.
- Baiju, M.R., Mohapatra, K.K., Kanchan, R.S., and Gopakumar, K. (2004). A dual two-level inverter scheme with common mode voltage elimination for an induction motor drive. *IEEE Transactions on Power Electronics*, vol. 19, no. 3, pp. 794–805.
- Balasubramanian, A.K. and John, V. (2013). Analysis and design of split-capacitor resistive-inductive passive damping for LCL filters in grid-connected inverters. *IET Power Electronics*, vol. 6, no. 9, pp. 1822–1832.

- Bennet, W.R. (1933). New Results in the Calculation of Modulation Products. *The Bell Systems Technical Journal*, vol. 12, no. 2, pp. 228–243.
- Beres, R., Wang, X., Bak, C.L., and Liserres, M. (2014). Comparative evaluation of passive damping topologies for parallel grid-connected converters with LCL filters. In: *2014 International Power Electronics Conference (IPEC-Hiroshima 2014 - ECCE Asia)*, pp. 3320–3327. Hiroshima: IEEE. doi: 10.1109/IPEC.2014.6870163.
- Beres, R.N., et al. (2016). Optimal Design of High-Order Passive-Damped Filters for Grid-Connected Applications. *IEEE Transactions on Power Electronics*, vol. 31, no. 3, pp. 2083–2098.
- Blaabjerg, F., Teodorescu, R., Liserre, M., and Timbus, A.V. (2006). Overview of Control and Grid Synchronization for Distributed Power Generation Systems. *IEEE Transactions on Industrial Electronics*, vol. 53, no. 5, pp. 1398–1409.
- Black, H.S. (1953). *Modulation Theory*, 1st edn. New York, NY: D. Van Nostrand Company Inc. ISBN: 9781258813666.
- Borrega, M., González, R., Balda, J., and Agorreta, J.L. (2013). Modeling and Control of a Master-Slave PV Inverter with N-Paralleled Inverters and Three-Phase Three-Limb Inductors. *IEEE Transactions on Power Electronics*, vol. 28, no. 6, pp. 2841–2855.
- Bowes, S. and Bird, B.M. (1975). Novel Approach to the Analysis and Synthesis of Modulation Processes in Power Converters. *IEE Proceedings (London)*, vol. 122, no. 5, pp. 507–513.
- Cacciato, M., Consoli, A., Scarella, G., and Testa, A. (1999). Reduction of Common-Mode Currents in PWM Inverter Motor Drives. *IEEE Transactions on Industry Applications*, vol. 35, no. 2, pp. 469–476.
- Channegowda, P. and John, V. (2010). Filter Optimization for Grid Interactive Voltage Source Inverters. *IEEE Transactions on Industrial Electronics*, vol. 57, no. 12, pp. 4106–4114.
- Chen, S., Lipo, T.A., and Fitzgerald, D. (1996). Source of induction motor bearing currents caused by PWM inverters. *IEEE Transactions on Energy Conversion*, vol. 11, no. 1, pp. 25–32.
- Chen, C.-L., et al. (2010). Design of parallel inverters for smooth mode transfer microgrid applications. *IEEE Transaction on Power Electronics*, vol. 25, no. 1, pp. 6–15.
- Clarke, E. (1943). *Circuit Analysis of AC Power Systems*. New York, NY: John Wiley & Sons, Inc.

- Dahono, P.A. (2002). A control method to damp oscillation in the input LC filter of AC-DC PWM Converters. In: *2002 IEEE 33rd Annual IEEE Power Electronics Specialists Conference*, pp. 1630–1635. Cairns, Qld: IEEE. doi: 10.1109/PSEC.2002.1023044.
- Dannehl, J., Fuchs, F.W., Hansen, S., and Thøgersen, P.B. (2010). Investigation of Active Damping Approaches for PI-Based Current Control of Grid-Connected Pulse Width Modulation Converters with LCL Filters. *IEEE Transactions on Industry Applications*, vol. 46, no. 4, pp. 1509–1517.
- Dannehl, J., Lisserre, M., and Fuchs, F.W. (2011). Filter-based active damping of voltage source converters with LCL filter. *IEEE Transactions on industrial electronics*, vol. 58, no. 8, pp. 3623–3633.
- Daut, I., et al. (2010). Harmonic Content as the Indicator of Transformer Core Saturation. In: *The 4th International Power Engineering and Optimization Conference*, pp. 382–385. Shah Alam: IEEE. DOI: 10.1109/PEOCO.2010.5559192.
- del Blanco, F.B., Degner, M.W., and Lorenz, R.D. (1999). Dynamic analysis of current regulators for AC motors using complex vectors. *IEEE Transactions on Industry Applications*, vol. 35, no. 6, pp. 1424–1432.
- Dick, E.P. and Watson, W. (1981). Transformer Models for Transient Studies Based on Field Measurements. *IEEE Transactions on Power Apparatus and Systems*, vol. 100, no. 1, pp. 409–419.
- entso-e, ed., (2013). ENTSO-E Network Code for Requirements for Grid Connection Applicable to all Generators.. Available: [https://www.entsoe.eu/fileadmin/user\\_upload/\\_library/resources/RfG/130308\\_Final\\_Version\\_NC\\_RfG.pdf](https://www.entsoe.eu/fileadmin/user_upload/_library/resources/RfG/130308_Final_Version_NC_RfG.pdf).
- Erdman, J.M., Kerkman, R.J., Schlegel, D.W., and Skibinski, G.L. (1996). Effect of PWM inverters on AC motor bearing currents and shaft voltages. *IEEE Transactions on Industry Applications*, vol. 32, no. 2, pp. 250–259.
- Erickson, R.W. (1999). Chapter 13. Basic Magnetics Theory. In: Erickson, R.W., *Fundamentals of power electronics* (Repr.), chap. 13. Norwell (MA); New York: Kluwer Academic Publishers; Chapman & Hall. 0-412-08541-0.
- Fingrid (2013). *Specifications for the Operational Performance of Power Generating Facilities VJV2013*. Fingrid. Available: <http://www.fingrid.fi/en/customers/Customer%20attachments/Connection/2013/Specifications%20for%20the%20Operational%20Performance%20of%20Power%20Generating%20Facilities%20VJV2013.pdf>.
- Fingrid (2015). *Power quality in Fingrid's 110 kV grid*. Helsinki: TSO of Finland.

- Franquelo, L.G., et al. (2008). The Age of Multilevel Converters Arrives. *IEEE Industrial Electronics Magazine*, vol. 2, no. 2, pp. 28–39.
- Garcia, C.E. and Morari, M. (1985). Internal Model Control. 2. Design Procedure for Multivariable Systems. *Industrial & Engineering Chemistry Process Design and Development*, vol. 24, no. 2, pp. 472–484. DOI: 10.1021/i200029a043.
- Grandi, G., Ostoic, D., Rossi, C., and Lega, A. (2007). Control Strategy for a Multilevel Inverter in Grid-Connected Photovoltaic Applications. In: *International Aegean Conference on Electrical Machines and Power Electronics, 2007.*, pp. 156–161. Bodrum: IEEE.
- Harnefors, L. and Nee, H.-P. (1995). Robust Current Control of AC Machines Using the Internal Model Control Method. In: *Conference Record of the 1995 IEEE Industry Applications Conference, 1995. Thirtieth IAS Annual Meeting, IAS '95*, 1, pp. 303–309. Orlando, FL.
- Harnefors, L. and Nee, H.-P. (1998). Model-Based Current Control of AC Machines Using the Internal Model Control Method. *IEEE Transactions on Industry Applications*, vol. 34, no. 1, pp. 133–141.
- Hedayati, M.H., Acharya, A.B., and Vinod, J. (2013). Common-Mode Filter Design for PWM Rectifier-Based Motor Drives. *IEEE Transactions on Power Electronics*, vol. 28, no. 11, pp. 5364–5371.
- Heldwein, M.L., Dalessandro, L., and Kolar, J.W. (2011). The Three-Phase Common-Mode Inductor Modelling and Design Issues. *IEEE Transactions on Industrial Electronics*, vol. 58, no. 8, pp. 3264–3274.
- Heldwein, M.L., Nussbaumer, T., and Kolar, J.W. (2010). Common mode modelling and filter desing for a three-phase buck-type pulse width modulated rectifier system. *IET Power Electronics*, vol. 3, no. 2, pp. 209–218.
- He, J., Li, Y.W., Bosnjak, D., and Harris, B. (2012). Investigation and Resonances Damping of Multiple PV Inverters. In: *2012 Twenty-Seventh Annual IEEE Applied Power Electronics Conference and Exposition (APEC)*, pp. 246–253. Orlando, FL: IEEE. doi: 10.1109/APEC.2012.6165827.
- He, J., Li, Y.W., Bosnjak, D., and Harris, B. (2013). Investigation and active damping of multiple resonances in a parallel-inverter-based microgrid. *IEEE Transactions on Power Electronics*, vol. 28, no. 1, pp. 234–245.
- Hemphill, H. and Wallertz, B. (1995). Critical core parameters in the design of common mode suppression chokes. In: IEEE, ed., *1995 International Conference on Electromagnetic Interference and Compatibility (INCEMIC)*, pp. 334–336. Madras: IEEE. doi: 10.1109/INCEMIC.1995.501606.

- Hiltunen, J., Väisänen, V., and Silventoinen, P. (2014). Input filter damping without external passive components. In: *2014 16th European Conference on Power Electronics and Applications*, pp. 1–7. Lappeenranta: IEEE. doi: 10.1109/EPE.2014.6911025.
- Holmes, D.G. and Lipo, T.A. (2003). *Pulse Width Modulation for Power Converters*, 1st edn. Hoboken, NJ: John Wiley & Sons, Inc. ISBN 0-471-20814-0.
- Huan, M., Wang, X., Loh, P.C., and Blaabjerg, F. (2015). Active Damping of LLCL-Filter Resonance Based on LC-Trap Voltage or Current Feedback. *IEEE Transactions on Power Electronics*, vol. PP, no. 99, pp. 1–10.
- IEC (2009). Limits for Harmonic Current Emissions (Equipment Input Current  $\leq 16$  A per Phase). *IEC 61000 Electromagnetic compatibility (EMC) Part 3-2*, pp. 1–32. ISBN: 2-8318-1034-6.
- IEEE (2003). IEEE Standard for Interconnecting Distributed Resources with Electric Power Systems. *IEEE Std 1547-2003*, pp. 1–28. ISBN: 0-7381-3721-9.
- IEEE (2014). IEEE Recommended Practice and Requirements for Harmonic Control in Electrical Power Systems. *IEEE Std 519-2014 (Revision of IEEE Std 519-1992)*, pp. 1–29. ISBN: 978-0-7381-9006-8.
- Isidori, A., Rossi, F.M., Blaabjerg, F., and Ma, K. (2014). Thermal Loading and Reliability of 10-MW Multilevel Wind Power Converters at Different Wind Roughness Classes. *IEEE Transactions on Industry Applications*, vol. 50, no. 1, pp. 484–494.
- Itkonen, T. (2010). *Parallel-Operating Three-Phase Voltage Source Inverters - Circulating Current Modeling, Analysis and Mitigation*. Lappeenranta: Dissertation, Lappeenranta University of Technology. ISBN 978-952-214-944-2 (PDF). available <http://www.doria.fi/bitstream/handle/10024/62956/isbn9789522149442.pdf?sequence=1>.
- Jiao, Y. and Lee, F.C. (2015). LCL Filter Design and Inductor Current Ripple Analysis for a Three-Level NPC Grid Interface Converter. *IEEE Transactions on Power Electronics*, vol. 30, no. 9, pp. 4659–4668.
- Juntunen, R., et al. (2015). Identification of resonances in parallel connected grid inverters with LC- and LCL-filters. In: IEEE, ed., *IEEE 2015 Applied Power Electronics Conference and Exposition (APEC)*, pp. 2122–2127. Charlotte, NC: IEEE.
- Juntunen, R., et al. (2015). Comparative analysis of LCL-filter designs for paralleled inverters. In: IEEE, ed., *IEEE 2015 Energy Conversion Congress and Exposition (ECCE)*, pp. 2664–2672. Montreal, QC: IEEE.

- Kaura, V. and Blasko, V. (1997). Operation of a Phase Locked Loop System under Distorted Utility Conditions. *IEEE Transactions on Industry Applications*, vol. 33, no. 1, pp. 58–93.
- Kawabata, Y., et al. (2004). SVG using Open-winding Transformer and Two Inverters. In: *35th Annual IEEE Power Electronics Specialists Conference*, pp. 3039–3044. Aachen: IEEE.
- Kiadehi, A.D., Drissi, K.E.K., and Pasquier, C. (2016). Adapted NSPWM for Single DC-Link Dual-Inverter Fed Open-End Motor with Negligible Low-Order Harmonics and Efficiency Enhancement. *IEEE Transactions on Power Electronics*, vol. 31, no. 12, pp. 8271–8281.
- Kirubakaran, A., Jain, S., and Nema, R.K. (2011). DSP-Controlled Power Electronic Interface for Fuel-Cell-Based Distributed Generation. *IEEE Transactions on Power Electronics*, vol. 26, no. 12, pp. 3853–3864.
- Korhonen, J., et al. (2017). Modulation and control methods to reduce zero sequence current in open-end winding motors. In: IEEE, ed., *2017 IEEE International Electric Machines and Drives Conference (IEMDC)*, pp. 1–6. Miami, FL: IEEE. 978-1-5090-4281-4.
- Kovács, K. and Rácz, I. (1959). *Transiente Vorgänge in Wechselstrommaschinen [Transient Phenomena in AC Machines]*. Budapest: Verlag der Ungarischen Akademie der Wissenschaften.
- Lai, R., et al. (2010). An Integrated EMI Choke for Differential-Mode and Common-Mode Noise Suppression. *IEEE Transactions on Power Electronics Letters*, vol. 25, no. 3, pp. 539–544.
- Lee, K.-J., Lee, J.-P., Shin, D., and Yoo, D.-W. (2013). A Novel Grid Synchronization PLL Method Based on Adaptive Low-Pass Notch Filter for Grid-Connected PCS. *IEEE Transactions on Industrial Electronics*, vol. 61, no. 1, pp. 292–301.
- Lee, T.H., Low, T.S., Al-Mamum, A., and Tan, C.H. (1995). Internal Model Control (IMC) Approach for Designing Disk Drive Servo-Controller. *IEEE Transactions on Industrial Electronics*, vol. 42, no. 3, pp. 248–256.
- Leonhardt, W. (2001). *Control of Electrical Drives*. Berlin: Springer. ISBN: 3-540-41820-2.
- Liserre, M., Braabjerg, F., and Hansen, S. (2005). Design and Control of an LCL-Filter-Based Three-Phase Active Rectifier. *IEEE Transactions on Industry Applications*, vol. 41, no. 5, pp. 1281–1291.

- Liu, C., et al. (2012). Application of an LLCL Filter on Three-Phase Three-Wire Shunt Active Power Filter. In: *2912 IEEE 34th International Telecommunications Energy Conference (INTELEC)*, pp. 1–5. Scottsdale, AZ: IEEE. ISBN: 978-1-4673-0998-1.
- Liu, Y. and Zhenuyan, W. (1998). Calvin College. In: *Modeling of Harmonic Sources - Magnetic Core Saturation*. Virginia Tech, Blacksburg USA. [Retrieved September 17, 2016], url: [https://www.calvin.edu/~pribiero/IEEE/ieee\\_cd/chapters/pdffiles/c4pdf.pdf](https://www.calvin.edu/~pribiero/IEEE/ieee_cd/chapters/pdffiles/c4pdf.pdf).
- Lope, I., Hurley, W.G., and Zhang, J. (2013). Common-mode choke design considerations applied to domestic induction heating. In: IEEE, ed., *2013 48th International Universities' Power Engineering Conference (UPEC)*, pp. 1–5. Dublin: IEEE. doi: 10.1109/UPEC.2013.6714951.
- Luna, A., Rocabert, J., Candela, J.I., and Hermoso, J.R. (2015). Grid Voltage Synchronization for Distributed Generation Systems Under Grid Fault Conditions. *IEEE Transactions on Industry Applications*, vol. 51, no. 4, pp. 3414–3425.
- Lu, M., Wand, X., and Blaabjerg, F. (2016). Grid-voltage-feedforward active damping for grid-connected inverter with LCL filter. In: *2016 IEEE Applied Power Electronics Conference and Exposition (APEC)*, pp. 1941–1946. Long Beach, CA: IEEE. doi: 10.1109/APEC.2016.7468134.
- Lu, M., Wang, X., Blaabjerg, F., and Loh, P.C. (2015). An Analysis Method for Harmonic Resonance and Stability of Multi-Paralleled LCL-Filtered Inverters. In: *2015 IEEE 6th International Symposium on Power Electronics for Distributed Generation Systems (PEDG)*, pp. 1–6. Aachen: IEEE. doi: 10.1109/PEDG.2015.7223086.
- Lu, M., Wang, X., Loh, P.C., and Blaabjerg, F. (2017). Resonance Interaction of Multi-Parallel Grid-Connected Inverters with LCL-Filter. *IEEE Transactions on Power Electronics*, vol. 32, no. 2, pp. 894–899.
- McGrath, B.P., Holmes, D.G., and Galloway, J.J.H. (2005). Power Converter Line Synchronization using a Discrete Fourier Transform (DFT) based on a Variable Samplerate. *IEEE Transactions on Power Electronics*, vol. 20, no. 4, pp. 877–884.
- Meyer, R. and Mertens, A. (2012). Design of LCL Filters in Consideration of Parameter Variations for Grid-Connected Converters. In: *IEEE Energy Conversion Congress and Exposition (ECCE)*, pp. 557–564. Raleigh, NC.
- Miskovic, V., et al. (2014). Observer-Based Active Damping of LCL Resonance in Grid-Connected Voltage Source Converters. *IEEE Transactions on industry applications*, vol. 50, no. 6, pp. 3977–3985.

- Muetze, A. and Sullivan, C.R. (2011). Simplified Design of Common-Mode Chokes for Reduction of Motor Ground Currents in Inverter Drives. *IEEE Transactions on Industry Applications*, vol. 47, no. 6, pp. 2570–2577.
- Murad, G.A., Gu, D.-W., and Postlethwaite, I. (1996). Robust Internal Model Control of a Binary Distillation Column. In: *Proceedings of the IEEE International Conference on Industrial Technology (ICIT '96)*, pp. 194–198. Shanghai.
- Ott, H.W. (1988). Digital Circuit Radiation. In: Ott, H.W., *Noise Reduction Techniques in Electronic Systems*, 2nd edn, chap. 11, p. 298–301. New York, NY: John Wiley & Sons, Inc. ISBN: 0-471-85068-3.
- Park, R.H. (1929). Two-Reaction Theory of Synchronous Machines Generalized Method of Analysis - Part I. *Transactions of the AIEE*, vol. 48, no. 3, pp. 716–727.
- Parker, S.G., McGrath, B.P., and Holmes, D.G. (2014). Regions of Active Damping Control for LCL Filters. *IEEE Transactions on Industry Applications*, vol. 50, no. 1, pp. 424–432.
- Park, J.-H., Shin, D.-R., Kim, D.-W., and Lee, H.-W. (2001). Internal Model Control of Active Power Filter Using Resonance Model. In: *Proceedings of IEEE International Symposium on Industrial Electronics, 2001. ISIE 2001*, 3, pp. 1912–1918. Pusan. DOI: 10.1109/ISIE.2001.932004.
- Pawełek, R. and Wasiak, I. (2014). Comparative measurements of voltage harmonics in transmission grid of 400kV. In: *2014 16th International Conference on Harmonics and Quality of Power (ICHQP)*, pp. 606–610. Bucharest: IEEE. doi: 10.1109/ICHQP.2014.6842763.
- Pöllänen, R. (2003). *Converter-Flux-Based Current Control of Voltage Source PWM Rectifiers - Analysis and Implementation*. Dissertation, Lappeenranta University of Technology. ISBN: 951-764-834-0 (PDF). Available: <http://urn.fi/URN:ISBN:951-764-834-0>.
- Ponnaluri, S., et al. (2004). Design Comparison and Control of Medium Voltage STATCOM with Novel Twin Converter Topology. In: *35th Annual IEEE Power Electronics Specialists Conference*, pp. 2546–2552. Aachen: IEEE.
- Prasad, J.S.S. and Narayana, G. (2014). Minimization of grid current distortion in parallel-connected converters through carrier interleaving. *IEEE Transactions on Industrial Electronics*, vol. 61, no. 1, pp. 76–91.
- Purhonen, M. (2014). *Minimizing Circulating Current in Parallel-Connected Photovoltaic Inverters*. Lappeenranta: Dissertation, Lappeenranta University of Technology. ISBN: 978-952-265-677-3 (PDF). available <http://urn.fi/URN:ISBN:978-952-265-677-3>.

- Reznik, A., Simões, M.G., Al-Durra, A., and Muyeen, S.. (2014). LCL Filter Design and Performance Analysis for Grid-Interconnected Systems. *IEEE Transactions on Industry Applications*, vol. 50, no. 2, pp. 1225–1232.
- Rockhill, A.A., Liserre, M., Teodorescu, R., and Rodriguez, P. (2011). Grid-filter design for a multimegawatt medium-voltage voltage-source inverter. *IEEE Transactions on Power Electronics*, vol. 58, no. 4, pp. 1205 - 1217.
- Saunders, L.A., Skiblinski, G.L., Evon, S.T., and Kempkes, D.L. (1996). Riding the Reflected Wave - IGBT Drive Technology Demands New Motor and Cable Considerations. In: *The Institute of Electrical and Electronics Engineer Incorporated Industry Applications Society 43rd Annual Petroleum and Chemical Industry Conference.*, pp. 75–84. Philadelphia, PA.
- Seborg, D., Edgar, T., and Mellincamp, D. (1989). *Process Dynamics and Control*, 2nd edn. Hoboken, NJ: John Wiley & Sons, Inc. ISBN: 0-471-00077-9.
- Siva Prasad, J.S. and Narayanan, G. (2013). Minimization of Grid Current Distortion in Parallel-Connected Converters Through Carrier Interleaving. *IEEE Transactions on Industrial Electronics*, vol. 61, no. 1, pp. 76–91.
- Skibinski, G.L., Kerkman, R.J., and Schlegel, D. (1999). EMI emissions of modern PWM AC drives. *IEEE Industry Applications Magazine*, vol. 5, no. 6, pp. 47–80.
- Skogestad, S. and Postlethwaite, I. (2005). *Multivariable Feedback Control*, 2nd edn. Chichester, England: John Wiley & Sons Ltd. ISBN-13 978-0-470-01167-6.
- Somasekhar, V.T., Gopakumar, K., Pittet, A., and Rangathan, V.T. (2001). A novel PWM inverter switching strategy for a dual two-level inverter fed open-end winding induction motor drive. In: *2001 4th IEEE International Conference in Power electronics and Drive systems*, 1, pp. 196–202. IEEE.
- Srinivasan, P., Venugopal Reddy, B., and Somasekhar, V.T. (2010). PWM switching strategy for the elimination of common mode voltage of a two-level inverter drive with an open-end winding induction motor configuration. In: *2010 Joint International Conference on Power Electroncis, Drives and Energy Systems & 2010 Power India*, pp. 1–6. New Delhi: IEEE. doi: 10.1109/PEDES.2010.5712532.
- Stanley, H.C. (1938). An Analysis of the Induction Machine. *Electrical Engineering*, vol. 57, no. 12, pp. 751–757.
- Sun, J. (2011). Impedance-Based Stability Criterion for Grid-Connected Inverters. *IEEE Transactions on Power Electroncis (Letters)*, vol. 26, no. 11, pp. 3075–3078.

- Surendra Babu, N.N.V. and Fernandes, B.G. (2014). Cascaded Two-Level Inverter-Based Multilevel STATCOM for High-Power Applications. *IEEE Transactions on Power Delivery*, vol. 29, no. 3, pp. 993–1001.
- Tang, Y., Zhu, R., and Blaabjerg, F. (2015). Generalized stability regions of current control for LCL-filtered grid-connected converters without passive or active damping. In: *2015 IEEE Energy Conversion Congress and Exposition (ECCE)*, pp. 2040–2047. Montreal, QC: IEEE. doi: 10.1109/ECCE.2015.7309948.
- Teodorescu, R., Liserre, M., and Rodríguez, P. (2011). *Grid Converters for Photovoltaic and Wind Power Systems*, 1st edn. Chichester: John Wiley & Sons. ISBN: 978-0-470-05751-3.
- the Ministry of Employment and the Economy, Finland (2013). *National Energy and Climate Strategy*. the Ministry of Employment and the Economy. 978-952-227-750-3, 55 p.
- Tsili, M. and Papathanassiou, S. (2009). A Review of Grid Code Technical Requirements for Wind Farms. *IET Renewable Power Generation*, vol. 3, no. 3, pp. 308–332.
- Wessels, C., Dannehl, J., and Fuchs, F.W. (2008). Active damping of LCL-filter resonance based on virtual resistor for PWM rectifiers - stability analysis with different filter parameters. In: *2008 IEEE Power Electronics Specialist Conference*, pp. 3532–3538. Rhodes: IEEE. doi: 10.1109/PESC.2008.4592502.
- Wu, B. (2006). Cascaded H-bridge multilevel inverters. In: Wu, B., *High-power converters and AC drives*, 1st edn, chap. 7, p. 119–142. Hoboken, NJ: John Wiley & Sons, Inc. 978-0-471-73171-9.
- Wu, W., He, Y., and Blaabjerg, F. (2012). An LLCL Power Filter for Single-Phase Grid-Tied Inverter. *IEEE Transactions on Power Electronics*, vol. 27, no. 2, pp. 782–789.
- Wu, W., He, Y., Tang, T., and Blaabjerg, F. (2013). A new design method for the passive damped LCL and LLCL filter-based single-phase grid-tied inverters. *IEEE Transactions on Industrial Electronics*, vol. 60, no. 10, pp. 4339–4350.
- Wu, E. and Lehn, P.W. (2006). Digital Current Control of Voltage Source Converter with Active Damping of LCL Resonance. *IEEE Transactions on Power Electronics*, vol. 21, no. 5, pp. 1364–1373.
- Xiaonan, L., et al. (2012). Resonance propagation of parallel-operated DC-AC converters with LCL-filters. In: *APEC*, pp. 877–884. Orlando: IEEE.
- Yang, D., Wang, X., and Blaabjerg, F. (2018). Sideband Harmonic Instability of Paralleled Inverters with Asynchronous Carriers. *IEEE Transactions on Power Electronics*, vol. 33, no. 6, pp. 4571–4577.

- Yoon, D.-K., Jeong, H.-G., and Lee, K.-B. (2010). The design of an LCL-filter for the three-parallel opration of a power converter in a wind turbine. In: *ECCE*, pp. 1537–1544. Atlanta: IEEE.
- Yu, X. and Khambadkone, A.M. (2012). Reliability and Cost Optimization of Parallel-Inverter System. *IEEE Transactions on Industrial Electronics*, vol. 59, no. 10, pp. 3881–3889.
- Zhang, C., Dragicevic, T., Vasquez, J.C., and Guerrero, M. (2014). Resonance damping techniques for grid-connected voltage source converters with LCL filters - A review. In: IEEE, ed., *2014 IEEE International Energy Conference ENERGYCON*, pp. 169–176. Cavtat: IEEE. doi: 10.1109/ENERGYCON.2014.6850424.
- Zhang, D., et al. (2010). Impact of interleaving on AC passive components of paralleled three-phase voltage-source converters. *IEEE Transactions on Industry Applications*, vol. 46, no. 3, pp. 1042–1054.
- Zhang, X., et al. (2017). A Coordinate Control Strategy for Circulating Current Suppression in Multi-Paralleled Three-Phase Inverters. *IEEE Transactions on Industrial Electronics*, vol. 64, no. 1, pp. 838–847.
- Zhi, D. and Xu, L. (2007). Direct Power Control of DFIG with Constant Switching Frequency and Improved Transient Performance. *IEEE Transactions on Energy Conversion*, vol. 22, no. 1, pp. 110–118.
- Zhu, N., et al. (2012). An Integrated AC Choke Design for Common-Mode Current Suppression in Neutral-Connected Power Converter Systems. *IEEE Transactions on Power Electronics*, vol. 27, no. 3, pp. 1228–1236.



## **Appendices**

## Appendix A: Model derivations for a single inverter

Figure A.1 presents a stationary reference frame equivalent circuit for a three-phase grid-connected inverter with an *LCL* filter.  $\mathbf{u}^s_1$  denotes the inverter as a voltage source,  $\mathbf{u}^s_2$  is the point of common coupling (PCC) voltage between points A and B, and  $\mathbf{e}^s_g$  is the grid voltage. The impedances  $\mathbf{Z}_{L1}$ ,  $\mathbf{Z}_{L2}$  and  $\mathbf{Z}_C$  represent the impedance matrices of the filter components and  $\mathbf{Z}_{Lg}$  is the grid impedance matrix, which is commonly the transformer resistance and the leakage inductance. The voltage space vectors and impedance matrices of inductive and capacitive components are determined in a stationary reference frame as

$$\mathbf{u}^s = \begin{bmatrix} u_\alpha \\ u_\beta \end{bmatrix} \quad (\text{A.1})$$

$$\mathbf{i}^s = \begin{bmatrix} i_a \\ i_\beta \end{bmatrix} \quad (\text{A.2})$$

$$\mathbf{Z}_L^s = \begin{bmatrix} R_L + sL & 0 \\ 0 & R_L + sL \end{bmatrix} \quad (\text{A.3})$$

$$\mathbf{Z}_C^s = \begin{bmatrix} R_C + \frac{1}{sC} & 0 \\ 0 & R_C + \frac{1}{sC} \end{bmatrix}, \quad (\text{A.4})$$

where  $R_{L,C}$  are the resistances of the components,  $L$  and  $C$  are the inductance and capacitance of the component, respectively, and  $s$  is the Laplace-variable  $s = j\omega$ . The superscript  $s$  denotes a stationary reference frame.

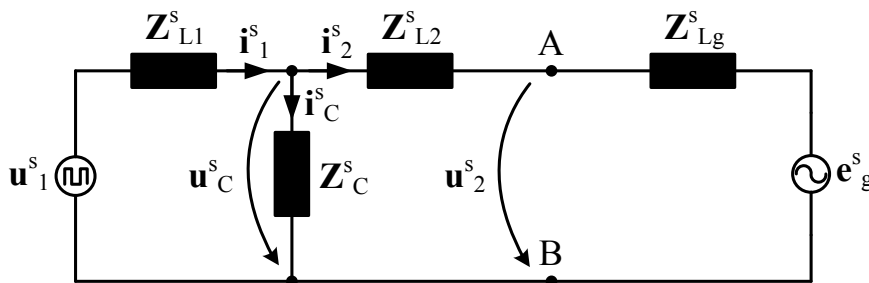


Figure A.1. Stationary reference frame equivalent circuit for a grid-connected inverter with an *LCL* filter.

If the resistances, inductances, and capacitances are considered to be constant over the frequency band in which the analysis is made, the transfer function matrix for the grid-connected inverter of Figure A.1 can be determined as follows. The inverter considered as a Thevenin's voltage source is determined as

$$\mathbf{u}_{\text{Th}}^s = \begin{bmatrix} \frac{Z_C}{Z_{L1} + Z_C} & 0 \\ 0 & \frac{Z_C}{Z_{L1} + Z_C} \end{bmatrix} \mathbf{u}_I^s, \quad (\text{A.5})$$

The equivalent impedance of a Thevenin's source (A.5) can be determined according to Figure A.2 as

$$\mathbf{Z}_{\text{Th}}^s = \mathbf{Z}_{L2}^s + \mathbf{Z}_{L1}^s \parallel \mathbf{Z}_C^s \quad (\text{A.6})$$

$$\mathbf{Z}_{\text{Th}}^s = \begin{bmatrix} \frac{Z_{L2}(Z_{L2} + Z_C) + Z_{L1}Z_C}{(Z_{L1} + Z_C)} & 0 \\ 0 & \frac{Z_{L2}(Z_{L2} + Z_C) + Z_{L1}Z_C}{(Z_{L1} + Z_C)} \end{bmatrix}. \quad (\text{A.7})$$

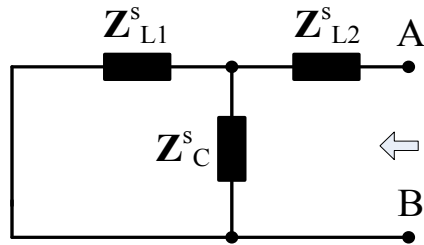


Figure A.2. Inverter voltage source is short circuited in order to determine the equivalent impedance for a Thevenin's source.

The equivalent model of (A.5) and (A.7) combined is depicted in Figure A.3. The full transfer function matrix for the grid-connected inverter can now be computed as

$$\mathbf{Y}_2^s = \mathbf{i}_2^s [\mathbf{u}_{\text{Th}}^s]^{-1} = \begin{bmatrix} \frac{1}{Z_{\text{Th}}^s + Z_{Lg}^s} & 0 \\ 0 & \frac{1}{Z_{\text{Th}}^s + Z_{Lg}^s} \end{bmatrix}, \quad (\text{A.8})$$

which, after substitution of (A.5), (A.7), (A.7), and  $\mathbf{Z}_{Lg}^s$  according to (A.3), becomes

$$\mathbf{Y}_2^s = \begin{bmatrix} \frac{Z_C^s}{Z_{L2}^s(Z_{L1}^s + Z_C^s) + Z_{L1}^sZ_C^s + Z_{Lg}^s(Z_{L1}^s + Z_C^s)} & 0 \\ 0 & \frac{Z_C^s}{Z_{L2}^s(Z_{L1}^s + Z_C^s) + Z_{L1}^sZ_C^s + Z_{Lg}^s(Z_{L1}^s + Z_C^s)} \end{bmatrix}. \quad (\text{A.9})$$

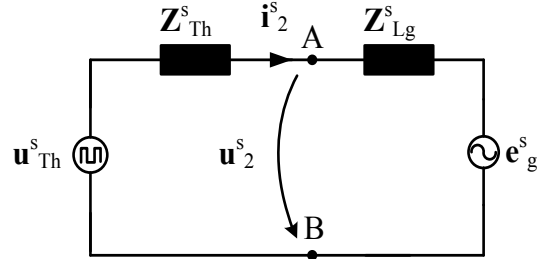


Figure A.3. Circuit of the equivalent model of the grid-connected inverter with an *LCL* filter.

The transfer function matrix for the inverter-side current  $\mathbf{i}^s_1$ , can be determined by lumping the filter impedances starting from  $\mathbf{Z}^s_C$  together with the grid impedance as in

$$\mathbf{Z}_{\text{lump}}^s = \mathbf{Z}_C^s \parallel (\mathbf{Z}_{L2}^s + \mathbf{Z}_{Lg}^s) \quad (\text{A.8})$$

Now, the transfer function matrix  $\mathbf{Y}^s_1$  becomes

$$\mathbf{Y}_1^s = \frac{\mathbf{i}_1^s}{\mathbf{u}_1^s} = \frac{1}{\mathbf{Z}_{L1}^s + \mathbf{Z}_{\text{lump}}^s} \quad (\text{A.9})$$

$$\mathbf{Y}_1^s = \begin{bmatrix} \frac{Z_C^s + Z_{L2}^s + Z_{Lg}^s}{Z_{L1}^s(Z_C^s + Z_{L2}^s + Z_{Lg}^s) + Z_C^s(Z_{L2}^s + Z_{Lg}^s)} & 0 \\ 0 & \frac{Z_C^s + Z_{L2}^s + Z_{Lg}^s}{Z_{L1}^s(Z_C^s + Z_{L2}^s + Z_{Lg}^s) + Z_C^s(Z_{L2}^s + Z_{Lg}^s)} \end{bmatrix}. \quad (\text{A.10})$$

Figure A.4 presents the equivalent circuit for (A.).

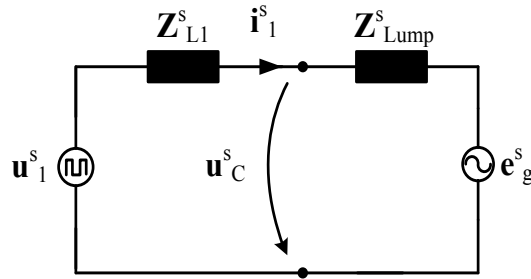


Figure A.4. Circuit of the equivalent model of the grid-connected inverter with an *LCL* filter when the inverter-side current is investigated.

The *LC* filter model is attained by setting the individual  $\mathbf{Z}^s_{L2} = [0]$ , and the *LLCL* filter model is obtained by adding the series inductor impedance to  $\mathbf{Z}^s_C$ . Modelling and the resonances were presented and discussed in (Juntunen et al., 2015).

## Appendix B: Model derivation for paralleled inverters

This appendix describes the model derivation for two parallel-connected inverters. The filters are chosen to be *LCL* filters but the methodology and steps in the model derivation can be used for any kind of a grid filter topology.

### Transfer function matrices

Figure B.1 presents the stationary reference frame equivalent circuits for two inverters with individual *LCL* filters connected to the same grid. The voltage sources  $\mathbf{u}^s_{11}$  and  $\mathbf{u}^s_{12}$  represent inverters 1 and 2, respectively, and  $\mathbf{e}^s_g$  the grid.  $\mathbf{u}^s_{C1}$  is the inverter 1 filter capacitor voltage and  $\mathbf{u}^s_{C2}$  is the inverter 2 filter capacitor voltage. The currents  $\mathbf{i}^s_{11}$  and  $\mathbf{i}^s_{21}$ , and  $\mathbf{i}^s_{12}$  and  $\mathbf{i}^s_{22}$  are the inverter-side and grid-side currents, and the currents  $\mathbf{i}^s_{C1}$  and  $\mathbf{i}^s_{C2}$  represent the capacitor currents for inverters 1 and 2, respectively.  $R_{11}$  and  $L_{11}$  are the inverter 1 inverter-side inductor and  $R_{12}$  and  $L_{12}$  the same for inverter 2. Similarly, the  $R_{21}$  and  $L_{21}$ , and  $R_{22}$  and  $L_{22}$  are the grid-side inductors of inverters 1 and 2, respectively.  $R_{C1}$  and  $C_1$  represent the inverter 1 filter capacitor and  $R_{C2}$  and  $C_2$ .  $R_g$  and  $L_g$  are used for the grid impedance. The capacitive part of the grid impedance can be neglected, because high frequencies on the grid-side are removed by the filter.

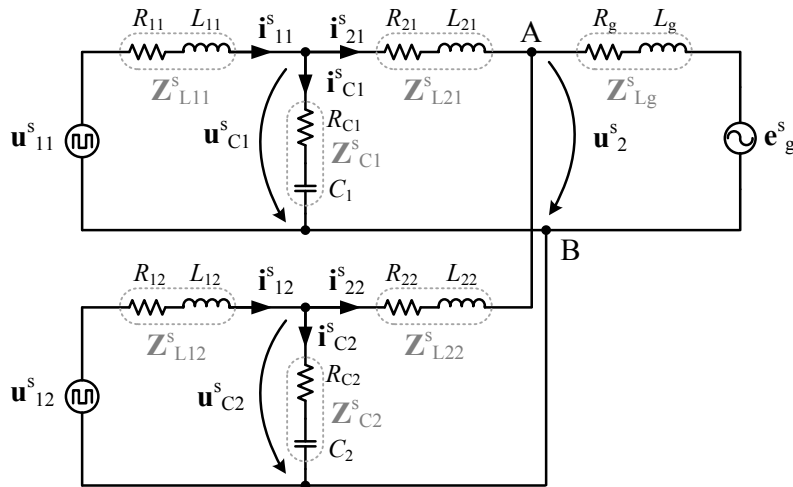


Figure B.1. Stationary reference frame equivalent circuits for two inverters with individual *LCL* filters connected in parallel to the same grid between points A and B. The inverter filter component impedances are indicated by the grey dashed line and the grey font.  $\mathbf{Z}_{L1x}^s$ ,  $\mathbf{Z}_{L2x}^s$ , and  $\mathbf{Z}_{Cx}^s$  represent the inverter-side inductor, grid-side inductor, and capacitor impedances for the paralleled inverters with  $x = 1$  and 2 for the corresponding inverter.  $\mathbf{Z}_{Lg}^s$  is the inductive grid impedance.

The equivalent voltage sources are determined as

$$\mathbf{u}_{\text{Th1}}^s = \begin{bmatrix} \frac{Z_{C1}^s}{Z_{L11}^s + Z_{C1}^s} & 0 \\ 0 & \frac{Z_{C1}^s}{Z_{L11}^s + Z_{C1}^s} \end{bmatrix} \mathbf{u}_{11}^s \quad (\text{B.1})$$

$$\mathbf{u}_{\text{Th2}}^s = \begin{bmatrix} \frac{Z_{C2}^s}{Z_{L12}^s + Z_{C2}^s} & 0 \\ 0 & \frac{Z_{C2}^s}{Z_{L12}^s + Z_{C2}^s} \end{bmatrix} \mathbf{u}_{12}^s, \quad (\text{B.2})$$

and the corresponding equivalent impedances as

$$\mathbf{Z}_{\text{Th1}}^s = \begin{bmatrix} \frac{Z_{L21}^s(Z_{L11}^s + Z_{C1}^s) + Z_{L11}^s Z_{C1}^s}{(Z_{L11}^s + Z_{C1}^s)} & 0 \\ 0 & \frac{Z_{L21}^s(Z_{L11}^s + Z_{C1}^s) + Z_{L11}^s Z_{C1}^s}{(Z_{L11}^s + Z_{C1}^s)} \end{bmatrix} \quad (\text{B.3})$$

$$\mathbf{Z}_{\text{Th2}}^s = \begin{bmatrix} \frac{Z_{L22}^s(Z_{L12}^s + Z_{C2}^s) + Z_{L12}^s Z_{C2}^s}{(Z_{L12}^s + Z_{C2}^s)} & 0 \\ 0 & \frac{Z_{L22}^s(Z_{L12}^s + Z_{C2}^s) + Z_{L12}^s Z_{C2}^s}{(Z_{L12}^s + Z_{C2}^s)} \end{bmatrix}. \quad (\text{B.4})$$

Figure B.2 presents the circuit of Figure B.1 with equivalent models, which are greatly simplified.

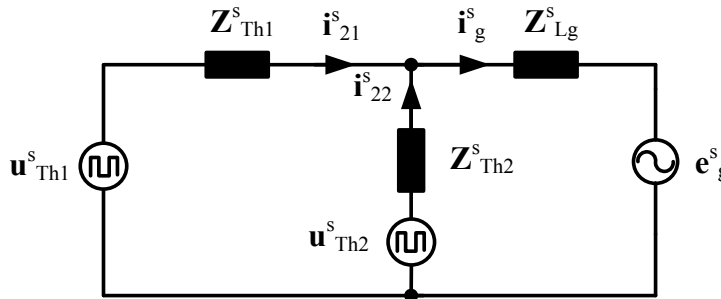


Figure B.2. Two paralleled inverters presented with the equivalent models.

The forward trans-admittance functions for the inverters can now be determined as

$$\mathbf{Y}_{21,1}^s = \begin{bmatrix} \frac{Z_{C1}^s(Z_{Th2}^s + Z_{Lg}^s)}{(Z_{L11}^s + Z_{C1}^s)(Z_{Th1}^s(Z_{Th2}^s + Z_{Lg}^s) + Z_{Th2}^s Z_{Lg}^s)} & 0 \\ 0 & \frac{Z_{C1}^s(Z_{Th2}^s + Z_{Lg}^s)}{(Z_{L11}^s + Z_{C1}^s)(Z_{Th1}^s(Z_{Th2}^s + Z_{Lg}^s) + Z_{Th2}^s Z_{Lg}^s)} \end{bmatrix} \quad (\text{B.5})$$

$$\mathbf{Y}_{22,2}^s = \begin{bmatrix} \frac{Z_{C2}(Z_{Th1}^s + Z_{Lg}^s)}{(Z_{L12}^s + Z_{C2}^s)(Z_{Th2}^s(Z_{Th1}^s + Z_{Lg}^s) + Z_{Th1}^s Z_{Lg}^s)} & 0 \\ 0 & \frac{Z_{C2}^s(Z_{Th1}^s + Z_{Lg}^s)}{(Z_{L12}^s + Z_{C2}^s)(Z_{Th2}^s(Z_{Th1}^s + Z_{Lg}^s) + Z_{Th1}^s Z_{Lg}^s)} \end{bmatrix}. \quad (\text{B.6})$$

$\mathbf{Y}_{21,1}^s$  is the forward trans-admittance function matrix that represents the effect of the inverter 1 voltage  $\mathbf{u}^s_{11}$  to its own grid-side current  $\mathbf{i}^s_{21,1}$ . Similarly,  $\mathbf{Y}_{22,2}^s$  describes the same relation for inverter 2. However, since every inverter in the system affects each other, not forgetting the effect of the grid, the forward trans-admittance functions matrices cannot be directly used in the parallel-inverter model. The transfer function matrices must be derived by the superposition method, which is depicted in Figure B.3.

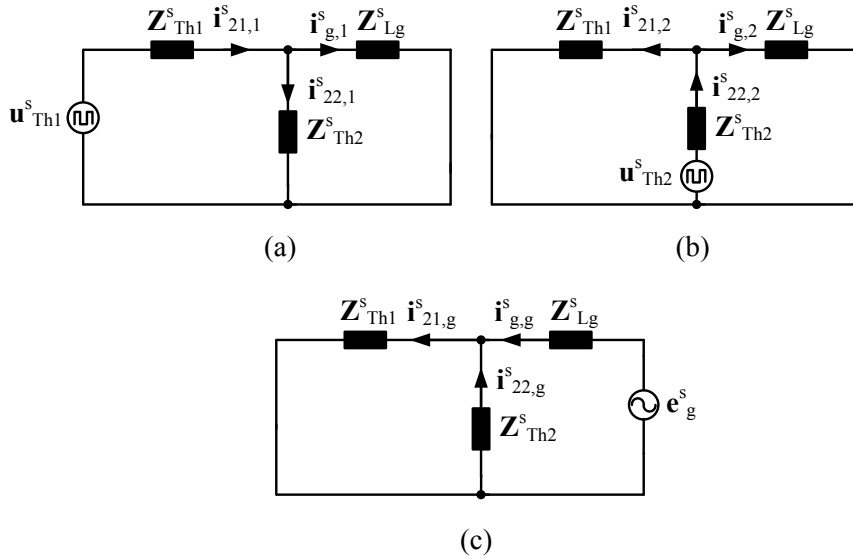


Figure B.3. Equivalent circuits for analysing the effect of (a) inverter 1, (b) inverter 2, and (c) grid voltage.

In Figure B.3 (a),  $\mathbf{u}^s_{Th2}$  and  $\mathbf{e}^s_g$  are short circuited in order to get the current components driven by the inverter 1 voltage. Similarly, in Figure B.3 (b) and (c) this action is done for  $\mathbf{u}^s_{Th1}$  and  $\mathbf{e}^s_g$  and  $\mathbf{u}^s_{Th1}$  and  $\mathbf{u}^s_{Th2}$ , respectively. The inverter 1 voltage causes the current  $\mathbf{i}^s_{21,1}$  in the grid-side inductor of its own filter,  $\mathbf{i}^s_{22,1}$  flowing into the inverter 2 branch and  $\mathbf{i}^s_{g,1}$  flowing into the grid branch. The inverter 2 voltage causes  $\mathbf{i}^s_{21,2}$  in the inverter 1 output filter grid-side inductor,  $\mathbf{i}^s_{22,2}$  in its own filter grid-side inductor, and  $\mathbf{i}^s_{g,2}$  in the grid branch. The grid voltage causes  $\mathbf{i}^s_{21,g}$  in the inverter grid-side inductor,  $\mathbf{i}^s_{22,g}$  in the inverter 2 grid-side inductor, and  $\mathbf{i}^s_{g,g}$  in the grid branch. Now, the summed currents depicted in Figure B.2 can be written as

$$\mathbf{i}_{21}^s = \mathbf{i}_{21,1}^s + \mathbf{i}_{21,2}^s + \mathbf{i}_{21,g}^s \quad (\text{B.7})$$

$$\mathbf{i}_{22}^s = \mathbf{i}_{22,1}^s + \mathbf{i}_{22,2}^s + \mathbf{i}_{22,g}^s \quad (\text{B.8})$$

$$i_g^s = i_{g,1}^s + i_{g,2}^s + i_{g,g}^s. \quad (\text{B.9})$$

The currents driven into the other branches can simply be calculated by current division

$$\mathbf{Y}_{21,2}^s = \begin{bmatrix} \frac{Z_{Lg}^s}{Z_{Lg}^s + Z_{Th2}^s} & 0 \\ 0 & \frac{Z_{Lg}^s}{Z_{Lg}^s + Z_{Th2}^s} \end{bmatrix} \mathbf{Y}_{22,2}^s \quad (\text{B.10})$$

$$\mathbf{Y}_{22,1}^s = \begin{bmatrix} \frac{Z_{Lg}^s}{Z_{Lg}^s + Z_{Th1}^s} & 0 \\ 0 & \frac{Z_{Lg}^s}{Z_{Lg}^s + Z_{Th1}^s} \end{bmatrix} \mathbf{Y}_{21,1}^s \quad (\text{B.11})$$

$$\mathbf{Y}_{21,g}^s = \begin{bmatrix} \frac{Z_{Th2}^s}{Z_{Th2}^s + Z_{Th1}^s} & 0 \\ 0 & \frac{Z_{Th2}^s}{Z_{Th2}^s + Z_{Th1}^s} \end{bmatrix} \mathbf{Y}_{g,g}^s \quad (\text{B.12})$$

$$\mathbf{Y}_{22,g}^s = \begin{bmatrix} \frac{Z_{Th1}^s}{Z_{Th1}^s + Z_{Th2}^s} & 0 \\ 0 & \frac{Z_{Th1}^s}{Z_{Th1}^s + Z_{Th2}^s} \end{bmatrix} \mathbf{Y}_{g,g}^s. \quad (\text{B.13})$$

Now, the whole system model for two parallel-connected grid inverters with *LCL* filters can be written as

$$\begin{bmatrix} i_{21}^s \\ i_{22}^s \\ i_g^s \end{bmatrix} = \begin{bmatrix} \mathbf{Y}_{21,1}^s & -\mathbf{Y}_{21,2}^s & -\mathbf{Y}_{21,g}^s \\ -\mathbf{Y}_{22,1}^s & \mathbf{Y}_{22,2}^s & -\mathbf{Y}_{22,g}^s \\ -\mathbf{Y}_{g,1}^s & -\mathbf{Y}_{g,2}^s & \mathbf{Y}_{g,g}^s \end{bmatrix} \begin{bmatrix} u_{11}^s \\ u_{12}^s \\ e_g^s \end{bmatrix}, \quad (\text{B.14})$$

where the off-diagonal matrices are negative because the currents from other sources counter the current caused by the source of the particular branch as indicated in Figure B.3. For clarity, the (B.14) is written fully open as follows

$$\begin{bmatrix} i_{21\alpha} \\ i_{21\beta} \\ i_{22\alpha} \\ i_{22\beta} \\ i_{g\alpha} \\ i_{g\beta} \end{bmatrix} = \begin{bmatrix} Y_{21,1\alpha} & 0 & -Y_{21,2\alpha} & 0 & -Y_{21,g\alpha} & 0 \\ 0 & Y_{21,1\beta} & 0 & -Y_{21,2\beta} & 0 & -Y_{21,g\beta} \\ -Y_{22,1\alpha} & 0 & Y_{22,2\alpha} & 0 & -Y_{22,g\alpha} & 0 \\ 0 & -Y_{22,1\beta} & 0 & Y_{22,2\beta} & 0 & -Y_{22,g\beta} \\ -Y_{g,1\alpha} & 0 & -Y_{g,2\alpha} & 0 & Y_{g,g\alpha} & 0 \\ 0 & -Y_{g,1\beta} & 0 & -Y_{g,2\beta} & 0 & Y_{g,g\beta} \end{bmatrix} \begin{bmatrix} u_{11\alpha} \\ u_{11\beta} \\ u_{12\alpha} \\ u_{12\beta} \\ e_{g\alpha} \\ e_{g\beta} \end{bmatrix}. \quad (\text{B.15})$$

The equivalent models (B.1)–(B.4) can also be used in derivation of the models for the inverter-side current. Figure B.4 presents the system for transfer function matrix derivation for the inverter 1 inverter-side current. The inverter 1 is presented as a voltage

source and the corresponding filter is presented with its individual components. The forward self-admittance matrix for inverter 1 can be determined as

$$\mathbf{Y}_{11,1}^s = \begin{bmatrix} \frac{1}{Z_{L11}^s + Z_{\text{Lump1}}^s} & 0 \\ 0 & \frac{1}{Z_{L11}^s + Z_{\text{Lump1}}^s} \end{bmatrix}, \quad (\text{B.15})$$

where the  $Z_{\text{Lump1}}^s$  is

$$Z_{\text{Lump1}}^s = Z_{C1}^s \parallel \left( Z_{L21}^s + \frac{Z_g^s Z_{\text{Th2}}^s}{Z_g^s + Z_{\text{Th2}}^s} \right). \quad (\text{B.16})$$

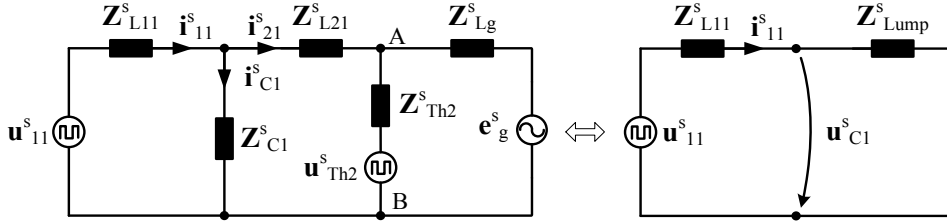


Figure B.4. On the left: Two paralleled inverters where inverter 1 is represented as a voltage source and its filter with its individual components while inverter 2 is represented with the equivalent model. On the right: Starting from the capacitor of inverter 1, all impedances are lumped together.

The off-diagonal components of the admittance function matrix can be determined as

$$\mathbf{Y}_{11,2}^s = \begin{bmatrix} \frac{Z_{C1}^s}{Z_{L11}^s + Z_{C1}^s} \frac{Z_{Lg}^s}{Z_{\text{Th2}}^s + Z_{Lg}^s} & 0 \\ 0 & \frac{Z_{C1}^s}{Z_{L11}^s + Z_{C1}^s} \frac{Z_{Lg}^s}{Z_{\text{Th2}}^s + Z_{Lg}^s} \end{bmatrix} \mathbf{Y}_{22,2}^s \quad (\text{B.17})$$

$$\mathbf{Y}_{12,1}^s = \begin{bmatrix} \frac{Z_{C2}^s}{Z_{L12}^s + Z_{C2}^s} \frac{Z_{Lg}^s}{Z_{\text{Th2}}^s + Z_{Lg}^s} & 0 \\ 0 & \frac{Z_{C2}^s}{Z_{L12}^s + Z_{C2}^s} \frac{Z_{Lg}^s}{Z_{\text{Th2}}^s + Z_{Lg}^s} \end{bmatrix} \mathbf{Y}_{21,1}^s \quad (\text{B.18})$$

$$\mathbf{Y}_{11,g}^s = \begin{bmatrix} \frac{Z_{\text{Th2}}^s Z_{C1}^s}{Z_{\text{Th2}}^s (Z_{C1}^s + Z_{L11}^s) + Z_{L21}^s (Z_{C1}^s + Z_{L11}^s) + Z_{C1}^s Z_{L11}^s} & 0 \\ 0 & \frac{Z_{\text{Th2}}^s Z_{C1}^s}{Z_{\text{Th2}}^s (Z_{C1}^s + Z_{L11}^s) + Z_{L21}^s (Z_{C1}^s + Z_{L11}^s) + Z_{C1}^s Z_{L11}^s} \end{bmatrix} \mathbf{Y}_{g,g}^s \quad (\text{B.19})$$

$$\mathbf{Y}_{12,g}^s = \begin{bmatrix} \frac{Z_{\text{Th1}}^s Z_{C2}^s}{Z_{\text{Th1}}^s (Z_{C2}^s + Z_{L12}^s) + Z_{L22}^s (Z_{C2}^s + Z_{L12}^s) + Z_{C2}^s Z_{L12}^s} & 0 \\ 0 & \frac{Z_{\text{Th1}}^s Z_{C2}^s}{Z_{\text{Th1}}^s (Z_{C2}^s + Z_{L12}^s) + Z_{L22}^s (Z_{C2}^s + Z_{L12}^s) + Z_{C2}^s Z_{L12}^s} \end{bmatrix} \mathbf{Y}_{g,g}^s \quad (\text{B.20})$$

The total system model in the matrix form is

$$\begin{bmatrix} \mathbf{i}_{11}^s \\ \mathbf{i}_{12}^s \\ \mathbf{i}_g^s \end{bmatrix} = \begin{bmatrix} \mathbf{Y}_{11,1}^s & -\mathbf{Y}_{11,g}^s \\ -\mathbf{Y}_{12,1}^s & \mathbf{Y}_{12,2}^s & -\mathbf{Y}_{12,g}^s \\ -\mathbf{Y}_{g,1}^s & -\mathbf{Y}_{g,2}^s & \mathbf{Y}_{g,g}^s \end{bmatrix} \begin{bmatrix} \mathbf{u}_{11}^s \\ \mathbf{u}_{12}^s \\ \mathbf{e}_g^s \end{bmatrix}. \quad (\text{B.21})$$

## Appendix C: Per-unit values

The per-unit (pu) value system is used to present a physical absolute quantity as a relative amount of a particular base value. For instance,

$$u_{\text{pu}} = \frac{u}{u_b}, \quad (\text{C.1})$$

where  $u$  is the measured value and  $u_b$  is the base value.

The base values in this dissertation are determined according to Table C.1.

Table C.1. Per-unit (pu) base values and formulas used in this dissertation.

Symbol	Quantity	Formula	Low Power	High Power
$u_b$	Voltage	$\sqrt{2/3} u_{\text{p-p,rms}}$	$\sqrt{2/3} 400 \text{ V}$	$\sqrt{2/3} 690 \text{ V}$
$i_b$	Current	$\sqrt{2} i_{\text{p,rms}}$	$\sqrt{2} \cdot 14.44 \text{ A}$	$\sqrt{2} \cdot 836.74 \text{ A}$
$S_b$	Power	$3/2 u_b i_b$	10 kVA	1000 kVA
$f_b$	Frequency	-	50 Hz	50 Hz
$\omega_b$	Angular frequency	$2\pi f_b$	314.16 rad/s	314.16 rad/s
$Z_b$	Impedance	$u_b / i_b$	$31.99 \Omega$	$0.4761 \Omega$
$L_b$	Inductance	$Z_b / \omega_b$	101.82 mH	1.5155 mH
$C_b$	Capacitance	$1 / (\omega_b Z_b)$	99.51 $\mu\text{F}$	6.6858 mF

Subscript p-p is a notation for *phase-to-phase* while p denotes *phase*.

## Appendix D: Nominal resonance frequencies

The nominal resonance frequencies for each filter configuration according to section 3.3 are shown in the tables below.

Table D.1. Nominal resonance frequencies in a stiff grid

Resonance	Inverter-side current ripple			Configuration
	10 %	15 %	25 %	
$f_{r1,LC,nom}$	33.334 pu (1666.7 Hz)	33.334 pu (1666.7 Hz)	33.334 pu (1666.7 Hz)	<i>LC</i>
$f_{r2,LC,nom}$	37.400 pu (1870.0 Hz)	37.458 pu (1872.9 Hz)	39.960 pu (1998.0 Hz)	<i>LC</i>
$f_{r1,LCL,nom}$	23.004 pu (1150.2 Hz)	23.004 pu (1150.2 Hz)	23.004 pu (1150.2 Hz)	<i>LCL, LC+L, L</i>
$f_{r2,LCL,nom}$	26.910 pu (1345.5 Hz)	28.656 pu (1432.8 Hz)	31.858 pu (1592.9 Hz)	<i>LCL, LC+L, L</i>
$f_{r1,LLCL,nom}$	21.478 pu (1073.9 Hz)	21.478 pu (1073.9 Hz)	21.478 pu (1073.9 Hz)	<i>LLCL</i>
$f_{r2,LLCL,nom}$	24.554 pu (1227.7 Hz)	25.858 pu (1292.9 Hz)	28.138 pu (1406.9 Hz)	<i>LLCL</i>

Table D.2. Nominal resonance frequencies in a weak grid

Resonance	Inverter-side current ripple			Configuration
	10 %	15 %	25 %	
$f_{r1,LC,nom}$	25.820 pu (1291.0 Hz)	25.820 pu (1291.0 Hz)	25.820 pu (1291.0 Hz)	<i>LC</i>
$f_{r2,LC,nom}$	32.508 pu (1625.4 Hz)	35.364 pu (1768.2 Hz)	40.474 pu (2023.7 Hz)	<i>LC</i>
$f_{r1,LCL,nom}$	24.268 pu (1213.4 Hz)	24.268 pu (1213.4 Hz)	24.268 pu (1213.4 Hz)	<i>LCL, LC+L, L</i>
$f_{r2,LCL,nom}$	31.290 pu (1564.5 Hz)	34.248 pu (1712.4 Hz)	39.502 pu (1975.1 Hz)	<i>LCL, LC+L, L</i>
$f_{r1,LLCL,nom}$	22.498 pu (1124.9 Hz)	22.498 pu (1124.9 Hz)	22.498 pu (1124.9 Hz)	<i>LLCL</i>
$f_{r2,LLCL,nom}$	27.744 pu (1387.2 Hz)	29.744 pu (1487.2 Hz)	32.994 pu (1649.7 Hz)	<i>LLCL</i>

## Appendix E: Derivation of phasor equations

Figure E.1 presents the single-phase equivalent circuit of a lossless *LCL* filter (a) and an *LLCL* filter (b).

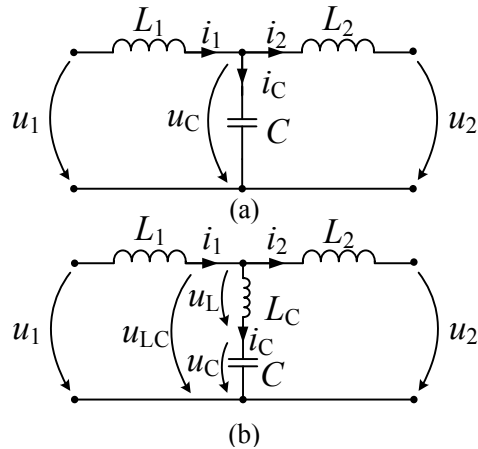


Figure E.1. Single-phase equivalent circuits of an *LCL* filter (a) and an *LLCL* filter (b) with no resistances.

For the phasors, the derivation is made by multiplication of  $j\omega$ . With the phasor notation (underlined), Kirchhoff's voltage law yields

$$\underline{u}_1 - \underline{u}_C = j\omega L_1 \underline{i}_1 \quad (\text{E.1})$$

$$\underline{u}_C - \underline{u}_2 = j\omega L_2 \underline{i}_2 \quad (\text{E.2})$$

$$\underline{i}_1 - \underline{i}_2 = j\omega C \underline{u}_C \quad (\text{E.3})$$

for an *LCL* filter and

$$\underline{u}_1 - \underline{u}_{LC} = j\omega L_1 \underline{i}_1 \quad (\text{E.4})$$

$$\underline{u}_{LC} - \underline{u}_2 = j\omega L_2 \underline{i}_2 \quad (\text{E.5})$$

$$\underline{u}_{LC} - \underline{u}_C = j\omega L_C (\underline{i}_1 - \underline{i}_2) \quad (\text{E.6})$$

$$\underline{i}_1 - \underline{i}_2 = j\omega C \underline{u}_C \quad (\text{E.7})$$

for an *LLCL* filter.

The aim is to solve the inverter-side current and capacitor voltage equations as a function of grid-side current and grid voltage. The *LCL* filter equations are handled first.

The capacitor voltage  $\underline{u}_C$  is solved from (E.3) and substituted into (E.1), yielding

$$\frac{\underline{i}_1 - \underline{i}_2}{j\omega C} - \underline{u}_2 - j\omega L_2 \underline{i}_2 = 0. \quad (\text{E.8})$$

Straightforwardly, other terms than those containing  $\underline{i}_1$  are moved to the other side. With the  $\underline{i}_2$  terms combined we get

$$\frac{\underline{i}_1}{j\omega C} = \underline{u}_2 + \left( \frac{1}{j\omega C} + j\omega L_2 \right) \underline{i}_2. \quad (\text{E.9})$$

When  $j\omega C$  is multiplied to the other side, the outcome is

$$\underline{i}_1 = j\omega C \underline{u}_2 + (1 - CL_2\omega^2) \underline{i}_2. \quad (\text{E.10})$$

The equation for  $\underline{i}_1$  can be obtained by solving  $\underline{u}_C$  from (E.2) and substituting it into (E.1), which then gives

$$\underline{i}_1 = \underline{u}_2 + j\omega L_1 \underline{i}_1 + j\omega L_2 \underline{i}_2. \quad (\text{E.11})$$

Now,  $\underline{i}_1$  can be removed from (E.11) by substituting (E.10) into (E.11). After some manipulation the equation becomes

$$\underline{i}_1 = (1 - CL_1\omega^2) \underline{u}_2 - j\omega(L_1 + L_2 - CL_1L_2\omega^2) \underline{i}_2. \quad (\text{E.12})$$

The capacitor voltage equation can directly be solved from (E.2) to give

$$\underline{u}_C = \underline{u}_2 - j\omega L_2 \underline{i}_2 \quad (\text{E.13})$$

or it can be obtained by solving  $\underline{i}_2$  from (E.2) and substituting it into (E.3), yielding

$$\underline{u}_C = \frac{1}{1 - CL_2\omega^2} \left( \underline{u}_2 + j\omega L_2 \underline{i}_1 \right). \quad (\text{E.14})$$

The form in (E.14) might be handy in a case where the resonance peak frequency is wanted to be substituted into the equation.

Similarly as for the *LCL* filter, the phasor equations for the *LLCL* filters are easy to derive. We obtain  $\underline{u}_{LC}$  from (E.6) by substituting the  $\underline{u}_C$  solved from (E.7), and the outcome of this operation is substituted into (E.4). After some simplification, the phasor equation for the inverter-side current of *LLCL* filter becomes

$$\underline{i}_1 = \frac{1}{1 - CL_C\omega^2} \left( j\omega C \underline{u}_2 + (1 - C(L_2 + L_C)\omega^2) \underline{i}_2 \right). \quad (\text{E.15})$$

The inverter-side voltage can be solved by substituting  $\underline{u}_{LC}$  and (E.15) into (E.4), which gives

$$\underline{u}_1 = \frac{1}{CL_C\omega^2 - 1} \left( (C\omega^2(L_2 + L_C) - 1)\underline{u}_2 + j\omega((CL_C\omega^2 - 1)(L_2 + L_C) + CL_1L_2\omega^2)\underline{i}_2 \right). \quad (\text{E.16})$$

The capacitor voltage is obtained by substituting (E.7) into (E.6), the result of which is then substituted to (E.5), yielding after some simplification

$$\underline{u}_C = \frac{1}{1 - CL_C\omega^2} \left( \underline{u}_2 + j\omega L_2 \underline{i}_2 \right). \quad (\text{E.17})$$

Further, the capacitor voltage can be solved by substituting (E.16) into (E.4) with the solved  $\underline{u}_{LC}$  to give

$$\underline{u}_C = \frac{1}{1 - C(L_2 + L_C)\omega^2} \left( \underline{u}_2 + j\omega L_2 \underline{i}_1 \right). \quad (\text{E.18})$$

To take into account the grid inductance  $L_g$  in (E.1)–(E.18), the  $L_2$  is only substituted by  $L_2 = (L_2 + L_g)$ .

## Appendix F: Filter fundamental energies

Table F.1. Total filter arrangement maximum energies for *LCL* and *LLCL* configurations with three different  $L_1$  values in a stiff grid.

<i>n</i>	<i>LCL</i>			<i>LLCL</i>		
	$L_{1,(10\%)}$	$L_{1,(15\%)}$	$L_{1,(25\%)}$	$L_{1,(10\%)}$	$L_{1,(15\%)}$	$L_{1,(25\%)}$
2	0.2354	0.1774	0.1322	0.2354	0.1774	0.1322
3	0.3517	0.2657	0.1996	0.3517	0.2657	0.1996
4	0.4673	0.3559	0.2679	0.4673	0.3559	0.2680
5	0.5838	0.4471	0.3373	0.5839	0.4471	0.3374
6	0.7031	0.5393	0.4079	0.7032	0.5394	0.4079

Table F.2. Total filter arrangement maximum energies for *LC*, *LC+L* and *L*-configuration with three different  $L_1$  values in a stiff grid.

<i>n</i>	<i>LC</i>			<i>LC+L</i>			<i>L</i>		
	$L_{1,(10\%)}$	$L_{1,(15\%)}$	$L_{1,(25\%)}$	$L_{1,(10\%)}$	$L_{1,(15\%)}$	$L_{1,(25\%)}$	$L_{1,(10\%)}$	$L_{1,(15\%)}$	$L_{1,(25\%)}$
2	0.2034	0.1454	0.0988	0.2674	0.2102	0.1661	0.2521	0.1951	0.1504
3	0.3037	0.2168	0.1487	0.4495	0.3675	0.3017	0.4197	0.3356	0.2681
4	0.4032	0.2881	0.2000	0.6690	0.5601	0.4727	0.6215	0.5092	0.4190
5	0.5018	0.3621	0.2522	0.9240	0.7883	0.6795	0.8564	0.7159	0.6030
6	0.6014	0.4372	0.3055	1.215	1.0526	0.9225	1.1245	0.9557	0.8202

Table F.3. Total filter arrangement maximum energies for *LCL* and *LLCL* configuration with three different  $L_1$  values in a weak grid.

<i>n</i>	<i>LCL</i>			<i>LLCL</i>		
	$L_{1,(10\%)}$	$L_{1,(15\%)}$	$L_{1,(25\%)}$	$L_{1,(10\%)}$	$L_{1,(15\%)}$	$L_{1,(25\%)}$
2	0.1993	0.1436	0.0990	0.1993	0.1436	0.0990
3	0.3013	0.2181	0.1513	0.3013	0.2181	0.1513
4	0.4055	0.2949	0.2061	0.4056	0.2949	0.2062
5	0.5124	0.3745	0.2639	0.5125	0.3746	0.2639
6	0.6224	0.4574	0.3251	0.6224	0.4575	0.3251

Table F.4. Total filter arrangement maximum energies for *LCL* and *LLCL* configuration with three different  $L_1$  values in a weak grid.

<i>n</i>	<i>LC</i>			<i>LC+L</i>			<i>L</i>		
	$L_{1,(10\%)}$	$L_{1,(15\%)}$	$L_{1,(25\%)}$	$L_{1,(10\%)}$	$L_{1,(15\%)}$	$L_{1,(25\%)}$	$L_{1,(10\%)}$	$L_{1,(15\%)}$	$L_{1,(25\%)}$
2	0.1859	0.1302	0.0856	0.2127	0.1570	0.1124	0.2050	0.1488	0.1037
3	0.2812	0.1979	0.1311	0.3416	0.2584	0.1917	0.3243	0.2399	0.1721
4	0.3786	0.2679	0.1791	0.4864	0.3759	0.2872	0.4571	0.3444	0.2539
5	0.4786	0.3407	0.2300	0.6476	0.5099	0.3995	0.6033	0.4622	0.3491
6	0.5817	0.4167	0.2843	0.8257	0.6611	0.5290	0.7628	0.5935	0.4577

## Appendix G: Randomized tolerances

These tolerances are used in some of the figures of section 3.6.2. The tolerances are presented here in the form of a matrix as

$$\Delta = \begin{bmatrix} \delta_{11} & \delta_{12} & \delta_{13} \\ \delta_{21} & \delta_{22} & \delta_{23} \\ \delta_{31} & \delta_{32} & \delta_{33} \\ \delta_{41} & \delta_{42} & \delta_{43} \\ \delta_{51} & \delta_{52} & \delta_{53} \\ \delta_{61} & \delta_{62} & \delta_{63} \end{bmatrix}, \quad (\text{G.1})$$

where each term is tolerance in a specific filter component;  $\delta_{11}$ ,  $\delta_{12}$ , and  $\delta_{13}$  represent the tolerances for the inverter 1 components 1, 2, and 3, which are  $L_1$ ,  $L_2$ , and  $C_f$  for the *LCL* filter 1. The tolerances generated by Matlab's rand function are

$$\Delta_1 = \begin{bmatrix} 0.8335 & 0.8916 & 1.1653 \\ 0.8610 & 1.1303 & 1.0153 \\ 1.1985 & 0.8313 & 0.9771 \\ 0.8427 & 1.1848 & 0.8019 \\ 1.1100 & 1.1269 & 1.1475 \\ 0.8338 & 0.9599 & 0.9039 \end{bmatrix}, \quad (\text{G.2})$$

$$\Delta_2 = \begin{bmatrix} 0.8736 & 0.8960 & 0.9669 \\ 0.8199 & 1.1611 & 1.1779 \\ 0.9963 & 0.9957 & 0.9351 \\ 1.1600 & 0.9477 & 0.8445 \\ 1.1121 & 0.9559 & 0.8967 \\ 0.9616 & 0.8386 & 0.8528 \end{bmatrix}, \quad (\text{G.3})$$

and

$$\Delta_3 = \begin{bmatrix} 0.8967 & 0.9616 & 0.8386 \\ 0.8528 & 1.1768 & 1.1825 \\ 1.0301 & 0.8239 & 0.8939 \\ 0.9413 & 1.1285 & 0.8062 \\ 0.8172 & 0.8676 & 1.0596 \\ 1.0927 & 1.0591 & 0.9804 \end{bmatrix}. \quad (\text{G.4})$$

## Appendix H: Basic simulation models

The simulation models were based on the same basic model from which all parallel-inverter and open-end inverter models were derived. Figure H.1 illustrates the main circuit in the simulation model of two parallel-connected inverters. The inverters were modelled using the universal bridge models. The snubber capacitance was  $C_s = 6.6858 \mu\text{F}$  and the snubber resistance  $R_s = 997.1415 \Omega$  to keep the leakage current through it at around 0.1 % of the nominal current of the application. Forward voltages for the diode and the IGBTs were 0.5 V for both and  $R_{\text{on}} = 0.1 \text{ m}\Omega$ . The DC links were supplied with controlled DC current sources, which input step sources were smoothed with a 25 Hz low-pass filters. Common for all simulations was the sample time of  $T_s = 0.6667 \mu\text{s}$ , which was determined by a sampling frequency of an integer multiple of the switching frequency. The common switching frequency was  $f_{\text{sw}} = 3 \text{ kHz}$ .

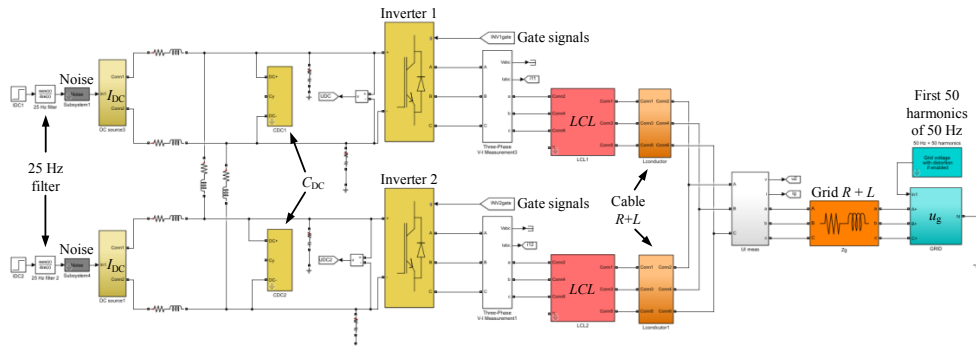


Figure H.1. Two parallel-inverter simulation model. The yellow subsystems from left to right; controlled DC current source, DC link capacitor, and 2-level inverter bridges. The red subsystems are the  $LCL$  filters and orange represents the conductor and grid impedances. White subsystems are for measurement, the cyan is the grid model with the first 50 harmonics, and the controlled voltage sources connected in wye.

The grid was modelled as a controlled voltage source, which had series resistance and inductance. The conductor inductance was added on the grid-side of the filters. A value of 100 nH was used for conductor inductance. The same value was also used in connections between the inverters. A capacitance of  $C = 4.516 \text{ nF}$  from the DC link plus and minus to the ground and from the grid neutral to the ground was used.

A single inverter control was used for all inverters. If the powers were not balanced, the reference voltages fed to the modulator were the same. Figure H.2 presents the control part with noise included in the measurements. The noise was included as a percentage of the base values and implemented with the Band-limited white noise block with a noise power of  $10^{-10}$  and a sample time of  $0.6667 \mu\text{s}$ . These values yield noise the maximum values of which are around 5–6 %.

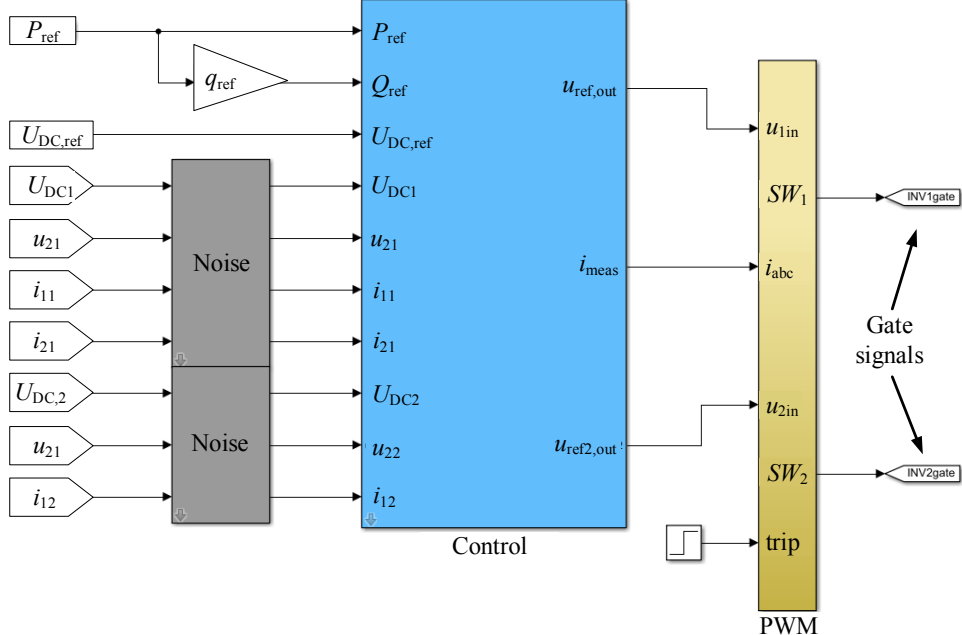


Figure H.2. Control section of the parallel-inverter simulation model for two inverters. The grey subsystems include the variables with around 6 % of measurement noise generated with a white noise generator. The light blue subsystem is the control part and the yellow the modulator.

Figure H.3 and Figure H.4 present the control system top level. The input registers of the control were updated at every peak, [-1 , 1], of the modulator carrier wave, and thus, the measurements and control were updated with a frequency of  $2f_{sw}$ . The digital control delay was implemented by updating the previous control value from the sample and hold blocks by triggering them when the carrier wave was in the value of [-0.5 , 0.5].

The measured abc coordinate currents were transformed into dq coordinates in which common PI controllers were used. The control system was implemented based on the theory presented in Chapter 2. The PLL was designed according to (2.49) and (2.50). The damping factor was increased by making  $\alpha = 10$  in (2.51). The current controllers were designed as a two-degrees-of-freedom controller with (2.74) and (2.77). The current controller bandwidth was designed as  $\alpha = 199.7477$ , which corresponds to a 11 ms rise time for the current controller. This was done to increase the disturbance rejection of the system after noise in the measurements was introduced.

The DC link voltage controller was designed with (2.84)–(2.86). The DC link controller was chosen to be overdamped by setting  $\alpha = 15$ , which yielded a good damping of oscillations and still a fast enough performance. The DC link capacitance was chosen as  $C_{DC} = 16.7 \text{ mF}$ , which, in retrospect, is perhaps a quite large value unless the input of the inverter is a 6-pulse rectifier and the DC link voltage ripple limits are tight.

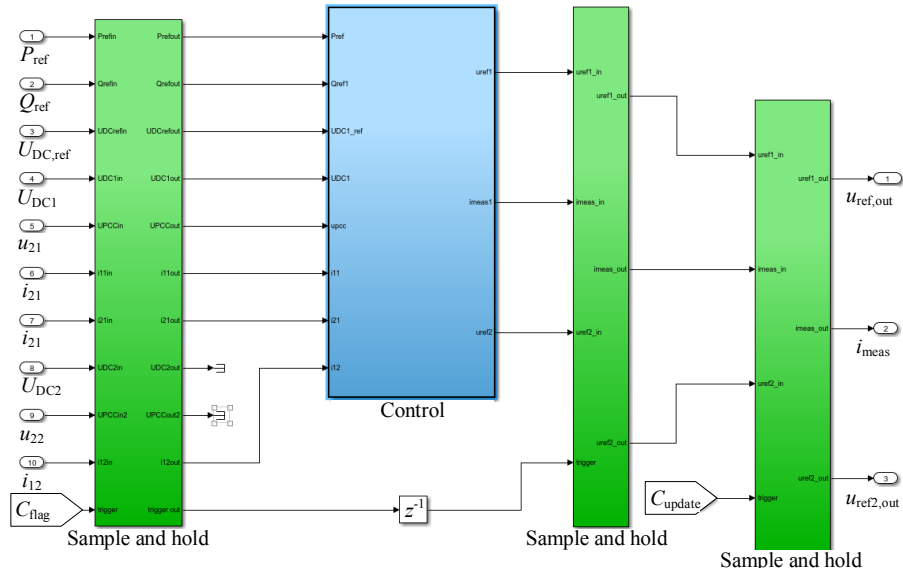


Figure H.3. Control system with an input and output register and an output update register.

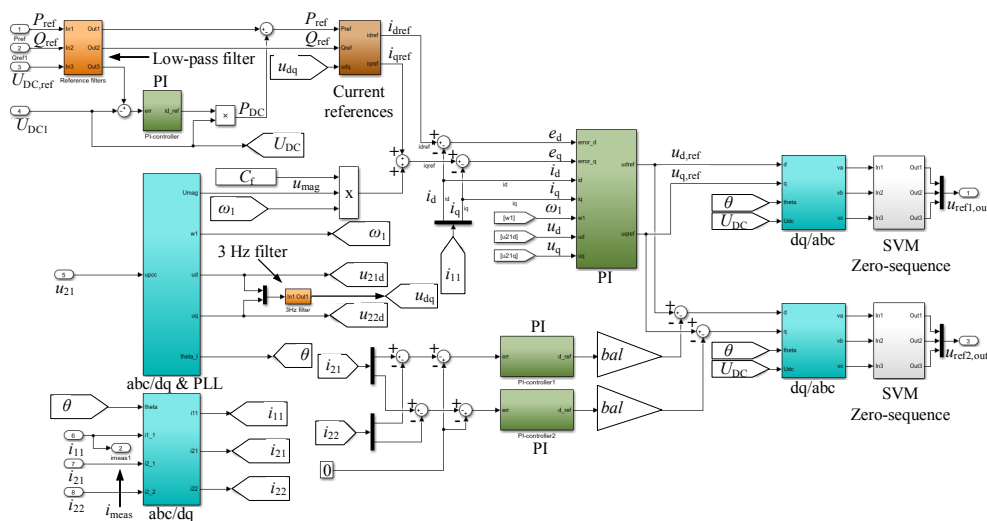


Figure H.4. Control system with cyan subsystems representing coordinate transformations, green indicating PI controllers, orange being the reference filters, brown the current reference calculation from the power references, and white subsystems the zero-sequence addition for the SVM.

The power balancing controllers were implemented with basic PI controllers with the same gains as the normal current controllers. The powers were balanced by controlling the other inverter currents to the same as the inverter 1 currents. The PI controller anti-windup was implemented by subtracting the unsaturated output from the saturated, and the result was added to the integrator input with a gain of  $1/k_p$ .

The PWM subsystem included the modulator and the dead time compensation. Figure H.5 illustrates the modulator. The green subsystem is the input register, which is updated at every peak of the carrier wave, which is generated in the light blue subsystem. The red subsystems include the dead time compensation, which, depending on the sign of the current, add the proper volt-seconds to the reference signal. The grey subsystems include the dead time generation, which was implemented by multiplying the gate signal with an appropriately delayed gate signal. The delay was chosen based on the number of samples so that the generated dead time was an integer multiple of the sample time. A dead time value of  $1.3333 \mu\text{s}$ , that is, two samples, was used.

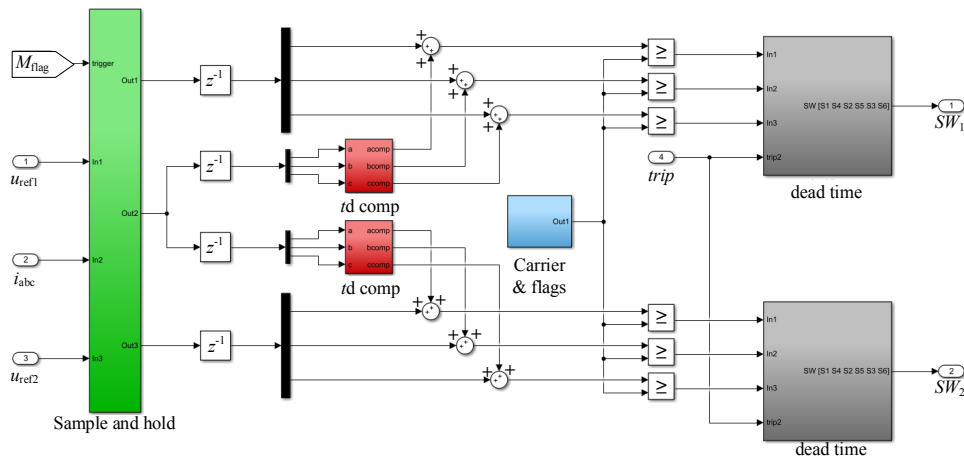


Figure H.5. PWM subsystem. The green subsystem includes the input registers, which are triggered by the signal  $M_{flag}$ . The red subsystems house the dead time compensation. The light blue subsystem contains the carrier generated with the SimPowerSystem triangle generator and the control flag signals. The grey subsystems include the dead time generator.

Table H.1 presents the filter values used in the simulations.

Table H.1. Nominal filter values used in parallel-inverter simulations

Symbol	Quantity	Value
$L_1$	Inverter-side inductor	$173 \mu\text{H}$
$L_2$	Grid-side inductor	$50 \mu\text{H}$
$C_f$	Filter total capacitor	$200.5733 \mu\text{F}$
$C_1$	Undamped capacitor	$0.1C_f$
$C_d$	Damped capacitor	$0.9C_f$
$R_d$	Damping resistance	$200 \text{ m}\Omega$

Figure H.6 presents the main circuit part of the open-end system simulator. The control system was the same as for the parallel-inverter models, only the main circuit and modulators were different. The open-end transformer was built with single phase

transformer blocks, which were connected to wye on the grid side. The same capacitance that was used from the DC link to the ground was connected over the phases of the transformer. Table H.2 presents the nominal values for the open-end filters used in the simulations. The sample times and switching frequencies were the same as for the parallel-inverter models.

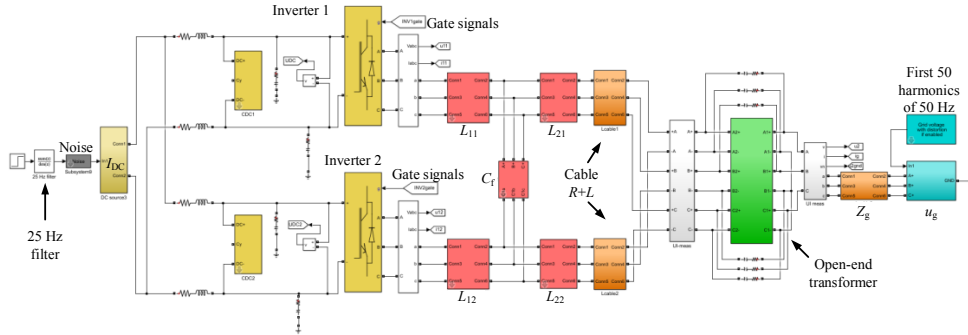


Figure H.6. Open-end inverter simulation model. The yellow subsystems from left to right; controlled DC current source, DC link capacitors, and 2-level inverter bridges. The red subsystems are the  $LCL$  filter components and orange represents the conductor impedances. The white subsystems are for measurement, green is the open-end transformer, and cyan indicates the grid model with the first 50 harmonics and the controlled voltage sources connected in wye.

Table H.2. Nominal open-end system filter values used in the simulations

Symbol	Quantity	Case 1	Case 2	ZCM
$L_{1,SVM}$	Inverter-side inductor, SVM	44 $\mu$ H	173 $\mu$ H	87 $\mu$ H
$L_{1,SPWM}$	Inverter-side inductor ,SPWM	60 $\mu$ H	199 $\mu$ H	-
$L_2$	Grid-side inductor	25 $\mu$ H	25 $\mu$ H	25 $\mu$ H
$C_f$	Filter total capacitor	401.15 $\mu$ F	100.29 $\mu$ F	401.15 $\mu$ F

## **ACTA UNIVERSITATIS LAPPEENRANTAENSIS**

788. ZHAO, WENLONG. Reliability based research on design, analysis and control of the remote handling maintenance system for fusion reactor. 2018. Diss.
789. IAKOVLEVA, EVGENIA. Novel sorbents from low-cost materials for water treatment. 2018. Diss.
790. KEDZIORA, DAMIAN. Service offshoring industry: systems engineering approach to its transitional challenges. 2018. Diss.
791. WU, JING. Soft computing methods for performance improvement of EAMA robot in fusion reactor application. 2018. Diss.
792. VOSTATEK, PAVEL. Blood vessel segmentation in the analysis of retinal and diaphragm images. 2018. Diss.
793. AJO, PETRI. Hydroxyl radical behavior in water treatment with gas-phase pulsed corona discharge. 2018. Diss.
794. BANAEIANJAHROMI, NEGIN. On the role of enterprise architecture in enterprise integration. 2018. Diss.
795. HASHEELA-MUFETI, VICTORIA TULIVAYE. Empirical studies on the adoption and implementation of ERP in SMEs in developing countries. 2018. Diss.
796. JANHUNEN, SARI. Determinants of the local acceptability of wind power in Finland. 2018. Diss.
797. TEPOV, ROMAN. A holistic approach to measuring open innovation: contribution to theory development. 2018. Diss.
798. ALBATS, EKATERINA. Facilitating university-industry collaboration with a multi-level stakeholder perspective. 2018. Diss.
799. TURA, NINA. Value creation for sustainability-oriented innovations: challenges and supporting methods. 2018. Diss.
800. TALIKKA, MARJA. Recognizing required changes to higher education engineering programs' information literacy education as a consequence of research problems becoming more complex. 2018. Diss.
801. MATTSSON, ALEksi. Design of customer-end converter systems for low voltage DC distribution from a life cycle cost perspective. 2018. Diss.
802. JÄRVI, HENNA. Customer engagement, a friend or a foe? Investigating the relationship between customer engagement and value co-destruction. 2018. Diss.
803. DABROWSKA, JUSTYNA. Organizing for open innovation: adding the human element. 2018. Diss.
804. TIAINEN, JONNA. Losses in low-Reynolds-number centrifugal compressors. 2018. Diss.
805. GYASI, EMMANUEL AFRANE. On adaptive intelligent welding: Technique feasibility in weld quality assurance for advanced steels. 2018. Diss.
806. PROSKURINA, SVETLANA. International trade in biomass for energy production: The local and global context. 2018. Diss.

- 807.** DABIRI, MOHAMMAD. The low-cycle fatigue of S960 MC direct-quenched high-strength steel. 2018. Diss.
- 808.** KOSKELA, VIRPI. Tapping experiences of presence to connect people and organizational creativity. 2018. Diss.
- 809.** HERALA, ANTTI. Benefits from Open Data: barriers to supply and demand of Open Data in private organizations. 2018. Diss.
- 810.** KÄYHKÖ, JORMA. Erityisen tuen toimintaprosessien nykytila ja kehittäminen suomalaisessa oppisopimuskoulutuksessa. 2018. Diss.
- 811.** HAJIKHANI, ARASH. Understanding and leveraging the social network services in innovation ecosystems. 2018. Diss.
- 812.** SKRIKO, TUOMAS. Dependence of manufacturing parameters on the performance quality of welded joints made of direct quenched ultra-high-strength steel. 2018. Diss.
- 813.** KARTTUNEN, ELINA. Management of technological resource dependencies in interorganizational networks. 2018. Diss.
- 814.** CHILD, MICHAEL. Transition towards long-term sustainability of the Finnish energy system. 2018. Diss.
- 815.** NUTAKOR, CHARLES. An experimental and theoretical investigation of power losses in planetary gearboxes. 2018. Diss.
- 816.** KONSTI-LAAKSO, SUVI. Co-creation, brokering and innovation networks: A model for innovating with users. 2018. Diss.
- 817.** HURSKAINEN, VESA-VILLE. Dynamic analysis of flexible multibody systems using finite elements based on the absolute nodal coordinate formulation. 2018. Diss.
- 818.** VASILYEV, FEDOR. Model-based design and optimisation of hydrometallurgical liquid-liquid extraction processes. 2018. Diss.
- 819.** DEMESA, ABAYNEH. Towards sustainable production of value-added chemicals and materials from lignocellulosic biomass: carboxylic acids and cellulose nanocrystals. 2018. Diss.
- 820.** SIKANEN, EERIK. Dynamic analysis of rotating systems including contact and thermal-induced effects. 2018. Diss.
- 821.** LIND, LOTTA. Identifying working capital models in value chains: Towards a generic framework. 2018. Diss.
- 822.** IMMONEN, KIRSI. Ligno-cellulose fibre poly(lactic acid) interfaces in biocomposites. 2018. Diss.
- 823.** YLÄ-KUJALA, ANTTI. Inter-organizational mediums: current state and underlying potential. 2018. Diss.
- 824.** ZAFARI, SAHAR. Segmentation of partially overlapping convex objects in silhouette images. 2018. Diss.
- 825.** MÄLKKI, HELENA. Identifying needs and ways to integrate sustainability into energy degree programmes. 2018. Diss.



Acta Universitatis  
Lappeenrantaensis  
826



ISBN 978-952-335-298-8  
ISBN 978-952-335-299-5 (PDF)  
ISSN-L 1456-4491  
ISSN 1456-4491  
Lappeenranta 2018